Heavy Flavour Physics with ATLAS

Andrew Mark Wharton

- Department of Physics -

This thesis is submitted for the degree of Doctor of Philosophy.

- March 2018 -

Acknowledgements

I would like to offer my thanks to the following:

- The Science and Technology Facilities Council and Lancaster University for providing me with the opportunity to complete this PhD;
- My supervisors Profs. Roger Jones and Vakhtang Kartvelishvili, and my technical supervisor, Dr. Maria Smizanska, for their guidance and supervision during my PhD;
- The Lancaster alumni Drs. Adam Barton, James Walder, Alastair Dewhurst, and James Catmore for their guidance, tutoring, and technical leadership during my time on ATLAS;
- My colleagues within the $\mathrm{B_s} \rightarrow \mathrm{J}/\psi\phi$ analysis, and the ATLAS b-physics, Primary Vertexing, and Inner Detector Tracking groups. Within this group I would like to offer special thanks to Dr Pavel Reznicek who spent countless hours correcting my misconceptions on 'the $\mathrm{B_s} \rightarrow \mathrm{J}/\psi\phi$ analysis would be better if …';
- My colleagues at Lancaster University, the ATLAS Collaboration, and CERN. Especially Prof. Guennadi Borissov, and Drs. Harald Fox and Robert Henderson.

On a personal note, I would like to thank my family, friends, and above all Emma, for their continued support and encouragement during my journey over the past few years.

Abstract

This thesis focuses on two measurements made by the ATLAS detector during Run1 of the LHC, and my contributions to these analyses.

The first analysis is a measurement of the $\mathcal{CP}$-violation phase ϕ_{s} in the flavour tagged $\mathrm{B_s} \to \mathrm{J}/\psi\phi$ decay. This analysis was performed using $14.3\,\mathrm{fb}^{-1}$ of ATLAS data collected during 2012 and is combined with the previous ATLAS 7 TeV analysis to produce the final ATLAS Run1 results for this decay. The results of this analysis are:

$$\begin{aligned} \phi_{\mathrm{s}} &= -0.090 \pm 0.078 \text{ (stat.)} \pm 0.041 \text{ (syst.) rad} \\ \Delta\Gamma_{\mathrm{s}} &= \ \ 0.085 \pm 0.011 \text{ (stat.)} \pm 0.007 \text{ (syst.) ps}^{-1} \\ \Gamma_{\mathrm{s}} &= \ \ 0.675 \pm 0.003 \text{ (stat.)} \pm 0.003 \text{ (syst.) ps}^{-1} \end{aligned}$$

and are competitive with, and complement, measurements made at other experiments around the world.

The second analysis is a search for a strongly decaying particle in the decay $\mathrm{X} \to \mathrm{B_s}\pi^{\pm}$; such a state has been claimed by the DØ Collaboration with a mass of $m_{\mathrm{X}} = (5567.8 \pm 2.9)\,\mathrm{MeV}$. No statistically significant observation of such a particle is observed within ATLAS Run1 data, and the 95 % upper confidence limit for the relative production ratio between non-prompt and prompt $\mathrm{B_s}$ candidates is set at $\rho_{\mathrm{X}} < 0.015$. For comparison, DØ report $\rho_{\mathrm{X}} = 0.091 \pm 0.026$ (stat.) $\pm$ 0.016 (syst.). The ATLAS result is compatible with recent results from LHCb, CMS, and CDF in similar searches.

Contents

Contents **iii**

List of Figures **ix**

List of Tables **xi**

1 Introduction **1**

1.1 Measuring $\mathcal{CP}$-Violation in the $\mathrm{B_s} \to \mathrm{J}/\psi\phi$ Decay 1

1.2 Searches for Resonant Structures in the $\mathrm{B_s}\pi^{\pm}$ Mass Spectrum 2

2 Flavour Physics **4**

2.1 The Standard Model of Particle Physics 5

2.1.1 Fundamental Particles 5

2.1.1.1 Quarks and Leptons 6

2.1.1.2 Gauge Bosons 7

2.1.1.3 The Higgs Boson 7

2.1.2 Yukawa Couplings 8

2.1.2.1 Quark Masses 8

2.1.2.2 Quark Mixing 9

2.2 Symmetries and Physics 10

2.2.1 Charge, Parity, and Time Conjugation 10

2.2.1.1 Charge Conjugation 10

2.2.1.2 Parity Conjugation 10

2.2.1.3 Time Conjugation 11

2.2.1.4 $\mathcal{C}$, $\mathcal{P}$, and $\mathcal{T}$ in Classical Electrodynamics . . 11

2.2.1.5 $\mathcal{C}$, $\mathcal{P}$, and $\mathcal{T}$ in Quantum Electrodynamics . . 12

2.2.1.6 The $\mathcal{CPT}$-Theorem 14

2.2.2 Experimental Observations of $\mathcal{C}$-, $\mathcal{P}$-, and $\mathcal{CP}$-Violation 15

2.2.2.1 Observations of $\mathcal{C}$- and $\mathcal{P}$-Violation 16

2.2.2.2 Observations of $\mathcal{CP}$-Violation 16

2.3 $\mathcal{CP}$-Violation in the Standard Model 16

2.3.1 $\mathcal{CP}$-Violation and the Electroweak Interaction Lagrangian . . . 17
2.3.2 The Cabibbo–Kobayashi–Maskawa Matrix . . . 17
2.3.2.1 The Unitarity Triangle(s) . . . 18
2.3.2.2 Alternative Parameterisations . . . 19
2.3.3 $\mathcal{CP}$-Violation in Neutral Meson Decays . . . 19
2.3.3.1 Neutral Meson Mixing . . . 21
2.3.3.2 Neutral Meson Decays . . . 24
2.3.3.3 $\mathcal{CP}$-Violating Effects . . . 26

3 Experimental Apparatus **28**
3.1 The CERN Accelerator Complex . . . 28
3.1.1 Accelerator Physics Nomenclature . . . 29
3.1.1.1 Luminosity . . . 30
3.1.1.2 Pile-Up . . . 30
3.1.1.3 Event Counts . . . 30
3.1.2 The Large Hadron Collider . . . 32
3.1.2.1 The Injector Chain . . . 32
3.1.2.2 The Main Ring . . . 33
3.2 The ATLAS Detector . . . 33
3.2.1 The ATLAS Coordinate Systems and Nomenclature . . . 34
3.2.1.1 Polar Coordinate . . . 36
3.2.1.2 Track Parameterisation . . . 36
3.2.1.3 Particle Properties . . . 36
3.2.1.4 ATLAS Nomenclature . . . 37
3.2.2 Magnet Systems . . . 38
3.2.2.1 Central Solenoid . . . 38
3.2.2.2 Barrel and End-Cap Toroids . . . 39
3.2.3 The Inner Detector . . . 39
3.2.3.1 The Pixel Detector . . . 40
3.2.3.2 The Semiconductor Tracker . . . 40
3.2.3.3 The Transition Radiation Tracker . . . 41
3.2.4 Calorimetry Systems . . . 42
3.2.4.1 Electromagnetic Calorimeters . . . 42
3.2.4.2 Hadronic Calorimeters . . . 44
3.2.4.3 The Forward Calorimeters . . . 45
3.2.5 The Muon Spectrometer . . . 45
3.2.5.1 Resistive Plate Chambers . . . 46
3.2.5.2 Thin Gap Chambers . . . 47
3.2.5.3 Monitored Drift Tube Chambers . . . 47

3.2.5.4 Cathode Strip Chambers 48
3.2.6 The Trigger and Data Acquisition System 48
3.2.6.1 Level-1 Triggers 51
3.2.6.2 The High-Level Trigger 51
3.3 The ATLAS Computing Model 53
3.3.1 Online Software 53
3.3.2 The Computing Grid 54
3.3.2.1 Tiers and Clouds 54
3.3.2.2 Data Management 54
3.3.2.3 Job Management 55
3.3.3 Offline Software 55
3.3.3.1 Data Formats 55
3.3.3.2 The Athena Software Framework 56
3.3.3.3 ROOT 58
3.3.4 Monte Carlo Simulation 58
3.3.4.1 Event Generation 60
3.3.4.2 Detector Simulation and Digitisation 61
3.3.5 Reconstruction 63
3.3.5.1 Track Reconstruction 63
3.3.5.2 Primary Vertex Reconstruction 64
3.3.5.3 Muon Reconstruction 65

4 Measuring $\mathcal{CP}$-Violation in the $\mathrm{B_s} \to \mathrm{J}/\psi\phi$ Decay 67
4.1 Theoretical Overview 67
4.1.1 Helicity and Transversity Formalisms 68
4.1.1.1 The $\mathrm{B_s} \to \mathrm{J}/\psi\phi$ Decay 68
4.1.1.2 The Helicity Basis 69
4.1.1.3 $\mathrm{B_s} \to \mathrm{J}/\psi(\mu^+\mu^-)\phi(\mathrm{K^+K^-})$ Angular Distributions 69
4.1.1.4 The Transversity Basis 71
4.1.2 S-Wave Contributions to the $\mathrm{J}/\psi\mathrm{K^+K^-}$ End-State . . . 72
4.2 $\mathrm{B_s} \to \mathrm{J}/\psi\phi$ Candidate Reconstruction 74
4.2.1 b-Physics Triggers 74
4.2.1.1 Muon Triggers 74
4.2.1.2 Di-Muon Triggers 76
4.2.1.3 Trigger Performance 77
4.2.2 Event Reconstruction 78
4.2.2.1 Event Selection 80
4.2.2.2 $\mathrm{J}/\psi \to \mu^+\mu^-$ Reconstruction 81
4.2.2.3 $\phi \to \mathrm{K^+K^-}$ Reconstruction 81

4.2.2.4 $B_s \to J/\psi(\mu^+\mu^-)\phi(K^+K^-)$ Reconstruction . . 82
4.2.2.5 Event Observables 82
4.3 Flavour Tagging 83
4.3.1 The $B^\pm \to J/\psi K^\pm$ Calibration Sample 83
4.3.1.1 Event Selection 84
4.3.1.2 Sideband Subtraction 84
4.3.2 Flavour Tagging Methods 85
4.3.2.1 Tagging Charge and Flavour Tag Probability 85
4.3.2.2 Lepton Based Tagging 87
4.3.2.3 Jet-Charge Tagging 88
4.3.2.4 Flavour Tagging Performance Metrics 89
4.3.3 The Flavour Tagged $B_s \to J/\psi\phi$ Fit 89
4.4 The Fit Procedure 90
4.4.1 Parameter Estimation 91
4.4.1.1 Likelihood Ratios 92
4.4.1.2 Constrained Fits 92
4.4.1.3 Punzi Terms 93
4.4.2 The $B_s \to J/\psi\phi$ Default Fit 93
4.4.3 Signal 94
4.4.3.1 Detector Acceptance PDF 94
4.4.3.2 Mass PDF 95
4.4.3.3 Proper Decay Time and Transversity Angle PDF 95
4.4.4 Physics Backgrounds 95
4.4.4.1 $B_d \to J/\psi K^{*0}$ Background 96
4.4.4.2 $\Lambda_b \to J/\psi pK^-$ Background 98
4.4.4.3 Observations on the Physics Backgrounds Models in the 7 TeV and 8 TeV Analyses 102
4.4.5 Combinatorial Background 106
4.4.5.1 Mass PDF 106
4.4.5.2 Proper Decay Time PDF 106
4.4.5.3 Transversity Angle PDF 106
4.4.6 Punzi Terms 109
4.4.6.1 Proper Decay Time Uncertainty 109
4.4.6.2 p_T 109
4.4.6.3 Flavour Tagging 110
4.4.7 Default Fit Results 113
4.4.7.1 Fit Projections 113
4.4.7.2 1D Likelihood Scans 114
4.4.7.3 2D Likelihood Scans 117

4.5 Stability Tests and Systematic Errors 121
  4.5.1 Stability Tests 121
    4.5.1.1 Event Selection and Trigger Re-weightings . . 121
    4.5.1.2 Flavour Tagging 123
    4.5.1.3 Inner Detector Alignment 123
    4.5.1.4 Detector Acceptance PDF 123
    4.5.1.5 Bias in the Default Model 125
  4.5.2 Signal and Combinatorial Background Model Variations 126
    4.5.2.1 Fit Model Variations 126
    4.5.2.2 Combinatorial Background Transversity Angle Model Variations 126
  4.5.3 Physics Background Model Variations 127
    4.5.3.1 Physics Background Fractions 127
    4.5.3.2 $\mathrm{B_d} \to \mathrm{J}/\psi\mathrm{K}^{*0}$ Background 127
    4.5.3.3 $\Lambda_\mathrm{b} \to \mathrm{J}/\psi\mathrm{pK}^-$ Background 128
  4.5.4 Flavour Tagging Systematic Errors 131
    4.5.4.1 Statistical Errors 131
    4.5.4.2 Systematic Errors 131
    4.5.4.3 Flavour Tagging Punzi Terms 133
  4.5.5 Results 134
4.6 Run1 Results 136
  4.6.1 Statistical Combination 136
  4.6.2 The Best Linear Unbiased Estimate Combination . . . 138
    4.6.2.1 The Best Linear Unbiased Estimate 138
    4.6.2.2 Best Linear Unbiased Estimate Results 138
    4.6.2.3 Stability Under Alternative Assumptions . . . 139

5 Searches for Resonant Structures in the $\mathrm{B_s}\pi^\pm$ Mass Spectrum 141
5.1 Theoretical Overview 141
5.2 Event Selection 142
  5.2.1 $\mathrm{B_s}$ Candidate Reconstruction 143
  5.2.2 $\mathrm{B_s}\pi^\pm$ Candidate Reconstruction 144
    5.2.2.1 Event Observables 144
    5.2.2.2 Optimisation of $\mathrm{B_s}$ Reconstruction Criteria . 144
    5.2.2.3 Optimisation of $\mathrm{B_s}\pi^\pm$ Reconstruction Criteria 144
5.3 Fit Models 146
  5.3.1 $\mathrm{B_s}$ Mass Fits 147
    5.3.1.1 Signal Component 147
    5.3.1.2 Combinatorial Background Component 147

5.3.1.3 The Fit Procedure 147
5.3.2 $B_s\pi^{\pm}$ Mass Fits 147
5.3.2.1 Signal Component 148
5.3.2.2 Background Component 148
5.3.2.3 The Fit Procedure 148
5.4 Results 149
5.4.1 B_s Mass Fits 149
5.4.2 $B_s\pi^{\pm}$ Mass Fits 149
5.4.3 Upper Limits on ρ_X 149
5.4.3.1 CLs Limits on Signal Event Counts 154
5.4.3.2 CLs Limits on ρ_X 155
5.4.3.3 Generalised Search for a $B_s\pi^{\pm}$ Resonance . . 156

6 Conclusions 158
6.1 Measuring $\mathcal{CP}$-Violation in the $B_s \to J/\psi\phi$ Decay 158
6.2 Searches for Resonant Structures in the $B_s\pi^{\pm}$ Mass Spectrum 160

A $B_s \to J/\psi\phi$, Additional Information 162

B Glossary of Terms 164

Bibliography 166

List of Figures

2.1 Unitarity triangles for the un-‘squashed’ triangles 20
2.2 The $B_s^0 \rightsquigarrow \overline{B}_s^0$ Mixing Diagrams 24

3.1 The CERN Accelerator Complex 29
3.2 LHC Run1 Performance 31
3.3 The ATLAS Detector 35
3.4 The ATLAS Coordinate System 35
3.5 The ATLAS Charged Track Parameterisation 37
3.6 The ATLAS Magnet Systems 38
3.7 The ATLAS Inner Detector 40
3.8 ATLAS Inner Detector Envelopes 42
3.9 The ATLAS Calorimetry Systems 43
3.10 ATLAS Calorimeter Modules 45
3.11 The ATLAS Muon Spectrometer 46
3.12 ATLAS Muon Spectrometer Components 49
3.13 ATLAS Muon Spectrometer Components 50
3.14 The ATLAS Trigger and Data Acquisition System 52
3.15 The Gaudi Framework 58
3.16 The ATLAS Simulation Infrastructure 59
3.17 Data Flow for the `PythiaB` Algorithm 62
3.18 PV Position Resolution 65

4.1 The $B_s \to J/\psi\phi$ Decay 69
4.2 Helicity Angles 71
4.3 Transversity Angles 72
4.4 ATLAS Trigger Rates 75
4.5 Di-Muon Triggers in ATLAS 77
4.6 b-Physics Trigger Efficiency 79
4.7 `L2StarB` Trigger Efficiency as a Function of Proper Decay Time . . 79
4.8 Mass Fit Projection for the $B^\pm \to J/\psi K^\pm$ Calibration Sample . . . 86
4.9 Tagging Charge Distributions for the Flavour Tagging Methods . . 88

4.10 $B_d \to J/\psi K^{*0}$ Helicity Angle Distributions 99
4.11 1D Transversity Angle Fit Projections for $B_d \to J/\psi K^{*0}$ Events . . 100
4.12 2D Transversity Angle Fit Projections for $B_d \to J/\psi K^{*0}$ Events . . 101
4.13 $m(pK^-)$ for the $\Lambda_b \to J/\psi pK^-$ Physics Background 102
4.14 1D Transversity Angle Fit Projections for $\Lambda_b \to J/\psi pK^-$ Events . 103
4.15 2D Transversity Angle Fit Projections for $\Lambda_b \to J/\psi pK^-$ Events . 104
4.16 $m(J/\psi K^+K^-)$ for Physics Background Components 105
4.17 $B_d \to J/\psi K^{*0}$ MC Events 107
4.18 B_d Background Mass Distributions 108
4.19 Proper Decay Time Uncertainty and p_T Punzi PDFs 111
4.20 Flavour Tag Probability Punzi Terms 112
4.21 Fit Projection for the $B_s \to J/\psi\phi$ Default Fit 115
4.22 Transversity Angle Fit Projections for the $B_s \to J/\psi\phi$ Default Fit . 116
4.23 1D Likelihood Scans for the $B_s \to J/\psi\phi$ Default Fit 118
4.24 1D Likelihood Scans with Multiple Minima 119
4.25 2D Likelihood Scans for the $B_s \to J/\psi\phi$ Default Fit 120
4.26 Stability of the Default Fit Under B_s Mass Window Variations . . 122
4.27 Tagging Power Variations of the $B_s \to J/\psi\phi$ Default Fit 124
4.28 Acceptance Maps Tests 125
4.29 2D Likelihood Scans for the $B_s \to J/\psi\phi$ Statistical Combination . 137

5.1 Possible X decays 142
5.2 $S/\sqrt{S+B}$ as a Function of $p_T(\pi^\pm)$ 146
5.3 B_s Mass Fit Projection 150
5.4 B_s Mass Fit Projections 151
5.5 $B_s\pi^\pm$ Mass Fit Projections 152
5.6 $B_s\pi^\pm$ Mass Fit Projections 153
5.7 ρ_X Scan as a Function of $m(X)$ 157

6.1 2D Likelihood Scans for the $B_s \to J/\psi\phi$ Decay 160

List of Tables

2.1 Quantum Numbers for the Standard Model Fields 6
2.2 Transformation Properties for QED Fields 14

4.1 $\mathcal{O}_k$ for P-Wave $\mathrm{B_s} \to \mathrm{J}/\psi(\mu^+\mu^-)\phi(\mathrm{K^+K^-})$ Decays 72
4.2 g_k for P-Wave $\mathrm{B_s} \to \mathrm{J}/\psi(\mu^+\mu^-)\phi(\mathrm{K^+K^-})$ Decays 73
4.3 $\mathcal{O}_k$ for S-Wave $\mathrm{B_s} \to \mathrm{J}/\psi(\mu^+\mu^-)\phi(\mathrm{K^+K^-})$ Decays 73
4.4 g_k for S-Wave $\mathrm{B_s} \to \mathrm{J}/\psi(\mu^+\mu^-)\phi(\mathrm{K^+K^-})$ Decays 73
4.5 Trigger Event Counts for the $\mathrm{B_s} \to \mathrm{J}/\psi\phi$ Default Fit 80
4.6 $\mathrm{B}^\pm \to \mathrm{J}/\psi\mathrm{K}^\pm$ Calibration Sample Event Counts 85
4.7 Opposite-Side Tagger Performance Metrics 90
4.8 T_k for S- and P-Wave $\mathrm{B_s} \to \mathrm{J}/\psi\mathrm{K^+K^-}$ Decays 90
4.9 Physics Background Fractions for the $\mathrm{B_d} \to \mathrm{J}/\psi\mathrm{K}^{*0}$ Background . 96
4.10 Physics Background Fractions for the $\Lambda_\mathrm{b} \to \mathrm{J}/\psi\mathrm{pK}^-$ Background . 96
4.11 Physics Background Selection Efficiencies 97
4.12 Flavour Tagging Method Punzi Terms 110
4.13 Flavour Tag Probability Punzi Terms 113
4.14 Fit Results for the $\mathrm{B_s} \to \mathrm{J}/\psi\phi$ Default Fit 114
4.15 Fit Correlations for the $\mathrm{B_s} \to \mathrm{J}/\psi\phi$ Default Fit 114
4.16 Systematic Errors due to b-Physics Backgrounds 130
4.17 Flavour Tagging Systematic Errors for the $\mathrm{B_s} \to \mathrm{J}/\psi\phi$ Default Fit 134
4.18 Summary of the Fit Systematics for the 8 TeV Fit 135
4.19 Fit Results for the 8 TeV $\mathrm{B_s} \to \mathrm{J}/\psi\phi$ Fit 136
4.20 Fit Results of the Run1 $\mathrm{B_s} \to \mathrm{J}/\psi\phi$ Statistical Combination 138
4.21 Fit Results for the $\mathrm{B_s} \to \mathrm{J}/\psi\phi$ Run1 Best Linear Unbiased Estimate 139
4.22 Alternative BLUE Combinations 140

5.1 ρ_X as a Function of Proper Decay Time Cuts 145
5.2 $\mathrm{B_s}$ Signal Candidates Event Counts 150
5.3 X Event Counts 151
5.4 95 % CLs Limits on N_X 155
5.5 95 % CLs Limits on ρ_X 156

A.1 DQ2 Datasets and GRLs 163

Chapter 1

Introduction

This thesis describes my contributions to two analyses performed within the ATLAS b-physics group. The first is a measurement of the properties of the $\mathrm{B_s} \to \mathrm{J}/\psi\phi$ decay, that is used as a method of searching for physics not predicted by the Standard Model. The second is a search for a new particle, reported by a single collaboration, where ATLAS seeks to serve as cross-confirmation of the particle's existence. Details about my specific contributions to these analyses are given in sections 1.1 and 1.2.

Chapters 2 and 3 are given over to introductory material on the theoretical and experimental aspects of modern high-energy particle physics. Descriptions of the $\mathrm{B_s} \to \mathrm{J}/\psi\phi$ analysis and the $\mathrm{B_s}\pi^{\pm}$ analysis can be found in chapters 4 and 5 respectively. The final chapter, chapter 6, places the results of the analyses in the context of the wider particle physics programme and offers ideas for future research.

The Feynman diagrams in this thesis have been prepared with the `TikZ-Feynman` LaTeX package [1].

A glossary of terms used in this thesis is provided in appendix B.

1.1 Measuring $\mathcal{CP}$-Violation in the $\mathrm{B_s} \to \mathrm{J}/\psi\phi$ Decay

This analysis is a precision measurement of the $\mathcal{CP}$-violation phase, ϕ_{s}, in the $\mathrm{B_s} \to \mathrm{J}/\psi\phi$ decay. Over the course of my PhD I have worked on most areas of this analysis, however my significant contributions (in roughly chronological order) are:

- Examination of multivariate and machine learning approaches to increase the tagging power available to the analysis. This work was not included in the 8 TeV and Run1 analyses, however it is ongoing for the Run2 analysis;

- Goodness of fit evaluation of the model PDFs to select the default fit model;
- Generation of Punzi PDFs, and automating their generation;
- Systematic review of the software used in the fit, resulting in a number of optimisations and bug-fixes of the default fit tool-chain;
- Development of a number of tools used to investigate the behaviour of the $\mathrm{B_s} \to \mathrm{J}/\psi\phi$ default fit around 'false-minima' in the likelihood function;
- Investigation of the b-physics background contributions to the $\mathrm{B_s} \to \mathrm{J}/\psi\phi$ dataset. This work uncovered a number of serious deficiencies in the analysis (and the previous 7 TeV analyses) and led to a complete re-implementation of the $\mathrm{B_d}$ backgrounds model, and the introduction of the Λ_b background model;
- Implementation of a new suite of flavour tagging systematic uncertainty tests.

In addition to these contributions, due to the limited manpower in the analysis team toward the final days of the analysis, I was responsible for minor updates to almost all areas of the analysis code[1].

1.2 Searches for Resonant Structures in the $\mathrm{B_s}\pi^{\pm}$ Mass Spectrum

This analysis is a search for a novel, exotic, four-flavour state reported by the DØ Collaboration. The entirety of this analysis was performed during my PhD, and I had the opportunity to contribute in the following areas:

- I was responsible for the development of the overall analysis strategy;
- I developed the initial `RooFit` based $\mathrm{B_s} \to \mathrm{J}/\psi\phi$ mass fit;
- I produced the $\mathrm{B_s}\pi^{\pm}$ mass fit, and the associated CLs limit[2] setting code for event counts and relative production ratios;

---

[1] Detector acceptance maps being the only component of the Run1 analysis I've not worked on.

[2] Throughout this thesis, the phrase "CLs (confidence) limit" should be read as "(confidence) limit set using the CLs method", see [2, 3, 4].

- I implemented the grid software required for the mass dependent CLs limit setting.

In addition to these significant contributions, I assisted Dr Barton with the validation of the methods used to optimise the candidate selection criteria, and tutored a number of new PhD students in the use of `ROOT`, `RooFit`, and `RooStats`.

Chapter 2

Flavour Physics

The *Standard Model of Particle Physics* (SM) [5, 6, 7, 8] is the currently accepted theory for physics at the smallest length scales and highest energy levels, and while the theory is inherently incomplete (the SM lacks a quantum theory for gravity, and does not offer viable dark matter or dark energy candidates), it stands as one of the most successful attempts to describe the fundamental physical laws of the universe.

The search for *Physics Beyond the Standard Model* (BSM) is possible through indirect methods where SM predictions are compared to measurements obtained from experimental data, and deviations from the Null hypothesis (No BSM physics observed in this measurement) infer BSM physics. The field of *Flavour Physics* provides many useful laboratories for these Null hypothesis searches as the parameters of the SM governing this regime may be measured directly and indirectly, with the direct measurements providing high-precision predictions for indirect processes. The $\mathrm{B_s} \to \mathrm{J}/\psi\phi$ decay, as an indirect process, has long been considered a 'golden-channel' for such measurements with various BSM models expected to affect the physical observables of the decay.

The remainder of this chapter provides a brief overview of the mathematical formulation of the SM (section 2.1) and introduces the field of quark flavour physics. The role of discrete symmetries in classical and quantum field theories (section 2.2), how these symmetries may be broken in nature, and the observable effects of such broken symmetries on the decays of neutral mesons (section 2.3) are then discussed.

Additional theoretical background material for the $\mathrm{B_s} \to \mathrm{J}/\psi\phi$ decay and possible tetraquark decays to a $\mathrm{B_s}\pi^{\pm}$ end-state is provided in sections 4.1 and 5.1

respectively.

2.1 The Standard Model of Particle Physics

The SM is a non-Abelian Yang-Mills relativistic quantum field theory [9] with an overall gauge symmetry of $\mathrm{SU(3)_C \times SU(2)_L \times U(1)_Y}$. The $\mathrm{SU(3)_C}$ group[1] gives rise to quantum chromodynamics [10], while the the $\mathrm{SU(2)_L \times U(1)_Y}$ groups, related to weak isospin and weak hypercharge respectively, undergo a *Spontaneous Symmetry Breaking* (SSB) [11, 12] of the ground state, leading to

$$\mathrm{SSB : SU(3)_C \times SU(2)_L \times U(1)_Y \xrightarrow{SSB} SU(3)_C \times U(1)_{EM}} \tag{2.1}$$

and resulting in electroweak unification, where the massless bosons of the $\mathrm{SU(2)_L \times U(1)_Y}$ symmetry transform to the three massive, physically observable bosons of the weak force, and the massless photon of quantum electrodynamics [13].

The Lagrangian of the SM, $\mathcal{L}_{\mathrm{SM}}$, consists of three components

$$\mathcal{L}_{\mathrm{SM}} = \mathcal{L}_{\mathrm{Kinetic}} + \mathcal{L}_{\mathrm{Higgs}} + \mathcal{L}_{\mathrm{Yukawa}} \tag{2.2}$$

where $\mathcal{L}_{\mathrm{Kinetic}}$ and $\mathcal{L}_{\mathrm{Higgs}}$ control the dynamics of the fermionic and scalar field content of the SM under the applied gauge symmetry (sections 2.1.1.1 and 2.1.1.3). The final component, $\mathcal{L}_{\mathrm{Yukawa}}$, couples the fermionic and scalar fields and is discussed in section 2.1.2.

2.1.1 Fundamental Particles

The fundamental fields of the SM are categorised according to their spin quantum number:

- *Fermions*– Defined by their half-integer spin, and further divided into the quark and lepton fields;
- *Bosons*– Fields of integer spin. The Higgs field, ϕ, is a spin-0 field, while the gauge fields arise from the gauge symmetries applied to the fermionic and Higgs fields, and provide interaction forces between the fundamental fields.

The following notation is used for the remainder of this thesis: the quark fields are labelled Q, u, and d with a superscript I denoting the interaction basis[2],

---

[1] The subscript C, L, and Y are historical, and used to differentiate these symmetries from other SU symmetries that arise in ad hoc models.

[2] as opposed to the more usual mass basis.

Field	$\mathrm{SU(3)_C}$	$\mathrm{SU(2)_L}$	q_Y	q_EM
$\mathrm{Q}^\mathrm{I}_\mathrm{L}$	3	2	$1/3$	$2/3,\ -1/3$
u^I_R	3	1	$4/3$	$2/3$
d^I_R	3	1	$-2/3$	$-1/3$
$\mathrm{L}^\mathrm{I}_\mathrm{L}$	1	2	-1	$0,\ -1$
$\nu^\mathrm{I}_\mathrm{R}$ †	1	1	0	0
$\ell^\mathrm{I}_\mathrm{R}$	1	1	-2	-1
ϕ	1	2	1	$1,\ 0$

† Not experimentally observed

Table 2.1: Quantum numbers for the Standard Model fields. Shown are the order of the representation of $\mathrm{SU(3)_C}$ and $\mathrm{SU(2)_L}$ the fields transform under, and the coupling to the $\mathrm{U(1)_Y}$ and $\mathrm{U(1)_{EM}}$ gauge symmetries (q_Y and q_EM respectively), with $q_\mathrm{EM} = T_z + q_\mathrm{Y}/2$, where T_z is the third component of weak isospin. Quantum numbers for the $\nu^\mathrm{I}_\mathrm{R}$ field are based on assumptions of an undiscovered SM sterile neutrino [14].

and subscript L's and R's[3] differentiate the doublet and singlet representations of the $\mathrm{SU(2)_L}$ symmetry group respectively with u^I_L and d^I_L the $T_z = \pm\frac{1}{2}$ components of $\mathrm{Q}^\mathrm{I}_\mathrm{L}$ under $\mathrm{SU(2)_L}$, where T_z is the third component of weak isospin. This arrangement is repeated with the lepton fields L, ν, and ℓ. For quark and lepton fields, subscript roman indices are used to specify generations ($1 \rightarrow 3$, see section 2.1.2). The gauge transformation properties and quantum charges for the quark, lepton, and Higgs fields are shown in table 2.1.

2.1.1.1 Quarks and Leptons

The quark and lepton fields are represented by Dirac spinors [15, 16], leading to the kinetic Lagrangian

$$\mathcal{L}^{\text{Fermions}}_{\text{Kinetic}} = i \cdot \overline{\psi}^\mathrm{I}(D^\mu \gamma_\mu)\psi^\mathrm{I} \tag{2.3}$$

where $\overline{\psi}^\mathrm{I} \equiv \psi^{\mathrm{I}\dagger}\gamma^0$ and the gauge covariant derivative D^μ [15, 16] is defined as

$$D^\mu = \partial^\mu + i\left(g_\mathrm{C} \cdot \lambda_\mathrm{a} \mathrm{G}^\mu_\mathrm{a} + \frac{g_\mathrm{L}}{2} \cdot \sigma_\mathrm{b} \mathrm{W}^\mu_\mathrm{b} + q_\mathrm{Y}\frac{g_\mathrm{Y}}{2} \cdot \mathrm{B}^\mu\right) \tag{2.4}$$

with g_C, g_L, and g_Y being the coupling constants for their respective gauge groups while λ and σ are the generators of SU(3) and SU(2) and sum over the components of the gauge fields G, W, and B.

---

[3] With the L and R denoting left and right chirality.

Fields that transform under the singlet representations of $\mathrm{SU(3)_C}$ and $\mathrm{SU(2)_L}$ omit the relevant terms from D^μ.

2.1.1.2 Gauge Bosons

The field strength tensor for a gauge field is given by

$$\mathrm{F}_{\mathrm{a}}^{\mu\nu} = \partial^\mu \mathrm{F}_{\mathrm{a}}^\nu - \partial^\nu \mathrm{F}_{\mathrm{a}}^\mu + g \cdot f^{abc} \mathrm{F}_{\mathrm{b}}^\mu \mathrm{F}_{\mathrm{c}}^\nu \tag{2.5}$$

where f^{abc} is the structure function for the gauge group and g the self-coupling. The contribution to the kinetic Lagrangian from the gauge fields is

$$\mathcal{L}_{\text{Kinetic}}^{\text{Bosons}} = -\frac{1}{2}\,\mathrm{Tr}(\mathrm{G}^{\mu\nu}\mathrm{G}_{\mu\nu}) - \frac{1}{2}\,\mathrm{Tr}(\mathrm{W}^{\mu\nu}\mathrm{W}_{\mu\nu}) - \frac{1}{4}\mathrm{B}^{\mu\nu}\mathrm{B}_{\mu\nu}. \tag{2.6}$$

Of particular interest is the charged current interaction that arises from the $\mathrm{SU(2)_L}$ gauge symmetry

$$\begin{aligned}\mathcal{L}_{\text{Electroweak}}^{\text{Quarks}} &= \overline{\mathrm{Q}}_{\mathrm{L,i}}^{\mathrm{I}} \left(-\frac{g_{\mathrm{L}}}{2} \cdot \sigma_{\mathrm{b}} \mathrm{W}_{\mathrm{b}}^\mu \cdot \gamma_\mu\right) \mathrm{Q}_{\mathrm{L,i}}^{\mathrm{I}} \\ &= -\frac{g_{\mathrm{L}}}{\sqrt{2}} \left(\overline{u}_{\mathrm{L,i}}^{\mathrm{I}} \mathrm{W}^{-,\mu} \gamma_\mu d_{\mathrm{L,i}}^{\mathrm{I}} + \overline{d}_{\mathrm{L,i}}^{\mathrm{I}} \mathrm{W}^{+,\mu} \gamma_\mu u_{\mathrm{L,i}}^{\mathrm{I}}\right) - \cdots\end{aligned} \tag{2.7}$$

where the charged electroweak fields are defined as

$$\mathrm{W}^\pm = \frac{1}{\sqrt{2}}(\mathrm{W}_1 \mp i \cdot \mathrm{W}_2). \tag{2.8}$$

2.1.1.3 The Higgs Boson

The Higgs field is a complex scalar field and has the Lagrangian

$$\mathcal{L}_{\text{Higgs}} = (D_\mu \phi)^\dagger (D^\mu \phi) - V(\phi^\dagger \phi) \tag{2.9}$$

with ϕ the $\mathrm{SU(2)_L}$ isospin doublet

$$\phi = \begin{bmatrix} \phi^+ \\ \phi^0 \end{bmatrix}_{\mathrm{L}} \tag{2.10}$$

and V is the Higgs self-interaction potential. The Higgs potential

$$V(\phi^\dagger \phi) = -\mu^2 \cdot \phi^\dagger \phi + \lambda \cdot (\phi^\dagger \phi)^2 \tag{2.11}$$

has a 'Mexican hat'[4] [17] form[5], leading to a SSB and reducing the Higgs field to

$$\text{SSB}: \begin{bmatrix} \phi^+ \\ \phi^0 \end{bmatrix}_{\mathrm{L}} \xrightarrow{\text{SSB}} \frac{1}{\sqrt{2}} \begin{bmatrix} 0 \\ v + h(\mathrm{x}) \end{bmatrix}_{\mathrm{L}} \tag{2.12}$$

---

[4] The term is attributed to Goldstone, as the shape of the potential mimics a Sombrero.

[5] With $\mu^2 > 0$ and $\lambda > 0$.

where v is the *Vacuum Expectation Value* (VEV) [18] and $h(\mathrm{x})$ is the observable Higgs field[6]. This SSB leads to a mass term for the Higgs boson (from h^2 terms in the expansion of the potential term of $\mathcal{L}_{\mathrm{Higgs}}$), and mass terms for the three of the electroweak bosons of the broken $\mathrm{SU}(2)_{\mathrm{L}} \times \mathrm{U}(1)_{\mathrm{Y}}$ gauge symmetry from the quadratic terms arising from the expansion of the kinetic component of $\mathcal{L}_{\mathrm{Higgs}}$.

The mixing between the W_3 and B fields due to the SSB is governed by the Weinberg angle, θ_{W}, and gives a rotation between the basis states, yielding the physically observable, neutral currents of the electroweak interaction

$$\mathrm{A} = \mathrm{W}_3 \cdot \sin(\theta_{\mathrm{W}}) + \mathrm{B} \cdot \cos(\theta_{\mathrm{W}}) \tag{2.13a}$$

$$\mathrm{Z} = \mathrm{W}_3 \cdot \cos(\theta_{\mathrm{W}}) - \mathrm{B} \cdot \sin(\theta_{\mathrm{W}}) \tag{2.13b}$$

where

$$\cos(\theta_{\mathrm{W}}) = \frac{g_{\mathrm{L}}}{\sqrt{g_{\mathrm{L}}^2 + g_{\mathrm{Y}}^2}} \tag{2.14a}$$

$$\sin(\theta_{\mathrm{W}}) = \frac{g_{\mathrm{Y}}}{\sqrt{g_{\mathrm{L}}^2 + g_{\mathrm{Y}}^2}}. \tag{2.14b}$$

2.1.2 Yukawa Couplings

The final component of the SM Lagrangian, $\mathcal{L}_{\mathrm{Yukawa}}$, is a coupling between the fermionic fields and the Higgs field, and provides mass terms for the fermionic fields that respect the overall chiral symmetry of the SM, and the mixing of quark generations that gives rise to the field of flavour physics. The SM *Yukawa Lagrangian*[19] is defined as

$$\mathcal{L}_{\mathrm{Yukawa}} = Y_{ij} \cdot \overline{\psi}^{\mathrm{I}}_{\mathrm{L,i}} \phi \psi^{\mathrm{I}}_{\mathrm{R,j}} + \mathrm{h.c.} \tag{2.15}$$

where Y is the *Yukawa Coupling*, an arbitrary complex matrix operating in generation space. For the coupling between the quark–quark fields, this leads to

$$\mathcal{L}^{\mathrm{Quarks}}_{\mathrm{Yukawa}} = Y^d_{ij} \cdot \overline{\mathrm{Q}}^{\mathrm{I}}_{\mathrm{L,i}} \phi d^{\mathrm{I}}_{\mathrm{R,j}} + Y^u_{ij} \cdot \overline{\mathrm{Q}}^{\mathrm{I}}_{\mathrm{L,i}} \widetilde{\phi} u^{\mathrm{I}}_{\mathrm{R,j}} + \mathrm{h.c.} \tag{2.16}$$

with

$$\widetilde{\phi} = i \cdot \sigma_2 \phi^*. \tag{2.17}$$

2.1.2.1 Quark Masses

Mass terms for the quarks are obtained through the Yukawa couplings when the Higgs field obtains a non-zero VEV (eq. (2.12)). Expanding the first term

---

[6] With its associated boson [12].

of eq. (2.16) leads to

$$Y_{ij}^{d}\cdot\overline{\mathrm{Q}}_{\mathrm{L,i}}^{\mathrm{I}}\phi d_{\mathrm{R,j}}^{\mathrm{I}}=\frac{Y_{ij}^{d}}{\sqrt{2}}\left(v\cdot\overline{d}_{\mathrm{L,i}}^{\mathrm{I}}d_{\mathrm{R,j}}^{\mathrm{I}}+h(\mathrm{x})\cdot\overline{d}_{\mathrm{L,i}}^{\mathrm{I}}d_{\mathrm{R,j}}^{\mathrm{I}}\right)\tag{2.18}$$

where the $h(\mathrm{x})\cdot\overline{d}_{\mathrm{L,i}}^{\mathrm{I}}d_{\mathrm{R,j}}^{\mathrm{I}}$ term gives an interaction between the quarks and the Higgs field, so eq. (2.16) may be recast as

$$\mathcal{L}_{\mathrm{Yukawa}}^{\mathrm{Quarks}}=M_{ij}^{d}\cdot\overline{d}_{\mathrm{L,i}}^{\mathrm{I}}d_{\mathrm{R,j}}^{\mathrm{I}}+M_{ij}^{u}\cdot\overline{u}_{\mathrm{L,i}}^{\mathrm{I}}u_{\mathrm{R,j}}^{\mathrm{I}}+\mathrm{h.c.}+\mathrm{interactions}\tag{2.19}$$

with

$$M_{ij}=\frac{v}{\sqrt{2}}Y_{ij}.\tag{2.20}$$

To form mass terms, the M matrices must be diagonal. This is achieved through four unitary matrices V with

$$M_{\mathrm{Diag}}^{d}=V_{\mathrm{L}}^{d}M^{d}V_{\mathrm{R}}^{d\dagger}\quad(2.21\mathrm{a})\qquad M_{\mathrm{Diag}}^{u}=V_{\mathrm{L}}^{u}M^{u}V_{\mathrm{R}}^{u\dagger}.\quad(2.21\mathrm{b})$$

Combining the first term of eq. (2.19) with eq. (2.21a) gives

$$\begin{aligned}\overline{d}_{\mathrm{L}}^{\mathrm{I}}M^{d}d_{\mathrm{R}}^{\mathrm{I}}&=\overline{d}_{\mathrm{L}}^{\mathrm{I}}\left(V_{\mathrm{L}}^{d\dagger}V_{\mathrm{L}}^{d}\right)M^{d}\left(V_{\mathrm{R}}^{d\dagger}V_{\mathrm{R}}^{d}\right)d_{\mathrm{R}}^{\mathrm{I}}\\&=\overline{d}_{\mathrm{L}}M_{\mathrm{Diag}}^{d}d_{\mathrm{R}}\end{aligned}\tag{2.22}$$

where d_{L} and d_{R} represent the quarks in the mass, rather than the interaction basis. The quark fields convert as

$$d_{\mathrm{L,i}}=V_{\mathrm{L}}^{d}ij\,d_{\mathrm{L,j}}^{\mathrm{I}}\quad(2.23\mathrm{a})\qquad u_{\mathrm{L,i}}=V_{\mathrm{L}}^{u}ij\,u_{\mathrm{L,j}}^{\mathrm{I}}\quad(2.23\mathrm{c})$$

$$d_{\mathrm{R,i}}=V_{\mathrm{R}}^{d}ij\,d_{\mathrm{R,j}}^{\mathrm{I}}\quad(2.23\mathrm{b})\qquad u_{\mathrm{R,i}}=V_{\mathrm{R}}^{u}ij\,u_{\mathrm{R,j}}^{\mathrm{I}}\quad(2.23\mathrm{d})$$

so neglecting the interaction terms with the Higgs field, $\mathcal{L}_{\mathrm{Yukawa}}$ for the quarks may now be expressed in the mass basis as

$$\mathcal{L}_{\mathrm{Yukawa}}^{\mathrm{Quarks,\ Mass}}=\overline{d}_{\mathrm{L}}M_{\mathrm{Diag}}^{d}d_{\mathrm{R}}+\overline{u}_{\mathrm{L}}M_{\mathrm{Diag}}^{u}u_{\mathrm{R}}+\mathrm{h.c.}\tag{2.24}$$

2.1.2.2 Quark Mixing

The other terms of the SM Lagrangian may also be expressed in the mass basis for the fermions. The first term of the charged current interaction, eq. (2.7), transforms as [20]

$$\overline{u}_{\mathrm{L,i}}^{\mathrm{I}}\mathrm{W}^{-,\mu}\gamma_{\mu}d_{\mathrm{L,i}}^{\mathrm{I}}\xrightarrow[\mathrm{Basis}]{\mathrm{Mass}}\overline{u}_{\mathrm{L,i}}\left(V_{\mathrm{L}}^{u}V_{\mathrm{L}}^{d\dagger}\right)_{ij}\mathrm{W}^{-,\mu}\gamma_{\mu}d_{\mathrm{L,j}}\tag{2.25}$$

where the unitary matrix V_{CKM}

$$V_{\mathrm{CKM}}=V_{\mathrm{L}}^{u}V_{\mathrm{L}}^{d\dagger}\tag{2.26}$$

is the *Cabibbo–Kobayashi–Maskawa* (CKM) matrix, mixing the interaction and mass eigenstates in weak interactions. By convention, the V matrices are defined such that the weak interaction states and mass eigenstates coincide for the up-type quarks, leading to

$$\begin{aligned} u^{\mathrm{I}} &= u \\ d^{\mathrm{I}}_{\mathrm{i}} &= V_{\mathrm{CKM},ij}\, d_{\mathrm{j}} \end{aligned} \tag{2.27}$$

or explicitly

$$\begin{bmatrix} \mathrm{d}^{\mathrm{I}} \\ \mathrm{s}^{\mathrm{I}} \\ \mathrm{b}^{\mathrm{I}} \end{bmatrix} = \begin{bmatrix} V_{\mathrm{ud}} & V_{\mathrm{us}} & V_{\mathrm{ub}} \\ V_{\mathrm{cd}} & V_{\mathrm{cs}} & V_{\mathrm{cb}} \\ V_{\mathrm{td}} & V_{\mathrm{ts}} & V_{\mathrm{tb}} \end{bmatrix} \begin{bmatrix} \mathrm{d} \\ \mathrm{s} \\ \mathrm{b} \end{bmatrix} . \tag{2.28}$$

2.2 Symmetries and Physics

Symmetries and their connection to conservation laws are a well established cornerstone of modern physics, with Noether's theorem [21] showing that every differentiable symmetry of the action functional for a system yields a corresponding conserved quantity. While the symmetries that give rise to these conservation laws are continuously connected to the origin, a second class of symmetries, that of discrete symmetries, is also of interest in classical and quantum physics.

2.2.1 Charge, Parity, and Time Conjugation

Symmetry transformations of discrete groups, occur in many branches of physics with discrete transformations of charge, space, and time of particular interest in particle physics.

2.2.1.1 Charge Conjugation

Charge Conjugation, $\mathcal{C}$, transforms a particle into an anti-particle of equal mass, momentum, and spin by negating all its (internal) quantum numbers, leading to

$$\mathcal{C} : |\mathrm{P}\rangle \xrightarrow{\mathcal{C}} |\overline{\mathrm{P}}\rangle \,. \tag{2.29}$$

This is well defined in the realm of relativistic field theories, but requires an ad hoc interpretation in classical physics.

2.2.1.2 Parity Conjugation

The *Parity Transformation*, $\mathcal{P}$, transforms a spacial-coordinate $\vec{\mathbf{x}}$ into $-\vec{\mathbf{x}}$. The temporal coordinate, t, of a space-time four-vector ($\mathrm{r} = [t \quad \vec{\mathbf{x}}]^{\mathrm{T}}$) remains unchanged, giving

$$\mathcal{P} : \mathrm{r} \xrightarrow{\mathcal{P}} \begin{bmatrix} t \\ -\vec{\mathbf{x}} \end{bmatrix}. \tag{2.30}$$

For momentum and angular-momentum $\vec{\mathbf{p}} \xrightarrow{\mathcal{P}} -\vec{\mathbf{p}}$ and $\vec{\mathbf{l}} \equiv \vec{\mathbf{x}} \times \vec{\mathbf{p}} \xrightarrow{\mathcal{P}} \vec{\mathbf{l}}$ respectively, leading to the distinction between vectors (change of sign under parity) and pseudo-vectors (invariant under parity). Conversely, scalars such as $\vec{\mathbf{p}} \cdot \vec{\mathbf{p}}$ are invariant under parity while pseudo-scalars ($\vec{\mathbf{x}} \cdot \vec{\mathbf{l}}$ for example) are negated.

2.2.1.3 Time Conjugation

Time Conjugation, $\mathcal{T}$, is the inversion of time coordinates, and transforms a space-time four-vector as

$$\mathcal{T} : \mathrm{r} \xrightarrow{\mathcal{T}} \begin{bmatrix} -t \\ \vec{\mathbf{x}} \end{bmatrix} \tag{2.31}$$

and represents reversal of motion of the system under observation.

2.2.1.4 $\mathcal{C}$, $\mathcal{P}$, and $\mathcal{T}$ in Classical Electrodynamics

The transformation of ρ, $\vec{\mathbf{J}}$, $\vec{\mathbf{E}}$, and $\vec{\mathbf{B}}$ after $\mathcal{C}$, $\mathcal{P}$, and $\mathcal{T}$ conjugation may be obtained from Maxwell's equations [22]

$$\vec{\nabla} \cdot \vec{\mathbf{E}} = 4\pi \cdot \rho \tag{2.32a}$$

$$\vec{\nabla} \times \vec{\mathbf{B}} - \frac{1}{c}\frac{\partial \vec{\mathbf{E}}}{\partial t} = \frac{4\pi}{c}\vec{\mathbf{J}} \tag{2.32b}$$

$$\vec{\nabla} \cdot \vec{\mathbf{B}} = 0 \tag{2.32c}$$

$$\vec{\nabla} \times \vec{\mathbf{E}} + \frac{1}{c}\frac{\partial \vec{\mathbf{B}}}{\partial t} = 0 \tag{2.32d}$$

under the (correct) assumption that classical electrodynamics is invariant under the conjugation transformations.

Assuming $q \xrightarrow{\mathcal{C}} -q$, it is clear that $\rho \xrightarrow{\mathcal{C}} -\rho$, $\rho \xrightarrow{\mathcal{P}} \rho$, and $\rho \xrightarrow{\mathcal{T}} \rho$, while from $\vec{\mathbf{J}} = \rho \cdot \vec{\mathbf{v}}$ it follows that $\vec{\mathbf{J}} \xrightarrow{\mathcal{C}} -\vec{\mathbf{J}}$, $\vec{\mathbf{J}} \xrightarrow{\mathcal{P}} -\vec{\mathbf{J}}$, and $\vec{\mathbf{J}} \xrightarrow{\mathcal{T}} -\vec{\mathbf{J}}$. Equations (2.32a) to (2.32d) then impose sufficient conditions on the transformation of $\vec{\mathbf{E}}$ and $\vec{\mathbf{B}}$ to resolve them unambiguously and lead to the following relations[7]:

$$\begin{array}{llll} \rho \xrightarrow{\mathcal{C}} -\rho & \vec{\mathbf{J}} \xrightarrow{\mathcal{C}} -\vec{\mathbf{J}} & \vec{\mathbf{E}} \xrightarrow{\mathcal{C}} -\vec{\mathbf{E}} & \vec{\mathbf{B}} \xrightarrow{\mathcal{C}} -\vec{\mathbf{B}} \\ \rho \xrightarrow{\mathcal{P}} \rho & \vec{\mathbf{J}} \xrightarrow{\mathcal{P}} -\vec{\mathbf{J}} & \vec{\mathbf{E}} \xrightarrow{\mathcal{P}} -\vec{\mathbf{E}} & \vec{\mathbf{B}} \xrightarrow{\mathcal{P}} \vec{\mathbf{B}} \\ \rho \xrightarrow{\mathcal{T}} \rho & \vec{\mathbf{J}} \xrightarrow{\mathcal{T}} -\vec{\mathbf{J}} & \vec{\mathbf{E}} \xrightarrow{\mathcal{T}} \vec{\mathbf{E}} & \vec{\mathbf{B}} \xrightarrow{\mathcal{T}} -\vec{\mathbf{B}}. \end{array} \tag{2.33}$$

---

[7] The transformation of Ohm's law [22], $\vec{\mathbf{J}} = \sigma \cdot \vec{\mathbf{E}}$, under $\mathcal{T}$ is left as an exercise for the reader.

This may be expressed in terms of the transformation of the scalar and vector potentials [22], ϕ and $\vec{\mathbf{A}}$, as

$$\begin{aligned} \phi(t,\vec{\mathbf{x}}) &\xrightarrow{\mathcal{C}} -\phi(t,\vec{\mathbf{x}}) & \qquad \vec{\mathbf{A}}(t,\vec{\mathbf{x}}) &\xrightarrow{\mathcal{C}} -\vec{\mathbf{A}}(t,\vec{\mathbf{x}}) \\ \phi(t,\vec{\mathbf{x}}) &\xrightarrow{\mathcal{P}} \phi(t,-\vec{\mathbf{x}}) & \vec{\mathbf{A}}(t,\vec{\mathbf{x}}) &\xrightarrow{\mathcal{P}} -\vec{\mathbf{A}}(t,-\vec{\mathbf{x}}) \\ \phi(t,\vec{\mathbf{x}}) &\xrightarrow{\mathcal{T}} \phi(-t,\vec{\mathbf{x}}) & \vec{\mathbf{A}}(t,\vec{\mathbf{x}}) &\xrightarrow{\mathcal{T}} -\vec{\mathbf{A}}(-t,\vec{\mathbf{x}}). \end{aligned} \tag{2.34}$$

where the transformations of ϕ are obtained from the transformations of q[8], and the transformations of $\vec{\mathbf{A}}$ follow immediately from $\vec{\mathbf{B}} = \vec{\nabla} \cdot \vec{\mathbf{A}}$[9].

2.2.1.5 $\mathcal{C}$, $\mathcal{P}$, and $\mathcal{T}$ in Quantum Electrodynamics

The manifestly covariant form of Maxwell's equations[10], $\partial_\mu \mathrm{A}^{\mu\nu} = q \cdot \mathrm{J}^\nu$, is obtained as the equations of motion from the Lagrangian

$$\mathcal{L}_{\mathrm{QED}} = -\frac{1}{4}\mathrm{A}^{\mu\nu}\mathrm{A}_{\mu\nu} - q \cdot \mathrm{J}^\mu \mathrm{A}_\mu. \tag{2.35}$$

By comparison with their classical analogues, the four-potential and four-current

$$\mathrm{A}^\mu = \begin{bmatrix} \phi \\ \vec{\mathbf{A}} \end{bmatrix} \tag{2.36a}$$

$$\mathrm{J}^\mu = \begin{bmatrix} \rho \\ \vec{\mathbf{J}} \end{bmatrix} \tag{2.36b}$$

allow determination of the transformation properties of A and J under $\mathcal{C}$-, $\mathcal{P}$-, and $\mathcal{T}$-parity. For example

$$\begin{aligned} \mathrm{A}^\mu = \begin{bmatrix} \phi \\ \vec{\mathbf{A}} \end{bmatrix} &\xrightarrow{\mathcal{C}} \begin{bmatrix} -\phi \\ -\vec{\mathbf{A}} \end{bmatrix} \\ &\xrightarrow{\mathcal{C}} -\mathrm{A}^\mu \end{aligned} \tag{2.37}$$

and

$$\begin{aligned} \mathrm{J}^\mu = \begin{bmatrix} \rho \\ \vec{\mathbf{J}} \end{bmatrix} &\xrightarrow{\mathcal{P}} \begin{bmatrix} \rho \\ -\vec{\mathbf{J}} \end{bmatrix} \\ &\xrightarrow{\mathcal{P}} \mathrm{J}_\mu. \end{aligned} \tag{2.38}$$

---

[8] The classical electrostatics problem, 'Consider a uniform field between two charged plates'...

[9] After noting that $\vec{\nabla} \xrightarrow{\mathcal{P}} -\vec{\nabla}$.

[10] For the Gauss–Ampére laws.

Repeated application of this logic results in

$$\begin{aligned}
\mathrm{A}_\mu(t,\vec{\mathbf{x}}) &\xrightarrow{\mathcal{C}} -\mathrm{A}_\mu(t,\vec{\mathbf{x}}) & \mathrm{J}^\mu(t,\vec{\mathbf{x}}) &\xrightarrow{\mathcal{C}} -\mathrm{J}^\mu(t,\vec{\mathbf{x}}) \\
\mathrm{A}_\mu(t,\vec{\mathbf{x}}) &\xrightarrow{\mathcal{P}} \mathrm{A}^\mu(t,-\vec{\mathbf{x}}) & \mathrm{J}^\mu(t,\vec{\mathbf{x}}) &\xrightarrow{\mathcal{P}} \mathrm{J}_\mu(t,-\vec{\mathbf{x}}) \\
\mathrm{A}_\mu(t,\vec{\mathbf{x}}) &\xrightarrow{\mathcal{T}} \mathrm{A}^\mu(-t,\vec{\mathbf{x}}) & \mathrm{J}^\mu(t,\vec{\mathbf{x}}) &\xrightarrow{\mathcal{T}} \mathrm{J}_\mu(-t,\vec{\mathbf{x}})
\end{aligned} \tag{2.39}$$

with the QED Lagrangian invariant under these transforms[11].

A free spin-0 particle is described by a complex field $\phi(t,\vec{\mathbf{x}})$ and the Lagrangian [19]

$$\mathcal{L}_{\text{Spin-0}} = \frac{1}{2}\cdot\partial_\mu\phi^\dagger\cdot\partial^\mu\phi - \frac{1}{2}m^2\cdot\phi^\dagger\phi \tag{2.40}$$

while the free Dirac field takes the Lagrangian [19]

$$\mathcal{L}_{\text{Dirac}} = \overline{\psi}(i\cdot\partial^\mu\gamma_\mu - m)\psi. \tag{2.41}$$

The currents associated to these Lagrangians are

$$\begin{aligned}
\mathrm{J}^\mu_{\text{Spin-0}} &= i(\phi^\dagger\cdot\partial^\mu\phi - \phi\cdot\partial^\mu\phi^\dagger) \\
\mathrm{J}^\mu_{\text{Dirac}} &= \overline{\psi}\gamma^\mu\psi
\end{aligned} \tag{2.42}$$

and requiring the $\mathcal{C}$-, $\mathcal{P}$-, and $\mathcal{T}$-parity transformations of the underlying fields to respect the expected transformation for $\mathrm{J}^\mu(t,\vec{\mathbf{x}})$ (eq. (2.39)) allows the transformation properties for the fields to be obtained[12].

For the scalar field ϕ, the $\mathcal{C}$- and $\mathcal{P}$-parity transformations[13]

$$\begin{aligned}
\phi(t,\vec{\mathbf{x}}) &\xrightarrow{\mathcal{C}} \phi^\dagger(t,\vec{\mathbf{x}}) & \phi^\dagger(t,\vec{\mathbf{x}}) &\xrightarrow{\mathcal{C}} \phi(t,\vec{\mathbf{x}}) \\
\phi(t,\vec{\mathbf{x}}) &\xrightarrow{\mathcal{P}} \phi(t,-\vec{\mathbf{x}}) & \phi^\dagger(t,\vec{\mathbf{x}}) &\xrightarrow{\mathcal{P}} \phi^\dagger(t,-\vec{\mathbf{x}})
\end{aligned} \tag{2.43}$$

result in the required transformation for J^μ as

$$\begin{aligned}
i(\phi^\dagger\cdot\partial^\mu\phi - \phi\cdot\partial^\mu\phi^\dagger) &\xrightarrow{\mathcal{C}} i(\phi\cdot\partial^\mu\phi^\dagger - \phi^\dagger\cdot\partial^\mu\phi) \\
&\xrightarrow{\mathcal{C}} -i(\phi^\dagger\cdot\partial^\mu\phi - \phi\cdot\partial^\mu\phi^\dagger) \\
&\xrightarrow{\mathcal{C}} -\mathrm{J}^\mu
\end{aligned} \tag{2.44}$$

---

[11] The change in sign of the integration variable(s) is immaterial as the required integrations are performed over all space-time.

[12] An approach to obtaining the field transformations from the field operators and the expected transformation properties of the creation and annihilation operators is given in [23]. An alternative approach, based on the invariance of the QED Lagrangian/action, is given in [24]. All three approaches lead to the same results, up to physically uninteresting phase factors.

[13] Ansätze, but the natural interpretation of $\mathcal{C}$- and $\mathcal{P}$-parity for a charged scalar field in QFT.

Field	$\xrightarrow{\mathcal{C}}$	$\xrightarrow{\mathcal{P}}$
$\phi(t,\vec{\mathbf{x}})$	$\phi^\dagger(t,\vec{\mathbf{x}})$	$\phi(t,-\vec{\mathbf{x}})$
$\phi^\dagger(t,\vec{\mathbf{x}})$	$\phi(t,\vec{\mathbf{x}})$	$\phi^\dagger(t,-\vec{\mathbf{x}})$
$\psi(t,\vec{\mathbf{x}})$	$C\cdot\overline{\psi}^{\mathrm{T}}(t,\vec{\mathbf{x}})$	$\gamma^0\cdot\psi(t,-\vec{\mathbf{x}})$
$\overline{\psi}(t,\vec{\mathbf{x}})$	$\psi^{\mathrm{T}}(t,\vec{\mathbf{x}})\cdot\gamma^0 C^\dagger\gamma^0$	$\overline{\psi}(t,-\vec{\mathbf{x}})\cdot\gamma^0$
$\mathrm{V}^+_\mu(t,\vec{\mathbf{x}})$	$-\mathrm{V}^-_\mu(t,\vec{\mathbf{x}})$	$\mathrm{V}^{+,\mu}(t,-\vec{\mathbf{x}})$
$\mathrm{A}^+_\mu(t,\vec{\mathbf{x}})$	$\mathrm{A}^-_\mu(t,\vec{\mathbf{x}})$	$-\mathrm{A}^{+,\mu}(t,-\vec{\mathbf{x}})$

Table 2.2: The transformation properties for scalar and Dirac spinors, and charged vector (V^+) and axial-vector (A^+) fields. Here $C = i\cdot\gamma^2\gamma^0$. Transformation properties for the vector and axial-vector fields are taken from [23], but may be derived by observing that $\overline{\psi}\gamma_\mu\psi$ ($\overline{\psi}\gamma_\mu\gamma_5\psi$) transforms as an (axial-)vector.

while

$$\begin{aligned} i(\phi^\dagger\cdot\partial^\mu\phi - \phi\cdot\partial^\mu\phi^\dagger) &\xrightarrow{\mathcal{P}} i(\phi^\dagger\cdot\partial_\mu\phi - \phi\cdot\partial_\mu\phi^\dagger) \\ &\xrightarrow{\mathcal{P}} \mathrm{J}_\mu \end{aligned} \tag{2.45}$$

where the Lorentz transformation of space has been suppressed, and $\partial^\mu \xrightarrow{\mathcal{P}} \partial_\mu$.

By analogy with the scalar case, the Dirac spinor ψ is expected to transform as $\psi \xrightarrow{\mathcal{C}} C\cdot\overline{\psi}^{\mathrm{T}}$ for some 4×4 matrix C. As $\overline{\psi}$ transforms as $\overline{\psi} \xrightarrow{\mathcal{C}} \psi^{\mathrm{T}}\cdot\gamma^0 C^\dagger\gamma^0$, the requirement that $\psi^{\mathrm{T}}\cdot\gamma^0 C^\dagger\gamma^0\gamma^\mu C\cdot\overline{\psi}^{\mathrm{T}} = -\mathrm{J}^\mu$ implies

$$\gamma^0 C^\dagger\gamma^0\gamma^\mu C = \gamma^{\mu\mathrm{T}}. \tag{2.46}$$

This is satisfied if $C = i\cdot\gamma^2\gamma^0$. For the parity transformation of the Dirac spinor, the identity $\gamma^0\gamma^\mu\gamma^0 = \gamma_\mu$ provides the ansätze $\psi \xrightarrow{\mathcal{P}} \gamma^0\cdot\psi$ and $\overline{\psi} \xrightarrow{\mathcal{P}} \overline{\psi}\cdot\gamma^0$

The validity of these transformations may be confirmed by the fact that the Lagrangian and canonical quantisation conditions are invariant under them [23], and the transforms applied to a charged field under a QED-like covariant derivative result in the expected transformation properties [23, 24]. A summery of the $\mathcal{C}$-, $\mathcal{P}$-, and $\mathcal{CP}$-transformations of these fields, and charged vector and axial-vector fields is provided in table 2.2.

2.2.1.6 The $\mathcal{CPT}$-Theorem

Any Lorentz-invariant local field theory with a Hermitian Hamiltonian and a unique ground state must display a combined $\mathcal{CPT}$-symmetry [25, 26], and as such all SM interactions are expected to be invariant under a $\mathcal{CPT}$-transformation.

Experimentally this means:

- particles and anti-particles must have the same mass;
- particles and anti-particles must have the same lifetime;
- particles and anti-particles must have the the same magnetic moment.

Additionally, any interaction theory that displays $\mathcal{CPT}$-violation must also violate Lorentz invariance [27]. No evidence of $\mathcal{CPT}$- or Lorentz-violation has yet been observed in nature [18].

The requirement for a combined $\mathcal{CPT}$-symmetry is considered such a basic requirement in modern particle physics that its violation in nature would invalidate many theories.

2.2.2 Experimental Observations of $\mathcal{C}$-, $\mathcal{P}$-, and $\mathcal{CP}$-Violation

By 1955, three long-lived, strange particles had been discovered in the decays

$$\begin{aligned} \tau^{\pm} &\to \pi^{\pm}\pi^{+}\pi^{-} \\ \tau'^{\pm} &\to \pi^{\pm}\pi^{0}\pi^{0} \\ \theta^{\pm} &\to \pi^{\pm}\pi^{0} \end{aligned} \tag{2.47}$$

with the particles[14] sharing a common mass and lifetime, as well as relative abundance (irrespective of their production method) and branching ratios in interactions with heavy nuclei. While the $\tau^{\pm}$ and $\tau'^{\pm}$ mesons could be described as different decay chains of the same initial particle, the difference in $\mathcal{P}$-parity between the $\tau^{\pm}$ and $\theta^{\pm}$ decay products implied distinct mother states. This anomaly, the τ–θ problem [24], dominated particle physics of the time.

That $\mathcal{C}$-, $\mathcal{P}$-, and $\mathcal{T}$-parity may not be inviolate symmetries of nature, and could offer a solution to the τ–θ problem, was first conjectured by Yang and Lee [28, 29]. After their systematic review of the literature offered no experimental evidence on the status of $\mathcal{C}$-, or $\mathcal{P}$-parity in weak decays (observations of $\mathcal{P}$-parity violation had already been reported in β-decays [30, 31], but were overlooked in their review), they suggested a number of possible experimental methods to establish $\mathcal{P}$-parity violation in weak decays.

---

[14] $\tau^{\pm}$ and $\theta^{\pm}$ are the historical names of the charged kaons.

2.2.2.1 Observations of $\mathcal{C}$- and $\mathcal{P}$-Violation

The first experimental evidence of a broken symmetry (as a result of Yang and Lee's suggestions) was Wu et al's[32] observation of parity violation in the β-decay of ^{60}Co. The helicity of the electrons in the decay showed that not only was $\mathcal{P}$-parity violated in the decay, it was nearly maximally violated. A second observation of $\mathcal{P}$-parity violation occurred in Garwin and Lederman's [33] study of the decay of pions in flight; this result included (though unreported at the time) an observation of $\mathcal{P}$-parity violation in the decay of muons in flight. Furthermore it established $\mathcal{C}$-parity violation in the weak decay, and extended Wu's result to show that both $\mathcal{C}$-, and $\mathcal{P}$-parity are near maximally violated in the weak decay.

2.2.2.2 Observations of $\mathcal{CP}$-Violation

With $\mathcal{C}$-, and $\mathcal{P}$-parity violation established in the weak interaction, it was assumed that $\mathcal{CP}$-parity was the fundamental symmetry of nature[15] and $\mathcal{CP}$-parity eigenvalues could be assigned to the recently discovered K_1^0 and K_2^0 components of the neutral kaon system.

However $\mathcal{CP}$-parity was also shown to be broken when Cronin and Fitch [34] exposed $\mathcal{CP}$-violation in the decay of the hitherto $\mathcal{CP}$-odd K_2^0, into a $\mathcal{CP}$-even configuration of two pions. This result, controversial at the time, was confirmed 18 months later when interference between the K_1^0 and K_2^0 decays in the two pion channel was observed [35]. These results involve indirect $\mathcal{CP}$-violation (see section 2.3.3.3). Additionally, in 1988, direct $\mathcal{CP}$-violation was observed by the NA31 experiment in the decay of neutral kaons to two pions [36].

With $\mathcal{CP}$-violation established in the strange sector, the subsequent discovery of the charm [37, 38] and bottom [39] quarks led to searches for $\mathcal{CP}$-violation in these systems. Recent results in these sectors have been used to confirm the form of the CKM matrix, and cemented the CKM matrix (and the leptonic equivalent, the PMNS matrix [40]) at the heart of modern particle physics.

2.3 $\mathcal{CP}$-Violation in the Standard Model

From the form of the CKM matrix in section 2.1.2.2, it is possible to examine how $\mathcal{CP}$-violation may arise from the CKM matrix, and how the nature of the CKM matrix may be used to constrain the physically observable parameters

---

[15] Though the possibility that $\mathcal{P}$-violation was unique to leptons left the τ–θ problem unresolved in some minds [23, 24].

of the matrix. This is performed in sections 2.3.1 and 2.3.2, while section 2.3.3 concludes with a review of the phenomenology of the oscillation and decay of neutral mesons, and provides a framework for the classification of CP-violating effects.

2.3.1 $\mathcal{CP}$-Violation and the Electroweak Interaction Lagrangian

Expansion of the Hermitian conjugate in eq. (2.15) leads to

$$\mathcal{L}_{\text{Yukawa}} = Y_{ij} \cdot \overline{\psi}^{\text{I}}_{\text{L,i}} \phi \psi^{\text{I}}_{\text{R,j}} + Y^*_{ij} \cdot \overline{\psi}^{\text{I}}_{\text{R,j}} \phi^\dagger \psi^{\text{I}}_{\text{L,i}} \tag{2.48}$$

while from the transformation properties of the fields (table 2.2)

$$\overline{\psi}^{\text{I}}_{\text{L,i}} \phi \psi^{\text{I}}_{\text{R,j}} \xrightarrow{\mathcal{CP}} \overline{\psi}^{\text{I}}_{\text{R,j}} \phi^\dagger \psi^{\text{I}}_{\text{L,i}} \tag{2.49}$$

therefore the Yukawa Lagrangian remains invariant under $\mathcal{CP}$-transforms if $Y_{ij} = Y^*_{ij}$ for all i and j. Similar logic may be applied to both terms of eq. (2.7), observing that the terms, when expressed in the mass basis, transform as

$$\overline{u}_{\text{L,i}} V_{\text{CKM}} ij \text{W}^{-,\mu} \gamma_\mu d_{\text{L,j}} \xrightarrow{\mathcal{CP}} \overline{d}_{\text{L,j}} V_{\text{CKM}} ij \text{W}^+_\mu \gamma^\mu u_{\text{L,i}} \tag{2.50a}$$

and

$$\overline{d}_{\text{L,i}} V^*_{\text{CKM}} ij \text{W}^{+,\mu} \gamma_\mu u_{\text{L,j}} \xrightarrow{\mathcal{CP}} \overline{u}_{\text{L,j}} V^*_{\text{CKM}} ij \text{W}^-_\mu \gamma^\mu d_{\text{L,i}} \tag{2.50b}$$

so $\mathcal{CP}$-violating terms arise in the SM Lagrangian if the Yukawa coupling, and subsequently the CKM matrix, are complex in nature.

2.3.2 The Cabibbo–Kobayashi–Maskawa Matrix

A general $n \times n$ complex matrix contains $2 \cdot n^2$ parameters; the unitary nature of the CKM matrix, however, reduces this number by half [41], to n^2 parameters. For the CKM matrix, the phases of the quark fields may be freely rotated, and the overall phase is physically uninteresting, so an additional $2 \cdot n - 1$ parameters may be removed, leaving $(n-1)^2$ free parameters. By comparison with a real, orthogonal, $n \times n$ rotation matrix containing $1/2 \cdot n(n-1)$ independent rotations [41], the number of independent complex phases in the CKM matrix is given by

$$\begin{aligned} n_{\text{Phases}} &= n_{\text{All}} - n_{\text{Rotations}} \\ &= (n-1)^2 - \frac{1}{2} \cdot n(n-1) \\ &= \frac{1}{2}(n-1)(n-2). \end{aligned} \tag{2.51}$$

For a two generation SM, no free complex phases exist, consequently the model does not directly support $\mathcal{CP}$-violation; for a three generation SM, a single complex phase exists, naturally permitting $\mathcal{CP}$-violation[16].

2.3.2.1 The Unitarity Triangle(s)

Unitarity of the CKM matrix requires that

$$V_{\mathrm{CKM}} V_{\mathrm{CKM}}^{\dagger} = \begin{bmatrix} V_{\mathrm{ud}} & V_{\mathrm{us}} & V_{\mathrm{ub}} \\ V_{\mathrm{cd}} & V_{\mathrm{cs}} & V_{\mathrm{cb}} \\ V_{\mathrm{td}} & V_{\mathrm{ts}} & V_{\mathrm{tb}} \end{bmatrix} \begin{bmatrix} V_{\mathrm{ud}}^* & V_{\mathrm{cd}}^* & V_{\mathrm{td}}^* \\ V_{\mathrm{us}}^* & V_{\mathrm{cs}}^* & V_{\mathrm{ts}}^* \\ V_{\mathrm{ub}}^* & V_{\mathrm{cb}}^* & V_{\mathrm{tb}}^* \end{bmatrix} = \mathbb{I}. \tag{2.52}$$

Expanding this leads to the three normalisation relations

$$\begin{aligned} 1 &= V_{\mathrm{ud}} V_{\mathrm{ud}}^* + V_{\mathrm{us}} V_{\mathrm{us}}^* + V_{\mathrm{ub}} V_{\mathrm{ub}}^* \\ 1 &= V_{\mathrm{cd}} V_{\mathrm{cd}}^* + V_{\mathrm{cs}} V_{\mathrm{cs}}^* + V_{\mathrm{cb}} V_{\mathrm{cb}}^* \\ 1 &= V_{\mathrm{td}} V_{\mathrm{td}}^* + V_{\mathrm{ts}} V_{\mathrm{ts}}^* + V_{\mathrm{tb}} V_{\mathrm{tb}}^* \end{aligned} \tag{2.53}$$

and three orthogonality relations

$$\begin{aligned} 0 &= V_{\mathrm{ud}} V_{\mathrm{cd}}^* + V_{\mathrm{us}} V_{\mathrm{cs}}^* + V_{\mathrm{ub}} V_{\mathrm{cb}}^* \\ 0 &= V_{\mathrm{ud}} V_{\mathrm{td}}^* + V_{\mathrm{us}} V_{\mathrm{ts}}^* + V_{\mathrm{ub}} V_{\mathrm{tb}}^* \\ 0 &= V_{\mathrm{cd}} V_{\mathrm{td}}^* + V_{\mathrm{cs}} V_{\mathrm{ts}}^* + V_{\mathrm{cb}} V_{\mathrm{tb}}^* \end{aligned} \tag{2.54}$$

while $V_{\mathrm{CKM}}^{\dagger} V_{\mathrm{CKM}} = \mathbb{I}$ leads to three additional normalisation relations and the final three further orthogonality relations

$$\begin{aligned} 0 &= V_{\mathrm{ud}}^* V_{\mathrm{us}} + V_{\mathrm{cd}}^* V_{\mathrm{cs}} + V_{\mathrm{td}}^* V_{\mathrm{ts}} \\ 0 &= V_{\mathrm{ud}}^* V_{\mathrm{ub}} + V_{\mathrm{cd}}^* V_{\mathrm{cb}} + V_{\mathrm{td}}^* V_{\mathrm{tb}} \\ 0 &= V_{\mathrm{us}}^* V_{\mathrm{ub}} + V_{\mathrm{cs}}^* V_{\mathrm{cb}} + V_{\mathrm{ts}}^* V_{\mathrm{tb}}. \end{aligned} \tag{2.55}$$

The six orthogonality relations allow the construction of *Unitarity Triangles*, as each term of the relation may be taken as a vector in the complex plane, with each trio summing identically to zero leading to a triangular shape. For each of these triangles, the lengths of the component vectors and the angles forming the triangle are physical observables [42], while the area of the triangle (all six unitarity triangles share a common area in the complex plane, see [42]) is fixed by the magnitude of the $\mathcal{CP}$-violating phase.

---

[16] The lack of a $\mathcal{CP}$-violating phase in Cabibbo's two generation SM model, where the Cabibbo angle is the only free parameter, led to the prediction of the third generation by Kobayashi and Maskawa in 1973, before the discovery of the charm quark.

2.3.2.2 Alternative Parameterisations

A standard parameterisation of the CKM matrix, adopted by the PDG [18], divides the CKM matrix into three orthogonal quark generation mixing matrices, with the complex phase absorbed into the mixing of the first and third generations. If the Euler mixing angle between the i^{th} and j^{th} generations is given by θ_{ij}, and c_{ij} and s_{ij} are the cosine and sine of the mixing angle respectively, then the PDG parameterisation may be described by

$$\begin{aligned} V_{\text{CKM}} &= \begin{bmatrix} 1 & 0 & 0 \\ 0 & c_{23} & s_{23} \\ 0 & -s_{23} & c_{23} \end{bmatrix} \begin{bmatrix} c_{13} & 0 & s_{13}e^{-i\delta} \\ 0 & 1 & 0 \\ -s_{13}e^{i\delta} & 0 & c_{13} \end{bmatrix} \begin{bmatrix} c_{12} & s_{12} & 0 \\ -s_{12} & c_{12} & 0 \\ 0 & 0 & 1 \end{bmatrix} \\ &= \begin{bmatrix} c_{12}c_{13} & s_{12}c_{13} & s_{13}e^{-i\delta} \\ -s_{12}c_{23} - c_{12}s_{13}s_{23}e^{i\delta} & c_{12}c_{23} - s_{12}s_{13}s_{23}e^{i\delta} & c_{13}s_{23} \\ s_{12}s_{23} - c_{12}s_{13}c_{23}e^{i\delta} & -c_{12}s_{23} - s_{12}s_{13}c_{23}e^{i\delta} & c_{13}c_{23} \end{bmatrix} \end{aligned} \tag{2.56}$$

where $e^{-i\delta}$ is the CKM matrix's complex phase. An alternative parameterisation, due to Wolfenstein [43], is based on the experimental observation that $s_{13} \ll s_{23} \ll s_{12} \ll 1$

$$V_{\text{CKM}} = \begin{bmatrix} 1-\lambda^2/2 & \lambda & A\cdot\lambda^3(\rho - i\eta) \\ -\lambda & 1-\lambda^2/2 & A\cdot\lambda^2 \\ A\cdot\lambda^3(1-\rho-i\eta) & -A\cdot\lambda^2 & 1 \end{bmatrix} + \mathcal{O}(\lambda^4) \tag{2.57}$$

where

$$s_{12} = \lambda \tag{2.58a}$$

$$s_{23} = A\cdot\lambda^2 \tag{2.58b}$$

$$s_{13}e^{-i\delta} = A\cdot\lambda^3(\rho - i\eta) \tag{2.58c}$$

and A, ρ, and η are of order unity. Expressed in terms of the Wolfenstein parameterisation, four of the unitarity triangles are 'squashed' in that the lengths of the sides are expressed in different orders of λ. The remaining unitarity triangles however,

$$\begin{aligned} V_{\text{ud}}V^*_{\text{td}} + V_{\text{us}}V^*_{\text{ts}} + V_{\text{ub}}V^*_{\text{tb}} &= 0 \\ V^*_{\text{ud}}V_{\text{ub}} + V^*_{\text{cd}}V_{\text{cb}} + V^*_{\text{td}}V_{\text{tb}} &= 0 \end{aligned} \tag{2.59}$$

have sides of order $\mathcal{O}(\lambda^3)$, and result in the unitarity triangles shown in fig. 2.1.

2.3.3 $\mathcal{CP}$-Violation in Neutral Meson Decays

Flavoured neutral mesons - those with a net non-zero strangeness, charm, or beauty - are a useful tool for investigating the weak interaction and its CKM

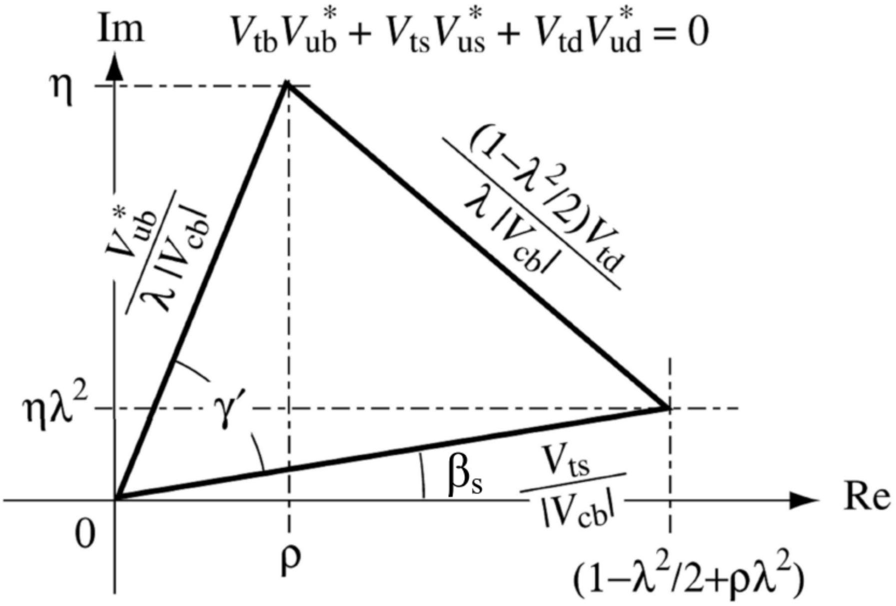

(a) $V_{\mathrm{ud}}V_{\mathrm{td}}^* + V_{\mathrm{us}}V_{\mathrm{ts}}^* + V_{\mathrm{ub}}V_{\mathrm{tb}}^* = 0$

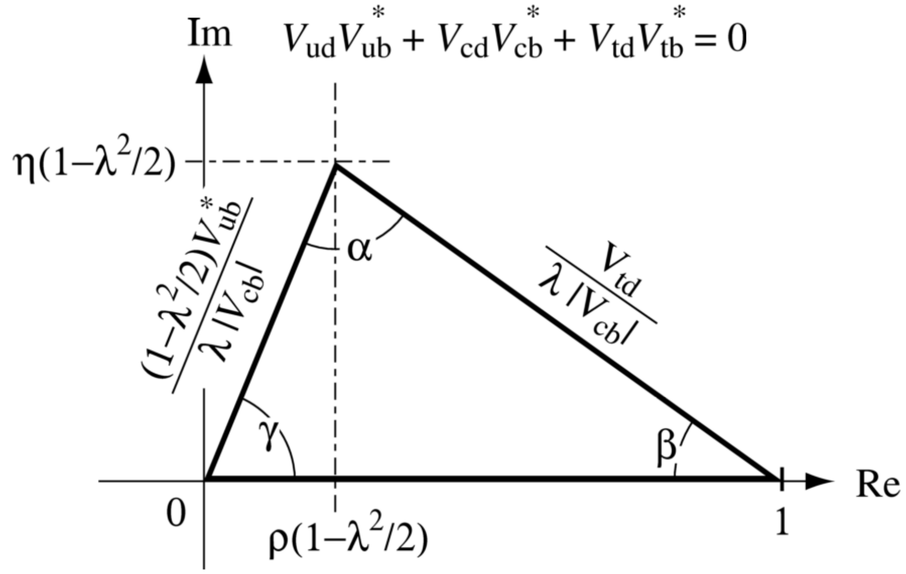

(b) $V_{\mathrm{ud}}^*V_{\mathrm{ub}} + V_{\mathrm{cd}}^*V_{\mathrm{cb}} + V_{\mathrm{td}}^*V_{\mathrm{tb}} = 0$

Figure 2.1: Unitarity triangles for the un-‘squashed’ triangles in the Argand plane. Angle names and normalisation of side lengths are by convention, see [43, 44]. Images from [44].

matrix elements. These particles, and their associated anti-particle, are distinguished only by their flavour quantum numbers that are not conserved by the weak interaction.

2.3.3.1 Neutral Meson Mixing

The flavour states F^0 and $\overline{\mathrm{F}}^0$ are flavoured, neutral mesons. An arbitrary superposition of these states, $|\psi\rangle$, and their possible decay products, f_n, is given by

$$|\psi(t)\rangle = a(t)\,|\mathrm{F}^0\rangle + b(t)\,|\overline{\mathrm{F}}^0\rangle + c(t)\,|f_1\rangle + d(t)\,|f_2\rangle + \cdots \tag{2.60}$$

with the time evolution of this system governed by the time-dependent Schrödinger wave equation [45]

$$i\frac{\partial}{\partial t}\,|\psi\rangle = \widehat{H}\,|\psi\rangle \tag{2.61}$$

where $\widehat{H}$ is an infinite-dimension matrix. The full time-dependence of $|\psi\rangle$ cannot be obtained rigorously, as at a minimum this would require a complete description of the strong interaction. The problem may be simplified, however, with the following assumptions:

- the initial state, $|\tilde{\psi}\rangle$, is given by $|\tilde{\psi}(0)\rangle = a(0)\,|\mathrm{F}^0\rangle + b(0)\,|\overline{\mathrm{F}}^0\rangle$;
- we are interested in $a(t)$ and $b(t)$, and no other coefficients;
- we consider times that are much larger than the strong interaction scale - the Weisskopf-Wigner approximation [46, 47].

With these assumptions, we may express $|\tilde{\psi}(t)\rangle$ in the basis of the flavour states [48] as

$$|\tilde{\psi}(t)\rangle = \begin{bmatrix} a(t) \\ b(t) \end{bmatrix} \tag{2.62}$$

where its time evolution is given by the time-dependent Schrödinger wave equation with a non-Hermitian effective Hamiltonian $\widehat{\mathcal{H}}$, where the non-Hermiticity of $\widehat{\mathcal{H}}$ reflects the non-conservation of the total probability to observe a particle.

$\widehat{\mathcal{H}}$ may be defined in terms of the Hermitian matrices $\widehat{M}$ and $\widehat{\Gamma}$

$$\widehat{M} = \frac{1}{2}(\widehat{\mathcal{H}} + \widehat{\mathcal{H}}^\dagger) \tag{2.63a}$$

$$\widehat{\Gamma} = i(\widehat{\mathcal{H}} - \widehat{\mathcal{H}}^\dagger) \tag{2.63b}$$

as

$$\widehat{\mathcal{H}} = \widehat{M} - \frac{i}{2}\widehat{\Gamma} \tag{2.64}$$

where

$$\widehat{M} = \begin{bmatrix} M_{11} & M_{12} \\ M_{12}^* & M_{22} \end{bmatrix} \quad (2.65a) \qquad \widehat{\Gamma} = \begin{bmatrix} \Gamma_{11} & \Gamma_{12} \\ \Gamma_{12}^* & \Gamma_{22} \end{bmatrix}. \quad (2.65b)$$

Assuming $\mathcal{CPT}$-parity (section 2.2.1.6), and that $\mathcal{C}$, $\mathcal{P}$, and $\mathcal{T}$ commute with $\widehat{\mathcal{H}}$ [23, 24], it follows that $M_{11} = M_{22} = M$, and $\Gamma_{11} = \Gamma_{22} = \Gamma$. Furthermore, combining eqs. (2.61) and (2.64) gives

$$\frac{\mathrm{d}}{\mathrm{d}t} \langle\tilde{\psi}|\tilde{\psi}\rangle = -\langle\tilde{\psi}|\widehat{\Gamma}|\tilde{\psi}\rangle \tag{2.66}$$

constraining $\widehat{\Gamma}$ to be positive-definite.

The off-diagonal elements of $\widehat{\mathcal{H}}$ contain two components detailing the oscillation of the flavour eigenstates. M_{12} describes the short-distance (off-shell) oscillations via electroweak box diagrams, as shown in fig. 2.2, while Γ_{12} quantifies the oscillation contribution from virtual (on-shell) intermediate states f via $\mathrm{F}^0 \to f \to \overline{\mathrm{F}}^0$.

The propagating states of $\widehat{\mathcal{H}}$ are given by its eigenvectors. The characteristic equation of $\widehat{\mathcal{H}}$ gives eigenvalues of

$$\lambda^{\pm} = M - \frac{i}{2}\Gamma \pm L \tag{2.67}$$

with

$$L = \sqrt{(M_{12} - \frac{i}{2}\Gamma_{12}) \cdot (M_{12}^* - \frac{i}{2}\Gamma_{12}^*)}. \tag{2.68}$$

Solving for the eigenvectors with

$$\widehat{\mathcal{H}} \begin{bmatrix} p \\ q \end{bmatrix} = \lambda^{\pm} \begin{bmatrix} p \\ q \end{bmatrix} \tag{2.69}$$

gives

$$\frac{q}{p} = \pm\sqrt{\frac{M_{12}^* - \frac{i}{2}\Gamma_{12}^*}{M_{12} - \frac{i}{2}\Gamma_{12}}}. \tag{2.70}$$

By convention, it is assumed $q/p > 0$, and the eigenvectors are labelled[17] $\mathrm{P^H}$ and $\mathrm{P^L}$ with

$$|\mathrm{P^H}\rangle = p\,|\mathrm{F}^0\rangle + q\,|\overline{\mathrm{F}}^0\rangle \quad (2.71a) \qquad |\mathrm{P^L}\rangle = p\,|\mathrm{F}^0\rangle - q\,|\overline{\mathrm{F}}^0\rangle \quad (2.71c)$$

$$|\mathrm{F}^0\rangle = \frac{1}{2p}(|\mathrm{P^H}\rangle + |\mathrm{P^L}\rangle) \quad (2.71b) \qquad |\overline{\mathrm{F}}^0\rangle = \frac{1}{2q}(|\mathrm{P^H}\rangle - |\mathrm{P^L}\rangle). \quad (2.71d)$$

---

[17] Light and Heavy.

Diagonalisation of $\widehat{\mathcal{H}}$ allows us to obtain the time-dependent Schrödinger wave equations for the physically propagating states

$$|\mathrm{P}^{\mathrm{H}}(t)\rangle = e^{-i(m^{\mathrm{H}}-\frac{i}{2}\Gamma^{\mathrm{H}})t}\,|\mathrm{P}^{\mathrm{H}}(0)\rangle \tag{2.72a}$$

$$|\mathrm{P}^{\mathrm{L}}(t)\rangle = e^{-i(m^{\mathrm{L}}-\frac{i}{2}\Gamma^{\mathrm{L}})t}\,|\mathrm{P}^{\mathrm{L}}(0)\rangle \tag{2.72b}$$

where the mass terms, m^{H} and m^{L}, and the decay constants, Γ^{H} and Γ^{L}, are given by the real and imaginary components of the associated eigenvalue. The average of these constants is given by

$$m = \frac{m^{\mathrm{H}}+m^{\mathrm{L}}}{2} \tag{2.73a}$$

$$\Gamma = \frac{\Gamma^{\mathrm{H}}+\Gamma^{\mathrm{L}}}{2} \tag{2.73b}$$

while their differences are given by

$$\begin{aligned}\Delta m &= m^{\mathrm{H}} - m^{\mathrm{L}}\\ &= 2\Re(L) \geq 0\end{aligned} \tag{2.74a}$$

$$\begin{aligned}\Delta\Gamma &= \Gamma^{\mathrm{L}} - \Gamma^{\mathrm{H}}\\ &= 4\Im(L)\end{aligned} \tag{2.74b}$$

where the inequality in eq. (2.74a) is due to the sign convention adopted for eq. (2.70).

Combining eqs. (2.71) and (2.72), we obtain the time-evolution for the flavour states as

$$|\mathrm{F}^0(t)\rangle = g_+(t)\,|\mathrm{F}^0\rangle + g_-(t)\cdot\frac{q}{p}\,|\overline{\mathrm{F}}^0\rangle \tag{2.75a}$$

$$|\overline{\mathrm{F}}^0(t)\rangle = g_-(t)\cdot\frac{p}{q}\,|\mathrm{F}^0\rangle + g_+(t)\,|\overline{\mathrm{F}}^0\rangle \tag{2.75b}$$

where

$$g_\pm(t) = \frac{1}{2}\left(e^{-i\left(m^{\mathrm{H}}-\frac{i}{2}\Gamma^{\mathrm{H}}\right)t} \pm e^{-i\left(m^{\mathrm{L}}-\frac{i}{2}\Gamma^{\mathrm{L}}\right)t}\right). \tag{2.76}$$

So for a particle produced as a pure F^0 state, as might be obtained from a strong interaction, the probability of finding a F^0 or $\overline{\mathrm{F}}^0$ state at some later time is given by

$$|\langle\mathrm{F}^0|\mathrm{F}^0(t)\rangle|^2 = |g_+(t)|^2 \tag{2.77a}$$

$$|\langle\overline{\mathrm{F}}^0|\mathrm{F}^0(t)\rangle|^2 = \left|\frac{q}{p}\right|^2\cdot|g_-(t)|^2 \tag{2.77b}$$

where

$$|g_\pm(t)|^2 = \frac{e^{-\Gamma t}}{2}\left(\cosh\left(\frac{\Delta\Gamma}{2}t\right) \pm \cos(\Delta m t)\right) \tag{2.78}$$

and

$$|\langle\mathrm{F}^0|\overline{\mathrm{F}}^0(t)\rangle|^2 = \left|\frac{p}{q}\right|^2\cdot|g_-(t)|^2 \tag{2.79a}$$

$$|\langle\overline{\mathrm{F}}^0|\overline{\mathrm{F}}^0(t)\rangle|^2 = |g_+(t)|^2 \tag{2.79b}$$

for an initially pure $\overline{\mathrm{F}}^0$ state.

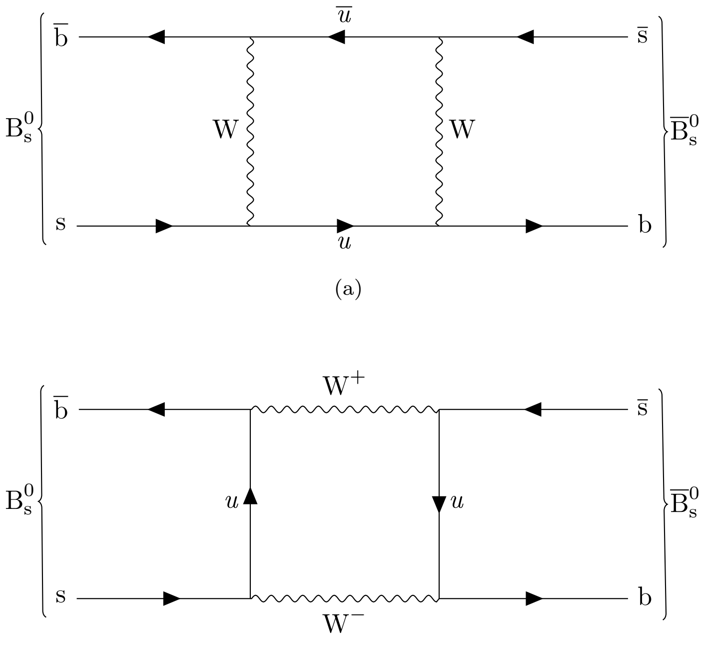

(a)

(b)

Figure 2.2: The $\mathrm{B}_\mathrm{s}^0 \rightsquigarrow \overline{\mathrm{B}}_\mathrm{s}^0$ mixing diagrams with u representing an up-type (u, c, or t) quark. Mixing though t quark exchange is expected to dominate due to kinematic arguments.

2.3.3.2 Neutral Meson Decays

With the dynamics of flavour oscillation established, we may now examine the decays of the flavour eigenstates. The amplitudes for the decays of the flavour eigenstates into a final state f, or its charge conjugate, are given by

$$A_f = \langle f|\widehat{T}|\mathrm{F}^0\rangle \qquad (2.80a) \qquad\qquad \bar{A}_f = \langle f|\widehat{T}|\overline{\mathrm{F}}^0\rangle \qquad (2.80c)$$

$$A_{\bar{f}} = \langle \bar{f}|\widehat{T}|\mathrm{F}^0\rangle \qquad (2.80b) \qquad\qquad \bar{A}_{\bar{f}} = \langle \bar{f}|\widehat{T}|\overline{\mathrm{F}}^0\rangle \qquad (2.80d)$$

where $\widehat{T}$ is the transition operator due to a weak decay. Combining eqs. (2.75) and (2.80) gives

$$\begin{aligned}\Gamma_{\mathrm{F}^0\to f}(t) = \ & |A_f|^2 \\ & \cdot \Big(|g_+(t)|^2 + |\lambda_f|^2 |g_-(t)|^2 + 2\Re(\lambda_f g_+^*(t) g_-(t))\Big)\end{aligned} \qquad (2.81a)$$

and

$$\begin{aligned}\Gamma_{\mathrm{F}^0\to\bar{f}}(t) = &\left|\frac{q}{p}\right|^2 \cdot |\bar{A}_{\bar{f}}|^2 \\ &\cdot \Big(|g_-(t)|^2 + |\bar{\lambda}_{\bar{f}}|^2|g_+(t)|^2 + 2\Re(\bar{\lambda}_{\bar{f}}\, g_+(t)g_-^*(t))\Big)\end{aligned} \tag{2.81b}$$

as the time-dependent decay widths for particles produced as a pure F^0 state to decay into the final states f or $\bar{f}$, where

$$\lambda_f = \frac{q}{p}\frac{\bar{A}_f}{A_f} \tag{2.82a}$$

$$\bar{\lambda}_f = \frac{1}{\lambda_f} \tag{2.82b}$$

$$\lambda_{\bar{f}} = \frac{q}{p}\frac{\bar{A}_{\bar{f}}}{A_{\bar{f}}} \tag{2.82c}$$

$$\bar{\lambda}_{\bar{f}} = \frac{1}{\lambda_{\bar{f}}} \tag{2.82d}$$

and

$$g_+^*(t)g_-(t) = \frac{e^{-\Gamma t}}{2}\left(\sinh\left(\frac{\Delta\Gamma}{2}t\right) + i\sin(\Delta m t)\right) \tag{2.83a}$$

$$g_+(t)g_-^*(t) = \frac{e^{-\Gamma t}}{2}\left(\sinh\left(\frac{\Delta\Gamma}{2}t\right) - i\sin(\Delta m t)\right) \tag{2.83b}$$

while for an initially pure $\overline{\mathrm{F}}^0$ state

$$\begin{aligned}\Gamma_{\overline{\mathrm{F}}^0\to f}(t) = &\left|\frac{p}{q}\right|^2 \cdot |A_f|^2 \\ &\cdot \Big(|g_-(t)|^2 + |\lambda_f|^2|g_+(t)|^2 + 2\Re(\lambda_f\, g_+(t)g_-^*(t))\Big)\end{aligned} \tag{2.84a}$$

and

$$\begin{aligned}\Gamma_{\overline{\mathrm{F}}^0\to\bar{f}}(t) = &\ |\bar{A}_{\bar{f}}|^2 \\ &\cdot \Big(|g_+(t)|^2 + |\bar{\lambda}_{\bar{f}}|^2|g_-(t)|^2 + 2\Re(\bar{\lambda}_{\bar{f}} g_+^*(t)g_-(t))\Big)\,.\end{aligned} \tag{2.84b}$$

By convention, eqs. (2.81a) and (2.84a) are recast as the ‘Master Equations’ [23]

$$\begin{aligned}\Gamma_{\mathrm{F}^0\to f}(t) = &\ |A_f|^2 \cdot (1+|\lambda_f|^2)\frac{e^{-\Gamma t}}{2} \\ &\cdot \left(\cosh\left(\frac{\Delta\Gamma}{2}t\right) + D_f \sinh\left(\frac{\Delta\Gamma}{2}t\right) + T_f\right)\end{aligned} \tag{2.85a}$$

and

$$\begin{aligned}\Gamma_{\overline{\mathrm{F}}^0\to f}(t) = &\left|\frac{p}{q}\right|^2 \cdot |A_f|^2 \cdot (1+|\lambda_f|^2)\frac{e^{-\Gamma t}}{2} \\ &\cdot \left(\cosh\left(\frac{\Delta\Gamma}{2}t\right) + D_f \sinh\left(\frac{\Delta\Gamma}{2}t\right) - T_f\right)\end{aligned} \tag{2.85b}$$

with

$$D_f = \frac{2\Re(\lambda_f)}{1+|\lambda_f|^2} \tag{2.86}$$

and

$$T_f = C_f \cos(\Delta m t) - S_f \sin(\Delta m t) \tag{2.87}$$

where

$$C_f = \frac{1 - |\lambda_f|^2}{1 + |\lambda_f|^2} \quad (2.88a) \qquad S_f = \frac{2\Im(\lambda_f)}{1 + |\lambda_f|^2}. \quad (2.88b)$$

Subsequently, for a final state that is common between the flavour eigenstates, we need only determine one parameter, λ_f, to completely define the decay of the oscillating neutral meson.

2.3.3.3 $\mathcal{CP}$-Violating Effects

We may now classify the possible $\mathcal{CP}$-violating effects:

- $\mathcal{CP}$-violation in mixing:
  This occurs if the probability of oscillation from the particle to the anti-particle differs from that of the anti-particle to the particle, that is

  $$P(\mathrm{F}^0 \rightsquigarrow \overline{\mathrm{F}}^0) \neq P(\overline{\mathrm{F}}^0 \rightsquigarrow \mathrm{F}^0) \tag{2.89a}$$

  and is possible if

  $$\left|\frac{p}{q}\right| \neq 1. \tag{2.89b}$$

  Experimental searches are possible through the semi-leptonic decays of coherently produced B^0_d–$\overline{\mathrm{B}}^0_\mathrm{d}$ pairs, leading to the asymmetry

  $$A_{\mathcal{CP}} = \frac{N_{++} - N_{--}}{N_{++} + N_{--}} = \frac{|p/q|^2 - |q/p|^2}{|p/q|^2 + |q/p|^2} \tag{2.89c}$$

  where $N_{\pm\pm}$ is the number of same-sign leptons observed. This has not yet been observed in the B^0_d system, but is observed in neutral kaon mixing.

- $\mathcal{CP}$-violation in decays:
  This occurs if the decay rate of F^0 to the state f differs from the decay of $\overline{\mathrm{F}}^0$ to the $\mathcal{CP}$-conjugate state $\overline{f}$, therefore

  $$\Gamma_{\mathrm{F}^0 \to f} \neq \Gamma_{\overline{\mathrm{F}}^0 \to \overline{f}}. \tag{2.90a}$$

  This is satisfied when

  $$\left|\frac{A_f}{\bar{A}_{\bar{f}}}\right| \neq 1. \tag{2.90b}$$

  As this does not depend on mixing between the F^0 and $\overline{\mathrm{F}}^0$ flavour-states, it is the only form of $\mathcal{CP}$-violation available to charged mesons.

This has been observed in neutral B-mesons, for example, as an asymmetry in the time-dependent decay $\mathrm{B}^0_\mathrm{d} \to \mathrm{K}^+\pi^-$ where it has been shown [49]

$$A_{\mathrm{K}^\pm\pi^\mp} = \frac{\Gamma_{\mathrm{B}^0_\mathrm{d}\to\mathrm{K}^+\pi^-} - \Gamma_{\overline{\mathrm{B}}^0_\mathrm{d}\to\mathrm{K}^-\pi^+}}{\Gamma_{\mathrm{B}^0_\mathrm{d}\to\mathrm{K}^+\pi^-} + \Gamma_{\overline{\mathrm{B}}^0_\mathrm{d}\to\mathrm{K}^-\pi^+}} < 0. \tag{2.90c}$$

- $\mathcal{CP}$-violation through interference:
  This occurs when the F^0 and $\overline{\mathrm{F}}^0$ decay to a common state f, and interference between direct decays, and decays after a net oscillation, is observed.

Of most interest are the cases where f is a $\mathcal{CP}$-eigenstate ($f = \overline{f}$) and $\mathcal{CP}$-parity is violated if

$$\Gamma_{(\mathrm{F}^0 \rightsquigarrow \overline{\mathrm{F}}^0)\to f}(t) \neq \Gamma_{(\overline{\mathrm{F}}^0 \rightsquigarrow \mathrm{F}^0)\to f}(t). \tag{2.91a}$$

Assuming $|p/q| = 1$ (no $\mathcal{CP}$-violation in mixing), the master equations (eq. (2.85)) may be used to form the asymmetry

$$A_{\mathcal{CP}}(t) = \frac{\Gamma_{\mathrm{F}^0\to f} - \Gamma_{\overline{\mathrm{F}}^0\to f}}{\Gamma_{\mathrm{F}^0\to f} + \Gamma_{\overline{\mathrm{F}}^0\to f}} = \frac{2C_f \cdot \cos(\Delta m t) - 2S_f \cdot \sin(\Delta m t)}{2\cosh(\frac{\Delta\Gamma}{2}t) + 2D_f \cdot \sinh(\frac{\Delta\Gamma}{2}t)} \tag{2.91b}$$

furthermore we may assume $|A_f| = |\bar{A}_{\overline{f}}|$ (no $\mathcal{CP}$-violation in decays), reducing eq. (2.91b) to

$$A_{\mathcal{CP}}(t) = \frac{-\Im(\lambda_f) \cdot \sin(\Delta m t)}{\cosh(\frac{\Delta\Gamma}{2}t) + \Re(\lambda_f) \cdot \sinh(\frac{\Delta\Gamma}{2}t)} \tag{2.91c}$$

therefore $\mathcal{CP}$-violation may still occur if $\Im(\lambda_f) \neq 0$.

Chapter 3

Experimental Apparatus

To perform precision measurements on the SM, three elements are required:

- a method of producing the SM processes under investigation;
- the ability to record the information of significance from the production or decay channel under analysis;
- infrastructure for the storage, and subsequent evaluation, of the data collected.

The *European Organisation for Nuclear Research* (CERN), the world's largest physics laboratory, hosts a number of international collaborations operating particle colliders, detectors, and computing services to meet these exacting requirements and satisfy the diverse needs of the particle physics community.

The remainder of this chapter provides an overview of the Large Hadron Collider (section 3.1), the ATLAS detector (section 3.2), and its associated software and computing frameworks (section 3.3) as designed and built for the start of Run1 (the data taking period between 2009 and 2013). Run1 and LS1 (Long Shutdown 1, 2013–2015) updates are discussed where relevant to the analyses.

3.1 The CERN Accelerator Complex

The CERN accelerator complex [50, 51, 52] (fig. 3.1) aims to provide high-energy protons, neutrons, electrons, and heavy-ions to a wide-range of engineering and scientific collaborations[1] with the stated aim of addressing some

---

[1] Additional fixed targets are installed to provide anti-protons, (anti-)neutrinos, and radioactive ion beams where required.

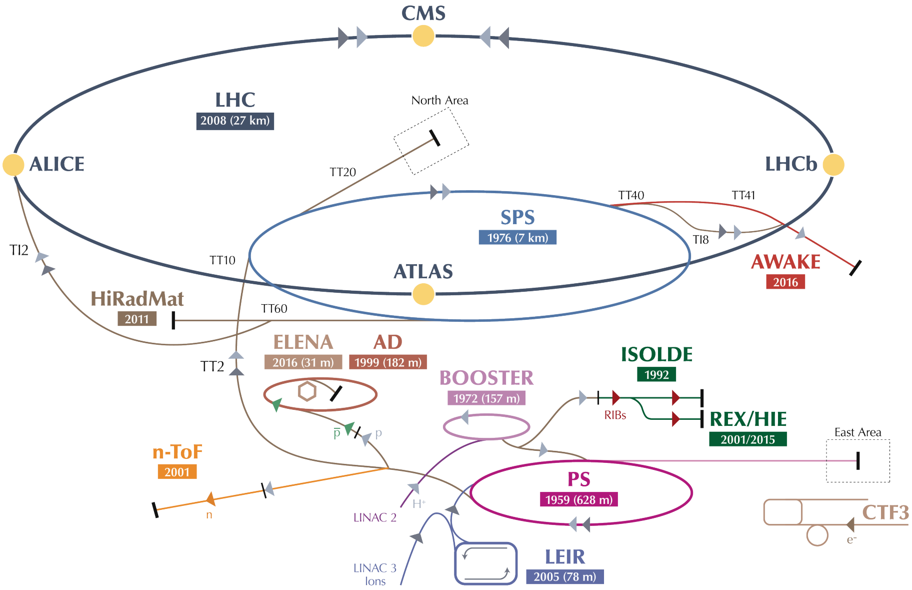

Figure 3.1: The CERN accelerator complex and its major experiments. Image adapted from [61].

of the fundamental open questions in particle physics[2].

The centrepiece of CERN's recent scientific endeavours is the main ring, the final stage of the *Large Hadron Collider* (LHC), a dual-beam synchrotron capable of operating in pp, pPb, or PbPb modes at the energy-frontier.

Seven particle detectors are installed around the LHC's main ring. The large general purpose detectors, ATLAS [54] and CMS [55], aim to investigate the largest range of physics possible while serving as cross-confirmation for each other. ALICE [56] and LHCb [57] are specialised detectors; ALICE focuses on heavy-ion collisions while LHCb aims to make precision measurements of $\mathcal{CP}$-violating processes. LHCf [58] and TOTEM [59] focus on physics in the far-forward regions of ATLAS and CMS respectively while MoEDAL [60] is dedicated to the detection of magnetic monopoles and other massive (pseudo-) stable charged particles.

3.1.1 Accelerator Physics Nomenclature

For additional background material in this field see [62, 63].

---

[2] The 'fundamental open questions' have evolved significantly over time, see [53] for the view circa 1984, and section 3.2 for the current aims of the ATLAS detector.

3.1.1.1 Luminosity

The *Luminosity*, $\mathcal{L}$, of a particle collider is a process-independent measure of the rate of particle interactions it produces, and is defined as [64]

$$\mathcal{L} = \frac{\mathrm{d}N}{\mathrm{d}t} \cdot \frac{1}{\sigma_N} \tag{3.1}$$

where N is the count of events for some process of cross-section σ_N. For head-on collisions of similar Gaussian bunches in a dual-beam collider, this is usually expressed as [64]

$$\mathcal{L} = f \cdot L_{\mathrm{bc}} \tag{3.2a}$$

$$L_{\mathrm{bc}} = \frac{n_1 n_2}{4\pi \cdot \sigma_X \sigma_Y} \tag{3.2b}$$

where f is the frequency of bunch crossings, $n_{1,2}$ is the number of particles in each bunch, and $\sigma_{X,Y}$ are the Gaussian widths of the bunches in the plane transverse to the crossing. As $\mathcal{L}$ is typically a function of time, the *Integrated Luminosity*, L, is defined as [64]

$$L = \int \mathcal{L}(t)\,\mathrm{d}t \tag{3.3}$$

and provides a useful figure of merit for the possible scientific output of a collider.

A further distinction may be made between the integrated luminosity delivered by the collider and that available for analysis from the detector. The integrated luminosity delivered by the LHC, and the subset considered ‘Good for Physics’ by ATLAS [65] during Run1, as defined by the ATLAS *Good Run Lists* (GRL), are shown in fig. 3.2(a).

3.1.1.2 Pile-Up

During any bunch crossing it is possible that more than one pp interaction may occur, this is *Pile-Up*. Pile-up events are independent of other pp interactions in the bunch crossing and the number of pile-up events in a bunch crossing is characterised by a Poisson distribution with mean μ

$$\mu = L_{\mathrm{bc}} \cdot \sigma_{\mathrm{pp}} \tag{3.4}$$

where σ_{pp} is the pp interaction cross-section. The luminosity-weighted distribution of μ for Run1 is shown in fig. 3.2(b).

3.1.1.3 Event Counts

For a physics analysis, the number of observed signal events, N_{Obs}, available for analysis is given by

$$N_{\mathrm{Obs}} = L \cdot \sigma_{\mathrm{P}} \cdot \mathrm{BR}(\mathrm{P} \to f) \cdot \epsilon_f \tag{3.5}$$

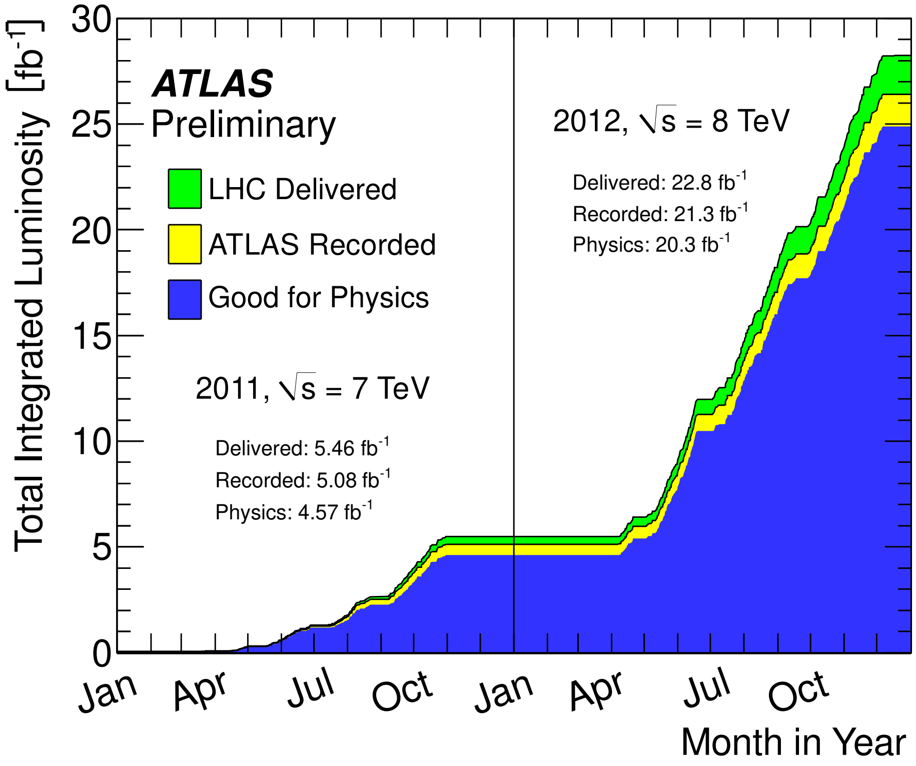

(a) Cumulative luminosity versus time as delivered by the LHC (green), recorded by ATLAS (yellow), and certified to be ‘Good for Physics’ (blue) during Run1 data taking.

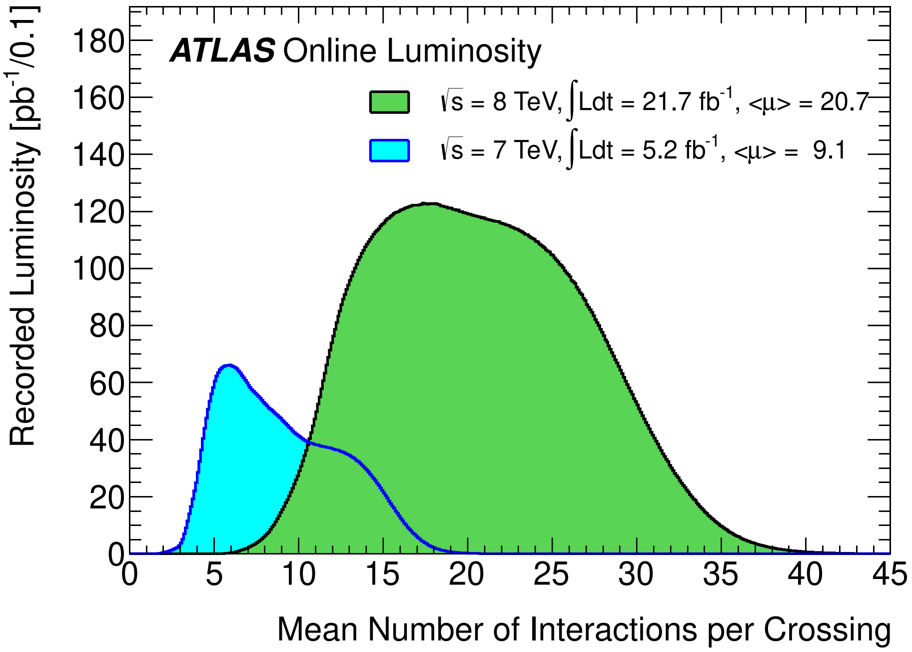

(b) Luminosity-weighted distribution of μ for $\sqrt{s} = 7\,\text{TeV}$ (blue) and $\sqrt{s} = 8\,\text{TeV}$ (green) data during Run1 data taking. μ is calculated using eq. (3.4) with σ_{pp} taken as 71.5 mb for 7 TeV collisions and 73.0 mb for 8 TeV collisions.

Figure 3.2: LHC Run1 Performance. Figures from [66].

where σ_{P} is the production cross-section for the particle of interest, $\mathrm{BR}(\mathrm{P} \to f)$ is the branching ratio to the final state, and ϵ_f is the reconstruction efficiency for that state. Therefore, to improve the statistical power available to any analysis[3], we may increase the integrated luminosity used in the analysis (take more data) or improve the detector and reconstruction efficiencies (optimise data selection and/or analysis cuts).

3.1.2 The Large Hadron Collider

The LHC, a composite particle accelerator consisting of the main ring and its six stage injector chain, supersedes the now retired Tevatron at Fermilab (the Fermi National Accelerator Laboratory in Chicago, Illinois) as the energy-frontier in particle physics.

Approved for construction in 1994, and completed in 2008, the LHC is designed to produce $\sqrt{s} = 14\,\mathrm{TeV}$ pp collisions at a luminosity of $10^{34}\,\mathrm{cm}^{-2}\,\mathrm{s}^{-1}$. To achieve these aims the LHC utilises contra-rotating beams with each beam containing up to 2808 bunches of $\approx 1.15 \times 10^{11}$ protons per bunch, with a bunch crossing rate of 40 MHz.

3.1.2.1 The Injector Chain

Input to the LHC's main ring is achieved through the LHC's injector chain, and consists of six pre-existing, re-purposed accelerators. For pp runs the injector chain consists of *LINAC2*, the *Proton Synchrotron Booster* (PSB), the *Proton Synchrotron* (PS), and finally the *Super Proton Synchrotron* (SPS)[4].

Gaseous H_2 is introduced to LINAC2 from a bottled source with an electric field used to ionise the gas and produce protons. LINAC2's series of coupled RF cavities and quadrapole magnets are used to form 50 MeV proton bunches that pass through a transfer beamline to the four superimposed synchrotron rings (157 m diameter) of the PSB. The PSB accelerates the proton bunches to 1.4 GeV before conveyance to the remaining stages of the injector chain.

The 72 m radius PS accelerates the proton bunches to 26 GeV before forwarding the proton bunches to the SPS. Within the 7 km circumference SPS, the bunches are accelerated to 450 GeV and compressed to an RMS bunch length of 11 cm for injection into the main ring.

---

[3] In the absence of background.

[4] The final two components of the injector chain, LINAC3 and LEIR, are specific to heavy-ion runs [52].

3.1.2.2 The Main Ring

The LHC's main ring is contained within a 27 km circumference circular tunnel under the Franco–Swiss border between Geneva and Saint-Genis-Pouilly. The tunnel was constructed between 1983 and 1988 to house LEP (the Large Electron-Positron Collider), with the main ring replacing LEP at the termination of LEP's activities in 2000.

The main ring accepts proton bunches from the injector chain, and further accelerates them from 450 GeV to the nominal energy of 7 TeV per beam. This acceleration is provided by 16 superconducting RF cavities housed in four cryomodules (two per beam). The contra-rotating beams are contained in a '2-in-1' dipole structure [50] with 1232 dipole magnets providing the Lorentz force required to manipulate the beams around the ring. Over 6000 additional higher-order multipole magnets are used to shape and focus the bunch packets, remove imperfections in the beam, and suppress undesired electromagnetic resonances.

Cryogenic support for the NbTi main ring magnets is provided by ≈100 t of liquid-He at 1.7 K, making the LHC main ring the largest liquid-He cryogenic facility in the world.

3.2 The ATLAS Detector

The ATLAS experiment [54, 67] is one of two general purpose detectors installed on the LHC main ring. With an overall length of 44 m, a diameter of 25 m, and weighing over 7000 t, it is the largest collider detector ever constructed. Approved for construction in 1997 and completed in 2008, ATLAS is installed at Point 1 on the main ring.

As a general purpose detector, ATLAS is expected to engage in a wide range of physics measurements during its lifetime. These measurements include [68, 69]:

- precision measurements of SM processes and parameters;
- discovery, and subsequent measurement of the properties of the SM Higgs boson;
- searches for evidence of BSM physics:
    - super symmetry (SUSY);

  - extra dimensions;
  - heavy vector bosons and quarks, and excited fermions;
  - dark matter and magnetic monopoles.

From these physics goals, a set of general requirements for the ATLAS detector may be derived [70, 71, 72]:

- fast, high-granularity, and radiation-hard sensor elements and electronics;
- near 4π acceptance;
- excellent charged-particle momentum resolution and reconstruction efficiency;
- full-coverage electromagnetic and hadronic calorimetry;
- muon identification and good momentum resolution over a wide range of momenta and unambiguous charge identification at high momentum;
- efficient triggering, especially for low momentum objects;
- storage of large datasets and their distributed analysis.

To achieve these design goals, the ATLAS detector consists of a number of integrated components. The magnet systems (section 3.2.2) and Inner Detector (section 3.2.3) combine to produce precision tracking measurements while the accompanying high granularity electromagnetic and hadronic calorimeters (section 3.2.4) offer exceptional energy resolution. Coupled to these is a muon spectrometer (section 3.2.5) with excellent temporal and spacial resolution. The overall layout of these components is shown in fig. 3.3. To capture events for further analysis, the detector incorporates a flexible three-level trigger system (section 3.2.6); the ATLAS computing infrastructure (section 3.3) ensures safekeeping of the collected data while allowing its analysis on ‘the grid’.

3.2.1 The ATLAS Coordinate Systems and Nomenclature

ATLAS uses a right-handed coordinate system with the origin at the nominal interaction point [54]. The beam axis at the interaction point defines the z-axis, with the axis pointing toward Point 8 (see fig. 3.4). The x-axis points towards the centre of the LHC ring, leaving the y-axis slightly offset from the local vertical due to the tilt of the LHC tunnel. This system is shown in fig. 3.4.

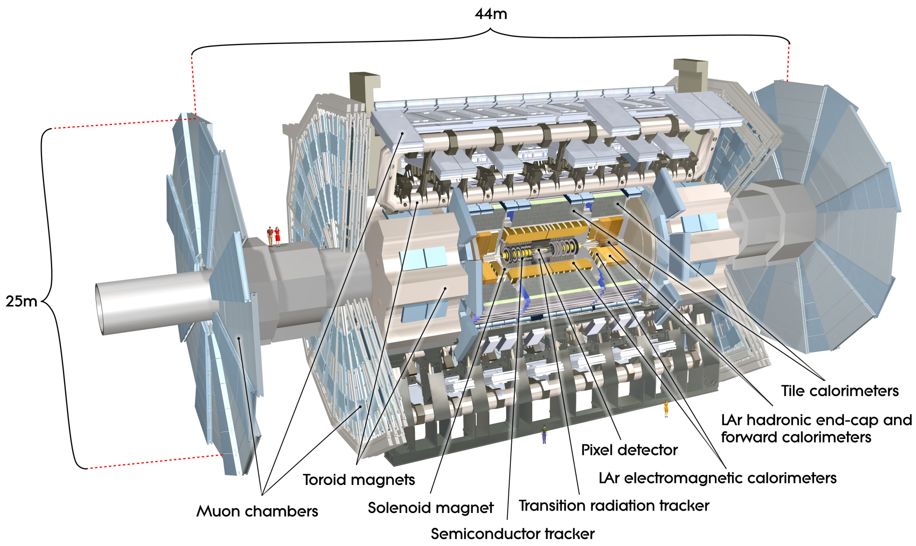

Figure 3.3: The ATLAS detector. Image from [54].

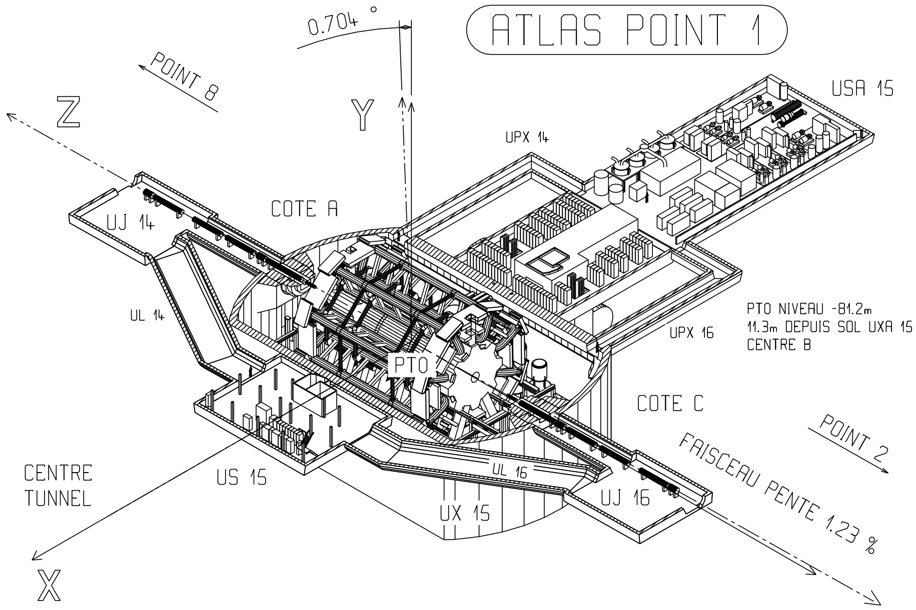

Figure 3.4: The ATLAS coordinate system.. Image adapted from [73].

3.2.1.1 Polar Coordinate

The radial distance, r (some early ATLAS documentation uses R), is taken relative to the z-axis, while the polar angle, θ, is the angle relative to the positive z-axis. The azimuthal angle, ϕ, is the angle in the x–y plane taken counter-clockwise from the positive x-axis when viewed from the zenith (positive z) side of the plane. *Pseudo-Rapidity*, η, is defined as [54]

$$\eta = -\ln \tan \left(\frac{\theta}{2} \right) \tag{3.6}$$

with $\eta = \pm\infty$ parallel to the z-axis, and $\eta = 0$ perpendicular. The pseudo-rapidity–azimuthal angle distance, ΔR, is defined as [54]

$$\Delta R = \Delta\eta \oplus \Delta\phi \tag{3.7}$$

where $\oplus$ denotes addition in quadrature.

3.2.1.2 Track Parameterisation

The helical path of a charged particle through ATLAS is characterised by five *Perigee Parameters*[74, 75]:

- q/p, the charge of the particle, q, divided by its momentum;
- θ, the polar angle of the track;
- ϕ, the azimuthal angle of the track;
- d_0, the signed distance to the z-axis. The sign of d_0 is positive when $\phi_0 - \phi = \pi/2 \pmod{2\pi}$, where ϕ_0 is the azimuthal angle to the point of perigee;
- z_0, the z coordinate of the track.

All quantities are measured at the point of closest approach to the nominal beam axis. This parameterisation is shown in fig. 3.5.

3.2.1.3 Particle Properties

For a particle of energy E, and momentum $\vec{\mathbf{p}}$, its *Rapidity*, y, is defined as [54]

$$y = \frac{1}{2} \ln \left(\frac{E + \mathrm{p}_z}{E - \mathrm{p}_z} \right) \tag{3.8}$$

while its *Transverse Momentum*, $\vec{\mathbf{p}}_\mathrm{T}$, and *Transverse Energy*, E_T, are defined in the x–y plane [54] (transverse energy may be defined vectorially).

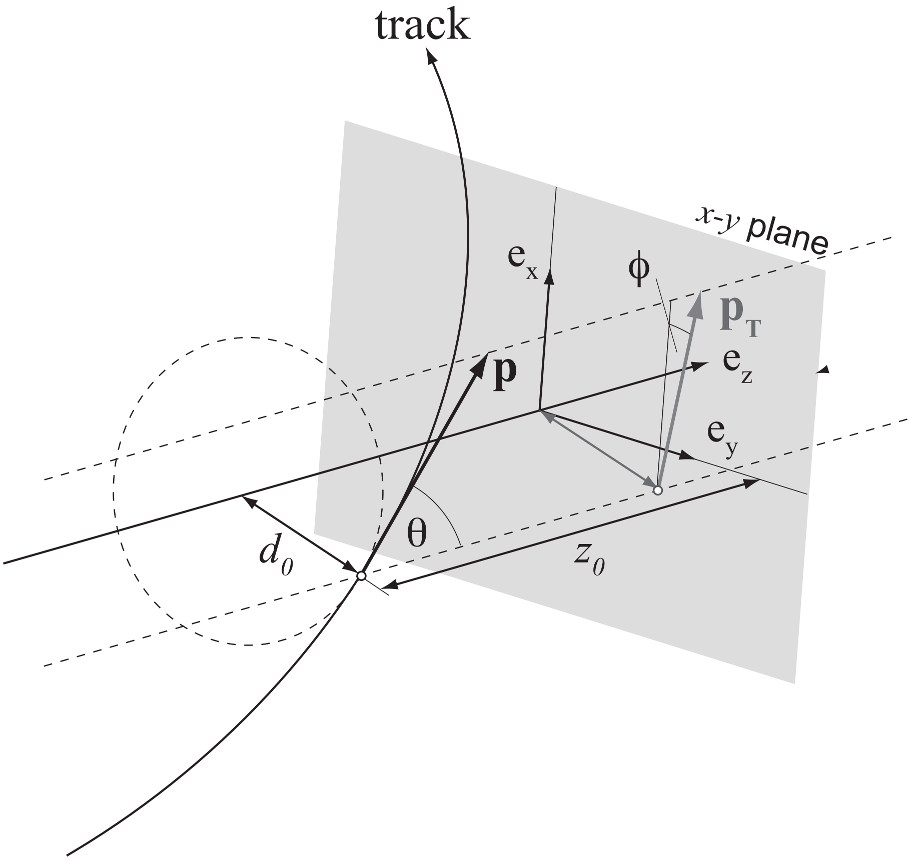

Figure 3.5: The ATLAS charged track parameterisation. Image from [75].

3.2.1.4 ATLAS Nomenclature

An *Event* within ATLAS is all the data extracted for a single LHC bunch crossing, while a *Candidate* is the subset of data from an event that matches some physics process of interest. A *Track* is the reconstruction of the path of a charged particle through the detector (and may be constructed from Inner Detector, calorimetry, or Muon Spectrometer information, or any combination thereof), while *Primary Vertices* (PVs) and *Secondary Vertices* (SVs) are reconstructions of pp interactions and decay processes respectively.

The radially symmetric nature of LHC bunch crossings allow the *Missing Transverse Momentum*, $p_{\mathrm{T}}^{\mathrm{miss}}$, and *Missing Transverse Energy* (MET), $E_{\mathrm{T}}^{\mathrm{miss}}$, of an event (or PV) to be defined as the magnitude of the imbalance of vectoral momentum and energy in the transverse plane [54].

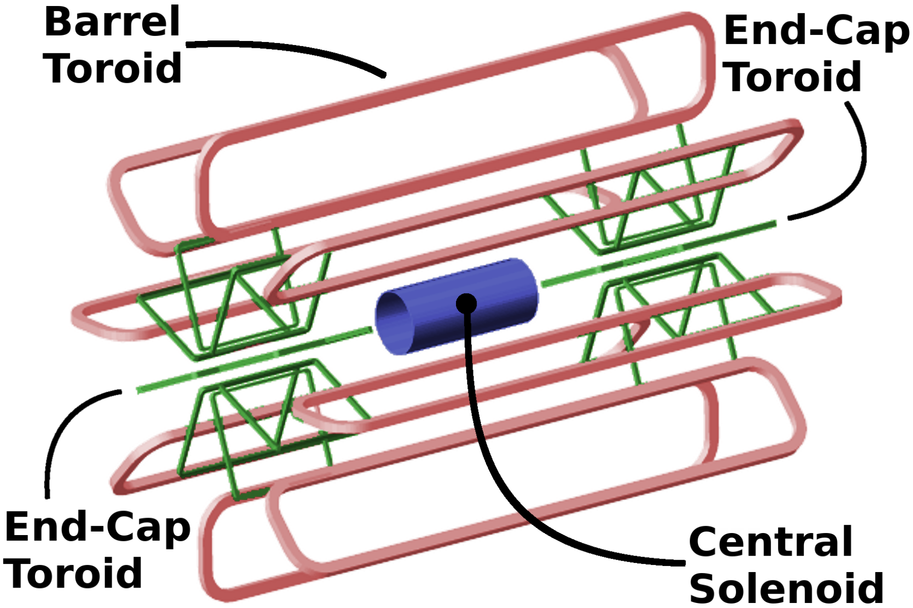

Figure 3.6: The ATLAS magnet systems. Image adapted from [80].

3.2.2 Magnet Systems

In order to measure the momentum of a charged particle, a magnetic field is used to bend its trajectory. There are three magnet systems in ATLAS [76]: the *Central Solenoid*[77] provides a longitudinal field in the Inner Detector, while the *Barrel Toroid* and *End-Cap Toroids*[78, 79] produce an azimuthal magnetic field in the Muon Spectrometer. In each system, the coil winding is formed from an Al-stabilised NbTi/Cu superconductor operating at cryogenic temperatures with cooling supplied by liquid He at ∼4.5 K. The overall layout of the magnet systems is shown in fig. 3.6.

3.2.2.1 Central Solenoid

The Central Solenoid is composed of a mono-layer of 1154 turns mounted in an Al support cylinder of length 5.8 m and interior diameter 2.46 m that encompasses the Inner Detector. The nominal operating current (7.7 kA) produces a 2 T field at the origin and a peak field strength of 2.6 T at the coil winding. To reduce the detector material budget, the Central Solenoid and the electromagnetic calorimeter share a common cryostat.

3.2.2.2 Barrel and End-Cap Toroids

The toroid system provides the magnetic field used in the Muon Spectrometer, and is composed of two sub-systems. The Barrel Toroid consists of eight air-core coils in a 'racetrack' configuration, assembled radially and symmetrically around the beam axis. Each coil consists of 120 turns formed from two 2×30 'pancakes' of length 25.3 m and width 5.4 m. Each coil is contained within its own cryostat and covers the region $|\eta| < 1.4$. The Barrel Toroid provides a peak field strength of 2.5 T in the bore at the toroidal nominal operating current (20.5 kA).

The second sub-system, the two End-Cap Toroids, are positioned within the Barrel Toroid in the forward regions of the detector ($1.6 < |\eta| < 2.7$). As with the Barrel Toroid, eight coils of 116 turns are arranged to provide an azimuthal magnetic field. The eight coils that form an end-cap, each of length 5.0 m and width 4.5 m, are contained within a single cryostat and produce a peak field of 3.5 T. The End-Cap coils are rotated by 22.5°, with respect to the barrel coils, to optimise the field strength in the interface region ($1.4 < |\eta| < 1.6$) between the two sub-systems.

3.2.3 The Inner Detector

The aim of the ATLAS *Inner Detector* (ID) [81, 82] is to provide robust and efficient measurement of the motion of charged particles in the high-fluence region near the interaction point, with sufficient granularity to allow PV and SV reconstruction. The design and construction of the ID is further constrained by the physical dimensions of the Central Solenoid and the requirement to maintain adequate detector stability during operation and well understood position reproducibility following repeated freeze–thaw cycles during ATLAS's lifetime.

The ID makes use of three sub-detectors to achieve these aims. The Pixel Detector [83] and *Semiconductor Tracker* (SCT) are silicon-based detectors providing high-resolution measurements in the high particle-flux region close to the beampipe. The *Transition Radiation Tracker* (TRT) provides additional track measurements and some particle identification functionality. The overall configuration of the ID sub-systems is shown in fig. 3.7.

The use of three disparate sensor technologies is designed to optimise track p_{T} and spatial resolution, while maintaining reconstruction efficiency and minimising the material budget and fiscal cost of the ID [54].

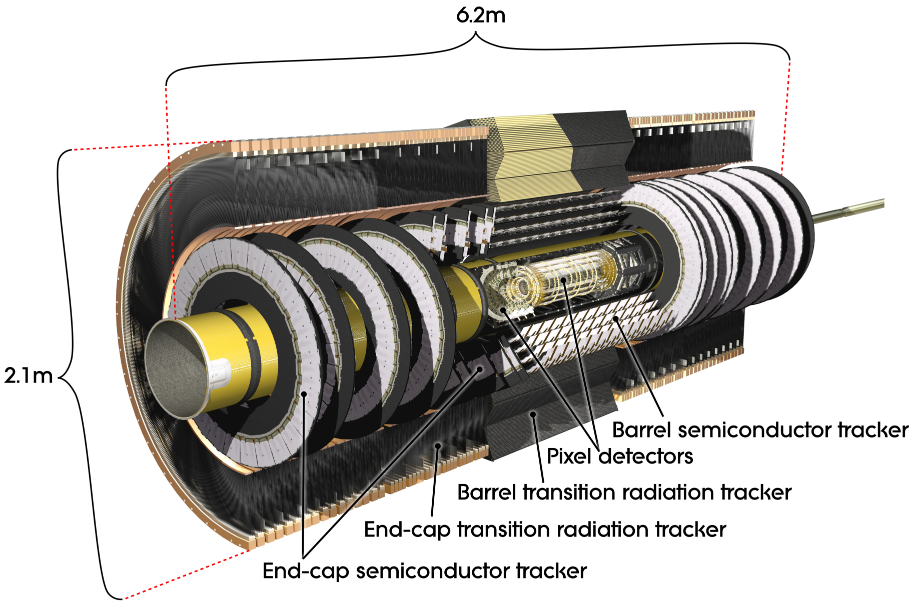

Figure 3.7: The ATLAS Inner Detector. Image from [54].

3.2.3.1 The Pixel Detector

The common sensor element employed on the three barrel and six end-caps of the pixel detector is a 250 µm thick Si sensor tile (63.4 mm × 24.4 mm) with 47 232 50 µm × 400 µm pixel elements bump-bonded onto 16 front-end read-out chips. A flexible polyimide printed-circuit board and the module control electronics is mounted to the opposite-side of the sensor tile with wrap-around fly-leads connecting to the front-end electronics.

1744 such sensor elements are mounted onto 112 barrel staves and 48 end-cap sectors to form the barrel and end-cap pixel layers as shown in fig. 3.8. Barrel sensor elements are arranged to align the long side of each pixel with the beampipe, similarly end-cap sensors project along r. Charge sharing between adjacent pixels, from the physical orientation of the sensor elements (and the induced Lorentz angle on the staves) result in an intrinsic position resolution of $\approx 10\,\mu\text{m} \times 115\,\mu\text{m}$.

3.2.3.2 The Semiconductor Tracker

The SCT is composed of 4088 Si sensor elements divided between four barrel layers (2112 elements) and nine end-cap disks in each end-cap (as shown in fig. 3.8). Each sensor element is a pair of Si micro-strip detectors glued back-to-back on a TPG mounting plate with a small stereo-angle between them to allow the reconstruction of a 2D space-point.

Barrel detectors contain 768 parallel strips with a pitch of 80 µm on wafer, with two wafers daisy-chained to produce a detector element. The daisy-chained wafers are bonded to the 380 µm mounting board with a ±20 mrad angle between them. The five designs used in the end-cap modules also contain 768 strips, with the inter-strip angle producing an isosceles trapezoidal geometry such that one micro-strip detector in each pair has an approximately projective geometry in R with a mean inter-strip pitch of $\sim$80 µm.

2D space-point resolution in the barrel (end-cap) is 17 µm in R–ϕ and 580 µm in z (r).

3.2.3.3 The Transition Radiation Tracker

The TRT sensor element (often refered to as a straw) in the TRT detector is a carbon-fibre reinforced polyimide drift tube of 4 mm diameter containing an Au-plated W wire. The tube is filled, at a slight over-pressure, with an operating gas[5] and a potential difference of 1530 V is applied between a 0.2 µm Al layer in the inner tube wall and the wire. The intrinsic resolution of the TRT straw is $\approx$ 130 µm.

The barrel TRT detector is formed of three rings of sensor elements, each consisting of 32 modules in an alternating chevron arrangement. Within each module, the TRT straws form a uniform axial array with a mean spacing of $\approx$7 mm embedded in a matrix of polypropylene fibres that serve as a generator for transition radiation photons.

The TRT end-cap detectors consist of TRT wheels of two distinct designs. The 12 inner-wheels of each end-cap contain eight layers of 768 radially aligned straws equidistant in azimuthal spacing, with 8 mm between layers, while the eight outer wheels utilise a 15 mm gap between layers. In both end-cap wheels, polypropylene radiator foils are inserted between the straw layers to stimulate emission of transition radiation photons. The physical layout of the TRT cells is shown in fig. 3.8.

The construction of the TRT ensures any particle originating at the nominal interaction point must cross at least 32 (avg 36) straws while traversing the ID.

---

[5] $Xe/CO_2/O_2$ (70:27:3), though a number of other combinations have been used to evaluate performance, and reduce the running cost associated with leaking TRT straws.

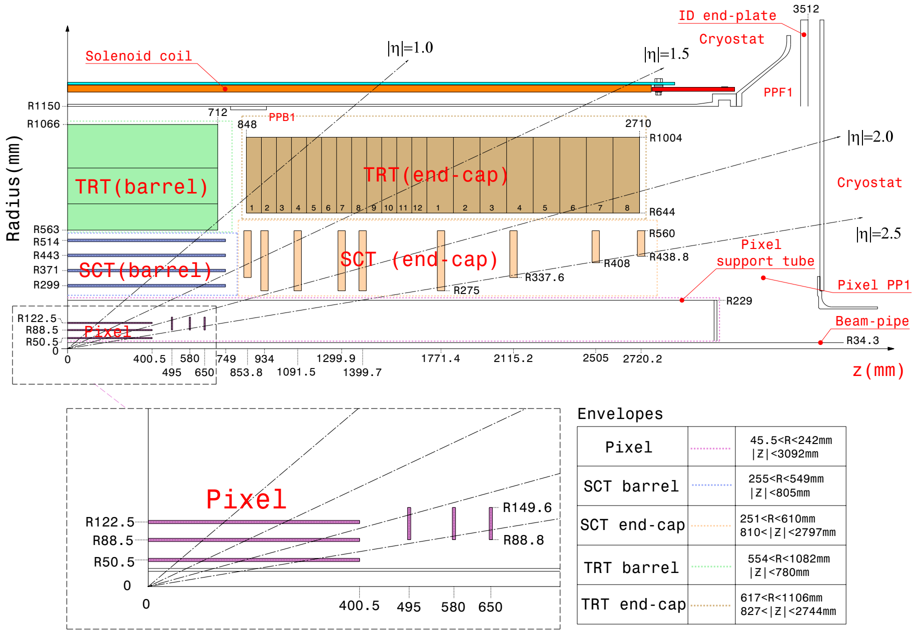

Pixel	┈	45.5<R<242mm |Z|<3092mm
SCT barrel	┈	255<R<549mm |Z|<805mm
SCT end-cap	┈	251<R<610mm 810<|Z|<2797mm
TRT barrel	┈	554<R<1082mm |Z|<780mm
TRT end-cap	┈	617<R<1106mm 827<|Z|<2744mm

Figure 3.8: ATLAS Inner Detector Envelopes. PP1, PPB1, and PPF1 indicate the position of the patch panels for this quarter cross-section. Image from [54].

Furthermore, low-energy transition radiation photons are re-absorbed by the gas mixture and consequently yield much larger signal currents than that of the passage of a minimally-ionising charged particle. Distinguishing between these high and low threshold hits allows electron/hadron separation in some momentum regimes.

3.2.4 Calorimetry Systems

Calorimetry in ATLAS is provided by a suite of sampling detectors. In the forward region of the detector, liquid Ar calorimeters [84, 85] are used for both electromagnetic and hadronic calorimetry; in the barrel region, an additional liquid Ar detector is used for electromagnetic calorimetry with a Steel/Pb calorimeter [84, 86] providing hadronic calorimetry. The components of the ATLAS calorimetry system are shown in fig. 3.9.

3.2.4.1 Electromagnetic Calorimeters

Electromagnetic calorimetry in the central region ($|\eta| < 1.475$) is provided by a Pb–liquid Ar *LAr Detector*. The barrel LAr detector is built from two half-barrels, each of length 3.2 m, with an internal and external diameter of 2.8 m

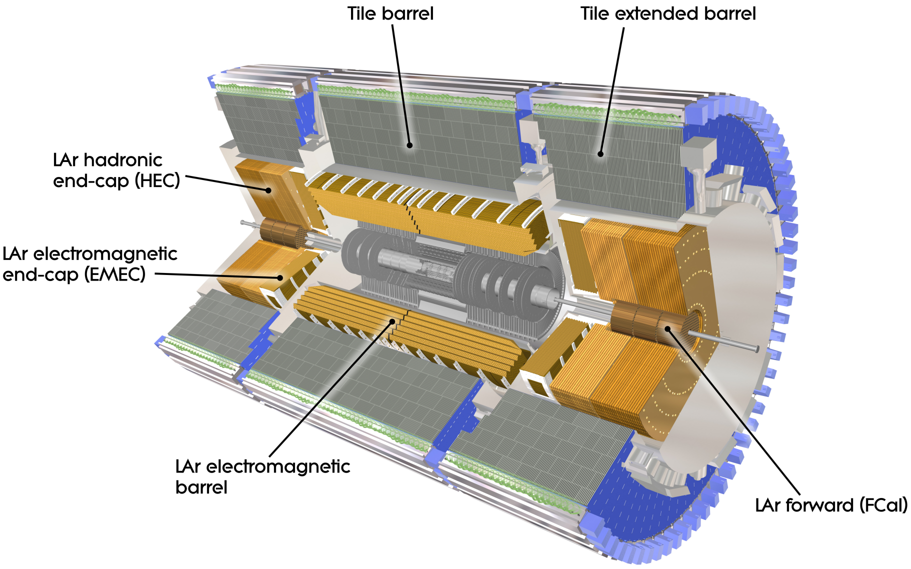

Figure 3.9: The ATLAS calorimetry systems. Image from [54].

and 4 m respectively. There is a 6 mm service gap between the two installed half-barrels. The half barrels are formed from layers of steel encased Pb sheets formed into accordion-shape absorbers with the remainder of the volume filled with liquid Ar as the active medium, and three Cu sheets forming the sensor elements. Readout cells are assigned to three logical layers. The dimensions of the readout cells vary in each layer to optimise the spatial resolution of the calorimeter. Cells are ganged to form a low-granularity readout usable by the online trigger system. This configuration is shown in fig. 3.10(a).

In the end-caps, the *Electromagnetic End-Caps* (EMECs), wheel shaped calorimeters are installed around the beampipe. Each wheel is 63 cm deep with internal and external radii of 330 mm and 2098 mm respectively. They are installed to provide coverage in the region $1.375 < |\eta| < 3.2$. The general configuration of the EMECs is the same as the LAr detector with two structural layers divided into three logical readout layers.

Energy resolution in both barrel and end-caps is $\frac{\sigma_E}{E} \approx \frac{10\,\%}{\sqrt{E}} \oplus 0.7\,\%$ and provides a minimum of 22 (24) radiation lengths of instrumented material in the barrel (end-cap) regions.

The Electromagnetic Calorimeters are contained in three cryostats. The central cryostat is shared between the barrel calorimeter and the Central Solenoid with the Central Solenoid contributing ≈0.66 radiation lengths to the material budget ahead of the barrel LAr detector at normal incidence. The two end-cap cryostats are shared between the EMECs, the hadronic end-cap calorimeters, and the Forward Calorimeters.

3.2.4.2 Hadronic Calorimeters

Hadronic calorimetry is provided in the region $|\eta| < 1.7$ by the *Tile Calorimeter* with a central tile calorimeter of length 5.8 m, inner radius 2.28 m, and exterior radius 4.25 m juxtaposed between two extended barrel calorimeters, each of length 2.6 m and similar radii. Each calorimeter consists of a number of self-supporting sub-modules (each subtending 5.3° in azimuth) containing Polystyrene/PTP scintillator pads, as the active medium, encased in a steel absorber structure, as shown in figure fig. 3.10(b).

Wavelength shifting fibres connect the scintillator pad edges to photo-multiplier tubes and are ganged to form cells with an approximately projective geometry in η. As with the electromagnetic LAr detectors, readout cells are divided into three logical layers with front-end electronics providing readout on a per-cell basis, as well as providing an analogue sum of subsets of adjacent cells for the online trigger system.

The *Hadronic End-Cap* (HEC) calorimeters provide calorimetry in the region $1.5 < |\eta| < 3.2$ of the detector. Each HEC contains two sub-modules composed of Cu–liquid Ar calorimeters of a flat-plate design. In the inner sub-module, 24 Cu plates, 25 mm thick and of outer radius 2030 mm, encase the beampipe and form an assembly containing 8.5 mm liquid Ar voids. Each void is further subdivided into four drift zones by Kapton-backed readout electrodes ganged to form readout cells.

Construction of the outermost sub-modules differs in the number and thickness of the Cu plates, with 16 plates of 50 mm preferred.

On-line calibration of the Tile Calorimeter maintains an energy-scale resolution of $\frac{\sigma_E}{E} \approx 3\,\%$ over its 7.4 interaction lengths. The HEC energy resolution is $\frac{\sigma_E}{E} = \frac{50\,\%}{\sqrt{E}} \oplus 3\,\%$ and provides a minimum of 9.4 interaction lengths of instrumented material. Additional shielding is installed to ensure a minimum of 11 interaction lengths of material between the nominal interaction point and the muon spectrometer.

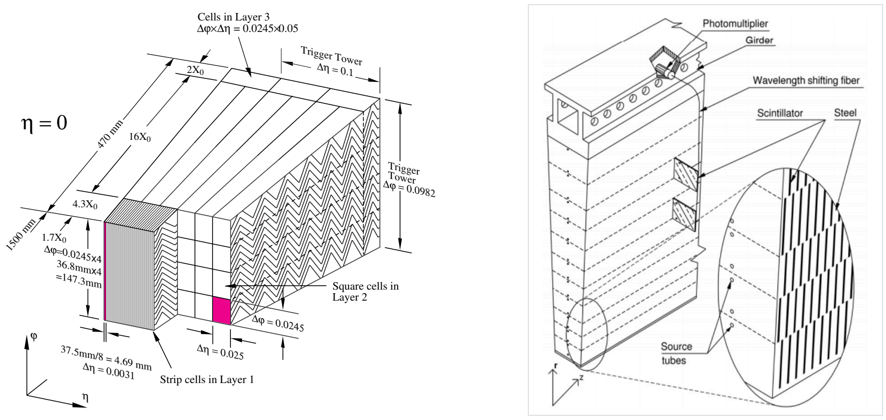

(a) Liquid Ar Calorimeter physical and logical layout

(b) A Tile Calorimeter sub-module

Figure 3.10: ATLAS calorimeter modules. Shown are physical and logical layout of a section of the barrel LAr calorimeter (left) and a submodule from the Tile Calorimeter (right). Images adapted from [54].

3.2.4.3 The Forward Calorimeters

In the far-forward region of the detector ($3.1 < |\eta| < 4.9$), both electromagnetic and hadronic calorimetry is provided by the *Forward Calorimeter* (FCal). The FCal consists of three modules in each end-cap. The innermost module, constructed from Cu, is optimised for electromagnetic calorimetry, while the middle and outer modules are W-based hadronic calorimeters. In each module, a matrix is formed of longitudinal channels filled with liquid Ar as an active medium between an electrode structure consisting of concentric rods and tubes, parallel to the beam axis, separated by PEEK fibers. The separation between the anode rod and cathode tube varies between the inner, middle, and outer module and is optimised to reduce ion drift time and charge build-up within the 12 260 sensor elements (ganged to provide 1762 read-out channels).

On-line calibration of the FCal maintains an energy-scale resolution of $\frac{\sigma_E}{E} < \frac{100\,\%}{\sqrt{E}} \oplus 10\,\%$.

3.2.5 The Muon Spectrometer

The *Muon Spectrometer* (MS) [73] serves two purposes. The first is to offer a triggering mechanism for events with muons in the final state, and the second is to provide precision tracking measurements for muons with a p_{T} between

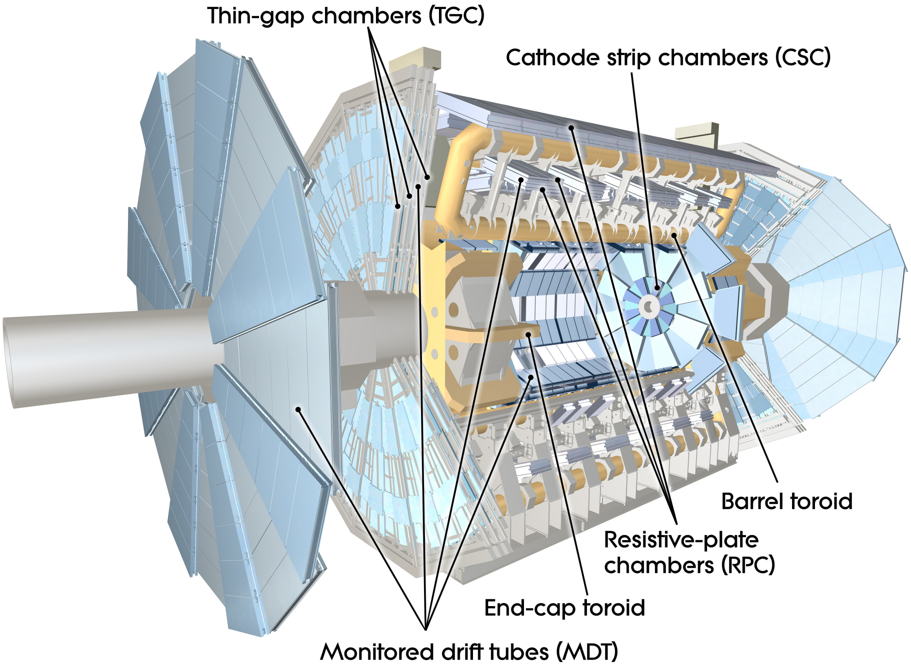

Figure 3.11: The ATLAS Muon Spectrometer. Image from [54].

3 GeV and 1 TeV. To serve these functions the MS consists of four sub-systems: *Resistive Plate Chambers* (RPCs) and *Thin Gap Chambers* (TGCs) provide trigger information for the barrel and end-cap regions, while *Monitored Drift Tube Chambers* (MDTs) and *Cathode Strip Chambers* (CSCs) provide tracking measurements in the central and forward regions respectively. The overall layout of the MS is show in fig. 3.11.

3.2.5.1 Resistive Plate Chambers

RPCs are gaseous parallel electrode-plate detectors used to provide trigger information in the region $|\eta| < 1.05$. An RPC is formed from two RPC cells, that are bonded between two support panels of polystyrene foam, backed by an earthed aluminium sheet as shown in fig. 3.12(a).

Each of the cells is a thin ionisation chamber consisting of two phenolic resin (Bakelite) plates separated by 2 mm polycarbonate spacers. The external surfaces of the plates are instrumented with 25 mm to 35 mm Cu readout sensors while graphite electrodes are used to provide a potential difference of $4.9\,\mathrm{kV\,mm^{-1}}$ between the plates. The combination of the gas used[6] and the

---

[6] $C_2H_2F_4$:Iso-C_4H_{10}:SF_6.

applied potential difference between the plates ensures the detector working mode is a Townsend mechanism avalanche [87], giving a space-time resolution of the order of 1 cm × 1 ns.

3.2.5.2 Thin Gap Chambers

TGCs provide muon trigger information in the region $1.05 < |\eta| < 2.4$. The TGCs are multi-wire proportional chambers with graphite backed FR4 cathode planes forming a gas volume[7] containing anode wires. The anode wires are ganged to provide a readout pitch of 7.2 mm to 36 mm while 14.6 mm to 49.1 mm Cu readout strips are bonded to the cathode plane with a stereo-angle between the wires and strips forming local x and y coordinates. The cathode–cathode gap of 2.8 mm, wire pitch of 1.8 mm, and nominal operating voltage of 2.9 kV ensure a short drift time with a typical timing resolution of 4 ns, allowing for bunch crossing identification.

The TGCs are grouped into doublet and triplet units with the readout strips omitted in the central chamber of the triplet. Mechanical rigidity of the units is provided by paper honeycomb substrates. Cross-sections of these units are shown in fig. 3.12(b).

3.2.5.3 Monitored Drift Tube Chambers

The basic detection element of the MDT chamber is an Al drift tube with a diameter of 29.6 mm, containing a central Au-plated W/Re wire and an[8] operating gas at 3 bar. A potential difference of 3 kV applied between the wire and tube wall produces a maximum drift time of 700 ns.

Three layers of MDT chambers are used in the region $|\eta| < 1.4$, with a further three ‘MDT wheels’ in each end-cap ($1.4 < |\eta| < 2.7$). The three MDT layers are assembled from 2×4 (inner) or 2×3 (middle and outer) mono-layers of drift tubes to improve spatial resolution and provide redundancy[9]. Structural support is provided by mounting the mono-layers onto a rigid spacer frame that is instrumented to provide precision position/alignment information on the MDT tubes. A typical barrel MDT chamber is shown is shown in fig. 3.13(a).

---

[7] CO_2:n-C_5H_{12}.

[8] Ar:CO_2.

[9] An average of 18 MDT hits per track over the fiducial volume of the MDT, and a resolution of ≈ 80 µm per tube.

3.2.5.4 Cathode Strip Chambers

Each CSC cell is a multi-wire proportional chamber consisting of anode wires with a pitch of 2.5 mm between two cathode plates with the anode–cathode spacing equal to the wire pitch. The cathode plates are lithographically etched with readout strips. Radial strips are capacitively coupled to provide a typical pitch of 5.5 mm while the azimuthal strips are of pitch 12.5 mm. A potential difference of 1.9 kV is applied in the gas gap[10] between the anode and cathode.

CSCs are used in the far-forward region of the detector ($2 < |\eta| < 2.7$) where occupancy prevents the use of MDT chambers. Four cells are bonded together using polyurethane foam to form a CSC; sixteen CSCs are arranged in a $2 \times 2 \times 4$ pattern in each end-cap. Each CSC is inclined by 11.6° to ensure a near optimal crossing angle for a muon originating near the nominal interaction point[11]. A cross-section of a CSC chamber is shown in fig. 3.13(b).

3.2.6 The Trigger and Data Acquisition System

The ATLAS *Trigger and Data Acquisition system* (TDAQ) is designed to reduce the LHC bunch crossing rate of 40 MHz to an event storage rate of ∼1000 Hz to ensure a manageable data transfer and storage environment. This requires a rejection factor of $\sim 10^5$ while still retaining pp interactions of interest at $\mathcal{O}(1)$. To service this requirement, ATLAS uses a three-level trigger system to perform real-time selection of bunch crossings of importance.

The *Level-1 trigger* (LVL1) [88] searches for bunch crossings that may contain: high-p_{T} electrons, muons, or photons; jets or hadronically decaying taus; large $E_{\mathrm{T}}^{\mathrm{miss}}$ or ΣE_{T}. LVL1 propagates these to the two-stage *High-Level Trigger* (HLT) [89] for further analysis. Within the HLT, the *Level-2 trigger* (LVL2), seeded by information from LVL1, designates events for full-reconstruction where the *Event Filter* (EF) makes the final selection of bunch crossings to record for subsequent off-line analysis.

In addition to the triggers that serve physics analyses, trigger bandwidth is also reserved for special purpose calibration triggers. Calibration triggers may select events from empty, unpaired, or paired bunch crossings at random, or from events that stimulate custom detector hardware such as the *Minimum Bias Trigger Scintillators* (MBTS) [54]. Additional calibration triggers are implemented as custom LVL1 and HLT triggers that simulate physics triggers

---

[10] Ar:CO_2.

[11] Resulting in a spatial resolution 5 mm in ϕ, and 40 µm in r.

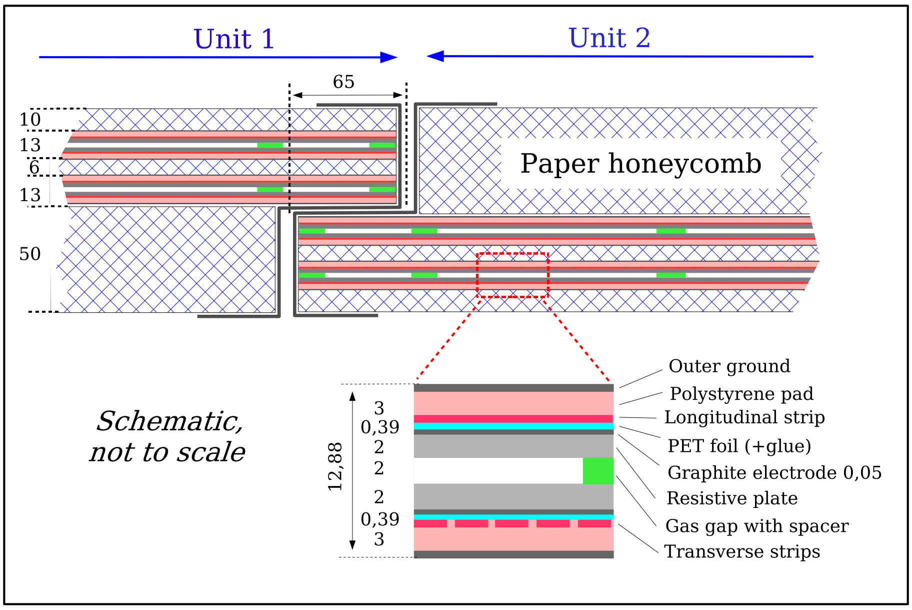

(a) Resistive Plate Chambers cross-section

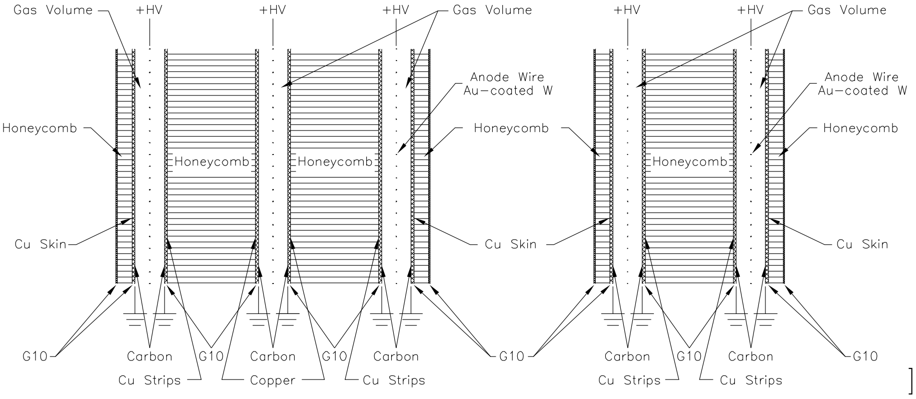

(b) Thin Gap Chamber units

Figure 3.12: ATLAS Muon Spectrometer components. Shown are the RPC (top) and TCG units (bottom). Images from [54].

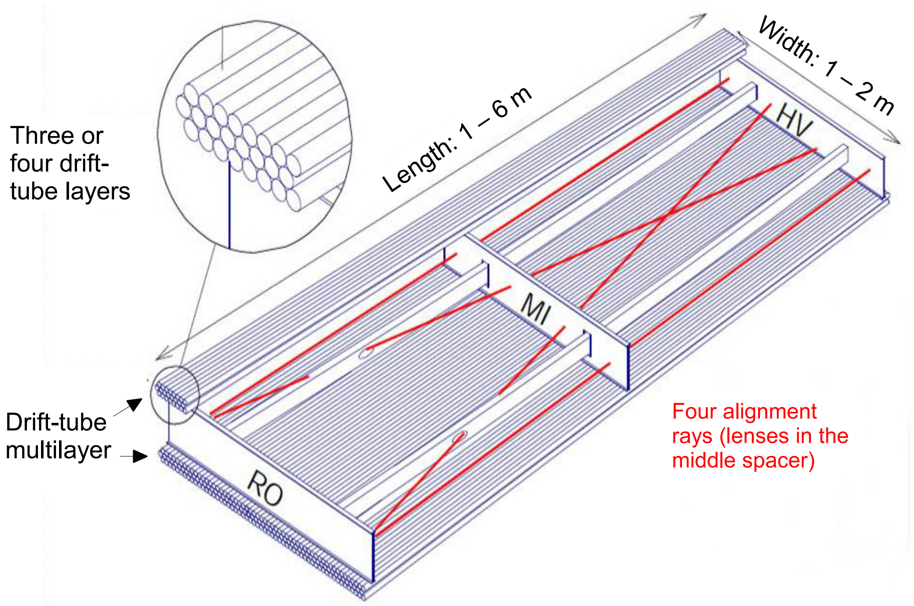

(a) A Monitored Drift Tube Chamber

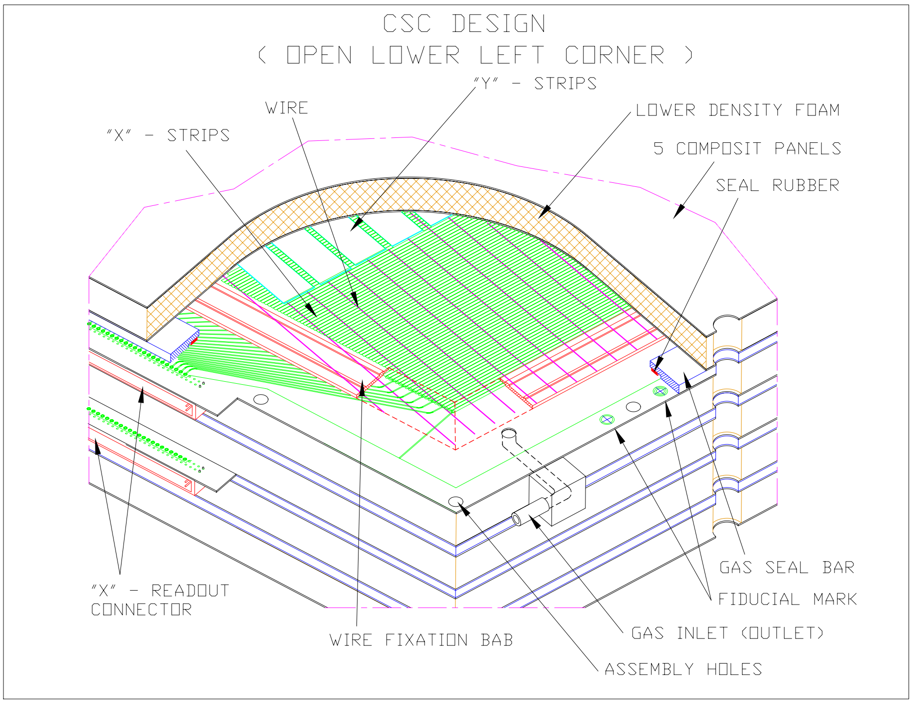

(b) Cathode Strip Chamber cross-section

Figure 3.13: ATLAS Muon Spectrometer components. Shown are the arrangement of the sensor elements for the MDT chambers (top) and a CSC cells (bottom). Images from [54].

with greatly relaxed selection criteria.

To support the trigger system, the *Data Acquisition system* (DAQ) [89] stores event information in on-detector pipeline memory and, dependent on the bunch crossings accepted by LVL1 and the HLT, forwards event data to the *Readout Drivers* (RODs), *Readout Buffers* (ROBs), and finally local mass storage. The flow of event data through the TDAQ is shown in fig. 3.14.

To accommodate changes in the LHC beam during data taking, triggers are dynamically prescaled [88, 89], where a prescale factor of n implies that only $^1/_n$ of the events passing a trigger selection are passed forward to the next stage of the trigger. Prescale factors may be applied at LVL1, and both stages of the HLT.

Additional information about the triggers used in the $\mathrm{B_s} \to \mathrm{J}/\psi\phi$ analysis are found in section 4.2.1.

3.2.6.1 Level-1 Triggers

LVL1 reduces the event rate from 40 MHz to ∼100 kHz by defining *Regions of Interest* (RoIs) within each event based on reduced-granularity information from the calorimeter and the trigger sub-systems of the MS. The RoIs of each event, regions in η–ϕ space with a feature tag and threshold, are then forwarded to the *Central Trigger Processor* (CTP) where they are matched to trigger items on the *Trigger Menu*.

Events that match items on the menu are selected for further analysis, with the RoIs for the event being forwarded to LVL2, and the pipeline data from the detector elements forwarded to the RODs. Data from events not selected are flushed from the pipeline. Event selection by LVL1 requires a latency of $<2.5\,\mu\mathrm{s}$. To achieve this, LVL1 consists of purpose-built hardware.

3.2.6.2 The High-Level Trigger

Within LVL2, events are processed through a suite of algorithms, the *Trigger Chains*, dependent on the LVL1 menu items that selected the event for further analysis. At each step of a trigger chain, additional high-granularity information for the RoIs may be requested from the detector to refine event selection or confirm the selections of LVL1. Each event may be processed through multiple chains, with events rejected for further analysis if no trigger chain can be satisfied for the event. Events retained for further analysis have full detector

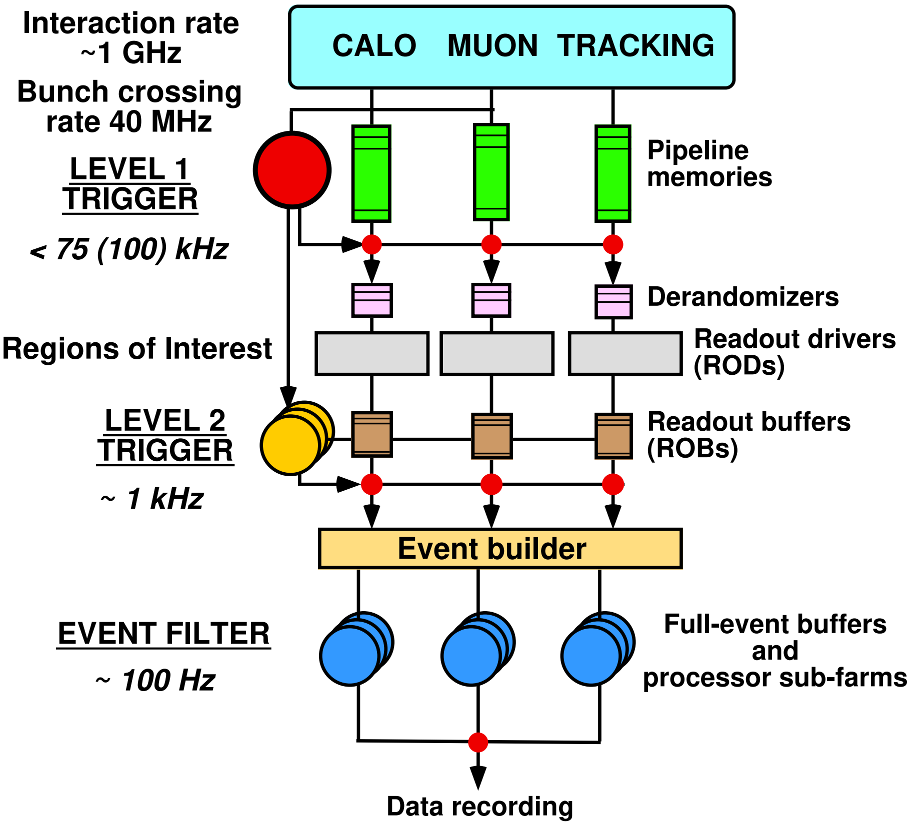

Figure 3.14: Schematic overview of the ATLAS TDAQ, and the data rates anticipated at the start of Run1. Event data flows from the detector elements (top) toward permanent storage (bottom) as the event passes each stage of the online trigger. The LHC did not achieve 25 ns bunch spacings until 2012-12-17 [90] while TDAQ rates exceeded those shown (see section 4.2.1). Image from [88].

information for the events forwarded to the ROBs.

LVL2 is implemented in software on a dedicated PC server farm, and reduces the selected event rate to between 1 kHz and 4.5 kHz with a typical latency of 30 ms to 50 ms, dependent on the active trigger chains.

Events fulfilling a chain at LVL2 are dispatched to the *Event Builder* where a full software-based ‘off-line’ reconstruction is performed using all available detector information. The reconstructed events are then forwarded to the EF where the final selection of events is made. The latency of event reconstruction and selection is typically 2 s to 10 s; during this step, the event rate is reduced to ∼1 kHz.

3.3 The ATLAS Computing Model

The ATLAS computing infrastructure [91] is a core component of the ATLAS experiment, and consists of a combination of ATLAS-specific hardware and software, and components of the *Worldwide LHC Computing Grid* (WLCG), CERN's global computing network.

The aims of the ATLAS computing infrastructure include:

- Monitoring the status of the detector, and its interaction with the LHC;
- Reconstructions of the raw data, as extracted from the detector, into formats suitable for use in physics analyses;
- Management of the raw data, reconstructed data, and user generated datasets;
- Infrastructure for the running of custom analysis code in a distributed, heterogeneous enviroment.

3.3.1 Online Software

The *Detector Control System* (DCS) [54, 92] ensures the coherent and safe operation of the detector and completes, alongside the TDAQ, the online component of the *ATLAS Operations Model*[91, 92].

The front-end components of the DCS are used to monitor and control the operation of the detector, and range from "Commercial, Off The Shelf" sensor elements and power distribution systems to the *Embedded Local Monitor Board* (ELMB), a custom, digital I/O board for use in the regions of the cavern where the magnetic field or ionising radiation prohibit the use of commercially available components.

The DCS back-end is arranged into three logical layers:

- The *Local Control Stations* (LCS) provides process control at the subsystem level (operating in a closed-loop mode), as well as I/O to the higher layers of the back-end through the commercial SCADA package PVSS [93];
- The *Sub-Detector Control Stations* (SCS) provides high-level control of individual sub-detectors, with each system modelled as a finite state machine. This hierarchy of state machines, down to the devices level, allows for standardised operation and error handling at each functional layer;

- The *Global Control Stations* (GCS) implements all required functionality needed by the ATLAS operators in the ATLAS control room, including the *Operator Interface* and *Alarm Monitors*[92] used to manipulate and monitor the SCS's finite state machines.

3.3.2 The Computing Grid

The WLCG is CERN's global computing infrastructure collaboration, and at the termination of the LHC Run1 data taking, consisted of over 170 computer centres, in 36 countries. Between these sites, over 200 000 CPU cores are available for use, with a combined storage capacity of over 150 PB.

3.3.2.1 Tiers and Clouds

The computing centres within the WLGC are assigned to one of three tiers:

- *Tier* 0: The single Tier 0 site is based at CERN's Geneva computing centre (with some distributed storage in Budapest, Hungary) and is configured for the immediate storage of raw data from the LHC experiments, and their initial pass through the experiment's reconstruction software[12];
- *Tier* 1: Tier 1 sites are connected directly to Tier 0 by the dedicated fibre-optic connections of the *LHC Optical Private Network* (LHCOPN). The Tier 1 sites serve to back-up the Tier 0 by storing some fraction of the raw data[13] and provide sources for the further distribution of data between the sites of the WLGC;
- *Tier* 2: Tier 2 sites represent the majority of centres within the WLGC, and are typically hosted at universities and scientific institutes. The Tier 2 sites are the primary resource for WLCG users performing physics analyses, as Tier 0 and Tier 1 sites are restricted to centrally organised production runs.

The computing centres are arranged into *Clouds*for management purposes, with each cloud containing a single Tier 1 site, and a number of geographically proximal Tier 2 sites.

3.3.2.2 Data Management

ATLAS data resources are arranged into a three level logical structure:

---

[12] The aim within the ATLAS experiment is to have a subset of any LHC run reconstructed within 12 h, and the full run reconstructed within 48 h.

[13] The worlds largest RAID (Redundant Array of Independent Disks) array?

- *File*: An individual file system object;
- *Dataset*: Collections of data files. Due to the distributed nature of file management within the WLGC, a dataset may exist at a number of sites;
- *Container*: Collections of datasets, and optionally other containers.

Data management, at the level of the analysis user, is performed through the `DQ2`[14] and `R2-D2` software packages [91], with `DQ2` responsible for the management of data files, sets, and containers, and `R2-D2`[15] used to distribute datasets between WLGC sites.

3.3.2.3 Job Management

Submission of units of computational work, *Grid Jobs*, to the WLGC is achieved in ATLAS through a number of grid middle-ware tools, with `PanDA` [95] and `Ganga` [95] the most commonly used tools at the end of Run1.

At the heart of both packages is the ability to compress a directory structure from the analysis user's local workstation and to distribute this structure to worker nodes in the WLGC that have access to the required datasets and containers. At the remote WLGC site, a subset of data files to be used as input to the job is uploaded onto the worker nodes, and the grid job run. As part of this process, the output from the job may be stored on the WLGC storage pools.

3.3.3 Offline Software

The ATLAS offline software consists of the `Athena` framework [91], and over 2000 packages delevoped within `Athena` to provide the functionalty required by analysis users. In addition to `Athena`, `ROOT` [96], a software framework developed by CERN is used as the final step in the $\mathrm{B_s} \to \mathrm{J}/\psi\phi$ analysis chain.

3.3.3.1 Data Formats

To ensure efficient use of the WLGC's computing and storage capacity, a number of common file formats are found throughout ATLAS:

- *Raw Data* (Raw, RDO): Raw data are extracted from the detector's ROBs, and a zero-suppressed byte-stream format is provided by the EF

---

[14] `DQ2` was replaced with `Rucio` [94] (Don Quixote's donkey) at the end of Run1.

[15] `R2-D2` does not manipulate any data itself, it creates and registers requests against the appropriate WLGC management infrastructure to transfer data files between WLGC sites.

as the output for triggered LHC bunch crossings. Events in this format average ≈1.6 MB, and technical limitations of the TDAQ system constrain the number of events in each data file such that the data files are <2 GB in size;

- *Event Summary Data* (ESD): ESD is the primary output of the default physics reconstruction chain, and is intended to make RDO files unnecessary for almost all physics analysis users. Events are stripped of much of the detector level information, e.g. times, currents and voltages as measured by the detector sensors are converted into pseudo-physics objects such as ID space-points (section 3.3.5.1) and calorimeter energy deposits, and the resultant reconstruction artefacts stored in an object-orientated paradigm using the POOL [97] file format. ESD files are typically produced centrally, at Tier 0, and distributed to Tier 1 sites as part of automated reconstruction of each LHC run;

- *Analysis Object Data* (AOD): The AOD files format is the first file format expected to be used in physics analyses (as opposed to detector and reconstruction studies) [98] and contains additional reconstructed physics objects (electrons, muons, jets, etc). As with ESD events, AODs are stored using the POOL file format, and produced centrally at the Tier 0 and Tier 1 sites, before distribution to Tier 2 sites for use in analysis code. As the centrally produced AOD files contain all events from a LHC run, two additional file formats are common within ATLAS, *Derived Analysis Object Data* (DAOD) and *Derived Physics Data* (DPD) [99] are produced by analysis teams where:

  - Skimming: Removal of events of no interest to the analysis;
  - Slimming: Removal of classes of reconstructed physics objects;
  - Thinning: Removal of reconstructed physics objects of no interest to the analysis;
  - Augmentation: Generation of physics objects specific to the analysis.

  has been applied to the AOD input;

- *nTuples*: Flat ntuples are commonly used at the final level of analysis, and as such are highly analysis specific.

3.3.3.2 The Athena Software Framework

The `Athena` framework is the object-orientated framework used in the processing of all ATLAS data [91]. The main components of `Athena` are:

- The *Application Manager*: The application manager singleton is an implementation of `Gaudi` [100], and provides the core management services for the operation of the `Athena` framework. This includes configuration of the framework through Python *Job Options*, messaging and performance monitoring services, and control of the logical flow of data through the analysis framework. `Gaudi` is designed such that storage, data objects, and analysis code are logically decoupled[16], and all are wrapped with python classes such that they may be manipulated through the python job options;

- The *Event Data Service*: The event data service consists of *StoreGate*for the management of the transient data store, the *Persistency Services*that are responsible for the loading/saving of POOL objects from/to the file system, and the *Converters*that serve to transform objects between their persistent and transient storage formats;

- *Algorithms*: Algorithms are the basic data processing class, and are required to inherit directly from the `Gaudi` algorithm base class and implement three functions: `initialize()` and `finalize()` provide the algorithms set-up and tear-down; the `execute()` method is invoked once per event by the application manager. Algorithms are frequently tied together using the sequencing service of the application manager, and use *Filter Algorithms*to remove uninteresting events from the data flow;

- *Tools*: Tools are used to process events, however they differ from algorithms in that they have no requirement to inherit from a tool base class. As they are driven from the `execute()` method of an algorithm, they may be invoked more than once per event. It is typical that an algorithm is implemented as little more than trivial control logic that uses a number of pre-configured tools to implement any data transformations.

The arrangement of these components is shown in fig. 3.15

`Athena` is used in a number of different forms in ATLAS. An online version is used to provide reconstruction functionality in the TDAQ, a *Derivation*release is used for the centrally controlled bulk reconstruction, AOD, DAOD, and DPD generation, while the *AnalysisBase*release includes integration with `PanDA` to allow user-level analysis jobs to be run on the WLGC.

---

[16] Data hiding, as defined by [91].

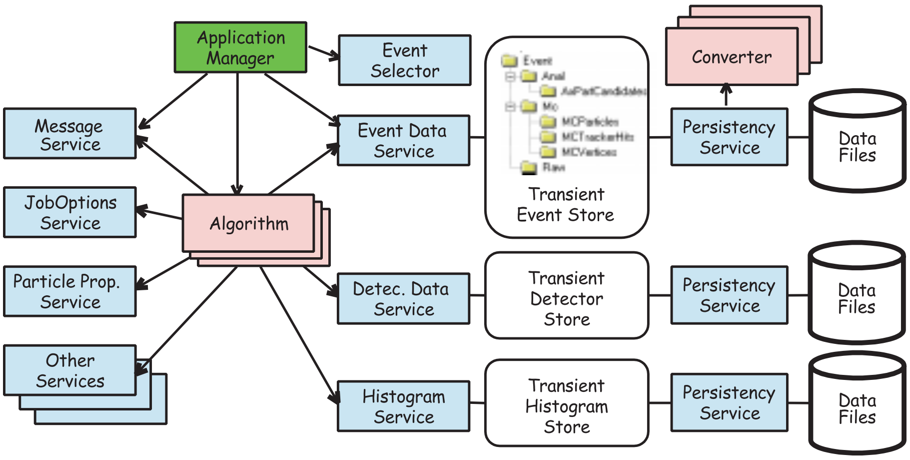

Figure 3.15: The Gaudi framework, as envisaged during the initial development of the framework. Image from [101].

3.3.3.3 ROOT

Since its introduction, `ROOT` [96, 102] has become the analysis tool-of-choice for almost all HEP experiments. `ROOT` is a modular C++ software framework, and provides many of the services, for example histogramming, plotting, and ntuple manipulation, that form the core of any particle physics analysis. In addition to the core `ROOT` functionality, a number of additional C++ libraries are integrated into `ROOT`. Of interest to the analysis presented in this thesis are the `MINUIT` package [103] used for functional minimisation, and `RooFit` [104] a data modeling package built atop `MINUIT`, that itself serves as the basis for `RooStats` [105], a statistical analysis package.

3.3.4 Monte Carlo Simulation

Simulated physics events are a crucial component of any particle physics experiment, from the initial detector simulations used to evaluate architectural choices [73, 76, 84], to production of specific physics decay processes for use in the design and implementation of physics analyses.

To produce simulated events within ATLAS, the ATLAS simulation infrastructure [106] implements a three-step approach:

- *Event Generation*: For simulated pp interactions, the generation of events requires the selection of the partons from each interacting proton and their initial four-momentum (selected using a *Parton Distribution Function* (PDF) [107]), the interaction of the partons in the *Hard-Scatter*process,

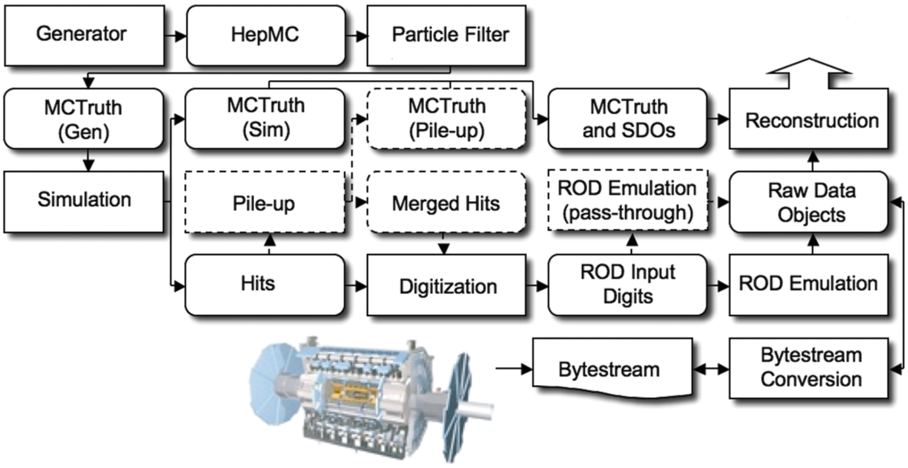

Figure 3.16: The ATLAS simulation infrastructure showing the event generation (Generator → HepMC → Particle Filter → MCTruth), simulation (Simulation → Hits → Pile-Up → Merged Hits), and digitisation (Digitisation → RDO Input/Emulation → Raw Data Objects) steps. Image from [106].

and the subsequent hadronisation and decay of the hard-scatter process and proton remnants. As these processes are inherently random, *Monte Carlo Simulation* (MC) [108, 109] methods are used;

- *Simulation*: The output from event generation is ignorant of any detector physics, and simulation of the passage of the quasi-stable particles from the event generator through the detector is required to reproduce what is to be expected by the sensor electronics under operational conditions. The output of this phase is the expected energy deposits within the detector for the hard-scatter event, and optionally, any pile-up events from the simulated bunch crossing;

- *Digitisation*: The final stage of simulation reproduces the response of the ATLAS detector's sensor electronics for the event's hits, and the subsequent flow of digital information through the trigger and RODs/ROBs. The output of this step, RDOs, as produced by the TDAQ on the physical detector, allows simulated events to be provided as-is, to the `Athena` reconstruction code.

These steps are shown in fig. 3.16.

3.3.4.1 Event Generation

A number of different event generators are used within the ATLAS experiment, with `Pythia` [110], `Herwig` [111] and `Hijing` [112] providing the bulk of simulated events within the collaboration. In addition to these general-purpose event generators, a number of special-case generators are also used to simulate specific physics phenomena, for example `Photos` [113] and `Tauola` [114], used to simulate QED radiative corrections and hadronic $\tau^{\pm}$ decays respectively. Where these decay specific tools are used, they are generally applied to the results of the hard-scatter process generated by `Pythia` or `Herwig`, to decay some subset of the hard-scatter event with additional physics modelling, this approach is adopted in most ATLAS b-physics studies with `Pythia`, in combination with `PythiaB` [115] and `EvtGen` [116] used to generate simulated events.

To model b-meson decays, b and $\overline{\mathrm{b}}$ quarks are generated from the parton interactions implemented in `Pythia`:

- Flavour excitation: $\mathrm{g}q \rightarrow \mathrm{g}q$ and $\mathrm{g}\overline{q} \rightarrow \mathrm{g}\overline{q}$;
- Flavour creation: $\mathrm{gg} \rightarrow q\overline{q}$ and $qq \rightarrow q'\overline{q}'$;
- Gluon splitting: $\mathrm{g} \rightarrow q\overline{q}$.

However, as only 1% of these events are expected to contain a b or $\overline{\mathrm{b}}$ quark after the parton level processing, it is inefficient to generate larges samples of a specific physics process using solely `Pythia`. For generation of $\mathrm{B_s} \rightarrow \mathrm{J}/\psi\phi$ events, the output of `Pythia`'s `PartonLevel` stage is passed to `PythiaB` where hard-scatter processes of interest, those that contain b and $\overline{\mathrm{b}}$ quarks passing user defined cuts, are cloned, with the cloned events returned to `Pythia` for hadronisation. The unstable particles within the event are then decayed using `Pythia`, and optionally `EvtGen`, with a final selection by `PythiaB` of the events to be recorded for further processing. This process is shown in fig. 3.17.

The *Cloning Factor* gives the average number of selected events of each suite of cloned parton processes, with numbers below unity suggesting that a larger number of cloned hadronisations may improve CPU efficiency of the event generation, while numbers larger than unity demonstrate the resultant dataset has been contaminated with large numbers of duplicated events due to the repeated hadronisation of the parton level input. The cross-section for a process generated using the repeated hadronisation method of `PythiaB`, σ_{B}, is given by

$$\sigma_{\mathrm{B}} = \sigma_{\mathrm{Hard}} \frac{N_{\mathrm{Signal}}}{N_{\mathrm{Hard}} \cdot N_{\mathrm{Loops}}} \tag{3.9}$$

where σ_{Hard} is the `Pythia` cross-section of the hard-scatter process and N_{Signal}, N_{Hard}, and N_{Loops} are the number of selected events, generated hard-scatter processes, and repeat hadronisations respectively.

For the decays of unstable particles, three approaches are used within ATLAS b-physics studies:

- `Pythia`: For $1 \to N$ decays, with $N > 2$ a matrix element may be provided to `Pythia`, and this used to decay the mother particle. While `Pythia` includes a number of matrix elements for the decays of B mesons, these are not used in the production of $\mathrm{B_s} \to \mathrm{J}/\psi\phi$ simulated events;
- `Pythia` + Rejection Sampling: For $1 \to N$ decay processes, a pure phase-space decay is implemented. For chained decays, such as the $\mathrm{B_s} \to \mathrm{J}/\psi(\mu^+\mu^-)\phi(\mathrm{K^+K^-})$ decay, this results in independent decays (Mother → Daughter and Daughter → Granddaughter), and subsequently independent distributions of the end-state decay products. Where additional shaping of the decay products (angular distribution, proper decay time, etc) is required, *Rejection Sampling* (also referred to as the accept–reject method) [108] is applied as a post-processing step;
- `EvtGen`: `EvtGen` implements decays as complex amplitudes, and therefore allows interference between competing decay processes. Furthermore, the use of spin-dependent decay amplitudes, where the decay matrices may involve non-trivial spin-configurations of both mother and daughter particles, and the ability to chain decay processes in a node-wise approach, allows full, angular dependent, simulation of decay processes such as $\mathrm{B_s} \to \mathrm{J}/\psi(\mu^+\mu^-)\phi(\mathrm{K^+K^-})$.

All MC samples used in the $\mathrm{B_s} \to \mathrm{J}/\psi\phi$ analysis are produced using `Pythia` with additional rejection sampling where required.

3.3.4.2 Detector Simulation and Digitisation

The `Athena` geometry service, `GeoModel` [106], stores the geometric models of the ATLAS detector that are used as the input, in combination with the output of the event generation, to the `Geant4` [118] based simulation stage.

`Geant4` models the passage of particles, from energies as low as 10 eV (the ionisation energy of the active gasses in the TRT and MDT drift tubes), through the material budget of the detector by MC simulations of electromagnetic and hadronic interactions between the particle and detector. Interactions between

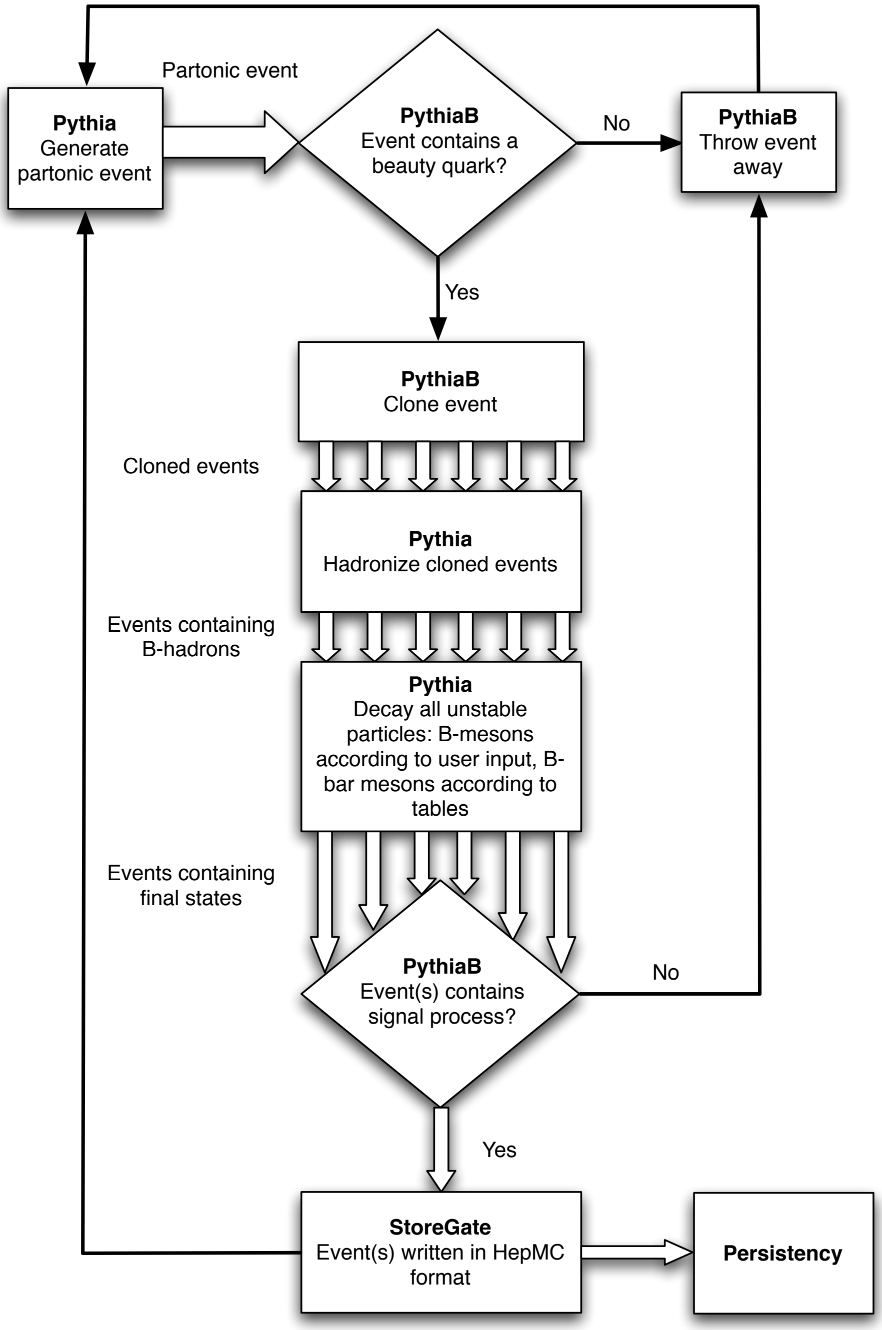

Figure 3.17: Data flow for the `PythiaB` algorithm. Image from [117].

detector material and simulated particles that result in secondary showers or energy deposits within the detector, bremsstrahlung and pair production being the most common, result in the removal of the particle from the event generator output, and appropriate daughter particles being introduced to the simulated event. The energy deposits within the active sensor components of the detector, *Hits*, may be merged with pre-generated hits from simulated pile-up events[17].

Hits produced during simulation are then processed through sub-detector specific digitisation software. This process reproduces the data expected from detector hardware, as RDOs, for a given collection of hits and can be streamed directly into the `Athena` off-line reconstruction software.

3.3.5 Reconstruction

Reconstruction in `Athena` is the collection of processes that converts the digital hits recorded by the detector (or from MC) into physics objects suitable for use in an analysis. While over 100 classes of physics and pseudo-physics objects are reconstructed by the default RDO → ESD → AOD reconstruction tool-chain, three classes of objects, tracks, PVs, and muons, are of particular interest to the analyses presented in this thesis.

3.3.5.1 Track Reconstruction

Tracks may be reconstructed using ‘inside-out’ or ‘outside-in’ approaches [119], however both share the common first stage of converting the digital information obtained from the detector into 3D *Space-Points* that provide the positions in 3-space that serve as the input to track formation. For the Si-based detectors, this is performed through clustering of charge deposits that are consistent with the passage of a charged particle. For the TRT, *Drift Circles* are generated from the TOT[18] information from activated TRT straws.

For the default Run1 ‘inside-out’ track reconstruction, a pattern-matching algorithm is applied to the space-points generated by the pixel and SCT detectors to obtain track seeds. These seeds require three hits in the first four Si layers, with a z-axis constraint used to ensure compatibility with the beam-spot. The track seeds are propagated toward the TRT using a combinatorial Kalman filter [120], with compatible Si space-points added to the seed. At the boundary between the SCT and TRT, an ambiguity resolution processing step is

---

[17] Large runs of various pile-up events are simulated, with only the hit information saved to reduce the storage requirements.

[18] *Time Over Threshold*, see [119].

performed to down-weight poor quality seed before the seed propagation continues through the TRT.

This method is complemented by an ‘outside-in’ track reconstruction approach where TRT track segments are built from the TRT drift circles, using the legacy `xKalman` `Athena` package [117, 121], and propagated toward the centre of the detector. The advantage of this approach is that tracks that could not be constructed using the ‘inside-out’ approach, for example from long-lived particles that decay beyond the second pixel layer, or particles where the reconstruction efficiency is low, may be recovered[19].

MC studies show an track reconstruction efficiency of >82 % for tracks with $p_{\mathrm{T}} > 1\,\mathrm{GeV}$ [122].

3.3.5.2 Primary Vertex Reconstruction

The default PV reconstruction adopted in ATLAS during Run1 is based on a ‘finding-through-fitting’ approach implemented in the `InDetAdaptiveMultiPriVxFinder` package [123, 124], and is implemented in a five step process:

- From all reconstructed tracks, a set of tracks that may be compatible with a PV candidate are selected. This step is performed only once;
- A seed position for the vertex is selected. The lateral position is based on the centre of the beam-spot [125], while the z-position of the seed is calculated as the mode of the z-coordinates of the tracks at their respective apogees;
- The tracks and the seed are used to estimate the best vertex position with a fit. This is an iterative processes with less compatible tracks down-weighted at the start of each iteration; various cut-off conditions are used to terminate this process;
- After the vertex position is determined, tracks incompatible with the newly constructed PV are retained for construction of a new seed;
- If enough tracks remain to form a new PV, the procedure is repeated.

All reconstructed PV with at least two associated tracks are retained as valid PV candidates.

---

[19] low-p_{T} electrons.

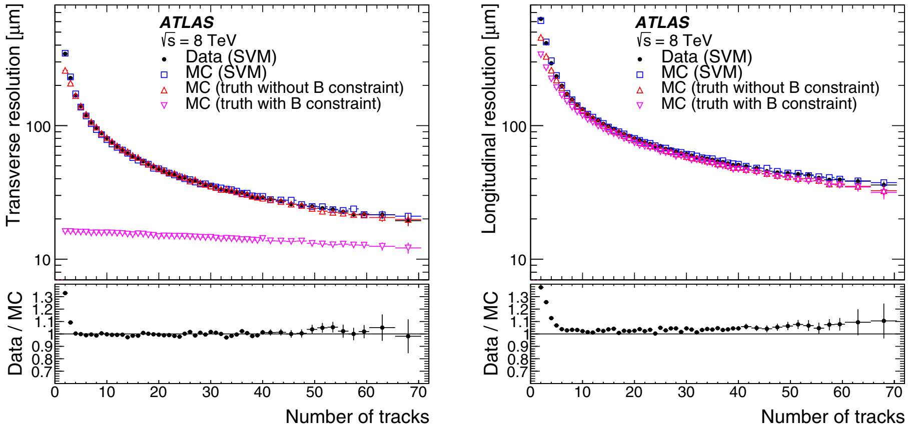

(a) Transverse Resolution

(b) Longitudinal resolution

Figure 3.18: PV position resolution for the transverse plane (left) and longitudinal axis (right). Shown are the intrinsic PV resolutions for reconstructed PVs obtained using the SVM for data (black) and reconstructed MC (blue), also shown is the intrinsic resolution for MC truth (no reconstruction) with (red) and without (pink) a beam-spot constraint. Figures from [124].

Performance of the PV reconstruction may be measured by two metrics, total reconstruction efficiency and positional resolution. PV reconstruction efficiency for minimum-bias events is found to be >92.6 % [124] in data and MC studies[20] and is compatible with data-driven estimations performed during Run1 data taking.

Position resolution of the reconstructed PVs is validated using the *Split-Vertex Method* (SVM) [124]. Distributions of transverse and longitudinal resolution, as a functions of the number of tracks used to form the vertex, are shown in fig. 3.18.

3.3.5.3 Muon Reconstruction

Muons are reconstructed using two families of algorithms in ATLAS, `STACO` and `Muid` [73], with each family performing three types of muon reconstruction:

- `StandAlone`: Reconstructed using information from the MS alone;
- `Combined`: Reconstructed from a combination of ID and MS information;

---

[20] A contribution of the author as part of his service work for ATLAS.

- `Tagged`: The muon track is reconstructed from ID information alone, and marked as `Tagged` due to its compatibility with activity in the MS.

Only `STACO-Combined` and `STACO-Tagged` are used in the $\mathrm{B_s} \to \mathrm{J}/\psi\phi$ analysis. Their reconstruction starts with the construction of a `StandAlone` muon, using the `Muonboy` package [126] with three *Segments*, linearised track components, produced during this process. This `STACO-StandAlone` track is back-projected into the ID, and matched with any compatible ID track. A statistical combination of the track vectors and covariance matrices from the ID track and `Muonboy` track at vertex is performed, and if this combination passes MCP quality cuts, it is retained as a `STACO-Combined` muon candidate. Where no `Combined` candidate is produced, and the ID track is found to be statistically compatible with the innermost of the segments, a `STACO-Tagged` candidate is formed.

Chapter 4

Measuring $\mathcal{CP}$-Violation in the $\mathrm{B_s} \to \mathrm{J}/\psi\phi$ Decay

The analysis presented here provides a measurement of the $\mathrm{B_s} \to \mathrm{J}/\psi\phi$ decay parameters, extracted using 14.3 fb^{-1} of ATLAS data collected during 2012 at a centre of mass energy of 8 TeV. In addition to the 8 TeV results, two combinations with the ATLAS 7 TeV result [127] are presented.

This analysis was published as [128].

4.1 Theoretical Overview

The phenomenology of decays with non-trivial spin configurations, and the angular distributions of their decay products, frequently play a central role in the analysis of $\mathcal{CP}$-violating decays as the time-dependent angular distributions often allow the statistical separation of the $\mathcal{CP}$-eigenstates and determination of any $\mathcal{CP}$-violating phase.

For the $\mathrm{B_s} \to \mathrm{J}/\psi\phi$ decay, eq. (2.91c) may be simplified by noting that $\Delta m_\mathrm{s} \gg \Gamma_\mathrm{s}$, and therefore $|\Gamma_{12}| \ll |M_{12}|$ [129]. Using this simplification to expand q/p in terms of Γ_{12}/M_{12} leads to

$$\frac{M_{12}}{\Gamma_{12}} = \left|\frac{M_{12}}{\Gamma_{12}}\right| e^{i\phi_M}. \tag{4.1}$$

and under the assumptions that[1]:

- The mixing diagrams (fig. 2.2) are dominated by t-quark exchange;

---

[1] Global fits to electroweak datasets show that deviations from these assumptions are to the order of 1 %

- Only a tree-level decay diagram contributes to the $\mathcal{CP}$-violation.

the phase $e^{-i\phi_M}$ is given by the interference between direct decays (at tree-level), and decays after a net oscillation. Assuming only SM contributions to these processes

$$e^{-i\phi_M} = \frac{V_{\mathrm{tb}}^* V_{\mathrm{ts}}}{V_{\mathrm{tb}} V_{\mathrm{ts}}^*} \tag{4.2}$$

and therefore

$$\lambda_f = -e^{i\phi_{\mathrm{s}}} \tag{4.3}$$

where ϕ_{s}, the $\mathcal{CP}$-violating phase for the $\mathrm{B_s} \to \mathrm{J}/\psi\phi$ decay, is

$$\phi_{\mathrm{s}} = 2 \cdot \arg \frac{V_{\mathrm{tb}}^* V_{\mathrm{ts}}}{V_{\mathrm{tb}} V_{\mathrm{ts}}^*}. \tag{4.4}$$

The remainder of this section introduces the formalism used to model the $\mathrm{B_s} \to \mathrm{J}/\psi\phi$ decay (section 4.1.1) and one irreducible background component of the $\mathrm{J}/\psi\mathrm{K}^+\mathrm{K}^-$ end-state (section 4.1.2).

4.1.1 Helicity and Transversity Formalisms

The *Helicity* of a particle is the projection of its spin onto its momentum, that is

$$\widehat{\lambda} = \widehat{s} \cdot \widehat{p}. \tag{4.5}$$

The helicity of a particle is a useful quantity when analysing decays of particles into non-trivial spin states as the expectation value of the helicity operator is invariant under rotations and boosts along $\vec{\mathbf{p}}$.

4.1.1.1 The $\mathrm{B_s} \to \mathrm{J}/\psi\phi$ Decay

The $\mathrm{B_s} \to \mathrm{J}/\psi\phi$ decay, whose Feynman diagrams are shown in fig. 4.1, is the decay of a pseudo-scalar particle ($J^{\mathrm{P}}(\mathrm{B_s}) = 0^-$) into two vector particles ($J^{\mathrm{PC}}(\mathrm{J}/\psi) = 1^{--}$, $J^{\mathrm{PC}}(\phi) = 1^{--}$) thus the possible orbital angular momenta, L, of the decay products is constrained to $L = 0, 1, 2$. The $\mathcal{CP}$-eigenvalues of the three possible decay states is given by

$$\mathcal{CP}(\mathrm{J}/\psi) \cdot \mathcal{CP}(\phi) \cdot -1^L = 1, -1, 1 \tag{4.6}$$

with the final state an admixture of two $\mathcal{CP}$-even states ($L = 0, 2$) and a single $\mathcal{CP}$-odd state ($L = 1$). These states may be disentangled statistically through the use of a time dependent angular analysis.

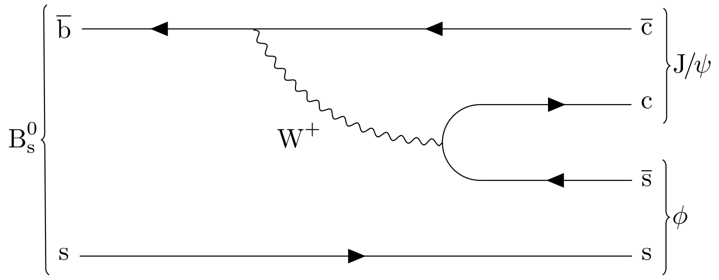

(a) Tree-level decay

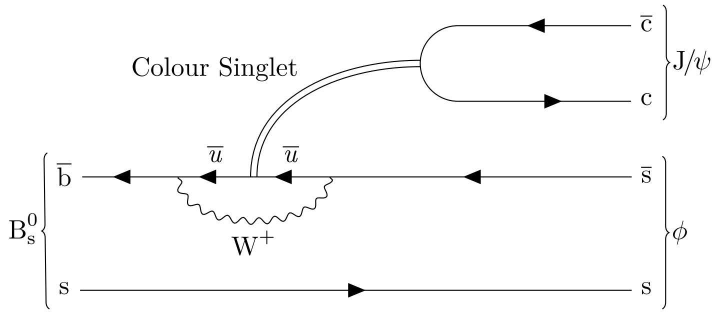

(b) Penguin decay

Figure 4.1: The $\mathrm{B_s} \to \mathrm{J}/\psi\phi$ decay with $\overline{u}$ representing an up-type (u, c, or t) anti-quark.

4.1.1.2 The Helicity Basis

For both daughter particles, the possible values of helicity, λ, are -1, 0, and 1. As the helicity of the daughter particles is constrained by the mother through

$$\left|\lambda_{\mathrm{J}/\psi} - \lambda_\phi\right| = J(\mathrm{B_s}) \tag{4.7}$$

the possible helicity configurations of the daughter particles are limited to

$$(\lambda_{\mathrm{J}/\psi}, \lambda_\phi) = (1,1), (0,0), (-1,-1). \tag{4.8}$$

A *Helicity Amplitude* is associated with each valid helicity eigenstate (H_1, H_0, and H_{-1}) for the $\mathrm{B_s} \to \mathrm{J}/\psi\phi$ decay, and the decay amplitude is given by the sum of the helicity amplitudes

$$A(\mathrm{B_s} \to \mathrm{J}/\psi\phi) = \frac{1}{\sqrt{4\pi}}(H_1 + H_0 + H_{-1}). \tag{4.9}$$

4.1.1.3 $\mathbf{B_s \to J/\psi(\mu^+\mu^-)\phi(K^+K^-)}$ Angular Distributions

The J/ψ and ϕ particles are ‘back-to-back’ in the rest frame of the decaying $\mathrm{B_s}$ particle, and no useful information about the helicity amplitudes can be recovered.

The subsequent decays of the J/ψ and ϕ, however, allow extraction of the helicity amplitudes through a second application of the helicity formalism. The $\phi \to \mathrm{K}^+\mathrm{K}^-$ decay has only a single helicity state $(\lambda_{\mathrm{K}^+}, \lambda_{\mathrm{K}^-}) = (0, 0)$, as $J^{\mathrm{P}}(\mathrm{K}^{\pm}) = 0^-$ while the $\mathrm{J}/\psi \to \mu^+\mu^-$ decay has two[2], $(\lambda_{\mu^+}, \lambda_{\mu^-}) = (-1/2, 1/2), (1/2, -1/2)$.

The first step in developing the helicity formalism is to define the coordinate system:

- The overall rest frame is taken to be the rest frame of the decaying $\mathrm{B_s}$;
- The polar angle for the J/ψ decay, θ_ℓ, is taken as the angle between the μ^+, and the z-axis defined as $p(\mathrm{J}/\psi)$ in the $\mathrm{B_s}$ rest frame;
- The polar angle for the ϕ decay, θ_{K}, is taken as the angle between the K^+, and the z-axis defined as $p(\phi)$ in the $\mathrm{B_s}$ rest frame;
- The angle ϕ_{H} is the angle between the planes formed by the momenta of the final state particles.

This system is shown in fig. 4.3.

Matrix elements may then be formed for all combinations of $(\lambda_{\mathrm{J}/\psi}, \lambda_\phi)$ and their subsequent decays into all possible (valid) helicity states of their decay products, with these matrix elements parameterised by the helicity angles of the decay[130].

The resultant $\mathrm{B_s} \to \mathrm{J}/\psi\phi$ angular distribution, expressed in the helicity basis, may be obtained from the incoherent sum of the mother → daughter → granddaughter helicity states of the endstate particles (see [130]). This allows the differential decay width to be expressed as

$$\frac{\mathrm{d}^4\Gamma}{\mathrm{d}t\,\mathrm{d}\Omega} = \sum\nolimits_k A_k \cdot K_k \cdot g_k \tag{4.10}$$

where the sum over k is taken over the helicity amplitude combinations (for the P-wave states this gives six terms in the sum, three P-wave amplitudes ($k = 1 \to 3$) and three interference terms ($k = 4 \to 6$)). A_k is the squared amplitude of the term while K_k is the kinematic terms for the component and

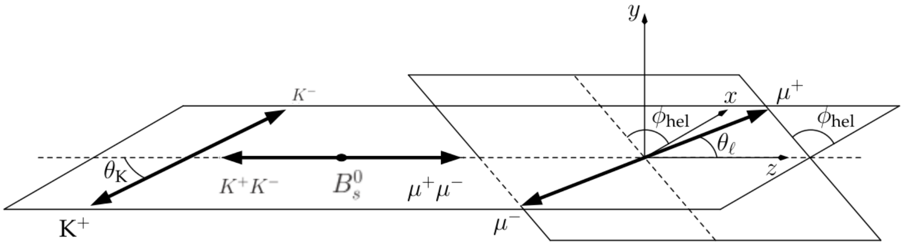

Figure 4.2: The helicity angles as defined for the $\mathrm{B_s} \to \mathrm{J}/\psi\phi$. Image from [129].

contains the $\mathcal{CP}$-violation terms relevant to the decay. By convention[128] the product $A_k \cdot K_k$ is labelled $\mathcal{O}_k$. g_k provides the end-state angular distribution.

4.1.1.4 The Transversity Basis

The helicity amplitudes are not eigenstates of $\mathcal{CP}$, and conversion to the transversity basis, where the transversity eigenstates are aligned with the $\mathcal{CP}$-eigenstates, allows cleaner extraction of the $\mathcal{CP}$-violation phase of the decay. Conversion of the basis states may be performed through the methods outlined in [130].

Within this basis it is conventional to express the angular distribution of the decay products terms of the transversity decay angles $\phi_{\rm T}$, $\theta_{\rm T}$, and $\psi_{\rm T}$. These angles are defined in the rest frames of the final state particles with the x-axis determined by the direction of the ϕ meson in the J/ψ rest frame and the x–y plane defined by the $\mathrm{K^+K^-}$ system with $p_y(\mathrm{K}^+) > 0$. Within this coordinate system, $\theta_{\rm T}$ and $\phi_{\rm T}$ define the polar and azimuthal angles of the μ^+ in the rest frame of the J/ψ, while $\phi_{\rm T}$ is the angle between $p(\mathrm{K}^+)$ and the x-axis.

A_k, K_k, and g_k for the P-wave contribution ($\phi \to \mathrm{K^+K^-}$) to the $\mathrm{J}/\psi\mathrm{K^+K^-}$ end-state, in the transversity basis, are given in tables 4.1 and 4.2.

Of importance to the analysis is a number of accidental symmetries in the resultant angular distributions

$$\phi_{\rm s}, \Delta\Gamma_{\rm s}, \delta_{\|}, \delta_{\perp}, \delta_{\rm S} \to \pi - \phi_{\rm s}, -\Delta\Gamma_{\rm s}, -\delta_{\|}, \pi - \delta_{\perp}, -\delta_{\rm S} \tag{4.11a}$$

$$\phi_{\rm s}, \Delta\Gamma_{\rm s}, \delta_{\|}, \delta_{\perp}, \delta_{\rm S} \to -\phi_{\rm s}, \Delta\Gamma_{\rm s}, -\delta_{\|}, \pi - \delta_{\perp}, -\delta_{\rm S} \tag{4.11b}$$

and lead to a four-fold ambiguity. These ambiguities are resolved through the use of a constraint on $\Delta\Gamma_{\rm s}$, and knowledge of the initial flavour of the $\mathrm{B_s}$

---

[2] $J(\mu^{\pm}) = 1/2$. The vectoral nature of the decay coupling restricts the available helicity states.

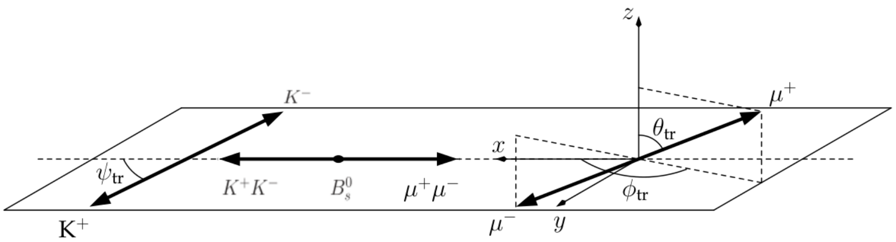

Figure 4.3: The transversity angles as defined for the $\mathrm{B_s} \to \mathrm{J}/\psi\phi$. These images use a subscript *tr* to denote the transversity basis. Image from [129].

	$\mathcal{O}_k$	
k	A_k	K_k
1	$\frac{1}{2}\lvert A_0\rvert^2$	$\big(1+\cos(\phi_\mathrm{s})\big)\cdot e^{-\Gamma_\mathrm{s}^\mathrm{L} t} + \big(1-\cos(\phi_\mathrm{s})\big)\cdot e^{-\Gamma_\mathrm{s}^\mathrm{H} t}$
2	$\frac{1}{2}\lvert A_\parallel\rvert^2$	$\big(1+\cos(\phi_\mathrm{s})\big)\cdot e^{-\Gamma_\mathrm{s}^\mathrm{L} t} + \big(1-\cos(\phi_\mathrm{s})\big)\cdot e^{-\Gamma_\mathrm{s}^\mathrm{H} t}$
3	$\frac{1}{2}\lvert A_\perp\rvert^2$	$\big(1-\cos(\phi_\mathrm{s})\big)\cdot e^{-\Gamma_\mathrm{s}^\mathrm{L} t} + \big(1+\cos(\phi_\mathrm{s})\big)\cdot e^{-\Gamma_\mathrm{s}^\mathrm{H} t}$
4	$\frac{1}{2}\lvert A_0\rvert\lvert A_\parallel\rvert\cdot\cos(\delta_\parallel)$	$\big(1+\cos(\phi_\mathrm{s})\big)\cdot e^{-\Gamma_\mathrm{s}^\mathrm{L} t} + \big(1-\cos(\phi_\mathrm{s})\big)\cdot e^{-\Gamma_\mathrm{s}^\mathrm{H} t}$
5	$\frac{1}{2}\lvert A_0\rvert\lvert A_\perp\rvert\cdot\cos(\delta_\perp)$	$\sin(\phi_\mathrm{s})\cdot(e^{-\Gamma_\mathrm{s}^\mathrm{L} t} - e^{-\Gamma_\mathrm{s}^\mathrm{H} t})$
6	$\frac{1}{2}\lvert A_\parallel\rvert\lvert A_\perp\rvert\cdot\cos(\delta_\perp-\delta_\parallel)$	$\sin(\phi_\mathrm{s})\cdot(e^{-\Gamma_\mathrm{s}^\mathrm{L} t} - e^{-\Gamma_\mathrm{s}^\mathrm{H} t})$

Table 4.1: $\mathcal{O}_k$ for P-wave $\mathrm{B_s} \to \mathrm{J}/\psi(\mu^+\mu^-)\phi(\mathrm{K^+K^-})$ decays.

particle.

4.1.2 S-Wave Contributions to the $\mathrm{J}/\psi\mathrm{K^+K^-}$ End-State

In addition to the $\mathrm{B_s} \to \mathrm{J}/\psi\phi$ P-wave contribution to the $\mathrm{J}/\psi\mathrm{K^+K^-}$ end-state, irreducible backgrounds from $\mathrm{B_s}$ decays are possible from the S-wave decays $\mathrm{B_s} \to \mathrm{J}/\psi\mathrm{K^+K^-}$ (a non-resonant, $L = 0$, $\mathrm{K^+K^-}$ configuration) and $\mathrm{B_s} \to \mathrm{J}/\psi\mathrm{f}_0(980)$[3] with $\mathrm{f}_0(980) \to \mathrm{K^+K^-}$.

In the $m(\mathrm{K^+K^-})$ mass region around m_ϕ the S- and P-wave contributions to the $\mathrm{J}/\psi\mathrm{K^+K^-}$ end-state are expected to dominate [131, 132] (see [133] for an analysis of the related $\mathrm{B^\pm} \to \mathrm{J}/\psi\mathrm{K^\pm}$ channel) and contributions from higher-order channels are negelected in the analysis.

---

[3] $J^{\mathrm{PC}}(\mathrm{f}_0(980)) = 0^{++}$.

k	g_k
1	$2 \cdot \cos^2(\psi_\mathrm{T}) \left(1 - \sin^2(\theta_\mathrm{T}) \cdot \cos^2(\phi_\mathrm{T})\right)$
2	$\sin^2(\psi_\mathrm{T}) \left(1 - \sin^2(\theta_\mathrm{T}) \cdot \sin^2(\phi_\mathrm{T})\right)$
3	$\sin^2(\psi_\mathrm{T}) \cdot \sin^2(\theta_\mathrm{T})$
4	$\frac{1}{\sqrt{2}} \sin(2 \cdot \psi_\mathrm{T}) \cdot \sin^2(\theta_\mathrm{T}) \cdot \sin(2 \cdot \phi_\mathrm{T})$
5	$\frac{1}{\sqrt{2}} \sin(2 \cdot \psi_\mathrm{T}) \cdot \sin(2 \cdot \theta_\mathrm{T}) \cdot \cos(\phi_\mathrm{T})$
6	$-\sin^2(\psi_\mathrm{T}) \cdot \sin(2 \cdot \theta_\mathrm{T}) \cdot \sin(\phi_\mathrm{T})$

Table 4.2: g_k for P-wave $\mathrm{B_s} \to \mathrm{J}/\psi(\mu^+\mu^-)\phi(\mathrm{K^+K^-})$ decays.

	$\mathcal{O}_k$	
k	A_k	K_k
7	$\frac{1}{2}\lvert A_\mathrm{S}\rvert^2$	$\left(1 - \cos(\phi_\mathrm{s})\right) \cdot e^{-\Gamma_\mathrm{s}^\mathrm{L} t} + \left(1 + \cos(\phi_\mathrm{s})\right) \cdot e^{-\Gamma_\mathrm{s}^\mathrm{H} t}$
8	$\frac{1}{2}\lvert A_\mathrm{S}\rvert\lvert A_0\rvert \cdot \sin(\delta_\mathrm{S})$	$\sin(\phi_\mathrm{s}) \cdot (e^{-\Gamma_\mathrm{s}^\mathrm{H} t} - e^{-\Gamma_\mathrm{s}^\mathrm{L} t})$
9	$\frac{1}{2}\lvert A_\mathrm{S}\rvert\lvert A_\parallel\rvert \cdot \sin(\delta_\parallel - \delta_\mathrm{S})$	$\sin(\phi_\mathrm{s}) \cdot (e^{-\Gamma_\mathrm{s}^\mathrm{L} t} - e^{-\Gamma_\mathrm{s}^\mathrm{H} t})$
10	$\frac{1}{2}\lvert A_\mathrm{S}\rvert\lvert A_\perp\rvert \cdot \sin(\delta_\perp - \delta_\mathrm{S})$	$\left(1 - \cos(\phi_\mathrm{s})\right) \cdot e^{-\Gamma_\mathrm{s}^\mathrm{L} t} + \left(1 + \cos(\phi_\mathrm{s})\right) \cdot e^{-\Gamma_\mathrm{s}^\mathrm{H} t}$

Table 4.3: $\mathcal{O}_k$ for S-wave $\mathrm{B_s} \to \mathrm{J}/\psi(\mu^+\mu^-)\phi(\mathrm{K^+K^-})$ decays.

k	g_k
7	$\frac{2}{3}\left(1 - \sin^2(\theta_\mathrm{T}) \cdot \cos^2(\phi_\mathrm{T})\right)$
8	$\frac{4}{3}\sqrt{3} \cdot \cos(\psi_\mathrm{T}) \left(1 - \sin^2(\theta_\mathrm{T}) \cdot \cos^2(\phi_\mathrm{T})\right)$
9	$\frac{1}{3}\sqrt{6} \cdot \sin(\psi_\mathrm{T}) \cdot \sin^2(\theta_\mathrm{T}) \cdot \sin(2 \cdot \phi_\mathrm{T})$
10	$\frac{1}{3}\sqrt{6} \cdot \sin(\psi_\mathrm{T}) \cdot \sin(2 \cdot \theta_\mathrm{T}) \cdot \cos(\phi_\mathrm{T})$

Table 4.4: g_k for S-wave $\mathrm{B_s} \to \mathrm{J}/\psi(\mu^+\mu^-)\phi(\mathrm{K^+K^-})$ decays.

The introduction of S-wave contributions an additional four terms to eq. (4.10) to accommodate the S-wave amplitude ($k = 7$) and interference between S- and P- wave decays ($k = 8 \to 10$).

Transversity angle distributions for the S-wave contribution, and the interference terms between S- and P-wave decays are obtainable via the transversity formalism and lead to the $\mathcal{O}_k$ and g_k terms shown in tables 4.3 and 4.4.

4.2 $\mathrm{B_s} \to \mathrm{J}/\psi\phi$ Candidate Reconstruction

Generation of the dataset for use in the $\mathrm{B_s} \to \mathrm{J}/\psi\phi$ default fit occurs in two stages. Events are collected from the detector using the online trigger (section 3.2.6), where events are retained on the basis that they may contain a $\mathrm{J}/\psi \to \mu^+\mu^-$ candidate. From those events, $\mathrm{B_s} \to \mathrm{J}/\psi(\mu^+\mu^-)\phi(\mathrm{K}^+\mathrm{K}^-)$ candidates are reconstructed for use in the analysis.

The b-physics triggers used in ATLAS are described in section 4.2.1 while the event selection and candidate reconstruction procedure used is described in section 4.2.2.

4.2.1 b-Physics Triggers

Technical limitations of the ATLAS Run1 trigger limit the recorded event storage rate to ∼1 kHz, with typical storage rates of 400 Hz to 600 Hz. Of this, only ≈15 % is dedicated to b-physics triggers. Due to this bandwidth limitation, and the desire to retain events of relatively low-p_T, ATLAS b-physics analyses and their triggers focus on decays with muons in the final state as the background rate for muons is low (compared to fully hadronic final states) and detection efficiency is high.

ATLAS trigger rates for ATLAS 2012 data taking are shown in fig. 4.4.

4.2.1.1 Muon Triggers

All muon triggers are seeded by LVL1 RoIs generated from activity in the MS's RPCs or TGCs. Collections of 'hits' in these detectors[4], whose spatial and temporal locales are consistent with a bunch crossing in the interaction region, are considered by the LVL1 trigger against the LVL1 muon p_T thresholds uploaded at the start of the LHC run. The p_T of the muon candidate is estimated from the degree of deviation between the recorded hit pattern and the expected hit pattern of a muon of infinite momentum, and muon candidates matching the p_T and quality criteria [136] for the LVL1 triggers are used to generate a RoI for forwarding to the HLT.

The LVL1 RoIs are processed at LVL2 in two distinct steps: the formation of a *Stand-Alone* (SA) muon candidate and the combination of the SA candidate with an ID track. MDT and CSC information from within the RoI is used to to form a SA muon. This step is performed through a number of dedicated

---

[4] Along well defined 'roads' [135].

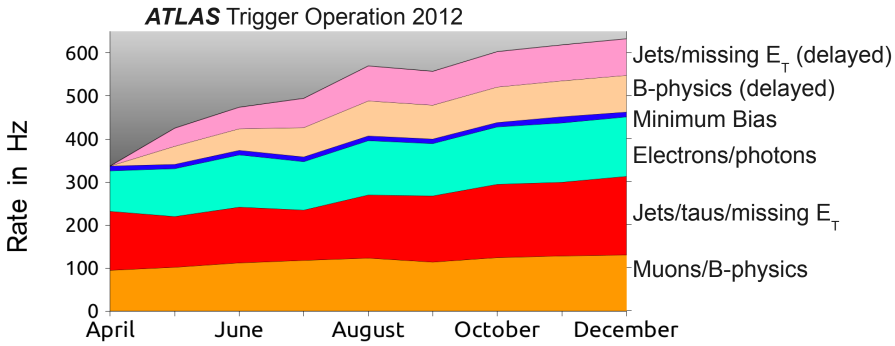

(a) By month

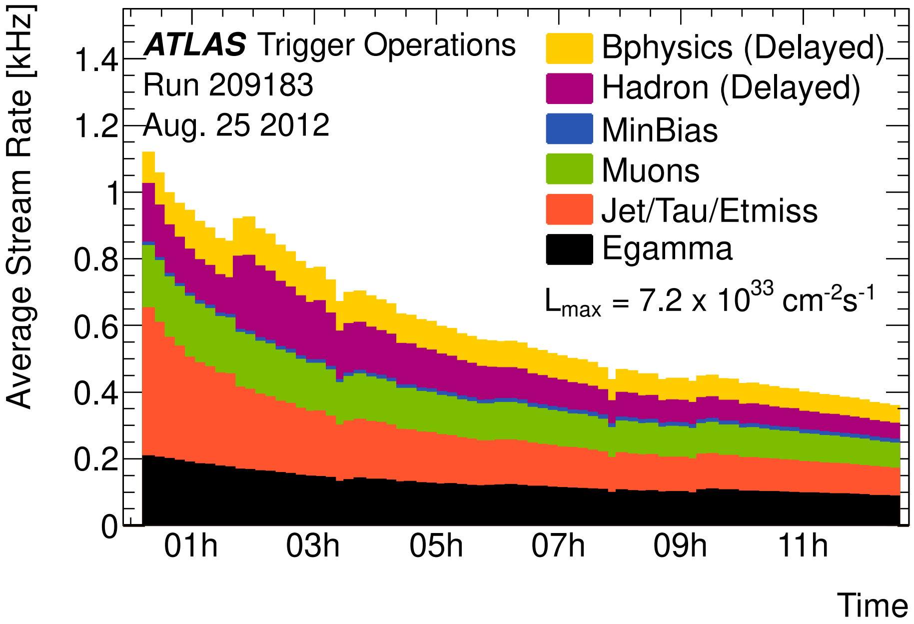

(b) Single run

Figure 4.4: ATLAS trigger rates. Shown are the average rates as a function of time by months (top), and for a typical single LHC run (bottom). Figures from [134].

algorithms, each optimised for a different region of the detector[136, 137]. The SA candidate is then combined with a track from the ID (via μ`Fast` and μ`Comb`, [138]), to form a *Combined* (CB) LVL2 muon[5]. The p_{T} of this CB muon is taken as the weighted-average of the ID and MS track p_{T}s and, assuming a degree of compatibility between the tracks, the CB muon is forwarded to the EF for further consideration.

With full ID and MS information available, the EF employs an 'outside-in' strategy to rebuild MS segments and tracks, before combining them with an ID track. Should this `TrigMuonEF` algorithm fail [138], `TrigMuGirl` attempts to extrapolate ID tracks ('inside-out') from the LVL2 RoIs onto hits in the MS to form a muon candidate appropriate for the trigger conditions.

4.2.1.2 Di-Muon Triggers

b-physics trigger rates may be further improved by applying additional requirements on the muons, thus di-muon triggers, that require requiring two muons, of opposite charge, originating from a common vertex, with an invariant mass constraint, and which have become the dominant triggers in b-physics analyses in ATLAS.

Di-muon triggers fall into two classes:

- Topological di-muon triggers are seeded from two LVL1 muon candidates. Each LVL1 muon seed is required to fire its LVL2 trigger, and at this point additional LVL2 triggers are run (feature extraction and hypothesis testing, roughly equivalent to vertexing and mass determination). This two-step process is then repeated at the EF to complete the trigger chain;
- TrigDiMuon triggers are seeded at LVL2 from a single LVL1 muon, but a larger RoI ($\Delta\eta \times \Delta\phi = 0.75 \times 0.75$, tuned to give 92% acceptance for a second muon from a $J/\psi \to \mu^+\mu^-$ decay) are used to search for a second muon candidate. In these trigger chains, there is no requirement for the original LVL1 muon to pass the LVL2 triggers, merely that a three step seeding → feature extraction → hypothesis testing succeed in the LVL2 and EF triggers.

These seeding strategies are shown in fig. 4.5. The mass windows applied in the Run1 b-physics triggers are:

---

[5] This step is not always performed, a number of LVL2 muon triggers are fired by successful construction of the SA muon.

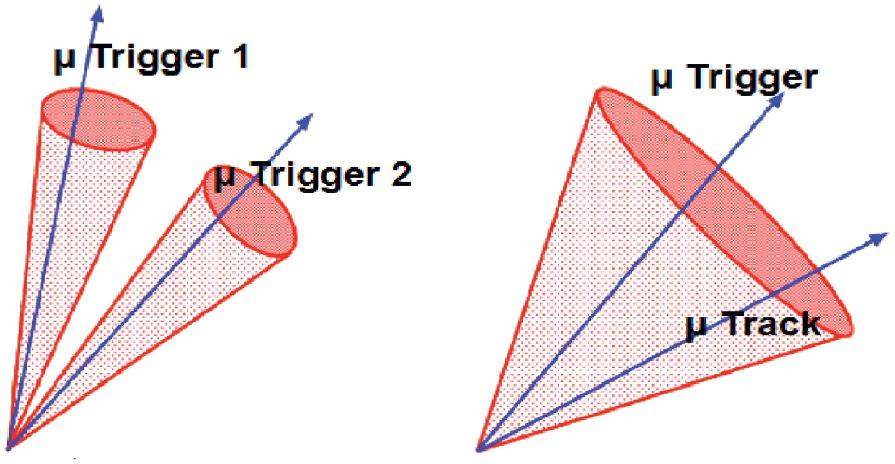

(a) Topological di-muon trigger (b) TrigDiMuon trigger

Figure 4.5: Di-muon triggers in ATLAS, showing the two LVL1 muon RoIs required for a topological trigger (left) while the the TrigDiMuon trigger (right) detects the second muon from inside the enlarged RoI by extrapolating ID tracks to the MS. Images from [139].

- 2.5 GeV to 4.3 GeV for $\mathrm{J}/\psi \to \mu^+\mu^-$ decays;
- 8.0 GeV to 12.0 GeV for $\Upsilon \to \mu^+\mu^-$;
- 4.0 GeV to 8.5 GeV for $\mathrm{B_d} \to \mu^+\mu^-$ and $\mathrm{B_s} \to \mu^+\mu^-$ decays of interest in SUSY searches;
- 1.5 GeV to 14.0 GeV for rare semi-leptonic $B \to \mu^+\mu^-\mathrm{X}$ decays.

with the topological $\mathrm{J}/\psi \to \mu^+\mu^-$ triggers of most use to the $\mathrm{B_s} \to \mathrm{J}/\psi\phi$ default fit.

4.2.1.3 Trigger Performance

Two metrics may be used to assess trigger performance in the $\mathrm{B_s} \to \mathrm{J}/\psi\phi$ analysis:

- Trigger Efficiency: The efficiency of the b-physics triggers is assessed by the ATLAS trigger, muon trigger, and b-physics trigger combined performance groups [140, 141, 142] using *Tag-and-Probe*studies with a number of single and di-muon triggers used to provide tag events. Results from these studies are shown in fig. 4.6;

- Selection Bias: Events used in the $\mathrm{B_s} \to \mathrm{J}/\psi\phi$ default fit may bias the measurement of interesting physics variables if the transversity angles or proper decay time of the reconstructed $\mathrm{B_s} \to \mathrm{J}/\psi(\mu^+\mu^-)\phi(\mathrm{K^+K^-})$ candidates suffer from selection bias in the event selection due to the triggers.

Previous studies, undertaken for [127, 128, 143], have shown negligible selection bias in the reconstruction of the transversity angles due to the triggers (and offline track reconstruction). A significant proper decay time selection bias is observed however, due to an impact parameter dependent efficiency in the online track reconstruction (see [144]). This bias is addressed through two methods. The `L2StarA`-based triggers, deployed at the start of 8 TeV data taking, were found to introduce a highly non-trivial proper decay time selection bias[6] [144] and as such are excluded from the $\mathrm{B_s} \to \mathrm{J}/\psi\phi$ default fit. The `L2StarB` triggers, introduced at LHC run 206 955, are used for all data taking for the $\mathrm{B_s} \to \mathrm{J}/\psi\phi$ default fit, and contain a small, correctable, proper decay time dependent bias.

A 40 000 000 event *Monte Carlo* (MC) sample (see section 4.4.3.1) is used to determine the `L2StarB` trigger efficiency, and the resultant efficiency distribution, as a function of proper decay time, is fitted with the re-weighting function

$$w = p_0 \cdot (1 - p_1 \cdot (\mathrm{Erf}((t - p_3)/p_2) + 1)) \tag{4.12}$$

where p_n are optimised on a per-trigger basis using a binned χ^2 fit. The results of these fits, for the dominant analysis triggers, are shown in fig. 4.7, while the total number of events selected into the $\mathrm{B_s} \to \mathrm{J}/\psi\phi$ default fit for each trigger is shown in table 4.5.

The effect of this re-weighting function on the $\mathrm{B_s} \to \mathrm{J}/\psi\phi$ default fit is examined in section 4.5.1.1.

4.2.2 Event Reconstruction

To maintain compatibility with the previous 7 TeV $\mathrm{B_s} \to \mathrm{J}/\psi\phi$ analyses [127, 143], the event reconstruction cuts are largely unchanged from the previous analyses[7].

---

[6] The selection bias was due to a number of software bugs related to ability to select the correct ID RoIs based on the MS trigger chamber information, leading to an inability to construct any valid muon candidates.

[7] Cuts imposed by ATLAS performance groups have been updated where required.

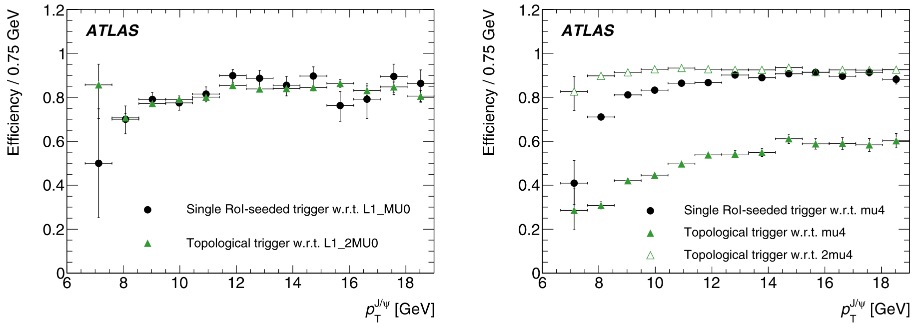

(a) $p_T > 0$ GeV muon tags (b) $p_T > 4$ GeV muon tags

Figure 4.6: b-Physics trigger efficiency from tag-and-probe studies using $p_T > 0$ GeV muons (left) and $p_T > 4$ GeV muons (right) as a function of the highest p_T muon used to reconstruct the off-line J/ψ candidate. Figures from [135].

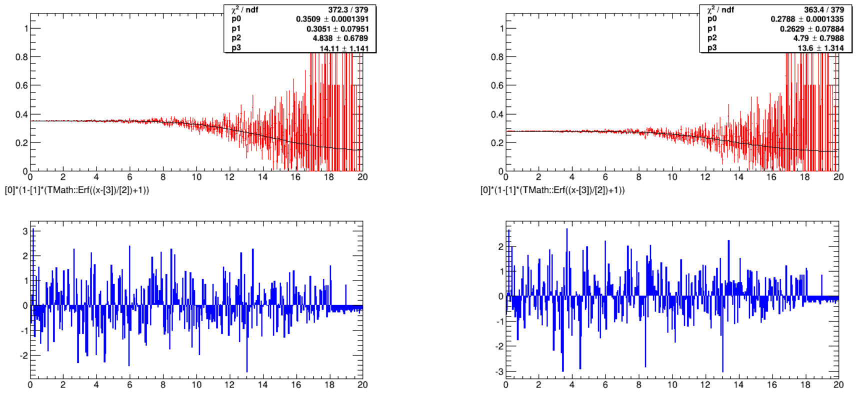

(a) `EF_2mu4T_Jpsimumu_L2StarB` (b) `EF_mu4Tmu6_Jpsimumu_L2StarB`

Figure 4.7: `L2StarB` trigger efficiency as a function of proper decay time for `EF_2mu4T_Jpsimumu_L2StarB` (left) and `EF_mu4Tmu6_Jpsimumu_L2StarB` (right) triggered events. Shown is the proper decay time dependent efficiency (red) and the fitted re-weighting function (black), with the pull distributions from the resultant fits are shown below (blue). Figures adapted from [145].

Trigger	Event Count
`EF_2mu4T_Jpsimumu_L2StarB`	209 336
`EF_2mu4T_Jpsimumu_Barrel_L2StarB`	149 306
`EF_2mu4T_Jpsimumu_BarrelOnly_L2StarB`	143 470
`EF_mu4Tmu6_Jpsimumu_L2StarB`	190 473
`EF_mu4Tmu6_Jpsimumu_Barrel_L2StarB`	114 880
`EF_2mu6_Jpsimumu_L2StarB`	81 864
Total	375 987

Table 4.5: Trigger event counts for events selected into the $\mathrm{B_s} \to \mathrm{J}/\psi\phi$ default fit. The event counts shown are before overlap removal.

The effects of the choices made in the event reconstruction on the extraction of physics parameters in the $\mathrm{B_s} \to \mathrm{J}/\psi\phi$ default fit are considered in section 4.5.1.1.

4.2.2.1 Event Selection

Events from the 8 TeV LHC pp run are retained for further analysis if:

- the event is considered ‘Good for Physics’;
- the event was selected by at least one of the topological di-muon triggers listed in section 4.2.1.3. These triggers require two opposite charge LVL1 muon candidates of:
  - $p_{\mathrm{T}}(\mu) > 4\,\mathrm{GeV}$ for the `EF_2mu4T` triggers;
  - $p_{\mathrm{T}}(\mu^{\pm}) > 4\,\mathrm{GeV}$ and $p_{\mathrm{T}}(\mu^{\mp}) > 6\,\mathrm{GeV}$ for the `EF_mu4Tmu6` triggers;
  - $p_{\mathrm{T}}(\mu) > 6\,\mathrm{GeV}$ for the `EF_2mu6T` triggers;
  - Fulfill any additional cuts on $|\eta(\mu)|$ required by `Barrel` and `BarrelOnly` triggers.

  and that pass the `Jpsimumu` di-muon vertex/mass constraint (as described in section 4.2.1.2);
- the event contains at least one PV, formed from at least four ID tracks;
- the event contains at least one pair of oppositely charged muon candidates.

Additional information on the DQ2 containers and GRL used can be found in appendix A.

4.2.2.2 $J/\psi \to \mu^+\mu^-$ Reconstruction

$J/\psi \to \mu^+\mu^-$ candidates are formed from all pairs of oppositely charged muon candidates (`STACO–Combined` or `STACO–Tagged`, and passing the 2012 *Muon Combined Performance* (MCP) quality cuts) and assigned to one of three categories:

- *Barrel–Barrel* (BB) candidates have $|\eta(\mu)| < 1.05$ for both muons;
- *Barrel–End-Cap* (BE) candidates have $|\eta(\mu)| < 1.05$ for one muon, and $1.05 < |\eta(\mu)| < 2.5$ for the other;
- *End-Cap–End-Cap* (EE) candidates have $1.05 < |\eta(\mu)| < 2.5$ for both muons.

The two tracks of each candidate are refitted to a common vertex and the candidate retained for further analysis if:

- the vertex fit has a χ^2/d.o.f < 10;
- the refitted tracks have:
  - $2.959\,\text{GeV} < m(\mu^+\mu^-) < 3.229\,\text{GeV}$, for BB candidates;
  - $2.913\,\text{GeV} < m(\mu^+\mu^-) < 3.273\,\text{GeV}$, for BE candidates;
  - $2.852\,\text{GeV} < m(\mu^+\mu^-) < 3.332\,\text{GeV}$, for EE candidates.

Events are rejected if no $J/\psi \to \mu^+\mu^-$ candidates are found.

4.2.2.3 $\phi \to K^+K^-$ Reconstruction

$\phi \to K^+K^-$ candidates are formed from all pairs of oppositely charged ID tracks not associated to muon candidates where:

- $p_T(K) > 1\,\text{GeV}$. This differs from the track selection criterion used in [127, 143] and was implemented to reduce the combinatorics associated with $\phi \to K^+K^-$ candidate reconstruction. This change has negligible effect on the resultant 8 TeV $B_s \to J/\psi\phi$ dataset;
- $|\eta(K)| < 2.5$;
- each track contains at least one pixel hit;
- each track contains at least four SCT hits.

Events are rejected if no $\phi \to K^+K^-$ candidates are found.

4.2.2.4 $\mathbf{B_s \to J/\psi(\mu^+\mu^-)\phi(K^+K^-)}$ Reconstruction

$\mathrm{B_s} \to \mathrm{J}/\psi\phi$ candidates are formed from all combinations of J/ψ and ϕ candidates in the event. The four tracks for each combination are refitted to a common vertex, with the invariant mass of the muon tracks constrained to the world average J/ψ mass as given in [146]. Candidates are retained for further analysis if:

- the vertex fit has a χ^2/d.o.f < 3;
- The refitted tracks have:
  - $1.0085\,\mathrm{GeV} < m(\mathrm{K^+K^-}) < 1.0305\,\mathrm{GeV}$;
  - $5.150\,\mathrm{GeV} < m(\mathrm{J}/\psi\mathrm{K^+K^-}) < 5.650\,\mathrm{GeV}$.

If there is more than one $\mathrm{B_s} \to \mathrm{J}/\psi\phi$ candidate in the event, the candidate with the lowest χ^2/d.o.f is retained for the $\mathrm{B_s} \to \mathrm{J}/\psi\phi$ default fit.

4.2.2.5 Event Observables

The $\mathrm{B_s}$ candidates mass, m_i (and its uncertainty, σ_{m_i}), and transverse momentum, $p_{\mathrm{T}i}$, are calculated from the four refitted tracks used to form the $\mathrm{B_s} \to \mathrm{J}/\psi\phi$ candidates.

The proper decay time of the $\mathrm{B_s}$ candidate, t_i, and its uncertainty, σ_{t_i}, is given by

$$t_i = \frac{L_{\mathrm{xy}} \cdot m_{\mathrm{B_s}}}{p_{\mathrm{T}i}} \tag{4.13}$$

where the transverse decay length, L_{xy}, is the transverse displacement between the production and decay vertices projected onto the $\mathrm{B_s}$ candidate's momentum and $m_{\mathrm{B_s}}$ is the world average $\mathrm{B_s}$ mass as given in [146].

The production PV is selected by choosing the PV with the minimum 3D impact parameter, a_0, between the $\mathrm{B_s}$ candidate's projected track and the PV. If the four tracks used to construct the $\mathrm{B_s^0}$ candidate have been associated to a PV during PV reconstruction, they are removed from the PV they are associated with, and the PV refit with the remaining tracks before production PV selection is performed. Previous MC studies [147] have shown this to provide stable proper decay time reconstruction over the nPV range of interest for the $\mathrm{B_s} \to \mathrm{J}/\psi\phi$ default fit.

The $\mathrm{B_s}$ candidate's transversity angles, Ω_i, are reconstructed using only the ID tracks associated to the selected muon candidates, as muon reconstruction performance is dominated by the ID tracks in the p_T regime of interest [148].

4.3 Flavour Tagging

It is possible to determine the initial flavour of the signal-side $\mathrm{B_s} \rightarrow \mathrm{J}/\psi\phi$ candidate through the use of *Opposite-Side Taggers* (OSTs) [149, 150], where the production flavour of the $\mathrm{B_s}$ is inferred from the decay products of the pair-produced B meson.

The incorporation of these taggers into the $\mathrm{B_s} \rightarrow \mathrm{J}/\psi\phi$ default fit is performed in three stages:

- To perform calibration and performance studies on the taggers, a calibration sample of $\mathrm{B}^\pm \rightarrow \mathrm{J}/\psi\mathrm{K}^\pm$ candidates is collected. This signal-side is both non-oscillating, and expected to have production kinematics similar to the $\mathrm{B_s} \rightarrow \mathrm{J}/\psi\phi$ signal-side of the default fit. Details of the calibration sample are given in section 4.3.1;
- Using the $\mathrm{B}^\pm \rightarrow \mathrm{J}/\psi\mathrm{K}^\pm$ calibration sample, the performance of the OSTs can be optimised, and their expected performance in the $\mathrm{B_s} \rightarrow \mathrm{J}/\psi\phi$ default fit determined. The optimised taggers used in the $\mathrm{B_s} \rightarrow \mathrm{J}/\psi\phi$ default fit and the tagging of the $\mathrm{B_s} \rightarrow \mathrm{J}/\psi\phi$ dataset is discussed in section 4.3.2;
- The final step is to modify the $\mathrm{B_s} \rightarrow \mathrm{J}/\psi\phi$ proper decay time–transversity angle PDF to include information on the initial flavour of the mother particle. The method adopted for including this information in the default fit is defined in section 4.3.3.

Possible systematic errors in the extraction of physics parameters from the $\mathrm{B_s} \rightarrow \mathrm{J}/\psi\phi$ default fit, due to the flavour tagging implementation, is examined in sections 4.5.1.2 and 4.5.4.

4.3.1 The $\mathrm{B}^\pm \rightarrow \mathrm{J}/\psi\mathrm{K}^\pm$ Calibration Sample

As the OSTs used in the $\mathrm{B_s} \rightarrow \mathrm{J}/\psi\phi$ default fit are probabilistic in nature, the optimisation of the taggers and analysis of the quality of the flavour tagging information provided to the $\mathrm{B_s} \rightarrow \mathrm{J}/\psi\phi$ default fit is required. This is performed through a $\mathrm{B}^\pm \rightarrow \mathrm{J}/\psi\mathrm{K}^\pm$ calibration sample as the signal-side is both non-oscillating and self-tagging; $\mathrm{B}^\pm$ and $\mathrm{B_s}$ production kinematics, and therefore opposite-side kinematics, are expected to be similar.

4.3.1.1 Event Selection

'Good for Physics' events from the 8 TeV LHC pp run that have been retained by any mono- or di-muon trigger are examined for possible $\mathrm{B}^{\pm} \to \mathrm{J}/\psi\mathrm{K}^{\pm}$ candidates. As no consideration is made of the proper decay time for the candidate, `L2StarA` triggers from LHC periods B–C are included in the event selection.

$\mathrm{J}/\psi \to \mu^{+}\mu^{-}$ candidates are formed from all pairs of oppositely charged muon candidates[8] where

- $p_{\mathrm{T}}(\mu^{\pm}) > 4\,\mathrm{GeV}$ and $|\eta(\mu^{\pm})| < 2.5$;
- the two-track vertex fit has a $\chi^{2}/\mathrm{d.o.f} < 10.8$;
- $2.8\,\mathrm{GeV} < m(\mu^{+}\mu^{-}) < 3.4\,\mathrm{GeV}$.

$\mathrm{B}^{\pm} \to \mathrm{J}/\psi\mathrm{K}^{\pm}$ candidates are formed from all combinations of $\mathrm{J}/\psi \to \mu^{+}\mu^{-}$ candidates and ID tracks[9] in the event not associated to the J/ψ muon candidates where $p_{\mathrm{T}}(\mathrm{K}^{\pm}) > 1\,\mathrm{GeV}$ and $|\eta(\mathrm{K}^{\pm})| < 2.5$. The three tracks for each candidate are fitted to a common vertex with the invariant mass of the muon tracks constrained to the world average J/ψ mass as given in [146], and the $\mathrm{B}^{\pm} \to \mathrm{J}/\psi\mathrm{K}^{\pm}$ retained for the calibration sample if

- $5.0\,\mathrm{GeV} < m(\mathrm{J}/\psi\mathrm{K}^{\pm}) < 5.6\,\mathrm{GeV}$;
- $|y(\mathrm{J}/\psi\mathrm{K}^{\pm})| < 2.5$;
- the three-track vertex fit has a $\chi^{2}/\mathrm{d.o.f} < 10.8$ and $L_{\mathrm{xy}} > 0.1\,\mathrm{cm}$.

The L_{xy} cut is applied to remove the majority of the prompt J/ψ + 1 track combinatorial background.

4.3.1.2 Sideband Subtraction

To extract useful information from the $\mathrm{B}^{\pm} \to \mathrm{J}/\psi\mathrm{K}^{\pm}$ signal decays, the events must be statistically disentangled from the background components of the $\mathrm{B}^{\pm} \to \mathrm{J}/\psi\mathrm{K}^{\pm}$ calibration sample. This is achieved using a sideband subtraction from a mass fit of the $\mathrm{B}^{\pm} \to \mathrm{J}/\psi\mathrm{K}^{\pm}$ candidates. The signal region is modelled as two Gaussians sharing a common mean, while the background consists of three components: a hyperbolic tangent models the background contributions from mis-reconstructed $\mathrm{B}^{\pm} \to \mathrm{J}/\psi X$ while a negative exponential is used to

---

[8] The muons are required to be `STACO–Combined`, and pass the 2012 MCP quality cuts [126, 151].

[9] Passing additional track quality cuts.

$\lvert y(\mathrm{J}/\psi\mathrm{K}^{\pm})\rvert$	Event Count ($\times 10^3$)
0.0–0.5	332 ± 1
0.5–1.0	308 ± 1
1.0–1.5	234 ± 1
1.5–2.0	223 ± 2
2.0–2.5	58 ± 2
All	1116 ± 2

Table 4.6: $\mathrm{B}^{\pm} \to \mathrm{J}/\psi\mathrm{K}^{\pm}$ calibration sample event counts.

model J/ψ + 2 track events respectively. The final background component is $\mathrm{B}^{\pm} \to \mathrm{J}/\psi\pi^{\pm}$ decays systematically mis-reconstructed, and is modelled as a single Gaussian whose relative normalisation to the signal contribution is fixed from the product of ratios of the branching ratios of the decays as listed in [146] and selection efficiencies taken from MC, and whose mean and width is obtained from MC studies.

The mass fit is performed in five partitions of rapidity to accommodate the varying momentum resolution of the ID. The rapidity bins, and their associated event counts are given in table 4.6, while the projection of the combined mass fit is shown in fig. 4.8.

4.3.2 Flavour Tagging Methods

Four OSTs are employed in the $\mathrm{B_s} \to \mathrm{J}/\psi\phi$ default fit, three are based around detecting $\mathrm{b} \to \ell$ transitions (section 4.3.2.2), while the final tagger is based on ATLAS's ability to reconstruct hadronic B decays (section 4.3.2.3).

For each event passing the selection cuts of one of the taggers, a common method, described in section 4.3.2.1, is used to assess the probability that the signal-side initially contained a $\overline{\mathrm{b}}$ quark.

4.3.2.1 Tagging Charge and Flavour Tag Probability

For events passing the selection criteria of one of the tagging methods, a *Tagging Charge*, Q, is calculated from the charge and p_{T} of some collection of tracks from the event as

$$Q = \frac{\sum_i q_i \cdot (p_{\mathrm{T}i})^{\kappa}}{\sum_i (p_{\mathrm{T}i})^{\kappa}} \tag{4.14}$$

where κ is a per-tagger constant that has been optimised to provide the maximal power for the tagger. The probability distributions $\mathrm{P}(Q|\mathrm{B}^{+})$, and $\mathrm{P}(Q|\mathrm{B}^{-})$

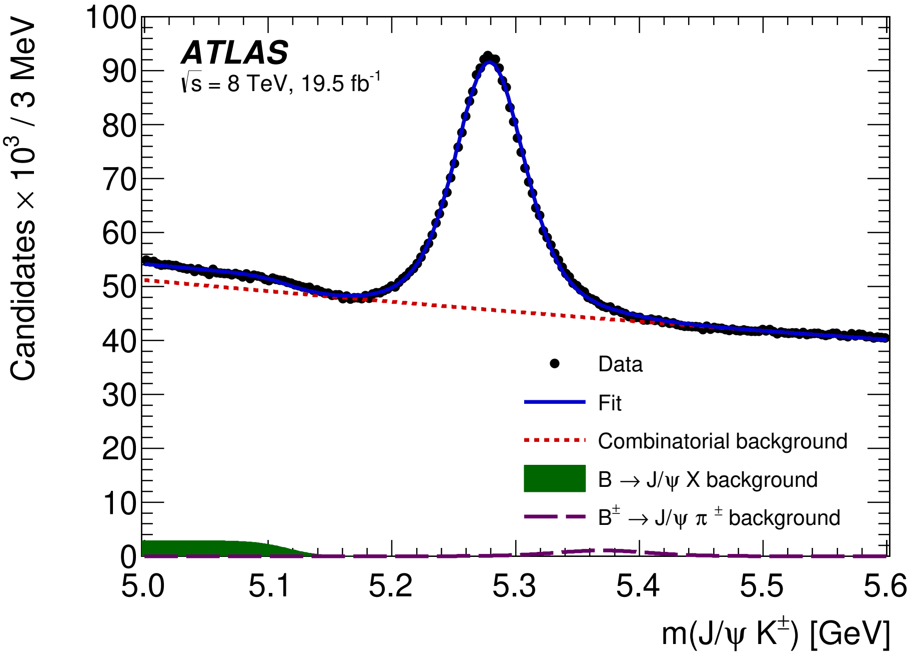

Figure 4.8: Mass fit projection for the $B^{\pm} \rightarrow J/\psi K^{\pm}$ calibration sample showing the data distribution (black), total fit PDF (blue), combinatorial background PDF (red). Also shown are PDF projections for the $B^{\pm} \rightarrow J/\psi X$ (green) and $B^{\pm} \rightarrow J/\psi\pi^{\pm}$ (purple) background components. Figure from [128].

are obtained from the $B^{\pm} \rightarrow J/\psi K^{\pm}$ calibration sample using a sideband-subtraction where the signal region is defined to be $\pm 2\sigma$ of the fitted $B^{\pm}$ mass, and σ is the normalisation-weighted average of the double Gaussian's standard deviations (retaining $\approx 90\%$ of signal events). The two background regions are each 2σ wide, and separated from the signal region by 1σ. The tagging charge distributions for the implemented taggers are shown in fig. 4.9.

Conversion of the tagging charge into a *Flavour Tag Probability*is performed through $P(B|Q)$ where

$$P(B|Q) = \frac{P(Q|B^{+})}{P(Q|B^{+}) \cdot P(Q|B^{-})} \tag{4.15}$$

under the assumption that $P(B^{+}) = P(B^{-})$.

For use in the $B_s \rightarrow J/\psi\phi$ default fit, $P(B|Q)$ is divided into three components. For events with $Q = \pm 1$, the discrete components of $P(B|Q)$ are given directly by eq. (4.15). For the remaining events, $P(B|Q)$ is calculated from event counts in 20 equal-sized bins of Q, and a third-order polynomial fitted to the binned distribution using a χ^2 fit to obtain a functional form for $\mathrm{P}(B|Q)$.

4.3.2.2 Lepton Based Tagging

Flavour tagging of opposite-side b $\to \ell$ transitions is performed by the muon and electron taggers.

The muon taggers require a third muon candidate in the event where:

- $p_{\mathrm{T}}(\mu) > 2.5\,\mathrm{GeV}$ and $|\eta(\mu)| < 2.5$;
- The muon's ID track is not associated to a signal-side track;
- $|\Delta z| < 5\,\mathrm{mm}$ between the muon's ID track and PV associated to the signal-side decay.

If more than one muon candidate passes the criteria then the highest p_{T} candidate is retained for further analysis.

The selected muon candidate is processed by the combined muon or segment-tagged muon tagger depending on the reconstruction class of the muon candidate. Both taggers use all ID tracks within a cone of $\Delta R < 0.5$ around the muon (where the ID tracks are not associated to the signal-side decay, $p_{\mathrm{T}} > 0.5\,\mathrm{GeV}$, and $|\eta| < 2.5$) to construct the tagging charge with $\kappa = 1.1$.

The electron tagger requires an electron candidate, reconstructed using information from the TRT and calorimeter, and passing the tight electron quality criteria as specified in [152], where:

- $p_{\mathrm{T}}(\mathrm{e}) > 0.5\,\mathrm{GeV}$ and $|\eta(\mu)| < 2.5$;
- The electron's ID track is not associated to a signal-side track;
- $a_0 < 5\,\mathrm{mm}$ between the electron's ID track and the PV associated to the signal-side decay;
- $\Delta R > 0.4$, and $\cos(\zeta) < 0.98$ between the electron's ID track and the signal-side candidate where ζ is the opening angle in the laboratory frame.

If more than one electron candidate passes these cuts, the tagging charge is formed from tracks within a cone of $\Delta R < 0.5$ around the highest p_{T} candidate with $\kappa = 1$.

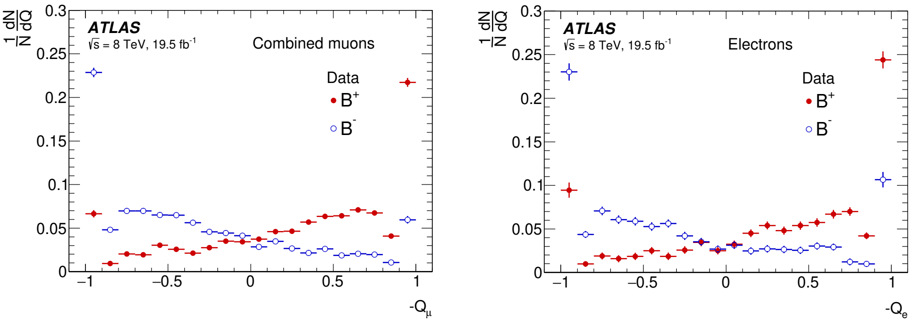

(a) Combined muon (b) Electron

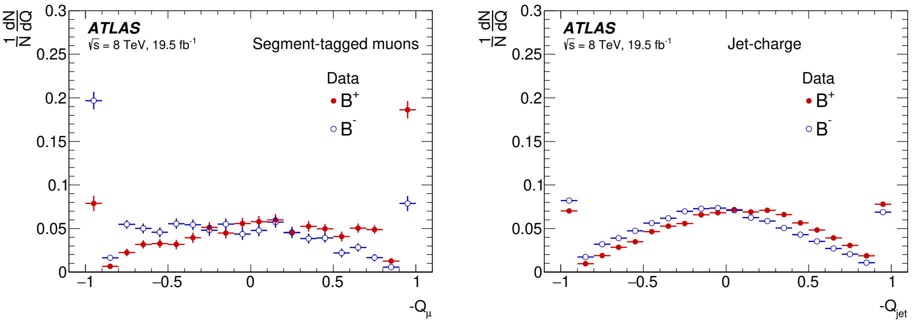

(c) Segment-tagged muon (d) Jet-charge

Figure 4.9: Tagging charge distributions for B^+ (red) and B^- (blue) candidates in the $\mathrm{B}^\pm \to \mathrm{J}/\psi\mathrm{K}^\pm$ calibration sample. Shown are the distributions for the combined and segment-tagged muon flavour taggers (left), the electron flavour tagger (upper-right) and the jet-charge flavour tagger (lower-left).

4.3.2.3 Jet-Charge Tagging

For events where no lepton candidates pass the required cuts, a b-tagged jet may be used to form a tagging charge. Track-based jets are formed using the *anti*-k_T algorithm [153] with $R = 0.8$, and those that are tagged as b-jets by the `MV1` b-tagger [154] with a tagging weight of $\omega > 0.7$ and separated from the signal-side decay by $\Delta R > 0.5$ are used to form a tagging charge[10]. Tracks associated to both the *anti*-k_T jet and the signal-side PV are used to obtain the tagging charge for the event with $\kappa = 1.1$.

---

[10] For the small fraction of events where more than one jet passes these cuts the jet with the highest b-tag weight is selected.

4.3.2.4 Flavour Tagging Performance Metrics

Three metrics are used to evaluate the performance of the flavour taggers:

- The efficiency, ϵ, of a tagger is the probability that any event may be tagged using the tagger in question;
- The *Dilution*, $\mathcal{D}$, of a tagger is defined as $\mathcal{D} = \mathrm{P}(B|Q) - \mathrm{P}(\overline{B}|Q)$, and measures the useful information provided by each tagged event. It is related to the more usual *Wrong Tag Fraction*[155], ω, by $\mathcal{D} = 1 - 2 \cdot \omega$;
- The *Tagging Power*, T, of a tagger is a measure of the useful information provided by the tagger overall.

The tagging power for a tagger is given by

$$T = \epsilon \cdot \mathcal{D}^2 \tag{4.16}$$

or

$$T = \sum\nolimits_i \epsilon_i \cdot \mathcal{D}_i^2 \tag{4.17}$$

over some partition i. Per-bin efficiencies and dilutions may be calculated from the binned tagging charge distributions (section 4.3.2.1) and the tagging power for each tagger determined. An effective (average) dilution for the tagger may then be determined as $\mathcal{D}_{\mathrm{Eff}} = \sqrt{\frac{T}{\epsilon}}$. The efficiency, effective dilution, and tagging power measured for the OSTs used in the $\mathrm{B_s} \to \mathrm{J}/\psi\phi$ default fit are shown in table 4.7.

By definition there is no overlap between the lepton and jet-charge taggers, however 0.4 % of all tagged events could be tagged by either class of the lepton-based taggers. For these events, a 'winner-takes-all' approach is adopted where the tagger with the highest tagging power (combined muon → electron → segment-tagged muon) is used to flavour tag the event (see section 4.5.1.2).

4.3.3 The Flavour Tagged $\mathrm{B_s} \to \mathrm{J}/\psi\phi$ Fit

The flavour tagging information is applied probabilisticly in the fit through the intoduction of two additional terms in the differential decay rate (eq. (4.10)) resulting in

$$\frac{\mathrm{d}^4\Gamma}{\mathrm{d}t\,\mathrm{d}\Omega} = \sum\nolimits_k A_k \cdot \big(K_k + \mathrm{P}(B|Q) \cdot T_k - \mathrm{P}(\overline{B}|Q) \cdot T_k\big) \cdot g_k. \tag{4.18}$$

The flavour tagging terms, T_k, are given in table 4.8.

Tagging Method	ϵ [%]	$\mathcal{D}_{\mathrm{Eff}}$ [%]	T [%]
Combined muon	4.12 ± 0.02	47.4 ± 0.2	0.92 ± 0.02
Electron	1.19 ± 0.01	49.2 ± 0.3	0.29 ± 0.01
Segment-tagged muon	1.20 ± 0.01	28.6 ± 0.2	0.10 ± 0.01
Jet-charge	13.15 ± 0.03	11.85 ± 0.03	0.19 ± 0.01
Total	19.66 ± 0.04	27.56 ± 0.06	1.49 ± 0.02

Table 4.7: Opposite-side tagger performance metrics for the flavour taggers used in the $\mathrm{B_s} \to \mathrm{J}/\psi\phi$ default fit.

k	T_k
1	$2 \cdot e^{-\Gamma_s t} \cdot \sin(\Delta m_s t) \cdot \sin(\phi_s)$
2	$2 \cdot e^{-\Gamma_s t} \cdot \sin(\Delta m_s t) \cdot \sin(\phi_s)$
3	$-2 \cdot e^{-\Gamma_s t} \cdot \sin(\Delta m_s t) \cdot \sin(\phi_s)$
4	$2 \cdot e^{-\Gamma_s t} \cdot \sin(\Delta m_s t) \cdot \sin(\phi_s)$
5	$e^{-\Gamma_s t} \left(\sin(\delta_\perp) \cdot \cos(\Delta m_s t) - \cos(\delta_\perp) \cdot \sin(\Delta m_s t) \cdot \cos(\phi_s)\right)$
6	$e^{-\Gamma_s t} \left(\sin(\delta_\perp - \delta_\parallel) \cdot \cos(\Delta m_s t) - \cos(\delta_\perp - \delta_\parallel) \cdot \sin(\Delta m_s t) \cdot \cos(\phi_s)\right)$
7	$-2 \cdot e^{-\Gamma_s t} \cdot \sin(\Delta m_s t) \cdot \sin(\phi_s)$
8	$e^{-\Gamma_s t} \left(\cos(\delta_S) \cdot \cos(\Delta m_s t) + \sin(\delta_S) \cdot \sin(\Delta m_s t) \cdot \cos(\phi_s)\right)$
9	$e^{-\Gamma_s t} \left(\cos(\delta_\parallel - \delta_S) \cdot \cos(\Delta m_s t) - \sin(\delta_\parallel - \delta_S) \cdot \sin(\Delta m_s t) \cdot \cos(\phi_s)\right)$
10	$-2 \cdot e^{-\Gamma_s t} \cdot \sin(\Delta m_s t) \cdot \sin(\phi_s)$

Table 4.8: T_k for S- and P-wave $\mathrm{B_s} \to \mathrm{J}/\psi \mathrm{K}^+\mathrm{K}^-$ decays.

4.4 The Fit Procedure

The $\mathrm{B_s} \to \mathrm{J}/\psi\phi$ default fit is used to extract the nine physics parameters[11] of interest from the $\mathrm{B_s} \to \mathrm{J}/\psi\phi$ dataset. These parameters are estimated using the method of Maximal Likelihood Fitting (section 4.4.1) and require PDFs that describing the signal and possible background components. The overall model fitted to the data is described in section 4.4.2, while detailed descriptions of the signal and background PDFs are given in sections 4.4.3 to 4.4.6.

In addition to the physics parameters extracted by the fit, a number of other parameters are estimated from the dataset to validate the performance of the fit software. The results of the $\mathrm{B_s} \to \mathrm{J}/\psi\phi$ default fit are presented in section 4.4.7.

---

[11] The three kinematic parameters of the decay (ϕ_s, $\Delta\Gamma_s$, and Γ_s), three amplitudes ($|A_0|^2$, $|A_\parallel|^2$, and $|A_S|^2$) and three strong phases ($\delta_\parallel$, $\delta_\perp$, and $\delta_\perp - \delta_S$). The remaining ampiltude and strong phase are fixed by convention.

4.4.1 Parameter Estimation

The method of *Maximal Likelihood Fitting* (MLF) [109, 156] is a technique used to estimate a set of parameters, $\vec{\lambda}$, from a dataset $\vec{\mathbf{x}}_1, \ldots, \vec{\mathbf{x}}_i$, such that the probability distribution $\mathrm{P}(\vec{\mathbf{x}}|\vec{\lambda})$ gives the best possible description of the dataset.

Assuming $\mathrm{P}(\vec{\mathbf{x}}|\vec{\lambda})$ to be correctly normalised

$$\int_D \mathrm{P}(\vec{\mathbf{x}}|\vec{\lambda})\,\mathrm{d}\vec{\mathbf{x}} = 1 \tag{4.19}$$

where D is the domain of $\vec{\mathbf{x}}$, the *Likelihood*, $\mathcal{L}$, of the parameter set is given by

$$\mathcal{L}(\vec{\lambda}) = \prod_i \mathrm{P}(\vec{\mathbf{x}}_i|\vec{\lambda}) \tag{4.20}$$

and the *Maximal-Likelihood Estimate* (MLE) of the parameters, $\hat{\lambda}$, are the values for which the likelihood function has its global maximum. For technical reasons[12], it is often more convenient to determine the MLE of the parameters by searching for the global minimum of the *Negative Log-Likelihood*function

$$-\ln\mathcal{L}(\vec{\lambda}) = -\sum_i \ln\mathrm{P}(\vec{\mathbf{x}}_i|\vec{\lambda}). \tag{4.21}$$

In the large sample limit (as the number of events in the dataset goes to infinity), the MLE of the parameters has a number of desirable features:

- it is consistent:
  For each parameter the MLE converges to its true value.
- it is unbiased:
  For a sample size of n events the bias is proportional to $1/n$ and the bias within the fit may be estimated through *Pull-Distributions*[108] (see also section 4.5.1.5).
- it reaches the minimum-variance bound [109, 156]:
  No other estimation technique can perform better.

The MLE of each parameter provides a point-estimate of the most likely value for that parameter. For a sufficiently large dataset, the distribution of the MLE under repeated experiments is Gaussian [157]; the width of this Gaussian is quoted as the uncertainty on the MLE for the parameter and is obtained from the likelihood function by

$$\sigma_j = \left(-\frac{\partial^2 \ln\mathcal{L}}{\partial{\lambda_j}^2}\right)^{-\frac{1}{2}} \tag{4.22}$$

---

[12] Addition is typically less computationally expensive than multiplication, and for probability distributions that vary over a few orders of magnitude rounding errors can become dominant when numerical integration/differentiation is performed.

evaluated at the MLE of $\vec{\lambda}$. In general, a number of parameters for the model are estimated, and the *Covariance*, U, between the maximal-likelihood estimates for parameters λ_i and λ_j is given by

$$U_{ij} = \left(- \frac{\partial^2 \ln \mathcal{L}}{\partial \lambda_i \partial \lambda_j} \right)^{-1} \tag{4.23}$$

evaluated at the MLE of $\vec{\lambda}$.

4.4.1.1 Likelihood Ratios

The *Likelihood Ratio*, $\Theta(\vec{\lambda})$, is the ratio between the likelihood at $\vec{\lambda}$ and the likelihood at the MLE of the model

$$\Theta(\vec{\lambda}) = \frac{\mathcal{L}(\vec{\lambda})}{\mathcal{L}(\hat{\lambda})} \tag{4.24}$$

in the large sample limit, $-2\ln\Theta(\vec{\lambda})$ follows a χ^2 distribution with n degrees of freedom (Wilks' theorem [158]) so a $1-\alpha$ confidence interval may be formed from the boundary of the region at

$$-2\ln\Theta(\vec{\lambda}) = F^{-1}_{\chi^2_n}(1-\alpha) \tag{4.25}$$

where $F^{-1}_{\chi^2_n}(1-\alpha)$ is the inverse cumulative distribution for a χ^2 distribution of degree n. This logic may be extended to form m-dimensional (with $m < n$) confidence intervals by defining the *Profile Likelihood Ratio*, $\Theta(\lambda_j, \lambda_k, \dots)$ as

$$\Theta(\lambda_j, \lambda_k, \dots) = \frac{\mathcal{L}(\lambda_j, \lambda_k, \dots, \hat{\mathbf{\Theta}})}{\mathcal{L}(\hat{\lambda})} \tag{4.26}$$

where $\hat{\mathbf{\Theta}}$ is the MLE of the remaining parameters of $\vec{\lambda}$ given $\lambda_j, \lambda_k, \dots$. The $1-\alpha$ confidence interval is then defined by the boundary of the region with $\Theta(\lambda_j, \lambda_k, \dots) = F^{-1}_{\chi^2_m}(1-\alpha)$

4.4.1.2 Constrained Fits

The likelihood function may include prior information about the fitted parameters. A prior distribution, $\mathrm{P}(\lambda_j)$, for the fitted parameter λ_j allows the likelihood function to be recast as

$$\ln\mathcal{L}(\vec{\lambda}) = \sum\nolimits_i \ln \mathrm{P}(\vec{\mathbf{x}}_i|\vec{\lambda}) \cdot \mathrm{P}(\lambda_j). \tag{4.27}$$

Typically, the constraint is in the form of a Gaussian distribution for the constrained parameters, therefore a multi-dimensional constraint $\vec{\lambda}_{j,k,\dots}$ may be applied through the use of the multivariate Gaussian

$$\mathrm{P}(\vec{\lambda}_{j,k,\dots}) = \frac{1}{(2\pi)^{n/2} \cdot |\Sigma|^{1/2}} e^{-\frac{1}{2}(\vec{\lambda}_{j,k,\dots} - \vec{\mu})^{\mathrm{T}} \cdot \Sigma \cdot (\vec{\lambda}_{j,k,\dots} - \vec{\mu})} \tag{4.28}$$

where $\vec{\mu}$ and Σ are the central values and covariance matrix of the constrained parameters respectively.

4.4.1.3 Punzi Terms

Where the PDFs used in the likelihood function are conditionally dependent on per-event observables, the addition of *Punzi Terms*may be required [159]. The axiomatic definition of conditional probability [160] is expressed as

$$\mathrm{P}(A \cap B) = \mathrm{P}(A|B) \cdot \mathrm{P}(B) \tag{4.29}$$

so the multivariate distribution for the observables x and σ (for some class of events C) may be be converted into a conditional probability $\mathrm{P}(x|\sigma \cap C)$ for use in the likelihood function by repeated applications of eq. (4.29)

$$\begin{aligned} \mathrm{P}(x \cap \sigma|C) &= \frac{\mathrm{P}(x \cap \sigma \cap C)}{\mathrm{P}(C)} \\ &= \frac{\mathrm{P}(x|\sigma \cap C) \cdot \mathrm{P}(\sigma \cap C)}{\mathrm{P}(C)} \\ &= \frac{\mathrm{P}(x|\sigma \cap C) \cdot \mathrm{P}(\sigma|C) \cdot \mathrm{P}(C)}{\mathrm{P}(C)} \\ &= \mathrm{P}(x|\sigma \cap C) \cdot \mathrm{P}(\sigma|C) \end{aligned} \tag{4.30}$$

leading to the introduction of the Punzi term $\mathrm{P}(\sigma|C)$. Exclusion of the Punzi term results, in general, in a biasing of the likelihood function.

4.4.2 The $\mathrm{B_s} \to \mathrm{J}/\psi\phi$ Default Fit

It is inevitable that a large number of background events will contaminate the signal in the data sample. In order to accurately extract the physics parameters of interest for the $\mathrm{B_s} \to \mathrm{J}/\psi\phi$ decay, the likelihood function must accommodate these components. The likelihood function used in the $\mathrm{B_s} \to \mathrm{J}/\psi\phi$ default fit has the following form:

$$\begin{aligned} \ln \mathcal{L} = \sum\nolimits_i w_i \cdot \ln \{ \quad & f_{\mathrm{S}} \cdot \mathcal{F}_{\mathrm{S}}(m_i, t_i, \sigma_{t_i}, \Omega_i, \mathrm{P}(B)_i, p_{\mathrm{T}i}) \\ & + f_{\mathrm{S}} \cdot f_{\mathrm{B_d}} \cdot \mathcal{F}_{\mathrm{B_d}}(m_i, t_i, \sigma_{t_i}, \Omega_i, \mathrm{P}(B)_i, p_{\mathrm{T}i}) \\ & + f_{\mathrm{S}} \cdot f_{\Lambda_{\mathrm{b}}} \cdot \mathcal{F}_{\Lambda_{\mathrm{b}}}(m_i, t_i, \sigma_{t_i}, \Omega_i, \mathrm{P}(B)_i, p_{\mathrm{T}i}) \\ & + f_{\mathrm{Bck}} \cdot \mathcal{F}_{\mathrm{Bck}}(m_i, t_i, \sigma_{t_i}, \Omega_i, \mathrm{P}(B)_i, p_{\mathrm{T}i}) \} \end{aligned} \tag{4.31}$$

where

$$f_{\mathrm{Bck}} = 1 - f_{\mathrm{S}} \cdot (1 + f_{\mathrm{B_d}} + f_{\Lambda_{\mathrm{b}}}) \tag{4.32}$$

and w_i is a per-event weight used to correct for the proper decay time bias introduced by the ATLAS triggers used to select $\mathrm{B_s} \to \mathrm{J}/\psi\phi$ events (as described in section 4.2.1.3). f_{S} is the fitted fraction of signal events that are described by the PDF $\mathcal{F}_{\mathrm{S}}$ (section 4.4.3). $f_{\mathrm{B_d}}$ and f_{Λ_b} are the fraction of events, relative to the signal fraction, expected due to $\mathrm{B_d} \rightarrow \mathrm{J}/\psi \mathrm{K}^+\pi^-$ and $\Lambda_\mathrm{b} \rightarrow \mathrm{J}/\psi \mathrm{pK}^-$ (and their charge conjugate) decays systematically mis-reconstructed as $\mathrm{B_s} \rightarrow \mathrm{J}/\psi\phi$ events. These physics background components are described by the PDFs $\mathcal{F}_{\mathrm{B_d}}$ and $\mathcal{F}_{\Lambda_\mathrm{b}}$ (section 4.4.4). $\mathcal{F}_{\mathrm{Bck}}$ (section 4.4.5) models the combinatorial background, with its description fixed from the mass side-bands of the dataset.

4.4.3 Signal

The signal PDF has the following composition:

$$\begin{aligned}\mathcal{F}_{\mathrm{S}} = \; & A_{\mathrm{S}}(\Omega_i|p_{\mathrm{T}i}) \\ & \cdot P_{\mathrm{S}}(m_i) \cdot P_{\mathrm{S}}(t_i, \Omega_i|\sigma_{t_i}, \mathrm{P}(B)_i) \\ & \cdot P_{\mathrm{S}}(\sigma_{t_i}) \cdot P_{\mathrm{S}}(p_{\mathrm{T}i}) \cdot P_{\mathrm{S}}(\mathrm{P}(B)_i)\end{aligned} \tag{4.33}$$

and models the detector acceptance, mass, and proper decay time and transversity angle distributions for the $\mathrm{B_s} \rightarrow \mathrm{J}/\psi(\mu^+\mu^-)\phi(\mathrm{K}^+\mathrm{K}^-)$ decay. Normalisation of $\mathcal{F}_{\mathrm{S}}$ over the transversity angles is performed numerically, and the use of alternative binnings during integration are considered as systematic variations in section 4.5.1.4.

The signal Punzi PDFs, $P_{\mathrm{S}}(\sigma_{t_i})$, $P_{\mathrm{S}}(p_{\mathrm{T}i})$, and $P_{\mathrm{S}}(\mathrm{P}(B)_i)$ are described in section 4.4.6.

4.4.3.1 Detector Acceptance PDF

To correct for the p_{T}-dependent angular acceptance of the ATLAS detector for $\mathrm{B_s} \rightarrow \mathrm{J}/\psi(\mu^+\mu^-)\phi(\mathrm{K}^+\mathrm{K}^-)$ events, an acceptance PDF, $A_{\mathrm{S}}(\Omega_i|p_{\mathrm{T}i})$, is included in the fit. A $\mathrm{B_s} \rightarrow \mathrm{J}/\psi\phi$ MC sample, produced using the ATLAS simulation tool-chain and tuned using ATLAS 7 TeV data [161, 162], is divided into sub-samples for each trigger, where the number of events in each sub-sample is weighted according to the prescaled luminosity of that trigger. p_{T}-dependent angular acceptance maps are then generated from each sub-sample and summed over to determine the trigger-weighted angular acceptance. The acceptance PDF is fixed for use in the $\mathrm{B_s} \rightarrow \mathrm{J}/\psi\phi$ fit to data.

Validation of the acceptance PDF is performed using a side-band subtracted signal sample from the $\mathrm{B_s} \rightarrow \mathrm{J}/\psi\phi$ data (see section 4.5.1.4).

4.4.3.2 Mass PDF

The signal mass PDF, $P_{\mathrm{S}}(m_i)$, is modelled as the sum of three Gaussians sharing a common mean. The mean, standard deviations, and relative fractions are fitted in the $\mathrm{B_s} \to \mathrm{J}/\psi\phi$ fit to data.

4.4.3.3 Proper Decay Time and Transversity Angle PDF

The proper decay time and transversity angle PDF, $P_{\mathrm{S}}(t_i, \Omega_i | \sigma_{t_i}, \mathrm{P}(B)_i)$, is formed from the flavour tagged transversity angle distribution, given in section 4.3.3 with the addition of a per-candidate Gaussian convolution. This convolution accommodates the proper decay time uncertainty associated with ATLAS's track and vertex reconstruction and is validated though the use of a scale-factor determined during the fit.

4.4.4 Physics Backgrounds

Contamination from $\mathrm{B_d} \to \mathrm{J}/\psi\mathrm{K}^{*0}$ and $\Lambda_\mathrm{b} \to \mathrm{J}/\psi\mathrm{pK}^-$ (and their charge-conjugate) decays mis-reconstructed as $\mathrm{B_s} \to \mathrm{J}/\psi\phi$ decays are accounted for in the fit through the terms $\mathcal{F}_{\mathrm{B_d}}$ and $\mathcal{F}_{\Lambda_\mathrm{b}}$. The fractions of these events, $f_{\mathrm{B_d}}$ and f_{Λ_b} respectively, are taken relative to the number of signal events as

$$f_{\mathrm{B_d}} = \frac{N_{K^*}}{N_{\mathrm{B_s}}} = \frac{F_{\mathrm{B_d}}}{F_{\mathrm{B_s}}} \frac{\mathrm{BR}(\mathrm{B_d} \to \mathrm{J}/\psi\mathrm{K}^{*0}) \cdot \mathrm{BR}(\mathrm{K}^{*0} \to \mathrm{K}^+\pi^-)}{\mathrm{BR}(\mathrm{B_s} \to \mathrm{J}/\psi\phi) \cdot \mathrm{BR}(\phi \to \mathrm{K}^+\mathrm{K}^-)} \frac{\epsilon_{K^*}}{\epsilon_{\mathrm{B_s}}} \tag{4.34a}$$

$$f_{\Lambda_\mathrm{b}} = \frac{N_{\Lambda_\mathrm{b}}}{N_{\mathrm{B_s}}} = \frac{F_{\Lambda_\mathrm{b}}}{F_{\mathrm{B_s}}} \frac{\mathrm{BR}(\Lambda_\mathrm{b} \to \mathrm{J}/\psi\mathrm{pK}^-)}{\mathrm{BR}(\mathrm{B_s} \to \mathrm{J}/\psi\phi) \cdot \mathrm{BR}(\phi \to \mathrm{K}^+\mathrm{K}^-)} \frac{\epsilon_{\Lambda_\mathrm{b}}}{\epsilon_{\mathrm{B_s}}} \tag{4.34b}$$

where N_x is the number of x-type events selected into the analysis given a fragmentation fraction of F_x and an analysis selection efficiency of ϵ_x.

To determine the product $\mathrm{BR}(\mathrm{B_d} \to \mathrm{J}/\psi\mathrm{K}^{*0}) \cdot \mathrm{BR}(\mathrm{K}^{*0} \to \mathrm{K}^+\pi^-)$, the total branching ratio for the $\mathrm{B_d} \to \mathrm{J}/\psi\mathrm{K}^+\pi^-$ end-state, $\mathrm{BR}(\mathrm{B_d} \to \mathrm{J}/\psi\mathrm{K}^+\pi^-)_{\mathrm{Total}}$, is scaled by the P-wave contribution to this end-state as measured by [133]. Contamination from $\mathrm{B_d} \to \mathrm{J}/\psi\mathrm{K}^+\pi^-$ S-wave decays is treated as a systematic error (section 4.5.3.2).

$F_{\Lambda_\mathrm{b}}/F_{\mathrm{B_s}}$ is obtained from LHCb event count [163, 164, 165] and efficiencies [163] corrected for ATLAS detector acceptance. Alternative calculations for $F_{\Lambda_\mathrm{b}}/F_{\mathrm{B_s}}$, based upon LHCb production cross-section ratios [164] or CDF results [146], yield compatible results and are considered as systematic variations in section 4.5.3.1.

Variable	Value	Source
$F_{\mathrm{B_s}}/F_{\mathrm{B_d}}$	0.259 ± 0.015	[163, 164]
$\mathrm{BR}(\mathrm{B_d} \to \mathrm{J}/\psi \mathrm{K}^+\pi^-)_{\mathrm{Total}}$	$(1.079 \pm 0.011) \times 10^{-3}$	[133]
S-Wave Fraction	0.157 ± 0.008	[133]
P-Wave Fraction	0.735 ± 0.007	[133]
$< \mathrm{BR}(\mathrm{B_s} \to \mathrm{J}/\psi\phi)$	$(1.07 \pm 0.09) \times 10^{-3}$	[146]
$\mathrm{BR}(\phi \to \mathrm{K}^+\mathrm{K}^-)$	0.489 ± 0.005	[146]

Table 4.9: Physics background fractions for the $\mathrm{B_d} \to \mathrm{J}/\psi \mathrm{K}^{*0}$ background.

Variable	Value	Source
$F_{\Lambda_\mathrm{b}}/F_{\mathrm{B_s}}$	1.455 ± 0.476	[163, 164, 165]
$\mathrm{BR}(\Lambda_\mathrm{b} \to \mathrm{J}/\psi \mathrm{pK}^-)$	$(3.17 \pm 0.57) \times 10^{-4}$	[166]
$\mathrm{BR}(\mathrm{B_s} \to \mathrm{J}/\psi\phi)$	$(1.07 \pm 0.09) \times 10^{-3}$	[146]
$\mathrm{BR}(\phi \to \mathrm{K}^+\mathrm{K}^-)$	0.489 ± 0.005	[146]

Table 4.10: Physics background fractions for the $\Lambda_\mathrm{b} \to \mathrm{J}/\psi \mathrm{pK}^-$ background.

The fragmentation ratios, branching fractions, S- and P-wave fractions, and their sources are given in table 4.9 for $f_{\mathrm{B_d}}$, and table 4.10 for f_{Λ_b}.

Selection efficiencies for S- and P-wave $\mathrm{B_d} \to \mathrm{J}/\psi \mathrm{K}^+\pi^-$ physics backgrounds, $\epsilon_{\mathrm{K}^+\pi^-}$ and ϵ_{K^*} respectively, are given in table 4.11(a). The selection efficiency for the $\Lambda_\mathrm{b} \to \mathrm{J}/\psi \mathrm{pK}^-$ physics background, $\epsilon_{\Lambda_\mathrm{b}}$, is given in table 4.11. The difference in the $\mathrm{B_s} \to \mathrm{J}/\psi\phi$ selection efficiency, $\epsilon_{\mathrm{B_s}}$, between table 4.11(a) and table 4.11(b) is due to changes in the default Pythia tuning and trigger simulation between the time of the generation of the MC samples for the $\mathrm{B_d} \to \mathrm{J}/\psi \mathrm{K}^{*0}$ studies (MC12), and the samples generated by the analysis team for the $\Lambda_\mathrm{b} \to \mathrm{J}/\psi \mathrm{pK}^-$ studies (Custom/MC14).

Combining eq. (4.34) and tables 4.9 to 4.11 give $f_{\mathrm{B_d}} = (3.3 \pm 0.5)\,\%$ and $f_{\Lambda_\mathrm{b}} = (1.6 \pm 0.6)\,\%$.

4.4.4.1 $\mathrm{B_d} \to \mathrm{J}/\psi \mathrm{K}^{*0}$ Background

Two MC samples are used to study the effect of $\mathrm{B_d} \to \mathrm{J}/\psi \mathrm{K}^{*0}$ contamination on the $\mathrm{B_s} \to \mathrm{J}/\psi\phi$ default fit. Both samples are taken from the ATLAS MC12 MC generation campaign, and use the default Pythia tuning from this campaign [161, 162]. The first is a fully-reconstructed sample used to determine detector

Variable	Value	Source
$\epsilon_{\mathrm{K}^+\pi^-}$	$0.002\,12 \pm 0.000\,16$	MC12
ϵ_{K^*}	$0.002\,09 \pm 0.000\,05$	MC12
$\epsilon_{\mathrm{B_s}}$	$0.368\,91 \pm 0.002\,51$	MC12

(a) $\mathrm{B_d} \to \mathrm{J}/\psi\mathrm{K}^{*0}$

Variable	Value	Source
$\epsilon_{\Lambda_\mathrm{b}}$	0.0101 ± 0.0001	Custom(MC14)
$\epsilon_{\mathrm{B_s}}$	$0.497 \quad \pm 0.198$	MC14

(b) $\Lambda_\mathrm{b} \to \mathrm{J}/\psi\mathrm{pK}^-$

Table 4.11: Physics background selection efficiencies.

response and selection efficiencies. The second sample is a larger (1 000 000 event) generator-level sample used in the modelling of the transversity angle distributions.

The $\mathrm{B_d} \to \mathrm{J}/\psi\mathrm{K}^{*0}$ background PDF has the following composition:

$$\begin{aligned}\mathcal{F}_{\mathrm{B_d}} = \;& P_{\mathrm{B_d}}(m_i) \cdot P_{\mathrm{B_d}}(t_i|\sigma_{t_i}) \cdot P_{\mathrm{B_d}}(\Omega_i|p_{\mathrm{T}i}) \\ & \cdot P_{\mathrm{Bck}}(\sigma_{t_i}) \cdot P_{\mathrm{Bck}}(p_{\mathrm{T}i}) \cdot P_{\mathrm{Bck}}(\mathrm{P}(B)_i).\end{aligned} \tag{4.35}$$

The $\mathrm{B_d}$ mass PDF, $P_{\mathrm{B_d}}(m_i)$, is determined from the fully-reconstructed $\mathrm{B_d}$ MC sample, with the pion track assigned a kaon mass to simulate a mis-reconstructed $\mathrm{B_s} \to \mathrm{J}/\psi\phi$ decay. The mis-reconstructed $m(\mathrm{J}/\psi\mathrm{K}^+\mathrm{K}^-)$ mass from events passing fiducial, trigger, and $\mathrm{B_s} \to \mathrm{J}/\psi\phi$ selection cuts are fitted with a Landau [41] function convoluted with a Gaussian, and the shape fixed for use in the $\mathrm{B_s} \to \mathrm{J}/\psi\phi$ fit to data. The mis-reconstructed $m(\mathrm{J}/\psi\mathrm{K}^+\mathrm{K}^-)$ mass distribution and the fitted PDF are shown in fig. 4.16(a).

The $\mathrm{B_d}$ proper decay time PDF, $P_{\mathrm{B_d}}(t_i|\sigma_{t_i})$, is a single positive exponential convoluted by a per-candidate Gaussian, with the $\mathrm{B_d}$ lifetime fixed to the world average and scaled by the ratio of the $\mathrm{B_d}$ and $\mathrm{B_s}$ world average masses[13] as listed in [146].

The $\mathrm{B_d}$ transversity angle PDF, $P_{\mathrm{B_d}}(\Omega_i|p_{\mathrm{T}i})$, is obtained from the generator level MC. Fiducial, trigger, and $\mathrm{B_s} \to \mathrm{J}/\psi\phi$ selection cuts after a wrong

---

[13] This scaling corrects for the incorrect $\mathrm{B_s}$ mass hypothesis introduced by eq. (4.13).

mass assignment are applied and consistency checks between this sample and the fully-reconstructed sample are used to ensure that the use of generator level MC does not introduce any additional biases in the angular distributions (see fig. 4.10). The generator level MC is generated with flat transversity angle distributions, so a re-weighting using the transversity amplitudes measured in [167] is performed. This re-weighting uses only the P-wave amplitudes and their interference terms. The S-wave contribution from non-resonant $\mathrm{B_d} \to \mathrm{J}/\psi\mathrm{K}^+\pi^-$ decays and their interference terms is considered as a systematic effect (section 4.5.3.2). The re-weighted $\mathrm{B_d} \to \mathrm{J}/\psi\mathrm{K}^{*0}$ sample, with half of the selected events used to simulate the charge-conjugate decay, is then fitted using the spherical harmonic fit used for the combinatorial background as described in section 4.4.5.3 and the spherical harmonics fixed for use in the $\mathrm{B_s} \to \mathrm{J}/\psi\phi$ fit to data. 1D and 2D projections of the re-weighted sample after cuts and their fitted spherical harmonics are shown in **??**.

The background Punzi PDFs, $P_{\mathrm{Bck}}(\sigma_{t_i})$, $P_{\mathrm{Bck}}(p_{\mathrm{T}i})$, and $P_{\mathrm{Bck}}(\mathrm{P}(B)_i)$ are common between the combinatorial and physics background PDFs and are described in section 4.4.6.

4.4.4.2 $\Lambda_\mathrm{b} \to \mathrm{J}/\psi\mathrm{pK}^-$ Background

A single generator level MC sample was produced for studies of the $\Lambda_\mathrm{b} \to \mathrm{J}/\psi\mathrm{pK}^-$ background contamination, with a subset of this sample processed through the full-reconstruction tool-chain. The Λ_b events were generated as $\Lambda_\mathrm{b} \to \mathrm{J}/\psi\mathrm{pK}^-$ non-resonant, and re-weighted at the generator level to match the $m(\mathrm{pK}^-)$ mass distribution given in [168], of interest to the $\mathrm{B_s} \to \mathrm{J}/\psi\phi$ default fit are the contributions from $\Lambda^0_\mathrm{b}(1520)$, $\Lambda^0_\mathrm{b}(1600)$, $\Lambda^0_\mathrm{b}(1670)$, and $\Lambda^0_\mathrm{b}(1690)$ decays, as higher mass resonances are mostly excluded by $\mathrm{B_s} \to \mathrm{J}/\psi\phi$ event selection cuts. The generated $m(\mathrm{pK}^-)$ spectra before and after re-weighting are shown in fig. 4.13.

The $\Lambda_\mathrm{b} \to \mathrm{J}/\psi\mathrm{pK}^-$ background PDF has the following composition:

$$\begin{aligned}\mathcal{F}_{\Lambda_\mathrm{b}} = \; & P_{\Lambda_\mathrm{b}}(m_i) \cdot P_{\Lambda_\mathrm{b}}(t_i|\sigma_{t_i}) \cdot P_{\Lambda_\mathrm{b}}(\Omega_i|p_{\mathrm{T}i}) \\ & \cdot P_{\mathrm{Bck}}(\sigma_{t_i}) \cdot P_{\mathrm{Bck}}(p_{\mathrm{T}i}) \cdot P_{\mathrm{Bck}}(\mathrm{P}(B)_i).\end{aligned} \tag{4.36}$$

The Λ_b mass PDF, $P_{\Lambda_\mathrm{b}}(m_i)$, is obtained from the fully reconstructed $\Lambda_\mathrm{b} \to \mathrm{J}/\psi\mathrm{pK}^-$ MC sub-sample. Fiducial, trigger, and $\mathrm{B_s} \to \mathrm{J}/\psi\phi$ selection cuts were applied after a wrong mass assignment and the resultant mis-reconstructed $m(\mathrm{J}/\psi\mathrm{K}^+\mathrm{K}^-)$ mass distribution binned in 40 bins covering the mass range 5.150 GeV to 5.650 GeV. Due to the limited MC statistics available, a numeric

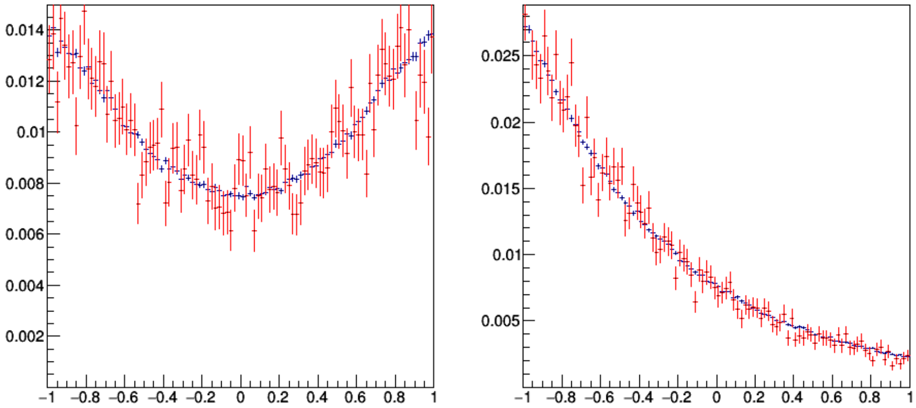

(a) $\cos(\theta_{\mathrm{K}})$ (b) $\cos(\theta_{\ell})$

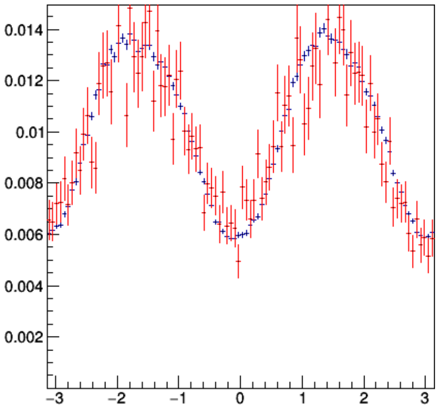

(c) ϕ_{H}

Figure 4.10: $\mathrm{B_d} \to \mathrm{J}/\psi\mathrm{K}^{*0}$ helicity angle distributions. Shown are generator level MC (blue) and reconstructed (red) distributions for the helicity angles of mis-reconstructed $\mathrm{B_d} \to \mathrm{J}/\psi\mathrm{K}^{*0}$ decays. The MC sample contains only $\mathrm{B_d^0}$ mesons, with neutral meson oscillation disabled during the MC generation, and this produces the asymmetry seen in the $\cos(\theta_\ell)$ helicity angle distribution.

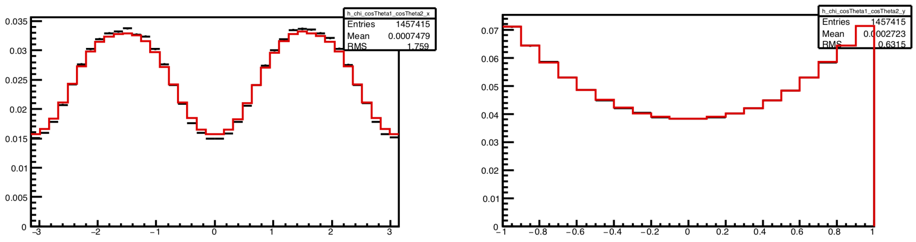

(a) ϕ_{T} (b) $\cos(\theta_{\mathrm{T}})$

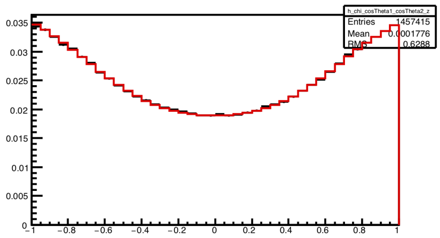

(c) $\cos(\psi_{\mathrm{T}})$

Figure 4.11: Transversity angle fit projections for ϕ_{T} (top-left), $\cos(\theta_{\mathrm{T}})$ (top-right), and $\cos(\psi_{\mathrm{T}})$ (bottom) for $\mathrm{B_d} \to \mathrm{J}/\psi\mathrm{K}^{*0}$ MC events mis-reconstructed as $\mathrm{B_s} \to \mathrm{J}/\psi\phi$ decays. Show are the 1D projections for MC events (black) and the $\mathrm{B_d}$ transversity angle PDF (red).

smoothing procedure (the '353 Running Medians' method of [169]) is applied before a second-order histogram-based interpolation PDF [104] is fitted to the binned data. This PDF is fixed for use in the $\mathrm{B_s} \to \mathrm{J}/\psi\phi$ fit to data. The mis-reconstructed $m(\mathrm{J}/\psi\mathrm{K}^{+}\mathrm{K}^{-})$ mass distribution and the fitted PDF are shown in fig. 4.16(b).

The Λ_{b} proper decay time PDF, $P_{\Lambda_{\mathrm{b}}}(t_i|\sigma_{t_i})$, is a single positive exponential convoluted by a per-candidate Gaussian, with the Λ_{b} lifetime fixed to the world average and scaled by the ratio of the Λ_{b} and $\mathrm{B_s}$ world average masses as listed in [146].

The Λ_{b} transversity angle PDF, $P_{\Lambda_{\mathrm{b}}}(\Omega_i|p_{\mathrm{T}i})$, is obtained from the generator level MC as no biasing of the transversity angles during reconstruction is observed. The MC was generated with flat transversity angle distributions and fitted using the spherical harmonic fit used for the combinatorial background as described in section 4.4.5.3 after fiducial, trigger, and $\mathrm{B_s} \to \mathrm{J}/\psi\phi$ selection cuts with a wrong mass assignment. Half of the selected events were used to simulate the charge-conjugate decay by swapping the charges on the pK^{-}

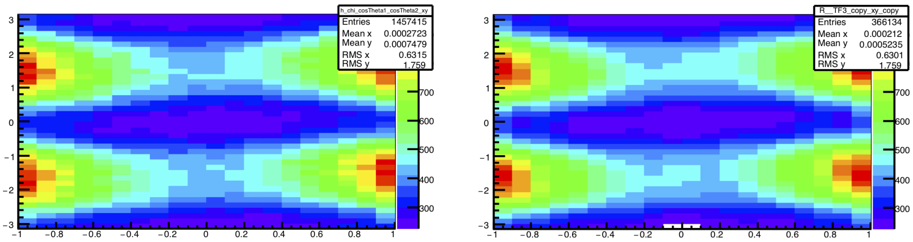

(a) ϕ_{T} v's $\cos(\theta_{\mathrm{T}})$, $\mathrm{B_d} \to \mathrm{J}/\psi\mathrm{K}^{*0}$ MC

(b) ϕ_{T} v's $\cos(\theta_{\mathrm{T}})$, $\mathrm{B_d}$ transversity angle PDF

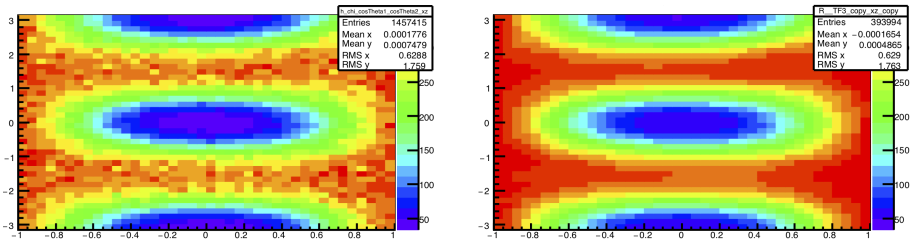

(c) ϕ_{T} v's $\cos(\psi_{\mathrm{T}})$, $\mathrm{B_d} \to \mathrm{J}/\psi\mathrm{K}^{*0}$ MC

(d) ϕ_{T} v's $\cos(\psi_{\mathrm{T}})$, $\mathrm{B_d}$ transversity angle PDF

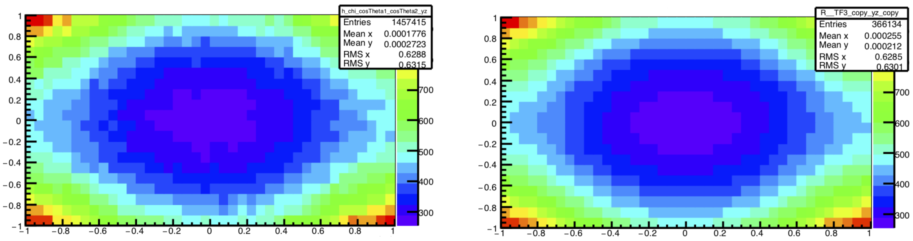

(e) $\cos(\theta_{\mathrm{T}})$ v's $\cos(\psi_{\mathrm{T}})$, $\mathrm{B_d} \to \mathrm{J}/\psi\mathrm{K}^{*0}$ MC

(f) $\cos(\theta_{\mathrm{T}})$ v's $\cos(\psi_{\mathrm{T}})$, $\mathrm{B_d}$ transversity angle PDF

Figure 4.12: Transversity angle fit projections for ϕ_{T} v's $\cos(\theta_{\mathrm{T}})$ (top), ϕ_{T} v's $\cos(\psi_{\mathrm{T}})$ (middle), and $\cos(\theta_{\mathrm{T}})$ v's $\cos(\psi_{\mathrm{T}})$ (bottom) for $\mathrm{B_d} \to \mathrm{J}/\psi\mathrm{K}^{*0}$ MC events mis-reconstructed as $\mathrm{B_s} \to \mathrm{J}/\psi\phi$ decays (left) and the $\mathrm{B_d}$ transversity angle PDF (right). A 3D histogram of the mis-reconstructed MC events is normalised to unity for compatibility with the fitted spherical harmonic PDF before the projections are formed. For each projections the the abscissa represents the independent component of the projection (see [102]).

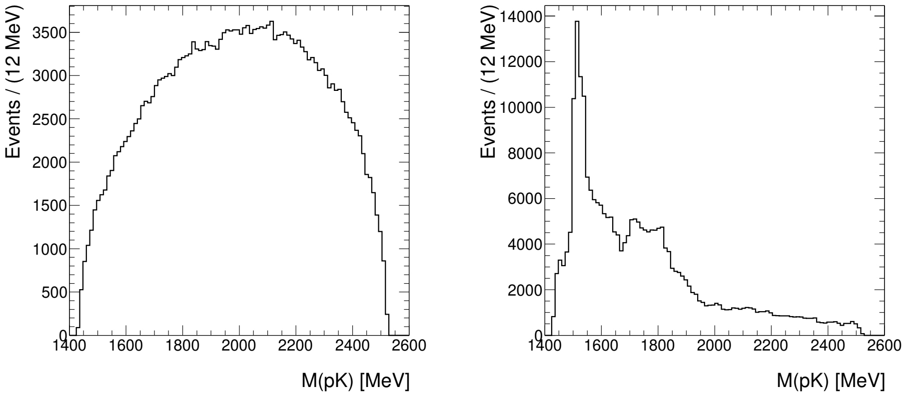

(a) Generated MC

(b) Re-weighted MC

Figure 4.13: $m(\mathrm{pK}^-)$ for the $\Lambda_\mathrm{b} \to \mathrm{J}/\psi\mathrm{pK}^-$ physics background. Significant contributions are observed for $\Lambda_\mathrm{b}^0(1520)$, $\Lambda_\mathrm{b}^0(1600)$, $\Lambda_\mathrm{b}^0(1690)$, and $\Lambda_\mathrm{b}^0(1810)$ decays.

decay products. The spherical harmonics are fixed for use in the $\mathrm{B_s} \to \mathrm{J}/\psi\phi$ fit to data. Alternative Λ_b transversity angle distributions are considered as systematic variations in section 4.5.3.3.

The background Punzi PDFs, $P_\mathrm{Bck}(\sigma_{t_i})$, $P_\mathrm{Bck}(p_{\mathrm{T}i})$, and $P_\mathrm{Bck}(\mathrm{P}(B)_i)$ are common between the combinatorial and physics background PDFs and are described in section 4.4.6.

4.4.4.3 Observations on the Physics Backgrounds Models in the 7 TeV and 8 TeV Analyses

ϵ_{K^*} and $\epsilon_{\mathrm{K}^+\pi^-}$ differ from their equivalents in [127, 143] by more than 1σ. This has been traced to a number of errors in the 7 TeV analyses:

- MC re-weighting was used in the 7 TeV analyses to correct some branching fractions as coded into `Pythia`, this procedure had been performed incorrectly, and resulted in a significant under-estimation of the $\mathrm{B_s}$ selection efficiencies;
- The $\mathrm{BR}(\phi \to \mathrm{K}^+\mathrm{K}^-)$ terms from eq. (4.34) had been omitted from the calculation. This error had been carried through into early versions of the $\mathrm{B_s} \to \mathrm{J}/\psi\phi$ default fit.

In addition to these errors, a change in the modelling of the K^{*0} line-shape in the low mass region introduces a difference between $\mathrm{B_d} \to \mathrm{J}/\psi\mathrm{K}^{*0}$ selec-

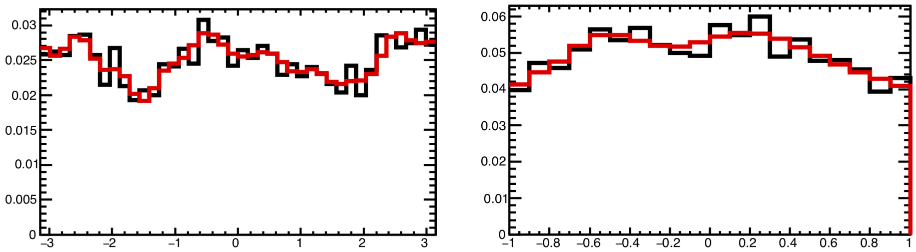

(a) ϕ_{T} (b) $\cos(\theta_{\mathrm{T}})$

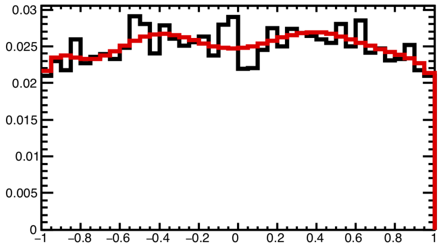

(c) $\cos(\psi_{\mathrm{T}})$

Figure 4.14: Transversity angle fit projections for ϕ_{T} (top-left), $\cos(\theta_{\mathrm{T}})$ (top-right), and $\cos(\psi_{\mathrm{T}})$ (bottom) for $\Lambda_{\mathrm{b}} \to \mathrm{J}/\psi \mathrm{p}\mathrm{K}^-$ MC events mis-reconstructed as $\mathrm{B_s} \to \mathrm{J}/\psi\phi$ decays. Show are the 1D projections for MC events (black) and the Λ_{b} transversity angle PDF (red).

tion efficiencies based on MC11 and MC12 MC (a factor of ≈1.5). As only $\mathrm{B_d} \to \mathrm{J}/\psi\mathrm{K}^{*0}$ events with low-mass K^{*0} are mis-reconstructed as $\mathrm{B_s} \to \mathrm{J}/\psi\phi$ events (due to the $m(\mathrm{K}^+\mathrm{K}^-)$ mass selection cuts as listed in section 4.2.2.3, after the wrong mass assignment of the $\pi^\pm$, see fig. 4.17(a)), changes in the nominal mass, width, and lower mass cut-off of the K^{*0} particle in `Pythia` result in a significant systematic difference between the 7 TeV and 8 TeV analyses. The $m(\mathrm{K}^+\pi^-)$ distributions for MC11 and MC12 based MC samples are shown in fig. 4.17(b).

The modelling of the S-wave, and S- and P-wave interference in the $\mathrm{B_d}$ background component is taken from [167]. The $m(\mathrm{K}^+\pi^-)$ mass ranges of the $\mathrm{B_d}$ decays accepted into the $\mathrm{B_s} \to \mathrm{J}/\psi\phi$ dataset is shown to differ between the S- and P-wave components (fig. 4.18) and limits the utility of the current LHCb result. In addition, the $m(\mathrm{K}^+\pi^-)$ mass range of interest to the $\mathrm{B_s} \to \mathrm{J}/\psi\phi$ default fit, 650 MeV to 840 MeV, is not fully covered by the lowest mass bin reported by LHCb (826 MeV to 861 MeV). To estimate the systematic effects of using [167] as the model for S- and P-wave interference, additional $\mathrm{B_s} \to \mathrm{J}/\psi\phi$ fits are performed where A_{S} for the $\mathrm{B_d}$ decay is modeled using the selection effi-

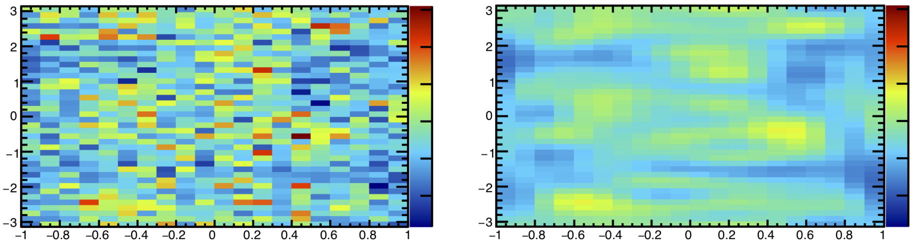

(a) $\cos(\theta_{\mathrm{T}})$, $\Lambda_{\mathrm{b}} \to \mathrm{J}/\psi\mathrm{pK}^-$ MC

(b) $\cos(\theta_{\mathrm{T}})$, Λ_{b} transversity angle PDF

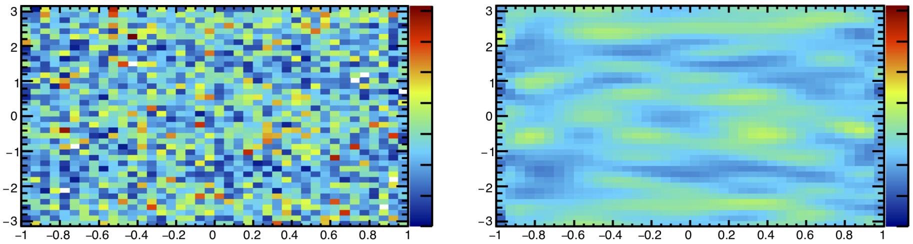

(c) ϕ_{T} v's $\cos(\psi_{\mathrm{T}})$, $\Lambda_{\mathrm{b}} \to \mathrm{J}/\psi\mathrm{pK}^-$ MC

(d) ϕ_{T} v's $\cos(\psi_{\mathrm{T}})$, Λ_{b} transversity angle PDF

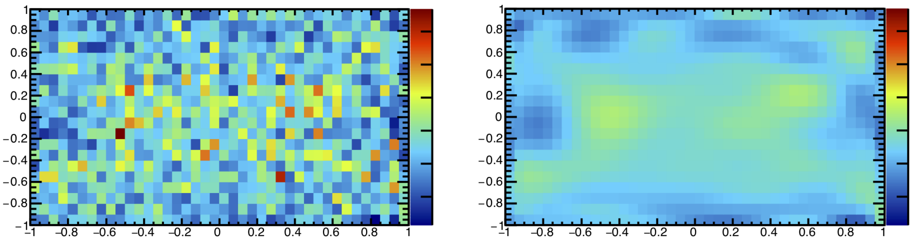

(e) $\cos(\theta_{\mathrm{T}})$ v's $\cos(\psi_{\mathrm{T}})$, $\Lambda_{\mathrm{b}} \to \mathrm{J}/\psi\mathrm{pK}^-$ MC

(f) $\cos(\theta_{\mathrm{T}})$ v's $\cos(\psi_{\mathrm{T}})$, Λ_{b} transversity angle PDF

Figure 4.15: Transversity angle fit projections for ϕ_{T} v's $\cos(\theta_{\mathrm{T}})$ (top), ϕ_{T} v's $\cos(\psi_{\mathrm{T}})$ (middle), and $\cos(\theta_{\mathrm{T}})$ v's $\cos(\psi_{\mathrm{T}})$ (bottom) for $\Lambda_{\mathrm{b}} \to \mathrm{J}/\psi\mathrm{pK}^-$ MC events mis-reconstructed as $\mathrm{B_s} \to \mathrm{J}/\psi\phi$ decays (left) and the Λ_{b} transversity angle PDF (right).

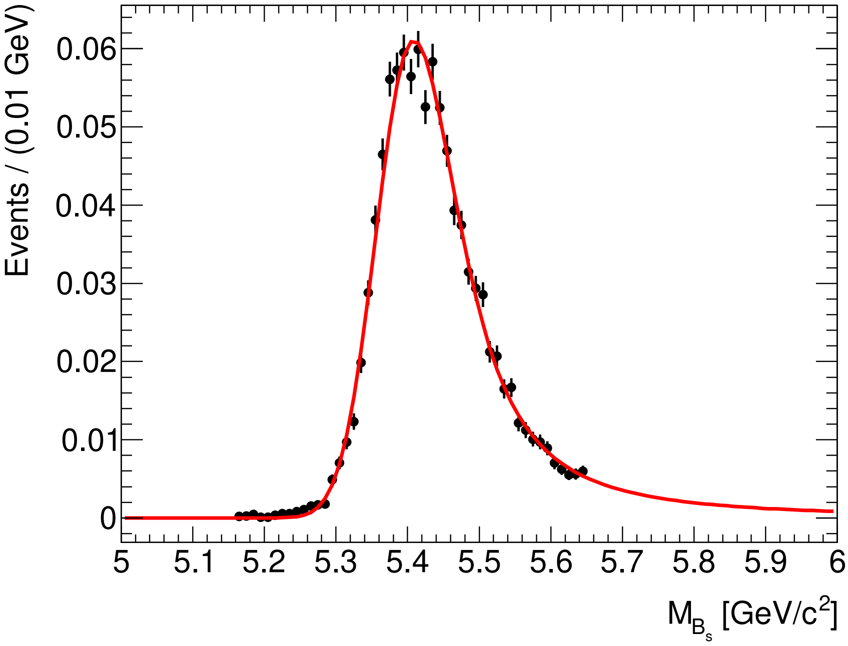

(a) $\mathrm{B_d} \to \mathrm{J}/\psi \mathrm{K}^{*0}$

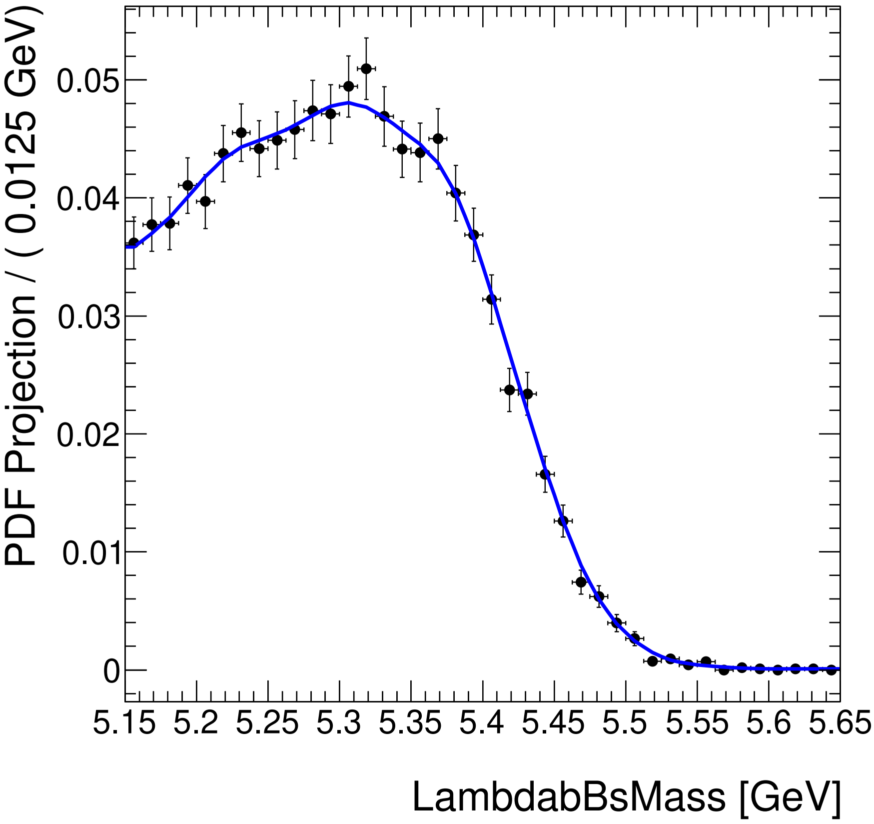

(b) $\Lambda_\mathrm{b} \to \mathrm{J}/\psi \mathrm{p}\mathrm{K}^-$

Figure 4.16: $m(\mathrm{J}/\psi \mathrm{K}^+\mathrm{K}^-)$ for physics background components.

cencies determined from ATLAS MC studies, and relative production fractions as given in [133].

4.4.5 Combinatorial Background

The combinatorial background PDF has the following composition:

$$\begin{aligned} \mathcal{F}_{\mathrm{Bck}} = \; & P_{\mathrm{Bck}}(m_i) \cdot P_{\mathrm{Bck}}(t_i|\sigma_{t_i}) \cdot P_{\mathrm{Bck}}(\Omega_i|p_{\mathrm{T}i}) \\ & \cdot P_{\mathrm{Bck}}(\sigma_{t_i}) \cdot P_{\mathrm{Bck}}(p_{\mathrm{T}i}) \cdot P_{\mathrm{Bck}}(\mathrm{P}(B)_i) \end{aligned} \tag{4.37}$$

and models the mass, proper decay time, and transversity angle distributions for the combinatorial background.

The background Punzi PDFs, $P_{\mathrm{Bck}}(\sigma_{t_i})$, $P_{\mathrm{Bck}}(p_{\mathrm{T}i})$, and $P_{\mathrm{Bck}}(\mathrm{P}(B)_i)$ are common between the combinatorial and physics background PDFs and are described in section 4.4.6.

4.4.5.1 Mass PDF

The combinatorial background mass PDF, $P_{\mathrm{Bck}}(m_i)$, is formed from an exponential decay and a constant function, with the exponential decay constant and fractions of the components determined from the $\mathrm{B_s} \to \mathrm{J}/\psi\phi$ fit to data.

4.4.5.2 Proper Decay Time PDF

The combinatorial background proper decay time PDF, $P_{\mathrm{Bck}}(t_i|\sigma_{t_i})$, is composed of a Gaussian with a fixed mean at $t = 0$ and a per-candidate standard deviation, two exponential decays for positive proper decay time events, and a single exponential decay for negative proper decay time events. Each of the exponential components is convoluted by a per-candidate Gaussian. The fixed Gaussian accommodates prompt $\mathrm{J}/\psi \to \mu^+\mu^-$ decays matched with two tracks from the production PV mis-reconstructed as $\mathrm{B_s} \to \mathrm{J}/\psi\phi$ candidates, the $t \geq 0$ exponentials model mis-reconstructed long-lived backgrounds, while the $t \leq 0$ exponential fits events with poor PV resolution or a mis-matched PV. The exponential decay constants and the relative fractions are fitted in the $\mathrm{B_s} \to \mathrm{J}/\psi\phi$ fit to data.

4.4.5.3 Transversity Angle PDF

Transversity angle distributions are modelled using a p_{T}-dependent spherical harmonic [41] based description. The functions, $K_{k,l,m}(\Omega)$, are defined as

$$K_{k,l,m}(\Omega) = \sqrt{2} \cdot P_k(\cos(\psi_{\mathrm{T}})) \cdot Y_l^m(\theta_{\mathrm{T}}) \tag{4.38}$$

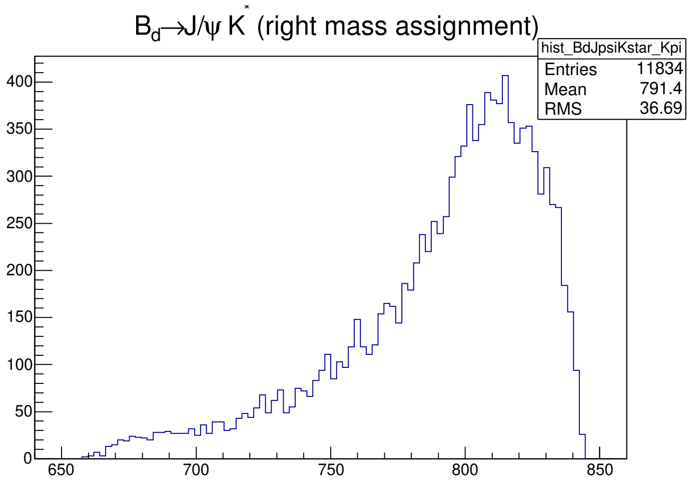

(a) $\mathrm{B_d} \to \mathrm{J}/\psi\mathrm{K}^{*0}$

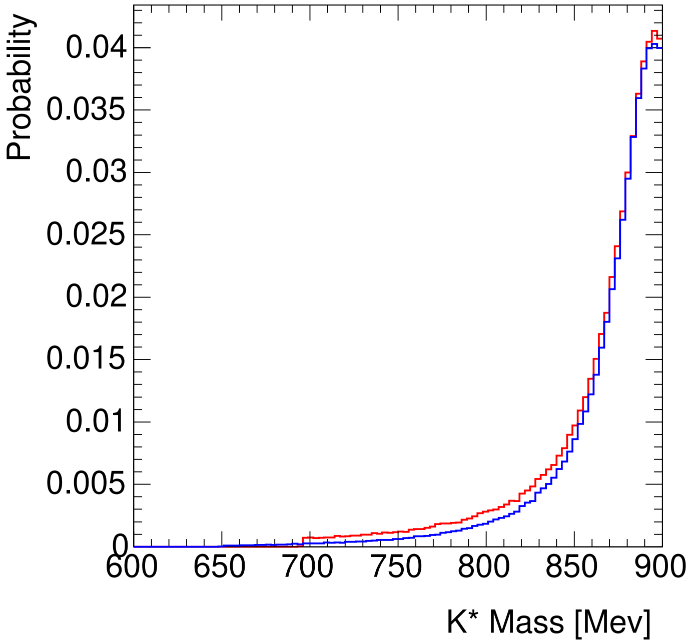

(b) MC Generated K^{*0} line-shapes

Figure 4.17: $m(\mathrm{K}^+\pi^-)$ for $\mathrm{B_d} \to \mathrm{J}/\psi\mathrm{K}^{*0}$ MC events selected after mis-reconstruction as $\mathrm{B_s} \to \mathrm{J}/\psi\phi$ events (top) and as generated (bottom) for MC11 (red) and MC12 (blue). MC11 and MC12 events are normalised to unit area. The $m(\mathrm{K}^+\pi^-)$ mass range of interest for $\mathrm{B_s} \to \mathrm{J}/\psi\phi$ event selection is between 650 MeV to 850 MeV.

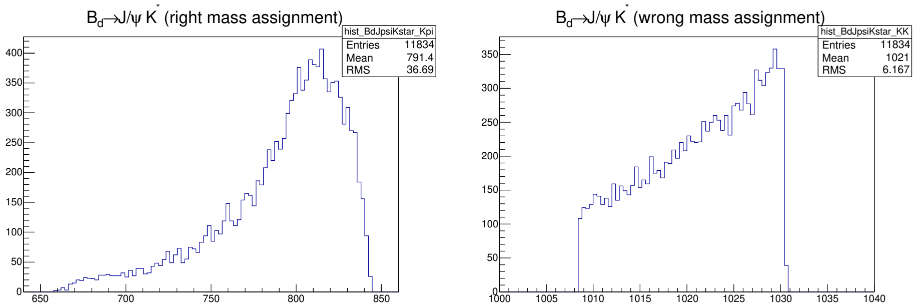

(a) $\mathrm{B_d} \to \mathrm{J}/\psi\mathrm{K}^{*0}$, $m(\mathrm{K}^+\pi^-)$ [MeV] (b) $\mathrm{B_d} \to \mathrm{J}/\psi\mathrm{K}^{*0}$, $m(\mathrm{K}^+\mathrm{K}^-)$ [MeV]

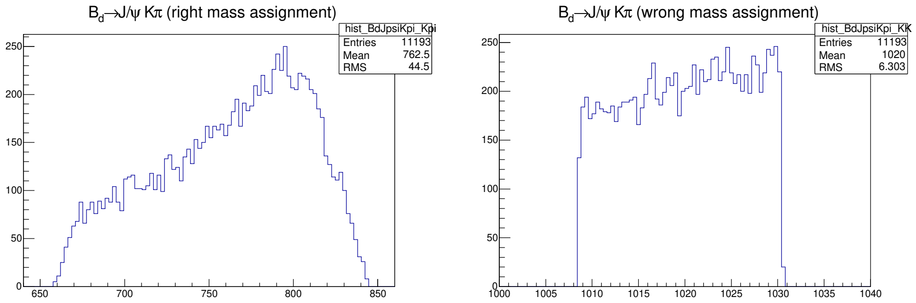

(c) $\mathrm{B_d} \to \mathrm{J}/\psi\mathrm{K}^+\pi^-$, $m(\mathrm{K}^+\pi^-)$ [MeV] (d) $\mathrm{B_d} \to \mathrm{J}/\psi\mathrm{K}^+\pi^-$, $m(\mathrm{K}^+\mathrm{K}^-)$ [MeV]

Figure 4.18: $\mathrm{B_d}$ background mass distributions for the $m(\mathrm{K}^+\pi^-)$ mass (left) and mis-reconstructed $m(\mathrm{K}^+\mathrm{K}^-)$ masses (right) after $\phi \to \mathrm{K}^+\mathrm{K}^-$ selection cuts of $\mathrm{B_d} \to \mathrm{J}/\psi\mathrm{K}^{*0}$ (top) and $\mathrm{B_d} \to \mathrm{J}/\psi\mathrm{K}^+\pi^-$ (bottom) events .

and formed from the associated Legendre polynomials [41]

$$P_k(x) = \frac{1}{2^k \cdot k!}\frac{\mathrm{d}^k}{\mathrm{d}x^k}(x^2-1)^k \tag{4.39a}$$

$$Y_l^m(x) = \sqrt{\frac{(2l+1)}{4\pi}} \cdot \sqrt{\frac{(l-|m|)!}{(l+|m|)!}} \cdot P_k^{|m|}(\cos(x)) \tag{4.39b}$$

resulting in the spherical harmonic functions

$$P_{\mathrm{Bck}}(\Omega_i|p_{\mathrm{T}i}) = \sum_{k=0}^{6}\sum_{l=0}^{6}\sum_{m=-l}^{l} \begin{cases} a_{k,l,m} \cdot K_{k,l,m}(\Omega) \cdot \cos(m \cdot \phi_{\mathrm{T}}) & m > 0 \\ a_{k,l,m} \cdot K_{k,l,m}(\Omega) & m = 0 \\ a_{k,l,m} \cdot K_{k,l,m}(\Omega) \cdot \sin(m \cdot \phi_{\mathrm{T}}) & m < 0 \end{cases} \tag{4.40}$$

where the coefficients $a_{k,l,m}$ are adjusted to describe the data using a numerical integration to form an inner product. Normalisation is performed by a re-scaling of the $a_{k,l,m}$ factors after the fit to data.

The p_T-dependence of the detector angular acceptance is absorbed into the transversity angles PDF by fitting the data in four $p_\mathrm{T}(\mathrm{B_s})$-dependent subsamples of 0 GeV to 13 GeV, 13 GeV to 18 GeV, 18 GeV to 25 GeV, and >25 GeV.

The combinatorial background transversity angle distribution is fit from events in the $\mathrm{B_s} \to \mathrm{J}/\psi\phi$ data where $|m(\mathrm{J}/\psi\mathrm{K}^+\mathrm{K}^-) - 5.366\,\mathrm{GeV}| \geq 0.110\,\mathrm{GeV}$ and the spherical harmonics fixed for use in the $\mathrm{B_s} \to \mathrm{J}/\psi\phi$ fit to data. The cuts selecting the combinatorial background component are determined from the world average $\mathrm{B_s}$ mass as listed in [146], and the $m(\mathrm{J}/\psi\mathrm{K}^+\mathrm{K}^-)$ distribution obtained from MC studies.

4.4.6 Punzi Terms

Punzi terms are included in the default fit to allow the use of conditionally dependent PDFs to describe proper decay time uncertainty distributions (sections 4.4.3.3, 4.4.4.1, 4.4.4.2 and 4.4.5.2), the p_T dependence of detector acceptance (sections 4.4.3.1 and 4.4.5.3), and the flavour dependence of the signal components proper decay time–transversity angle distribution (section 4.4.3.3).

Distributions for the signal and background Punzi PDFs are obtained using a side-band extraction method. A mass fit of the $\mathrm{B_s} \to \mathrm{J}/\psi\phi$ data is performed using the signal and combinatorial background models described in sections 4.4.3.2 and 4.4.5.1, and the fitted signal mass model is used to define $m(\mathrm{J}/\psi\mathrm{K}^+\mathrm{K}^-)$ regions that exclude 99.7% of the signal component, with background distributions obtained from these regions. Signal distributions are obtained, after correction for the expected background contamination, from the $\pm 1\sigma$ region around the fitted $\mathrm{B_s}$ mass for the proper decay time uncertainty and p_T Punzi terms, and from the full dataset for the flavour tagging Punzi term.

4.4.6.1 Proper Decay Time Uncertainty

The proper decay time uncertainty Punzi PDFs are modelled as the sum of three Gamma distributions [41], with the fitted shape and scale parameters, and the relative fractions fixed for use in the $\mathrm{B_s} \to \mathrm{J}/\psi\phi$ fit to data. The signal and background Proper Decay Time uncertainty Punzi PDFs are shown in fig. 4.19(a).

4.4.6.2 p_T

The p_T Punzi PDFs are modelled as the sum of two Gamma distributions, with the fitted shape and scale parameters, and the relative fractions fixed for use

Tagging Method	Signal	Background
Combined muon	0.047 ± 0.003	0.038 ± 0.001
Electron	0.012 ± 0.001	0.008 ± 0.001
Segment-tagged muon	0.013 ± 0.001	0.015 ± 0.001
Jet-charge	0.135 ± 0.003	0.100 ± 0.001
Untagged	0.793 ± 0.002	0.839 ± 0.002

Table 4.12: Flavour tagging methods Punzi terms.

in the $\mathrm{B_s} \to \mathrm{J}/\psi\phi$ fit to data. The signal and background p_T Punzi PDFs are shown in fig. 4.19(b).

4.4.6.3 Flavour Tagging

The flavour tagging Punzi PDFs are constructed as the product of distributions describing the tagging method and tag probability for the discrete and continuous components of $\mathrm{P}(B|Q)$ as required. All flavour tagging Punzi terms and PDFs are fixed for use in the $\mathrm{B_s} \to \mathrm{J}/\psi\phi$ fit to data.

Flavour-tagging-method Punzi terms use the 'winner-takes-all' prioritisation described in section 4.3.2.4. Punzi terms for the tagging method and tag probability of the discrete components of $\mathrm{P}(B|Q)$, are obtained assuming a binomial distribution, with uncertainties reported at the 68.2% confidence level under a central limit approximation. The tagging method and tag probability Punzi terms are given in tables 4.12 and 4.13.

Tag probability Punzi PDFs (abstracting the continuous component of $\mathrm{P}(B|Q)$) for combined muon and electron tagged events are modelled as the sum of a positive and negative exponential, with a polynomial of fourth- or second-order respectively. Segment-tagged muon tagged events are modelled as the sum of three Gaussian distributions sharing a common mean, while jet-charge tagged events are described by an eighth-order polynomial. The fitted Punzi PDFs are shown in fig. 4.20.

The *Bayesian Information Criterion* (BIC) [170] and *Akaike Information Criterion* (AIC) [171] suggest the selected models that describe the combined muon and jet-charge tag probability Punzi PDFs are over-parameterised. Use of the BIC/AIC preferred models is considered as a systematic variation and discussed in section 4.5.1.2.

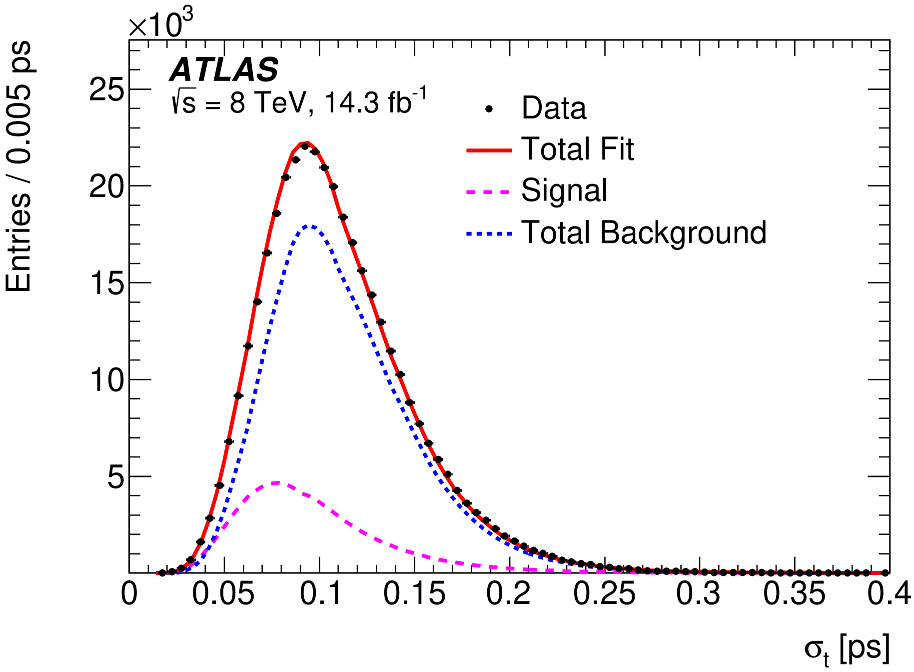

(a) Proper decay time uncertainty Punzi PDFs. Shown are the data distribution (black), signal (purple) and background (blue) Punzi PDFs, and the total fit (red).

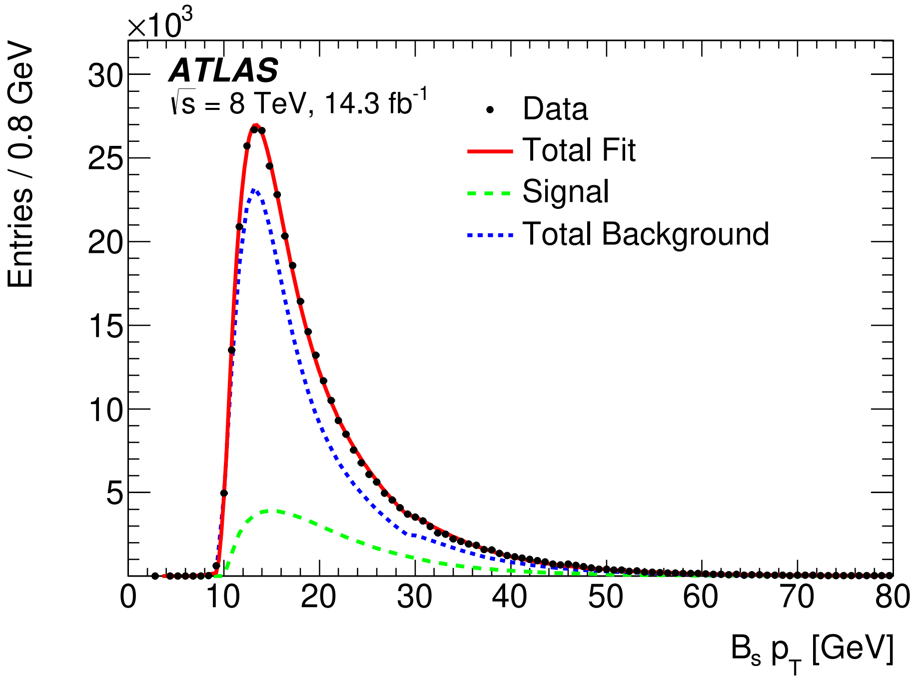

(b) p_{T} Punzi PDFs. Shown are the data distribution (black), signal (green) and background (blue) Punzi PDFs, and the total fit (red).

Figure 4.19: Proper decay time uncertainty (upper) and p_{T} (lower) Punzi PDFs.

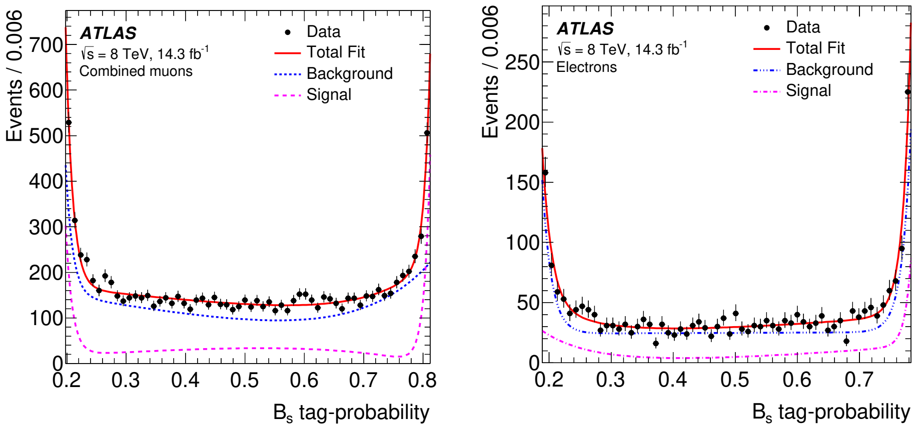

(a) Combined muon (b) Electron

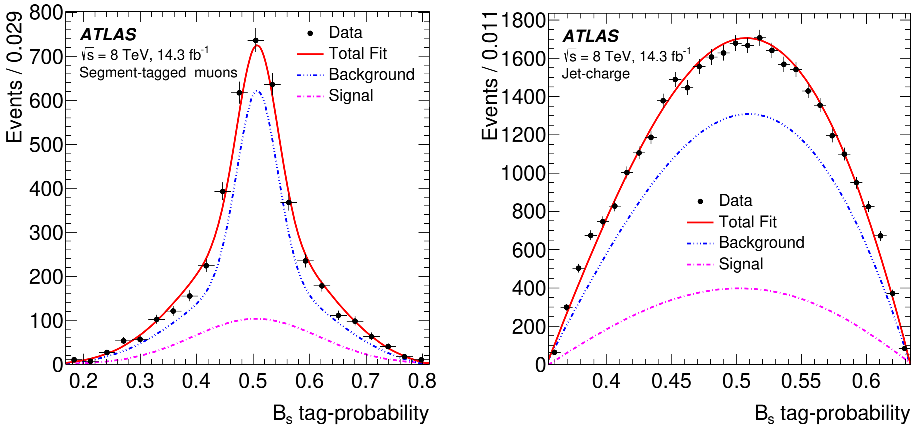

(c) Segment-tagged muon (d) Jet-charge

Figure 4.20: Flavour tag probability Punzi terms for combined muon (upper-left), electron (upper-right), segment-tagged muon (lower-left), and jet-charge (lower-right) based taggers. Shown are the flavour tag distributions for data (black), signal (purple) and background (blue) Punzi PDFs, and the total fit (red).

Tagging Method	Q_{-1}	Q_{+1}
Combined muon	0.124 ± 0.012	0.127 ± 0.012
Electron	0.105 ± 0.020	0.139 ± 0.021
Segment-tagged muon	0.147 ± 0.024	0.118 ± 0.023
Jet-charge	0.071 ± 0.005	0.069 ± 0.005

(a) Signal

Tag Method	Q_{-1}	Q_{+1}
Combined muon	0.093 ± 0.003	0.095 ± 0.003
Electron	0.110 ± 0.007	0.110 ± 0.007
Segment-tagged muon	0.083 ± 0.004	0.084 ± 0.004
Jet-charge	0.068 ± 0.002	0.069 ± 0.002

(b) Background

Table 4.13: Flavour tag probability Punzi terms for events with tagging charge $Q = -1$ (Q_{-1}) and $Q = +1$ (Q_{+1}).

4.4.7 Default Fit Results

Minimisation of the $\mathrm{B_s} \to \mathrm{J}/\psi\phi$ likelihood function (eq. (4.31)) is performed using `MINUIT` [103] within a custom `ROOT` [96] (version 5.34.19) framework. The MLE of the physics parameters of interest and their statistical uncertainties (as reported by the `HESSE` option of `MINUIT`) are shown in table 4.14 and the fit correlations are shown in table 4.15.

In addition to the physics parameters related to the $\mathrm{B_s} \to \mathrm{J}/\psi\phi$ decay, a number of parameters are used to validate the fit performance. The $\mathrm{B_s}$ mass is extracted from the fit, $(5.366\,58 \pm 0.000\,12)$ GeV, and is consistant with the world-average $\mathrm{B_s}$ mass given in [18][14], and the scale-factor used in the per-event proper decay time convolutions is consistant with unity (1.0333 ± 0.0029), as expected.

4.4.7.1 Fit Projections

Fit projections are used to examine possible mis-modelling between the $\mathrm{B_s} \to \mathrm{J}/\psi\phi$ default fit and data distributions. Mass and proper decay time fit projections are shown in fig. 4.21, and transversity angle fit projections are shown

---

[14] While the fitted $\mathrm{B_s}$ mass serves as a useful comparison to the world-average, it should not be considered as a result of the analysis. There is no consideration of possible systematic mass-scale mis-modelling due to p_{T}-resolution or ID mis-alignment effects.

Parameter	Fit Result
ϕ_s [rad]	-0.110 ± 0.082
$\Delta\Gamma_s$ [ps^{-1}]	0.101 ± 0.013
Γ_s [ps^{-1}]	0.676 ± 0.004
$\|A_0\|^2$	0.520 ± 0.004
$\|A_\parallel\|^2$	0.230 ± 0.005
$\|A_S\|^2$	0.097 ± 0.008
$\delta_\parallel$ [rad]	3.15 ± 0.10
$\delta_\perp$ [rad]	4.50 ± 0.45
$\delta_\perp - \delta_S$ [rad]	-0.08 ± 0.03

Table 4.14: Fit results for the $B_s \to J/\psi\phi$ default fit. Errors are statistical only.

	$\Delta\Gamma_s$	Γ_s	$\|A_0\|^2$	$\|A_\parallel\|^2$	$\|A_S\|^2$	$\delta_\parallel$	$\delta_\perp$	$\delta_\perp - \delta_S$
ϕ_s	0.097	−0.085	0.029	0.030	0.048	0.067	0.035	−0.008
$\Delta\Gamma_s$	1	−0.414	0.136	0.098	0.045	0.009	0.008	−0.011
Γ_s		1	−0.042	−0.119	0.167	−0.027	−0.009	0.018
$\|A_0\|^2$			1	−0.330	0.234	−0.011	0.007	0.014
$\|A_\parallel\|^2$				1	0.072	0.105	0.025	−0.018
$\|A_S\|^2$					1	−0.046	0.004	0.052
$\delta_\parallel$						1	0.158	−0.006
$\delta_\perp$							1	0.018

Table 4.15: Fit correlations for the $B_s \to J/\psi\phi$ default fit.

in fig. 4.22[15].

The possible mis-modelling in the low mass sideband shown in fig. 4.21(a) is considered as a possible systematic error in section 4.5.1.1.

4.4.7.2 1D Likelihood Scans

1D profile likelihood scans are performed on the physics parameters of interest (fig. 4.23), and used to confirm the statistical uncertainties returned by `MINUIT` as $-2\Delta\ln(\mathcal{L}) = 1$ is expected to correspond to the estimated 1σ confidence interval. There are small asymmetries in the likelihood scans, however at the level of one statistical σ, they are small compared to the statistical uncertainty of the parameters of interest, and therefore symmetric confidence intervals are

---

[15] The 'flat-topped' nature of the $\cos(\theta_T)$ fit projection is due to the p_T-dependence of the background distribution around $\cos(\theta_T) = \pm 1$, an effect neglected during the 7 TeV analysis.

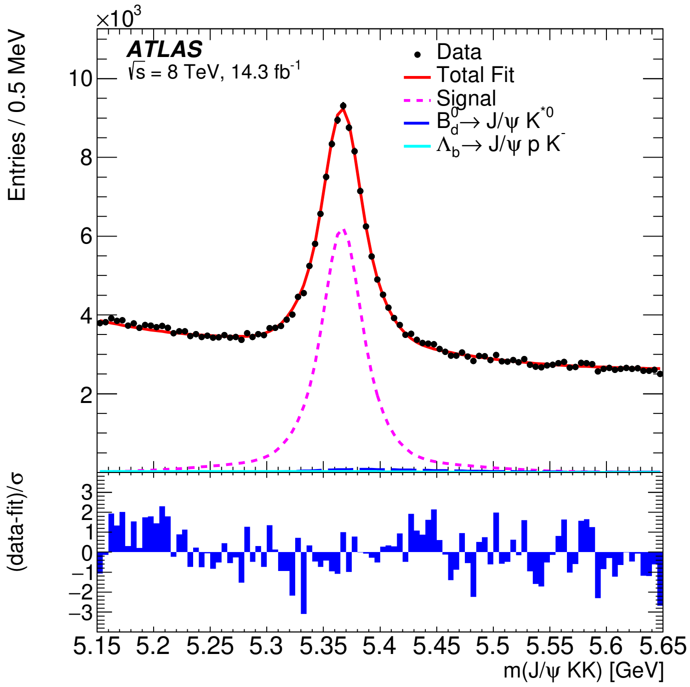

(a) Mass fit projection. Shown are the distributions for data (black), signal PDF (purple), physics background PDFs (blue and cyan), and the total fit (red).

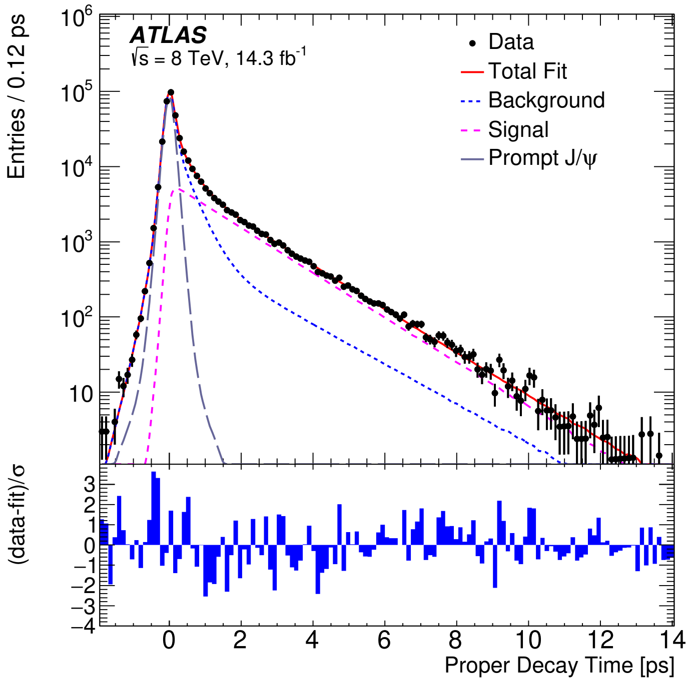

(b) Proper decay time fit projection. Shown are the distributions for data (black), signal PDF (purple), total background PDF and its prompt component (blue and grey respectively), and the total fit (red).

Figure 4.21: Fit projection for mass (top) and proper decay time (bottom) from the $\mathrm{B_s} \to \mathrm{J}/\psi\phi$ default fit. Pull distributions (blue) are shown below each fit.

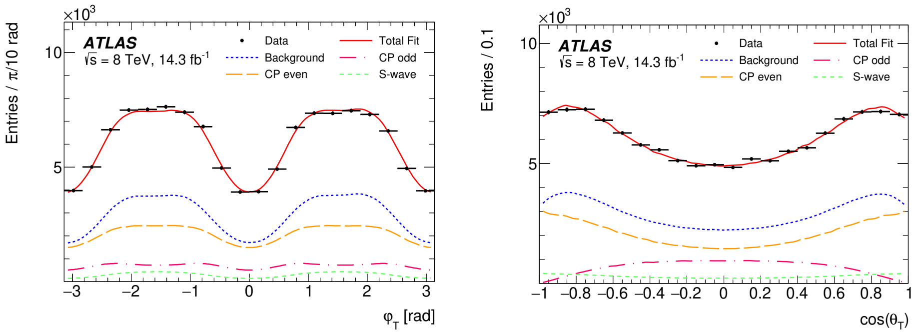

(a) ϕ_{T} (b) $\cos(\theta_{\mathrm{T}})$

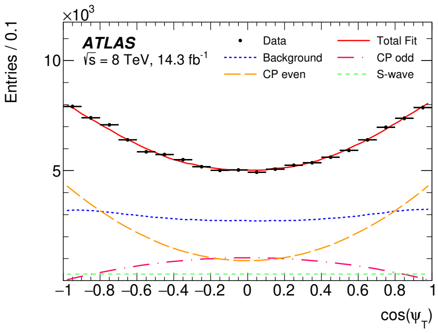

(c) $\cos(\psi_{\mathrm{T}})$

Figure 4.22: Transversity angle fit projections for ϕ_{T} (top-left), $\cos(\theta_{\mathrm{T}})$ (top-right), and $\cos(\psi_{\mathrm{T}})$ (bottom) from the $\mathrm{B_s} \to \mathrm{J}/\psi\phi$ Default Fit. Shown are the $\mathcal{CP}$-odd (pink), $\mathcal{CP}$-even (yellow), and S-wave (green) contributions to the signal PDF, as well as the background (blue) and total fit projections (red). The distribution for data (black) is taken from the signal-rich region where $5.317\,\mathrm{GeV} < m(\mathrm{J}/\psi\mathrm{K}^+\mathrm{K}^-) < 5.417\,\mathrm{GeV}$. Interference terms are negligible in these projections and are not shown. Figures from [128].

reported.

Due to the nature of the $\mathrm{B_s} \to \mathrm{J}/\psi\phi$ likelihood function (eq. (4.31)), there is the possibility that the `MINUIT` minimisation may converge to a secondary (non-global) minimum. The effects of these secondary minima are clearly shown in the 1D likelihood scans where `MINUIT` results alternate between minima, dependent on the fixed value of the scan parameter. To guard against this possibility, alternate $\mathrm{B_s} \to \mathrm{J}/\psi\phi$ fits are performed with the physics parameters (the P-wave strong phases) constrained around the global minimum identified in a modified 2D likelihood scan in the ϕ_s–$\Delta\Gamma_\mathrm{s}$ plane with `SIMPLEX` and `MIGRAD` minimisations performed to identify the 'nearest' [103] local minima.

Figure 4.24 shows 1D scans, obtained during the development of the default fit, displaying the effects of converging to secondary minima (figs. 4.24(a) and 4.24(c)), and the scans obtained after updates to the 1D scan software (figs. 4.24(b) and 4.24(d)).

4.4.7.3 2D Likelihood Scans

A 2D profile likelihood scan is performed in the ϕ_s–$\Delta\Gamma_\mathrm{s}$ plane for comparison against SM predictions [172]. Figure 4.25 shows the result of this scan and the 68 % and 95 % confidence limit contours. At the scale of the plot the statistical uncertainty on the SM prediction for ϕ_s, -0.036 ± 0.002 as given by [172], is not visible.

The scan is performed on a 101×101 grid in the ϕ_s–$\Delta\Gamma_\mathrm{s}$ plane with confidence limit contours extracted from the resultant 2D histogram.

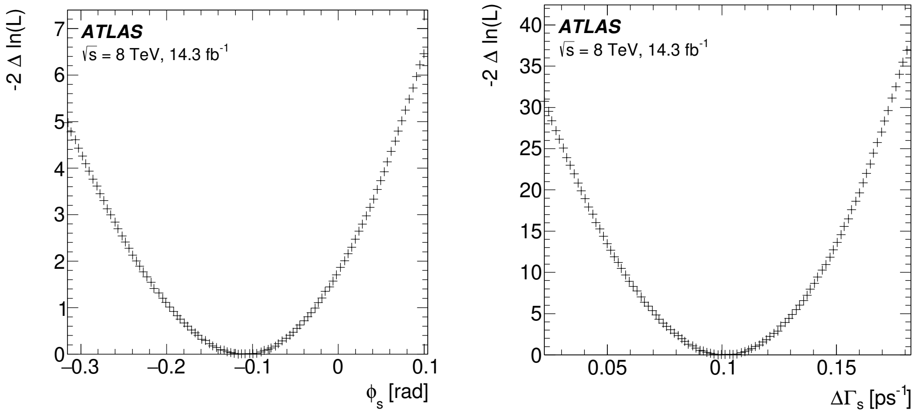

(a) ϕ_s (b) $\Delta\Gamma_\mathrm{s}$

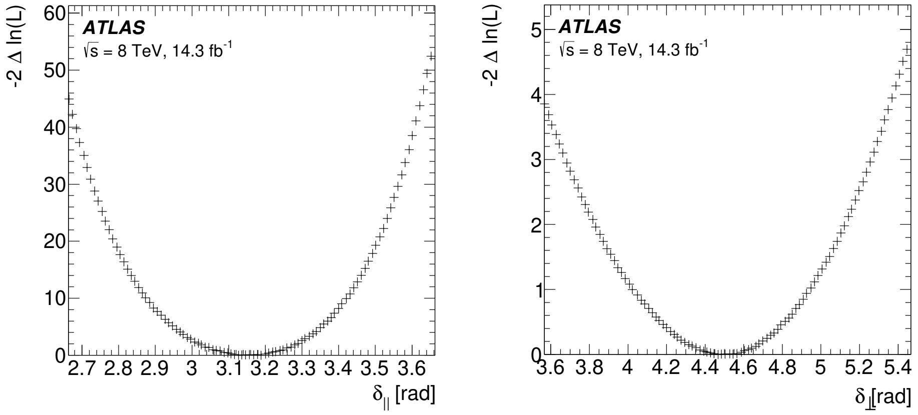

(c) $\delta_{||}$ (d) $\delta_\perp$

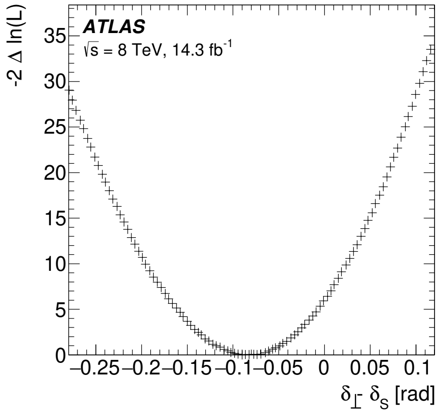

(e) $\delta_\perp - \delta_\mathrm{S}$

Figure 4.23: 1D Likelihood Scans for ϕ_s and $\Delta\Gamma_\mathrm{s}$ (upper left and right), $\delta_{||}$ and $\delta_\perp$ (centre left and right), and $\delta_\perp - \delta_\mathrm{S}$ (bottom) from the $\mathrm{B_s} \to \mathrm{J}/\psi\phi$ default fit.

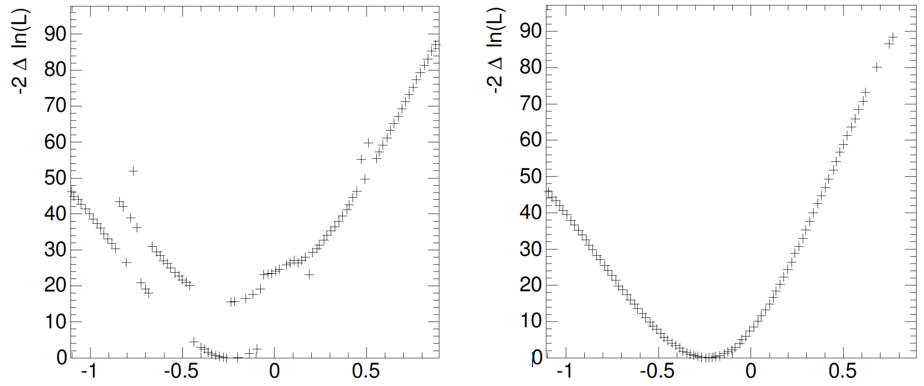

(a) ϕ_s, Preliminary (b) ϕ_s, Updated

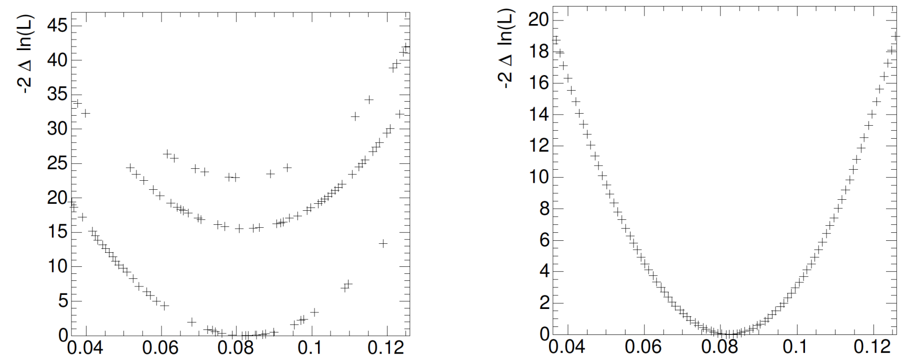

(c) $\Delta\Gamma_\mathrm{s}$, Preliminary (d) $\Delta\Gamma_\mathrm{s}$, Updated

Figure 4.24: 1D profile likelihood scans produced during the development of the $\mathrm{B_s} \to \mathrm{J}/\psi\phi$ default fit showing evidence of multiple minima. Shown are the preliminary scans (left), and the corrected scans (right) after software updates for ϕ_s (top) and $\Delta\Gamma_\mathrm{s}$ (bottom).

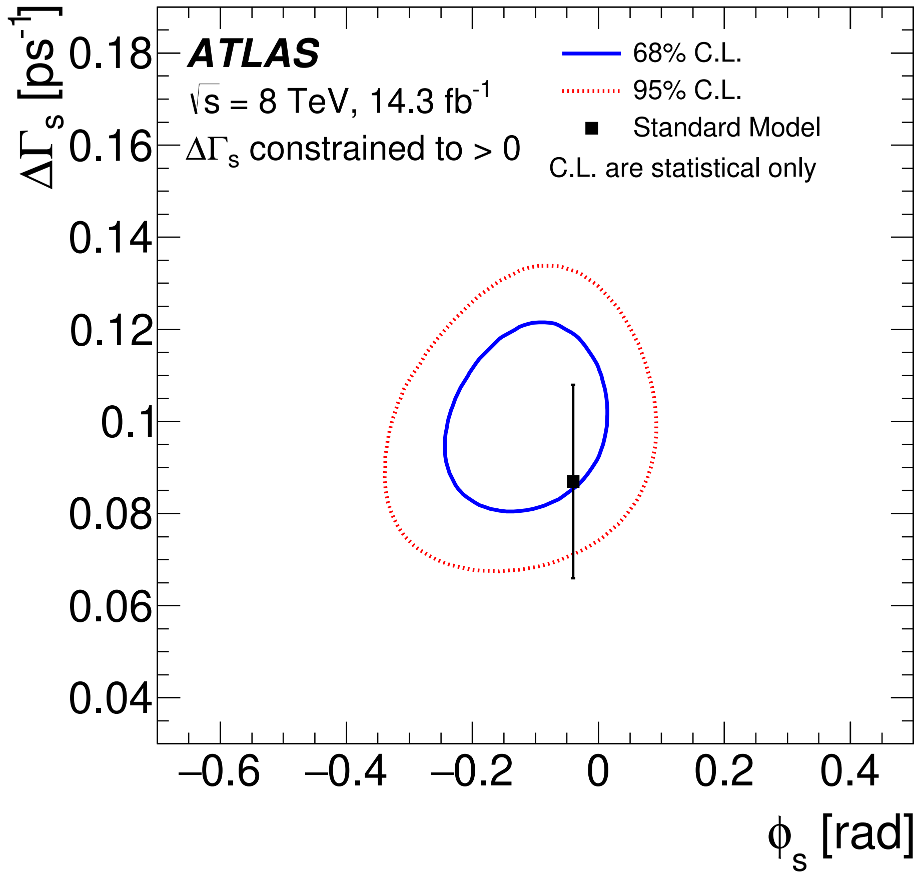

Figure 4.25: 2D profile likelihood scans in the ϕ_s–$\Delta\Gamma_s$ plane from the $B_s \to J/\psi\phi$ default fit. Shown are the 68 % and 95 % confidence limits (blue and red respectively) and the SM prediction [172] (black).

4.5 Stability Tests and Systematic Errors

Systematic uncertainties are assigned by considering effects that are not accounted for in the $\mathrm{B_s} \rightarrow \mathrm{J}/\psi\phi$ default fit. Validation of the $\mathrm{B_s} \rightarrow \mathrm{J}/\psi\phi$ default fit and the stability of the performance of the fit under alternative assumptions are given in section 4.5.1. The use of alternative models to describe the signal and combinatorial background components of the dataset are shown in sections 4.5.2.1 and 4.5.2.2, while systematic effects due to the physics background components and flavour tagging modelling are examined in sections 4.5.3 and 4.5.4.

The final 8 TeV results are presented in section 4.5.5.

4.5.1 Stability Tests

Stability tests are performed to examine the performance of the $\mathrm{B_s} \rightarrow \mathrm{J}/\psi\phi$ default fit under alternative assumptions of the fitted dataset.

4.5.1.1 Event Selection and Trigger Re-weightings

Due to the large combinatorial background content of the $\mathrm{B_s} \rightarrow \mathrm{J}/\psi\phi$ dataset, the sensitivity of the default fit to the combinatorial background event selection is assessed through alternative mass cuts when selecting the $\mathrm{B_s} \rightarrow \mathrm{J}/\psi\phi$ candidates. The result of these alternative fits, and the mass windows used are shown in fig. 4.26. These fit variations have negligible effect on the fit results, and are excluded from the reported systematics.

To evaluate the possible systematic errors introduced into the $\mathrm{B_s} \rightarrow \mathrm{J}/\psi\phi$ default fit by the re-weighting to correct inefficiency in the `L2StarB` triggers, a number of approaches are used:

- The fitted re-weighting function (eq. (4.12)) is shifted within its uncertainties;
- The number of bins used in the χ^2 fit is varied from the default 400;
- Alternate combinations of the `L2StarB` triggers are use to calculate w, the trigger dependent proper decay time re-weighting factor.

In each case the variations have negligible effect on the fit results and are excluded from the reported systematic errors.

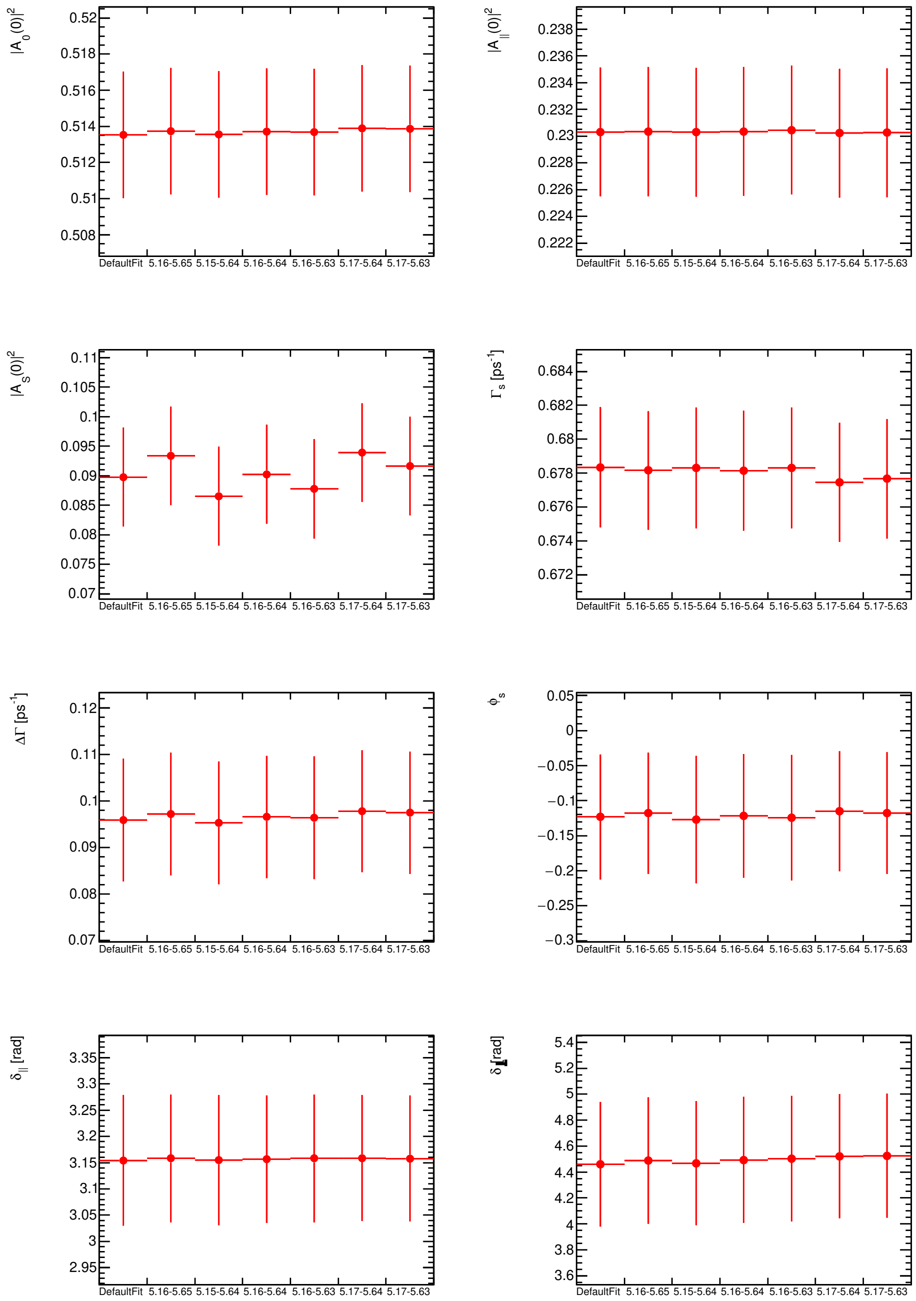

Figure 4.26: Stability of the $\mathrm{B_s} \to \mathrm{J}/\psi\phi$ default fit physics parameters under variations of the combinatorial background mass window. In these tests the transversity angle distributions for the combinatorial background, $P_{\mathrm{Bck}}(t_i|\sigma_{t_i})*$, is fitted after the alternate background is selected, however the background Punzi PDFs are left unchanged. The x-axis on each plot shows the internal name of the fit variation, and describes the background mass window variation (in GeV).

4.5.1.2 Flavour Tagging

The $\mathrm{B_s} \to \mathrm{J}/\psi\phi$ default fit performance under reduced tagging power is evaluated through the removal of tagging information from specific flavour tagging methods from the $\mathrm{B_s} \to \mathrm{J}/\psi\phi$ dataset. The fit performance is stable, until the tagging power falls to 0.57 % (exclusion of the combined muon flavour tagger from the fit). At this point, the tagging power is insufficient to break the symmetry given in eq. (4.11b), and the fitted value of ϕ_s and $\delta_\perp$ transform under the approximate symmetry. The MLE estimates of the physics parameters of interest under the alternate fits are shown in fig. 4.27.

Under the reduced tagging power fits, a small systematic effect is observed in the MLEs of A_S, and this is included as a flavour tagging related systematic.

The effect of the tagger selection for events that pass both lepton tagger's requirements is assessed by adopting alternate prioritisations for the tagger selection (combined muon → segment-tagged muon → electron; electron → combined muon → segment-tagged muon). These fit variations have negligible effect on the fit results.

Possible effects from the over-parameterisation of the tag probability Punzi PDFs for the combined muon and jet-charge taggers is assessed by use of the BIC/AIC preferred models (the sum of two exponentials and a third-order polynomial for the combined muon tag probability Punzi PDFs, and a sixth-order polynomial for the jet-charge tag probability Punzi PDFs). The effects of these fit variations on the fit results are negligible.

4.5.1.3 Inner Detector Alignment

The possibility of a mis-alignment of the ID components during reconstruction, and the subsequent systematic mis-reconstruction of ID tracks is considered [145] using the methods outlined in [173] and models two modes of mis-alignment: a radial deformation of the first pixel layer, and a radial deformation of the entire ID. Track parameters and transversity angles are recalculated based on these deformations, and alternative fits are performed with the modified datasets. Shifts in the MLE of A_S and $\delta_\perp$ are observed (at the order of 20 % of statistical σ), and included as systematic errors.

4.5.1.4 Detector Acceptance PDF

Validation of the detector acceptance PDF, $A_\mathrm{S}(\Omega_i|p_{\mathrm{T}i})$, is performed through comparison of the expected distributions of the leading and sub-leading muons

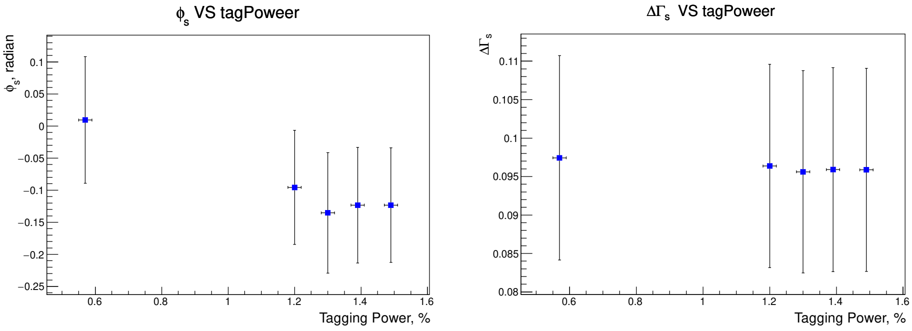

(a) ϕ_s (b) $\Delta\Gamma_\mathrm{s}$

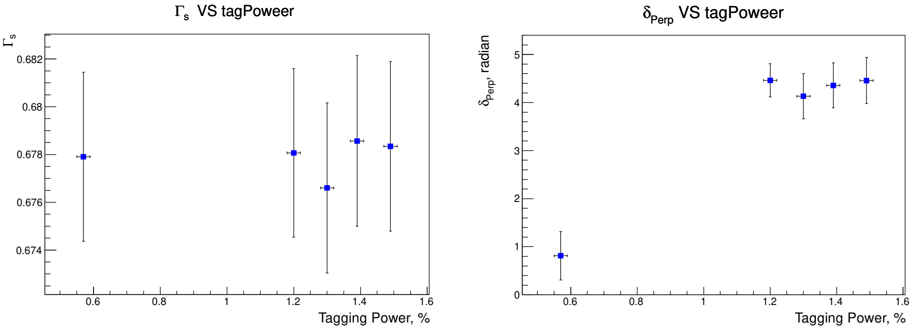

(c) Γ_s (d) $\delta_\perp$

Figure 4.27: Tagging power variations of the $\mathrm{B_s} \to \mathrm{J}/\psi\phi$ default fit. In these tests tagging power is reduced through the removal of information from specific flavour tagging methods.

from the $\mathrm{J}/\psi \to \mu^+\mu^-$ decay after MC trigger simulation, and that obtained from the $\mathrm{B_s} \to \mathrm{J}/\psi\phi$ dataset [145], see fig. 4.28. The distributions for data are obtained from the $\mathrm{B_s} \to \mathrm{J}/\psi\phi$ dataset using a sideband-subtraction method, and compared against the distribution obtained from MC after trigger simulation, both are normalised to unit area. No significant deviations are found, and additional tests of the transversity angle distributions between MC samples and the $\mathrm{B_s} \to \mathrm{J}/\psi\phi$ dataset [145] show no significant deviations.

Alternative p_T binnings to model the p_T dependence of the detector acceptance show no effect on the performance of the fit, and are neglected as a systematic effect.

The product $A_\mathrm{S}(\Omega_i|p_{\mathrm{T}i}) \cdot P_\mathrm{S}(t_i, \Omega_i|\sigma_{t_i}, \mathrm{P}(B)_i)$ in the signal PDF requires a numerical integration over the transversity angles. The choice of binning for

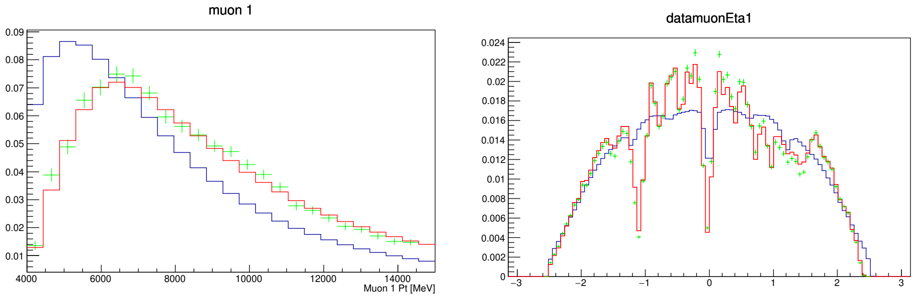

(a) Leading p_{T} (b) Leading η

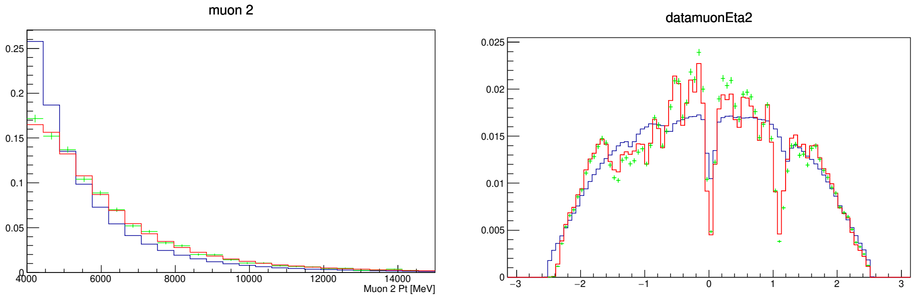

(c) Sub-leading p_{T} (d) Sub-leading η

Figure 4.28: Muon acceptance maps tests. The p_{T} (left) and η (right) distributions for the leading muon (upper) and sub-leading muon (lower), shown are the MC distributions (blue), after trigger simulations (red), and the $\mathrm{B_s} \to \mathrm{J}/\psi\phi$ candidate events (green). MC events passing trigger simulation, and events from data are normalised to unit area. Figures adapted from [145].

this intergation is considered as a possible source of systematic errors in the $\mathrm{B_s} \to \mathrm{J}/\psi\phi$ default fit. Alternative binnings are used in alternative fits, but have been shown [145] to have only a small systematic effect on the performance of the fit.

4.5.1.5 Bias in the Default Model

The 40 000 000 event fully reconstructed $\mathrm{B_s} \to \mathrm{J}/\psi\phi$ MC sample is used to validate the reconstruction and fit code [145]. The sample is shaped using the accept-reject method, and the $\mathrm{B_s} \to \mathrm{J}/\psi\phi$ default fit is used to recover the parameters used to shape the MC sample. No bias is found in the MLE central values.

In addition to these MC based fits, 2500 toy-MC datasets are produced [145], and these fitted with the $\mathrm{B_s} \to \mathrm{J}/\psi\phi$ default fit. Pull distributions are formed from the MLE results, where the pull, P, from an individual fit is given by

$$P = \frac{T - F_{\mathrm{MLE}}}{\sigma_{\mathrm{MLE}}} \tag{4.41}$$

where T is the true value of the parameters used to generate the toy-MC, and F_{MLE} and σ_{MLE} are the MLE estimate of the parameter and its statistical uncertainty respectivly. The distribution of P is expected to be Gaussian, with a mean of 0 and a standard deviation of 1. No deviation from this expectation is found in the pull distribution obtained from the toy-MC datasets.

4.5.2 Signal and Combinatorial Background Model Variations

Alternative fit models are examined to determine the possible systematic errors related to a mis-modeling of the $\mathrm{B_s} \to \mathrm{J}/\psi\phi$ dataset.

4.5.2.1 Fit Model Variations

To asses the sensitivity of the $\mathrm{B_s} \to \mathrm{J}/\psi\phi$ default fit to mis-modelling of the underlying data, a number of alternative models are used to generate toy-MC datasets that are then refitted with the default model [145]. The bias in pull-distributions for these (2500) pseudo-experiments is then reported as the systematic error due to this model variation. To obtain the parameters used for the toy-MC generation, the alternative model is fitted against the $\mathrm{B_s} \to \mathrm{J}/\psi\phi$ dataset.

The following variations are considered:

- The $\mathrm{B_s}$ mass is generated using the fitted mass from the $\mathrm{B_s} \to \mathrm{J}/\psi\phi$ dataset, convoluted by a per-event Gaussian whose standard deviation is taken from the signal mass uncertainty distribution obtained from data;
- The combinatorial background mass model is replaced with an exponential decay and linear function;
- The per-candidate Gaussian convolution of the $\mathrm{B_s}$ proper decay time is replaced with a convolution by a double Gaussian.

4.5.2.2 Combinatorial Background Transversity Angle Model Variations

To determine the possible effect of the choices of p_{T}-binning and mass side-bands used in the construction of $P_{\mathrm{Bck}}(\Omega_i|p_{\mathrm{T}i})$ a number of alternative fits are performed [145]. Three alternative p_{T}-binnings are considered, with the largest deviation from the MLE of the $\mathrm{B_s} \to \mathrm{J}/\psi\phi$ default fit taken as the systematic errors due to the p_{T}-binning. This approach is used to assess the sensitivity of the fit to possible $\mathrm{B_s} \to \mathrm{J}/\psi(\mu^+\mu^-)\phi(\mathrm{K^+K^-})$ contamination in the data used to fit the combinatorial background transversity angle description.

4.5.3 Physics Background Model Variations

Possible mis-modelling of the b-physics backgrounds, and the systematic error introduced into the $\mathrm{B_s} \to \mathrm{J}/\psi\phi$ default fit due to this mis-modelling is examined through a number of alternative fits to the $\mathrm{B_s} \to \mathrm{J}/\psi\phi$ dataset.

4.5.3.1 Physics Background Fractions

To estimate the effects of the uncertainty in the calculation of $f_{\mathrm{B_d}}$ (including the possible effects of the MC modelling of the $\mathrm{K}^{*0} \to \mathrm{K}^+\pi^-$ line-shape), variant fits are performed with the value of $f_{\mathrm{B_d}}$ shifted by $\pm\sigma$. The largest shift for each physics variable, compared to the $\mathrm{B_s} \to \mathrm{J}/\psi\phi$ default fit, is reported as the systematic error due to the background fraction. The same approach is adopted to assess the possible systematic error due to $f_{\Lambda_{\mathrm{b}}}$. The results of these variations are given in tables 4.16(a) and 4.16(b).

4.5.3.2 $\mathrm{B_d} \to \mathrm{J}/\psi\mathrm{K}^{*0}$ Background

Variations of the $\mathrm{B_d}$ mass PDF are used to assess the effects of the $\mathrm{B_d}$ mass description on the $\mathrm{B_s} \to \mathrm{J}/\psi\phi$ default fit. The variations are produced by shifting the parameters describing the $\mathrm{B_d}$ mass PDF by $\pm1\sigma$, and the systematic error assigned to these variations is the largest difference between the variant fits and the $\mathrm{B_s} \to \mathrm{J}/\psi\phi$ default fit. Results of these variations are shown in table 4.16(a).

To estimate the possible effects of uncertainty in the $\mathrm{B_d}$ proper decay time PDF, the pseudo-$\mathrm{B_s}$ lifetime is shifted by $\pm1\sigma$ from the default fit. The systematic error reported for these variations is the largest difference from the $\mathrm{B_s} \to \mathrm{J}/\psi\phi$ default fit. Results of these variations are shown in table 4.16(a).

To determine the possible effects of the choice of $\mathrm{B_d}$ transversity angle modelling assumptions two cases are considered: the first is the possible effect of the $\mathrm{B_d}$ P-wave model, and the second is the effect of the omission of the S-wave contribution from non-resonant $\mathrm{B_d} \to \mathrm{J}/\psi\mathrm{K}^+\pi^-$ decays.

Variations of the P-wave transversity angles are generated using the uncertainties of the fitted PDF given in [167]. These variations consider, in turn, $\pm 1\sigma$ shifts in each of the parameters affecting the P-wave transversity angle distributions. In addition to these variations, the limitations of the spherical harmonic fit, and its possible effect on the $\mathrm{B_s} \to \mathrm{J}/\psi\phi$ default fit, are estimated through fit variations where the order of the spherical harmonic description is modified ($k \pm 1$, $l \pm 1$). The systematic error for the $\mathrm{B_d}$ P-wave model is reported as the largest shift from the $\mathrm{B_s} \to \mathrm{J}/\psi\phi$ default fit for each form of variation added in quadrature. Results of these variations are shown in table 4.16(a).

Inclusion of a $\mathrm{B_d}$ S-wave component, and its effects on the default fit are considered through the modification of $f_{\mathrm{B_d}}$, $P_{\mathrm{B_d}}(m_i)$, and $P_{\mathrm{B_d}}(\Omega_i|p_{\mathrm{T}i})$. $f_{\mathrm{B_d}}$ is increased to 4.0 %[16] to represent the additional background contribution, while $P_{\mathrm{B_d}}(m_i)$ is modified to include the (weighted) contribution from $\mathrm{B_d} \to \mathrm{J}/\psi\mathrm{K}^+\pi^-$ decays as $m(\mathrm{J}/\psi\mathrm{K}^+\mathrm{K}^-)$ differ for $\mathrm{B_d} \to \mathrm{J}/\psi\mathrm{K}^{*0}$ and $\mathrm{B_d} \to \mathrm{J}/\psi\mathrm{K}^+\pi^-$ after $\mathrm{B_s} \to \mathrm{J}/\psi\phi$ selection cuts. To model the transversity angle distributions, the transversity amplitudes from the lowest $m(\mathrm{K}^+\pi^-)$ mass bin from [167] are used. An additional variation of this fit is performed where S-wave amplitude is taken from the ATLAS MC studies to account for the difference in $m(\mathrm{K}^+\pi^-)$ for S- and P-wave decays (see section 4.4.4.3). For discussion of the limitations of this approach see section 4.4.4.3. The systematic error due to the omission of the S-wave $\mathrm{B_d} \to \mathrm{J}/\psi\mathrm{K}^+\pi^-$ is taken as the largest difference from the $\mathrm{B_s} \to \mathrm{J}/\psi\phi$ default fit. Results of these variations are shown in table 4.16(a).

4.5.3.3 $\Lambda_\mathrm{b} \to \mathrm{J}/\psi\mathrm{pK}^-$ Background

To estimate the effects of the modelling assumptions made to perform the $m(\mathrm{pK}^-)$ re-weighting, two studies are performed. For the first, the binned $m(\mathrm{pK}^-)$ mass distribution obtained from [168] is randomly smeared by the statistical uncertainty of each bin, and an alternative re-weighting of the $\Lambda_\mathrm{b} \to \mathrm{J}/\psi\mathrm{pK}^-$ performed. 500 such random re-weightings are performed, and f_{Λ_b} and the Λ_b mass PDF are recalculated, and an alternative $\mathrm{B_s} \to \mathrm{J}/\psi\phi$ fit performed. No deviation from the results of the $\mathrm{B_s} \to \mathrm{J}/\psi\phi$ default fit are observed, and no systematic error is reported as a result of these fits. A second alternative fit was performed with the re-weighting step removed from the $\mathrm{B_s} \to \mathrm{J}/\psi\phi$ fit, the difference between this fit and the $\mathrm{B_s} \to \mathrm{J}/\psi\phi$ default fit is taken as the systematic error due to the Λ_b re-weighting, and is given in

---

[16] An additional test with $f_{\mathrm{B_d}} = 5.5\,\%$, is considered as an additional systematic when modelling the S- and P-wave $\mathrm{B_d}$ decays.

table 4.16(b).

A suite of Λ_b mass PDF variations are produced to assess the possible effects of the Λ_b mass model on the $B_s \to J/\psi\phi$ default fit:

- effects due to the limited MC statistics available, and the effect of the smoothing are assessed by varying the number of bins used (±5) and the number of iterations (±2) of the smoothing procedure. An additional variation with the smoothing removed is included in this suite;
- effects due to the choice of binning, and the PDF used to describe the Λ_b mass distribution are determined though the replacement of the second-order interpolation PDF with a fourth-order interpolation PDF, and varying the number of bins as described above.

The systematic error reported due to the Λ_b mass description is given as the largest shift from the $B_s \to J/\psi\phi$ default fit for each suite added in quadrature, and is shown in table 4.16(b).

To estimate the possible effects of uncertainty in the Λ_b proper decay time PDF, the pseudo-B_s lifetime is shifted by $\pm 1\sigma$ from the default fit. The systematic error reported for these variations is the largest difference from the $B_s \to J/\psi\phi$ default fit. Results of these variations are shown in table 4.16(b).

To estimate the effects of uncertainty in the Λ_b transversity angle model, 1000 alternative fits are performed with the weight of each Λ_b event smeared by an additional per-event Poisson term with a mean of 1. The MLE for each $B_s \to J/\psi\phi$ fit parameter is fitted with a Gaussian to investigate the possibility of bias in the $B_s \to J/\psi\phi$ default fit. No bias is observed in the results of these fits, and the width of each fitted Gaussian is reported as a systematic effect.

A second source of systematic error as a result of the Λ_b transversity angle model is due to the assumption of a flat angular distribution[17]. To assess the effect of this assumption a number of alternative fits are performed with alternative angular distributions, these include:

- Spherical harmonic distributions. The transversity angle distribution is assumed to be described by a single spherical harmonic function from the pool of spherical harmonic function defined by eq. (4.40). Each function from this pool is tested;

---

[17] This assumption is due to the lack of results with regard to the polarisation of Λ_b production in the central rapidity region.

				Transversity Angles	
Parameter	$f_{\mathrm{B_d}}$	$P_{\mathrm{B_d}}(m_i)$	$P_{\mathrm{B_d}}(t_i\vert\sigma_{t_i})$	P-Wave	S+P-Wave
$\phi_{\mathrm{s}}\,[\mathrm{rad}]$	0.0162	0.0001	$<10^{-4}$	0.0038	0.0165
$\Delta\Gamma_{\mathrm{s}}\,[\mathrm{ps}^{-1}]$	0.0012	$<10^{-4}$	$<10^{-4}$	0.0005	0.0002
$\Gamma_{\mathrm{s}}\,[\mathrm{ps}^{-1}]$	0.0003	$<10^{-4}$	0.003	$<10^{-4}$	0.0001
$\vert A_0\vert^2$	0.0012	$<10^{-4}$	0.006	0.0003	0.0021
$\vert A_{\Vert}\vert^2$	0.0008	$<10^{-4}$	$<10^{-4}$	0.0003	0.0015
$\vert A_{\mathrm{S}}\vert^2$	0.0080	0.001	$<10^{-4}$	0.0025	0.0150
$\delta_{\Vert}\,[\mathrm{rad}]$	0.0046	0.003	$<10^{-4}$	0.0038	0.0089
$\delta_{\perp}\,[\mathrm{rad}]$	0.0242	0.005	0.044	0.0062	0.0741
$\delta_{\perp}-\delta_{\mathrm{S}}\,[\mathrm{rad}]$	0.0023	$<10^{-4}$	$<10^{-4}$	0.0464	0.0074

(a) $\mathrm{B_d} \to \mathrm{J}/\psi\mathrm{K}^{*0}$

Parameter	$f_{\Lambda_{\mathrm{b}}}$	Weights	$P_{\Lambda_{\mathrm{b}}}(m_i)$	$P_{\Lambda_{\mathrm{b}}}(t_i\vert\sigma_{t_i})$	$P_{\Lambda_{\mathrm{b}}}(\Omega_i\vert p_{\mathrm{T}i})$
$\phi_{\mathrm{s}}\,[\mathrm{rad}]$	0.0020	0.0016	0.0012	0.0006	0.0113
$\Delta\Gamma_{\mathrm{s}}\,[\mathrm{ps}^{-1}]$	0.0009	0.0003	0.0001	0.0001	0.0023
$\Gamma_{\mathrm{s}}\,[\mathrm{ps}^{-1}]$	0.0003	0.0004	0.0004	0.0004	0.0016
$\vert A_0\vert^2$	0.0017	0.0007	0.0003	0.0003	0.0073
$\vert A_{\Vert}\vert^2$	0.0003	0.0008	0.0005	0.0005	0.0016
$\vert A_{\mathrm{S}}\vert^2$	0.0017	0.0000	0.0006	0.0005	0.0093
$\delta_{\Vert}\,[\mathrm{rad}]$	0.0010	0.0029	0.0031	0.0039	0.0062
$\delta_{\perp}\,[\mathrm{rad}]$	0.0110	0.0077	0.0025	0.0045	0.0457
$\delta_{\perp}-\delta_{\mathrm{S}}\,[\mathrm{rad}]$	0.0033	0.0036	0.0037	0.0037	0.0074

(b) $\Lambda_{\mathrm{b}} \to \mathrm{J}/\psi\mathrm{pK}^{-}$

Table 4.16: Systematic errors due to $\mathrm{B_d}$ background (top) and Λ_{b} background (bottom).

- Flat transversity angle distributions, ignoring detector acceptance effects;
- Replacing the Λ_{b} transversity angle model with the $\mathrm{B_d}$ transversity angle model.

The systematic effect due to this modelling assumption is taken as the largest difference between the alternative fits and the $\mathrm{B_s} \to \mathrm{J}/\psi\phi$ default fit.

These systematic errors are added in quadrature and shown in table 4.16(b).

4.5.4 Flavour Tagging Systematic Errors

Possible systematic errors in the $\mathrm{B_s} \to \mathrm{J}/\psi\phi$ default fit due to the flavour tagging are due to three sources:

- the limited size of the calibration sample used in the flavour tagging calibration;
- the choice of functions used to fit to the calibration sample;
- the choice of functions used to describe the flavour tagging Punzi PDFs for each tagging method and the range of values of tagging probability over which the flavour tagging Punzi PDFs are normalised.

4.5.4.1 Statistical Errors

To estimate the effects of the limited statistics available in the $\mathrm{B}^{\pm} \to \mathrm{J}/\psi\mathrm{K}^{\pm}$ calibration sample, variations of the taggers $\mathrm{P}(B|Q)$ probability functions are produced. The binned tag charge histograms (section 4.3.2.1) are randomly smeared by the statistical uncertainty of each bin and the $\mathrm{P}(B|Q)$ probability functions refitted. The updated functions are then used to re-tag the $\mathrm{B_s} \to \mathrm{J}/\psi\phi$ dataset and a varient $\mathrm{B_s} \to \mathrm{J}/\psi\phi$ fit performed with the flavour tagging Punzi PDFs disabled. 1000 random re-calibrations are performed, and the results for each $\mathrm{B_s} \to \mathrm{J}/\psi\phi$ physics variable fitted with a Gaussian distribution. The mean of each of the Gaussian distributions is compared to the results of the 'no-tag-Punzi' baseline fit (section 4.5.4.3) and no statistically significant shifts are observed.

The standard deviation of the fitted Gaussian for each $\mathrm{B_s} \to \mathrm{J}/\psi\phi$ physics variable is reported as the statistical error due to the $\mathrm{B}^{\pm} \to \mathrm{J}/\psi\mathrm{K}^{\pm}$ calibration sample size. The statistical errors due to these variations are shown in table 4.17.

4.5.4.2 Systematic Errors

Three variations of the $\mathrm{P}(B|Q)$ probability functions are considered as possible sources of systematic errors in the $\mathrm{B_s} \to \mathrm{J}/\psi\phi$ default fit:

- the functional form of $\mathrm{P}(B|Q)$;
- possible trigger dependence in the fitting of the $\mathrm{P}(B|Q)$;
- possible nPV dependence in the fitting of the $\mathrm{P}(B|Q)$.

These are considered in turn below.

The form of the function used to describe $\mathrm{P}(B|Q)$ for the flavour taggers is a possible source of systematic error in the $\mathrm{B_s} \to \mathrm{J}/\psi\phi$ default fit. To assess the possible effect of the functional form of $\mathrm{P}(B|Q)$, a number of alternate $\mathrm{B_s} \to \mathrm{J}/\psi\phi$ fits are performed. The variations considered are:

- ±2 bins in the binned tag charge histograms;
- alternate $\mathrm{P}(B|Q)$ functions described by:
    - linear functions;
    - fifth-order polynomials;
    - two third-order polynomials describing the positive and negative tag charge regions that share the constant and linear terms;
    - for the combined muon tagging, two third-order polynomials describing the positive and negative tagging charge regions that share the constant term.

For each variation, 500 random re-calibrations are performed using the method described in section 4.5.4.1, with the baseline fit using the default $\mathrm{P}(B|Q)$ functions calibrated against the updated tag charge histograms. The systematic error for each $\mathrm{B_s} \to \mathrm{J}/\psi\phi$ physics variable is taken as the difference between the mean of the 500 alternate fits and the mean of the baseline fits. Using this method decouples the statistical effects of the calibration sample (the standard deviation of the results from the alternate/baseline fits) from the systematic effects of the $\mathrm{P}(B|Q)$ functions.

As the triggers used to collect the $\mathrm{B}^\pm \to \mathrm{J}/\psi\mathrm{K}^\pm$ calibration sample and $\mathrm{B_s} \to \mathrm{J}/\psi\phi$ dataset differ, there is the possibility of a systematic error in the $\mathrm{B_s} \to \mathrm{J}/\psi\phi$ default fit result. To estimate the size of any possible effect an alternate $\mathrm{B}^\pm \to \mathrm{J}/\psi\mathrm{K}^\pm$ calibration sample is prepared using the $\mathrm{B_s} \to \mathrm{J}/\psi\phi$ analysis triggers. 500 random re-calibrations are performed using the method described in section 4.5.4.1. The mean of each of the fit variable's Gaussian distributions is compared to the results of the 'no-tag-Punzi' baseline fit and no statistically significant shifts are observed, while the width of the fitted Gaussian is reported as the possible systematic error due to the $\mathrm{B}^\pm \to \mathrm{J}/\psi\mathrm{K}^\pm$ calibration sample triggers.

The distribution of the number of PVs, nPV, differ between the $\mathrm{B}^\pm \to \mathrm{J}/\psi\mathrm{K}^\pm$ calibration sample and $\mathrm{B_s} \to \mathrm{J}/\psi\phi$ dataset, therefore any nPV-dependence in the flavour tagging may introduce a systematic error into the $\mathrm{B_s} \rightarrow \mathrm{J}/\psi\phi$ default fit. To estimate the size of any possible effect, an nPV-dependent flavour tagging is performed. The $\mathrm{B}^{\pm} \rightarrow \mathrm{J}/\psi\mathrm{K}^{\pm}$ calibration sample is divided into three sub-samples with nPV: 1 to 10; 11 to 14; and >15. The nPV-dependent taggers are calibrated against these sub-samples and used to re-tag the $\mathrm{B_s} \rightarrow \mathrm{J}/\psi\phi$ dataset. The re-tagged $\mathrm{B_s} \rightarrow \mathrm{J}/\psi\phi$ dataset is used in an alternate $\mathrm{B_s} \rightarrow \mathrm{J}/\psi\phi$ fit with the flavour tagging Punzi PDFs disabled. The systematic error is taken as the difference between this alternate fit and the 'no-tag-Punzi' baseline fit.

A summary of these systematic errors is given in table 4.17.

4.5.4.3 Flavour Tagging Punzi Terms

Alternate models to describe the flavour tagging Punzi PDFs are formed for the combined muon, electron, and jet-charge flavour tagging methods by varying the order of the polynomial in the default models by ±1. Additionally, the order of the polynomials used to describe the signal and background components are varied independently. To form alternate models for the segment-tagged muon flavour tag probability distributions, the number of Gaussians used in the default model are varied by ±1 with the signal and background descriptions allowed to vary independently. Alternate $\mathrm{B_s} \rightarrow \mathrm{J}/\psi\phi$ fits using the modified flavour tag probability Punzi PDFs are negligibly different from the $\mathrm{B_s} \rightarrow \mathrm{J}/\psi\phi$ default fit, and are excluded from the final systematic errors.

An alternative $\mathrm{B_s} \rightarrow \mathrm{J}/\psi\phi$ fit is performed with the flavour tagging Punzi terms removed from the $\mathrm{B_s} \rightarrow \mathrm{J}/\psi\phi$ likelihood function (eq. (4.31)). The difference between this alternative fit and the $\mathrm{B_s} \rightarrow \mathrm{J}/\psi\phi$ default fit is taken as the systematic error due to the flavour tagging Punzi terms as shown in table 4.17. This 'no-tag-Punzi' fit is also taken as the baseline fit for flavour tagging systematic studies that are found to be incompatible with the flavour tagging Punzi terms included in the $\mathrm{B_s} \rightarrow \mathrm{J}/\psi\phi$ default fit.

As the flavour tagging Punzi PDFs are normailsed over the range of tagging probabilities found in the $\mathrm{B_s} \rightarrow \mathrm{J}/\psi\phi$ dataset, alternative calibrations of the tagging functions may produce tag probabilities for the data outside of the range of default fit Punzis[18]. These events are then removed (the tagging Punzi term is zero) from the fit, and due to correlations between the p_{T} of the

---

[18] The flavour tagging Punzi PDFs are provided to the $\mathrm{B_s} \rightarrow \mathrm{J}/\psi\phi$ default fit, they are not fitted as part of the default fit procedure.

Parameter	Statistical	Systematic Calibration	 Triggers	 nPV	Punzi Terms
ϕ_s [rad]	0.0055	0.0127	0.0060	0.0203	0.0035
$\Delta\Gamma_s$ [ps^{-1}]	0.0001	0.0003	0.0002	0.0026	0.0002
Γ_s [ps^{-1}]	$<10^{-4}$	0.0001	$<10^{-4}$	0.0002	0.0002
$\|A_0\|^2$	$<10^{-4}$	$<10^{-4}$	$<10^{-4}$	0.0001	$<10^{-4}$
$\|A_\parallel\|^2$	$<10^{-4}$	0.0001	$<10^{-4}$	0.0002	0.0001
$\|A_S\|^2$	0.0002	0.0002	0.0002	0.0007	0.0004
$\delta_\parallel$ [rad]	0.0048	0.0123	0.0049	0.0013	0.0024
$\delta_\perp$ [rad]	0.0832	0.1973	0.0866	0.0349	0.0358
$\delta_\perp - \delta_S$ [rad]	0.0003	0.0002	0.0003	0.0041	0.0004

Table 4.17: Flavour tagging systematic errors for the $B_s \to J/\psi\phi$ default fit.

candidate B_s and flavour tagging method Punzi terms, there is a non-negligible systematic shift in the fitted value of Γ_s. These correlations introduce the need for the use of the 'no-tag-Punzi' baseline fits in sections 4.5.4.1 and 4.5.4.2.

4.5.5 Results

A summary of the fit systematic errors is given in table 4.18. Errors from different sources are assumed to be uncorrelated, and added in quadrature to produce the final systematic errors.

The results for the 8 TeV fit are given in table 4.19.

Source	ϕ_s [rad]	$\Delta\Gamma_\mathrm{s}$ [ps^{-1}]	Γ_s [ps^{-1}]	$\lvert A_0\rvert^2$	$\lvert A_\parallel\rvert^2$	$\lvert A_\mathrm{S}\rvert^2$	$\delta_\parallel$ [rad]	$\delta_\perp$ [rad]	$\delta_\perp - \delta_\mathrm{S}$ [rad]
ID Alignment	0.005	$<10^{-3}$	0.002	$<10^{-3}$	$<10^{-3}$	$<10^{-3}$	0.134	0.007	$<10^{-3}$
Detector Acceptance	$<10^{-3}$	$<10^{-3}$	$<10^{-3}$	0.003	$<10^{-3}$	0.001	0.004	0.008	$<10^{-3}$
Default Model	0.001	0.002	$<10^{-3}$	0.002	$<10^{-3}$	0.002	0.025	0.015	0.002
Fit Model:									
Signal Mass Model	0.004	$<10^{-3}$	$<10^{-3}$	0.002	$<10^{-3}$	0.001	0.015	0.017	$<10^{-3}$
Background Mass Model	$<10^{-3}$	0.002	$<10^{-3}$	0.002	$<10^{-3}$	0.002	0.027	0.038	$<10^{-3}$
Proper Decay Time Resolution	0.003	$<10^{-3}$	0.001	0.002	$<10^{-3}$	0.002	0.057	0.011	0.001
Background Transversity Angle Model:									
p_T-Binning	0.020	0.006	0.003	0.003	$<10^{-3}$	0.008	0.004	0.006	0.008
Mass Sidebands	0.008	0.001	0.001	$<10^{-3}$	$<10^{-3}$	0.002	0.021	0.005	0.003
b-Physics Backgrounds:									
$\mathrm{B_d}$ Background	0.023	0.001	$<10^{-3}$	0.002	0.002	0.017	0.090	0.011	0.009
Λ_b Background	0.011	0.002	0.001	0.001	0.007	0.009	0.045	0.006	0.007
Flavour Tagging	0.025	0.003	$<10^{-3}$	$<10^{-3}$	$<10^{-3}$	0.001	0.236	0.014	0.004
Total	0.042	0.007	0.004	0.007	0.006	0.022	0.05	0.30	0.01

Table 4.18: Summary of the fit systematics for the 8 TeV fit. Data from [145].

Parameter	Fit Result
ϕ_s [rad]	$-0.110 \pm 0.082 \pm 0.042$
$\Delta\Gamma_s$ [ps^{-1}]	$0.101 \pm 0.013 \pm 0.007$
Γ_s [ps^{-1}]	$0.676 \pm 0.004 \pm 0.004$
$\lvert A_0\rvert^2$	$0.520 \pm 0.004 \pm 0.007$
$\lvert A_\parallel\rvert^2$	$0.230 \pm 0.005 \pm 0.006$
$\lvert A_S\rvert^2$	$0.097 \pm 0.008 \pm 0.022$
$\delta_\parallel$ [rad]	$3.15 \pm 0.10 \pm 0.05$
$\delta_\perp$ [rad]	$4.50 \pm 0.45 \pm 0.30$
$\delta_\perp - \delta_S$ [rad]	$-0.08 \pm 0.03 \pm 0.01$

Table 4.19: Fit results for the 8 TeV $B_s \to J/\psi\phi$ fit. Errors are statistical and systematic.

4.6 Run1 Results

Two combinations are formed from the $B_s \to J/\psi\phi$ default fit and the previous ATLAS flavour tagged 7 TeV result [127].

A statistical combination is performed using the output of the likelihood functions in the ϕ_s–$\Delta\Gamma_s$ plane, while the ATLAS Run1 result [128] is based on the *Best Linear Unbiased Estimate* (BLUE) method, and includes estimates of the Run1 systematic errors based on the 7 TeV and 8 TeV results.

4.6.1 Statistical Combination

A statistical combination for ϕ_s and $\Delta\Gamma_s$ may be obtained from the 7 TeV and 8 TeV default fits through the summation of the fitted likelihoods obtained from the 2D profile likelihood scans performed in the ϕ_s–$\Delta\Gamma_s$ plane.

Compatibility of the 7 TeV and 8 TeV results are shown by comparison of the confidence limits obtained from the two default fits (fig. 4.29(a)). The 68 % and 95 % confidence limits in the ϕ_s–$\Delta\Gamma_s$ plane for the statistical combination are shown in fig. 4.29(b). Point estimates for ϕ_s and $\Delta\Gamma_s$ are obtained by forming 1D profile likelihood scans (with one scan variable, and one quantised fitted parameter) from projections of the 2D profile likelihood, with the global minimum taken as the central value, and $-2\Delta\ln(\mathcal{L}) = 1$ used to obtain the statistical uncertainty. The result of the statistical combination is given in table 4.20.

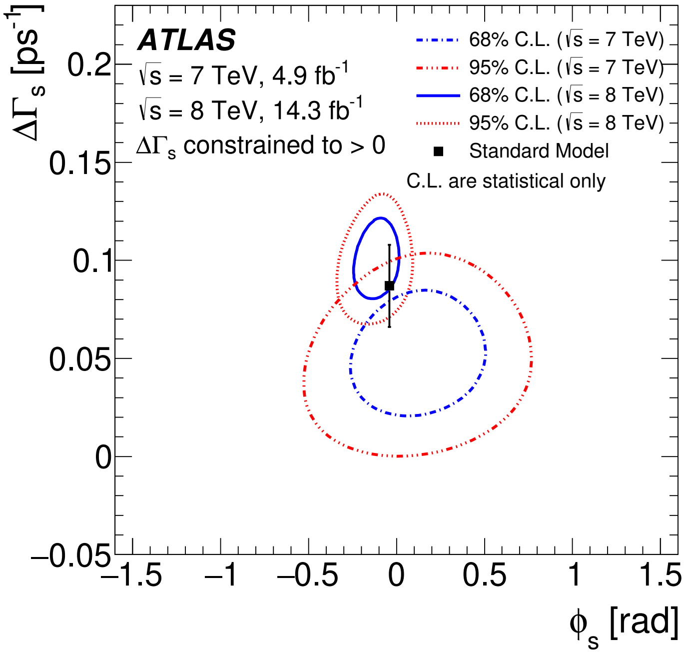

(a) 7 TeV and 8 TeV results

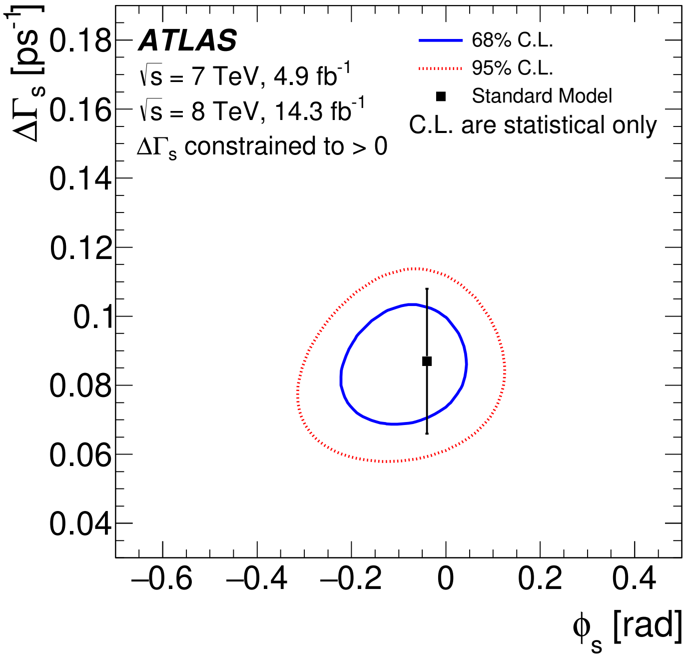

(b) Statistical combination

Figure 4.29: 2D profile likelihood scans in the ϕ_s–$\Delta\Gamma_s$ plane from the $B_s \rightarrow J/\psi\phi$ statistical combination. Shown are the 68 % and 95 % confidence limits (blue and red) and the SM prediction [172] (black) for the 7 TeV and 8 TeV default fits (top) and the Run1 statistical combination (bottom).

Parameter	Fit Result
$\phi_{\mathrm{s}}\,[\mathrm{rad}]$	-0.093 ± 0.081
$\Delta\Gamma_{\mathrm{s}}\,[\mathrm{ps}^{-1}]$	0.090 ± 0.012

Table 4.20: Fit results of the Run1 $\mathrm{B_s} \to \mathrm{J}/\psi\phi$ statistical combination. Errors are statistical only.

4.6.2 The Best Linear Unbiased Estimate Combination

The *Best Linear Unbiased Estimator* (BLUE) [174] is used to form the statistical combination of the 7 TeV and 8 TeV results.

4.6.2.1 The Best Linear Unbiased Estimate

The BLUE estimate for a collection of parameters, $\vec{\mathbf{x}}$, is given by

$$x_\alpha = \sum_{i=1}^{n} \lambda_{\alpha i} \cdot y_i \tag{4.42}$$

where λ is the weight assigned to each of the estimates y. The variance of each parameter is given by

$$\mathrm{var}(x_\alpha) = \sum_{i=1}^{n} \lambda_{\alpha i} \cdot M_{ij} \cdot \lambda_{\alpha j} \tag{4.43}$$

where M is a matrix encoding the intra- and inter-measurement correlations between sources of uncertainty. The BLUE estimate for x is obtained by finding λ such that $\mathrm{var}(\vec{\mathbf{x}})$ is minimised.

4.6.2.2 Best Linear Unbiased Estimate Results

The results of the 7 TeV and 8 TeV default fits are obtained from independent datasets, therefore there is no inter-measurement statistical correlation. Intra-measurement statistical correlations are taken from the `MINUIT` results for each dataset, while intra-measurement systematic errors are assumed to be uncorrelated. $\delta_{\parallel}$ and $\delta_{\perp} - \delta_{\mathrm{S}}$ are reported as confidence intervals in [127], and are excluded from the BLUE combination.

The ATLAS trigger efficiency is only considered as a systematic for the 7 TeV result. Similarly, the modelling of the combinatorial background transversity angle distributions and the Λ_{b} physics backgrounds are only considered in the 8 TeV result. These enter the BLUE combination with no correlation to the other result.

Parameter	Fit Result
ϕ_s [rad]	$-0.090 \pm 0.078 \pm 0.041$
$\Delta\Gamma_s$ [ps^{-1}]	$0.085 \pm 0.011 \pm 0.007$
Γ_s [ps^{-1}]	$0.675 \pm 0.003 \pm 0.003$
$\|A_0\|^2$	$0.522 \pm 0.003 \pm 0.007$
$\|A_{\|\|}\|^2$	$0.227 \pm 0.004 \pm 0.006$
$\|A_S\|^2$	$0.072 \pm 0.007 \pm 0.018$
$\delta_{\|\|}$ [rad]	$3.15 \pm 0.10 \pm 0.05$
$\delta_\perp$ [rad]	$4.15 \pm 0.32 \pm 0.16$
$\delta_\perp - \delta_S$ [rad]	$-0.08 \pm 0.03 \pm 0.01$

Table 4.21: Fit results for the $B_s \to J/\psi\phi$ Run1 best linear unbiased estimate. Errors are statistical and systematic.

Inter-measurement correlations between the flavour tagging systematics, ρ_{Tag}, detector acceptance systematics, ρ_{Acc}, and fit model, ρ_{Mod}, are assumed to be 0.5 [145], while the ID systematics, and B_d physics background systematics are unchanged between the results, and are assumed to be fully correlated [145].

The results of the BLUE combination are shown in table 4.21.

4.6.2.3 Stability Under Alternative Assumptions

To estimate the effects of the choices made for the BLUE combination, additional BLUE combinations with alternative values for ρ_{Tag}, ρ_{Acc}, and ρ_{Mod} are considered. 125 fits are performed with $\rho_i = 0.0, 0.25, 0.5, 0.75, 1.0$ with $i =$ Tag, Acc, Mod, and each correlation is allowed to vary independently. No significant deviations from the baseline BLUE combination are found.

The results for $\rho_{\text{Tag}} = \rho_{\text{Acc}} = \rho_{\text{Mod}} = 0.0, 0.25, 0.5, 0.75, 1.0$ are shown in table 4.22.

Parameter	ρ_i				
	0 %	25 %	50 %	75 %	100 %
ϕ_{s} [rad]	−0.087	−0.090	−0.090	−0.091	−0.092
$\Delta\Gamma_{\mathrm{s}}$ [ps^{-1}]	0.085	0.085	0.085	0.086	0.086
Γ_{s} [ps^{-1}]	0.675	0.675	0.675	0.675	0.675
$\|A_0\|^2$	0.523	0.522	0.522	0.522	0.522
$\|A_\parallel\|^2$	0.227	0.227	0.227	0.227	0.227
$\|A_{\mathrm{S}}\|^2$	0.071	0.072	0.072	0.073	0.073
$\delta_\perp$ [rad]	4.155	4.154	4.153	4.152	4.151

Table 4.22: Alternative BLUE combinations with ρ_i = 0.0, 0.25, 0.5, 0.75, 1.0 where $\rho_i = \rho_{\mathrm{Tag}} = \rho_{\mathrm{Acc}} = \rho_{\mathrm{Mod}}$.

Chapter 5

Searches for Resonant Structures in the $B_s\pi^\pm$ Mass Spectrum

In [175], the D∅ collaboration reported evidence of a structure in the invariant mass of the $B_s\pi^\pm$ system. This structure, the $X(5568)$, has been interpreted as a strongly decaying four-flavour tetraquark state [176, 177, 178, 179, 180].

The analysis presented here covers the ATLAS search for resonant structures in the $B_s\pi^\pm$ mass spectrum, and the limit set on the relative B_s production ratio, ρ_X, defined as

$$\rho_X = \frac{\sigma(pp \to X + \text{Anything}) \cdot \text{BR}(X \to B_s\pi^\pm)}{\sigma(pp \to B_s + \text{Anything})} \tag{5.1}$$

for the D∅ reported state, and over the mass range 5550 MeV to 5700 MeV using the combined ATLAS 7 TeV and 8 TeV datasets.

This analysis has been published as [181].

5.1 Theoretical Overview

Tetraquarks [182], exotic bound states of two quarks and two anti-quarks, are predicted by QCD [16] with a number of observed states (including the $X(3872)$ [183] and $Z(4430)$ [184]) proposed as tetraquark candidates. The lack of a comprehensive theoretical framework to classify tetraquarks has stimulated experimental searches for such states, as the four most popular phenomenological models offer predictions for states that should be observable at the LHC.

The recent D∅ claim of a tetraquark candidate has further focused research in this field, as it is the first claim of a four-flavour tetraquark state ($us\overline{d}\overline{b}$),

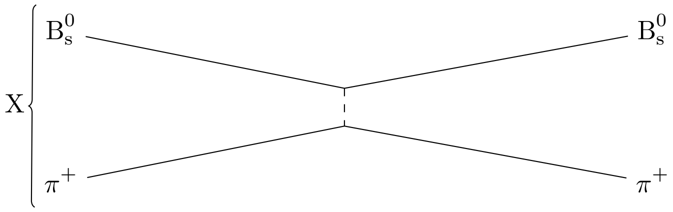

(a) Meson molecule decay

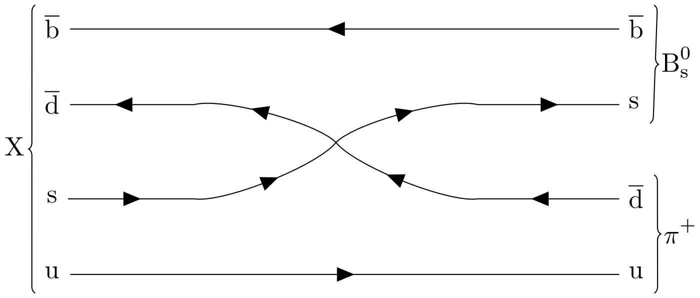

(b) Compact tetraquark decay

Figure 5.1: Possible $X(5568)$ decays to a $\mathrm{B_s^0}\pi^+$ state for a mesonic molecule (top) and compact tetraquark state (bottom).

with two of the phenomenological models, the compact tetraquark and loosely bound meson molecule, predicting such a state.

A loosely bound meson molecule interpretation of the $X(5568)$ is seemingly prohibited by its distance from the $\mathrm{B_d K^\pm}$ threshold mass (5774 MeV) and the weak bonding of the $\mathrm{B_s}\pi^\pm$ system [185]. Compact tetraquark models have been used to provide post-hoc predictions of the mass [178] and decay width [179] of a $[\mathrm{us}][\overline{\mathrm{d}}\overline{\mathrm{b}}]$ diquark-antidiquark system that is compatible with the D∅ observation, however the lack of an observation of a $\mathrm{B^+\overline{K}^0}$ end-state provides some evidence against this interpretation.

Possible Feynman diagrams for the theoretically favoured states are shown in fig. 5.1.

5.2 Event Selection

Event selection and candidate reconstruction occurs in two steps. $\mathrm{B_s} \to \mathrm{J}/\psi(\mu^+\mu^-)\phi(\mathrm{K^+K^-})$ candidates are constructed using a method adapted from that used to construct $\mathrm{B_s} \to \mathrm{J}/\psi\phi$ candidates for $\mathcal{CP}$-violation studies (section 5.2.1). These $\mathrm{B_s}$ candidates are then used to form the daughter particles for a possible $\mathrm{B_s}\pi^{\pm}$ end-state (section 5.2.2).

As there is no need to maintain backward-compatibility with a 7 TeV ATLAS analysis, optimisation of the selection cuts to maximise sensitivity to ρ_{X} is discussed where appropriate.

5.2.1 $\mathrm{B_s}$ Candidate Reconstruction

$\mathrm{B_s} \rightarrow \mathrm{J}/\psi(\mu^+\mu^-)\phi(\mathrm{K^+K^-})$ candidates are reconstructed using the method described in section 4.2.2 with the following updates:

- Events from the 7 TeV LHC run (periods B–M, 4.9 fb^{-1} of integrated luminosity) are included, with events passing any b-physics di-muon trigger retained for further analysis[1];
- as precision measurements of the $\mathrm{B_s}$ proper decay time are not required, the `L2StarA` triggers from 8 TeV LHC periods B–C (for a total of 19.5 fb^{-1} of integrated luminosity) are included in the event selection;
- the event must contain at least one PV, formed from at least six ID tracks[2];
- $\phi \rightarrow \mathrm{K^+K^-}$ candidates are formed from all pairs of oppositely charged ID tracks with $p_{\mathrm{T}}(\mathrm{K}) > 700\,\mathrm{MeV}$[3];
- The $\mathrm{B_s}$ candidates are required to have a proper decay time (as given by eq. (4.13)) of $t > 0.2\,\mathrm{ps}$. This cut is imposed to reduce the prompt $\mathrm{J}/\psi + 2$ track combinatorial background (see section 5.2.2.2).

The $\mathrm{B_s} \rightarrow \mathrm{J}/\psi\phi$ candidate that is selected from the event (based on the lowest χ^2 for the four track vertex fit) is retained for further analysis if $p_{\mathrm{T}}(\mathrm{B_s}) > 10\,\mathrm{GeV}$.

For the retained events, the $\mathrm{B_s} \rightarrow \mathrm{J}/\psi\phi$ candidate is associated with a production PV, using the method outlined in section 4.2.2.5, and $\mathrm{B_s}\pi^{\pm}$ candidate reconstruction is performed.

---

[1] See [186].

[2] As opposed to four.

[3] Relaxing the p_{T} requirement from 1 GeV.

5.2.2 $\mathrm{B_s}\pi^\pm$ Candidate Reconstruction

For retained $\mathrm{B_s} \to \mathrm{J}/\psi\phi$ candidates, $\mathrm{B_s}\pi^\pm$ candidates are formed using all ID tracks, under a pion mass hypothesis, where:

- The ID track is associated with the $\mathrm{B_s}$ production PV;
- $p_\mathrm{T}(\pi^\pm) > 500\,\mathrm{MeV}$, see section 5.2.2.3;
- The ID track is not associated with a lepton candidate. Electron candidates are taken as those passing the tight electron quality criteria given in [152]; muon candidates are taken from the `STACO-Combined` and `STACO-Tagged` muon candidates within the event.

5.2.2.1 Event Observables

The per-candidate observables extracted for use in the $\mathrm{B_s}\pi^\pm$ mass fits are the reconstructed $\mathrm{B_s}\pi^\pm$ mass, $m(\mathrm{B_s}\pi^\pm)$, and its uncertainty. $m(\mathrm{B_s}\pi^\pm)$ is defined as

$$m(\mathrm{B_s}\pi^\pm) = m(\mathrm{J}/\psi\mathrm{K}^+\mathrm{K}^-\pi^\pm) - m(\mathrm{J}/\psi\mathrm{K}^+\mathrm{K}^-) + m_\mathrm{Fit}(\mathrm{B_s}) \tag{5.2}$$

where $m_\mathrm{Fit}(\mathrm{B_s})$ is the $\mathrm{B_s}$ mass extracted from the $\mathrm{B_s} \to \mathrm{J}/\psi\phi$ mass fits (see section 5.4.1). The mass uncertainty is taken from the uncertainty in the five reconstructed tracks used to determine $m(\mathrm{J}/\psi\mathrm{K}^+\mathrm{K}^-\pi^\pm)$.

5.2.2.2 Optimisation of $\mathrm{B_s}$ Reconstruction Criteria

The use of a $\mathrm{B_s}$ proper decay time cut to reduce the combinatorial background contribution to the $\mathrm{B_s} \to \mathrm{J}/\psi\phi$ dataset allows optimisation of the dataset to maximise the sensitivity of ρ_X (see section 5.4.3) to a contribution from $X(5568) \to \mathrm{B_s}\pi^\pm$ decays. Maximal sensitivity to a signal contribution to ρ_X is achieved by minimising the fitted ρ_X value to a background only $\mathrm{B_s}\pi^\pm$ dataset.

A background only $\mathrm{B_s}\pi^\pm$ dataset is constructed using $\mathrm{B_s}$ candidates from the mass background sidebands of the $\mathrm{B_s} \to \mathrm{J}/\psi\phi$ dataset and MC $\mathrm{B_s} \to \mathrm{J}/\psi\phi$ events. The minimum of ρ_X as a function of the proper decay time cut is used to select the optimised proper decay time cut. The fitted values of ρ_X for a selection of alternative proper decay time cuts is shown in table 5.1.

5.2.2.3 Optimisation of $\mathrm{B_s}\pi^\pm$ Reconstruction Criteria

Optimisation of the pion p_T cut is performed by maximising the ratio $\frac{S}{\sqrt{S+B}}$, where S and B are the number of signal and background events selected into

Proper Decay Time Cut [ps]	ρ_X
0.10	0.0123
0.15	0.0121
0.20	0.0115
0.30	0.0121
0.40	0.0125
0.50	0.0123

Table 5.1: 95 % CLs limits on ρ_X, as a function of the proper decay time cut used to select B_s candidates for use in a background only $B_s\pi^\pm$ dataset.

the analysis dataset.

A number of signal and background $B_s\pi^\pm$ datasets are produced from MC samples, and $B_s\pi^\pm$ candidates selected from the $B_s \to J/\psi\phi$ mass background sidebands. These datasets differ in the relative ratios of signal ($B_s\pi^\pm$ MC events) and background ($B_s \to J/\psi\phi$ mass sidebands and MC) events, and are used to examine the effects of the pion p_T cuts under differing assumptions of ρ_X. For all datasets, $p_T(\pi^\pm) > 500$ MeV provides an optimal, or near optimal, $\frac{S}{\sqrt{S+B}}$ ratio, with lower assumed values of ρ_X slightly favouring a higher pion p_T cut. The measured $\frac{S}{\sqrt{S+B}}$ obtained from MC studies, as a function of the pion p_T cut for two values of ρ_X are given in fig. 5.2.

On average there are 1.8 $B_s\pi^\pm$ candidates for each B_s candidate. Removing the production PV pointing requirement from the $B_s\pi^\pm$ candidate reconstruction recovers ≈7 % of true $X(5568) \to B_s\pi^\pm$ decays (in MC) where the pion is not associated with the production PV. The increase in combinatorics, however, provides a strong preference for the pointing requirement. Similarly, no χ^2 cut is used to recover the single 'best' $B_s\pi^\pm$ candidate from an event. MC studies implementing such a cut result in a loss of 30 % of true signal events[4], and a subsequent loss of sensitivity to a possible signal contribution to ρ_X.

---

[4] Implementing the cut in data results in a loss of 44 % of $B_s\pi^\pm$ candidates, demonstrating some degree of physics mis-modelling in the underlying event implementation in `Pythia`.

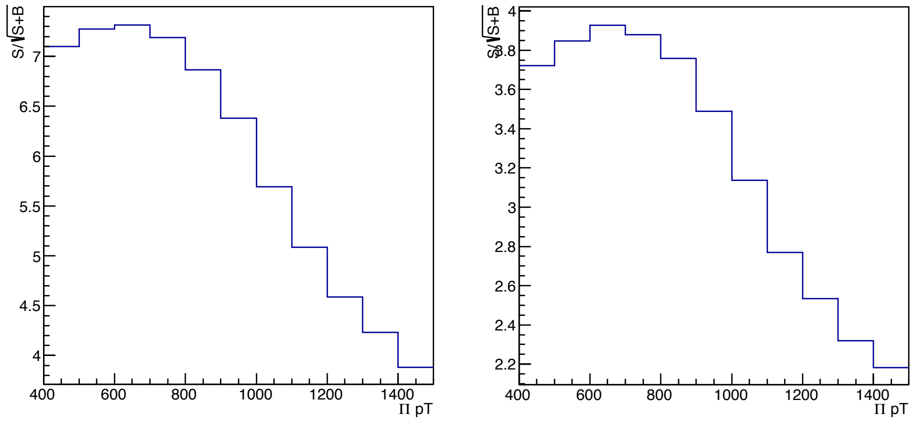

(a) $\rho_{\mathrm{X}} = 6.0\,\%$ (b) $\rho_{\mathrm{X}} = 3.0\,\%$

Figure 5.2: $\frac{S}{\sqrt{S+B}}$ as a function of the pion p_{T} [MeV] cut for $\rho_{\mathrm{X}} = 6.0\,\%$ (left) and $\rho_{\mathrm{X}} = 3.0\,\%$ (right).

5.3 Fit Models

To extract the physics parameters of interest from the resultant $\mathrm{B_s} \to \mathrm{J}/\psi\phi$ and $\mathrm{B_s}\pi^{\pm}$ datasets, four fits are performed:

- An unbinned maximal likelihood fit is performed on the $\mathrm{B_s}$ mass distribution in the $\mathrm{B_s} \to \mathrm{J}/\psi\phi$ dataset. This fit is used to extract the $\mathrm{B_s}$ mass, $m_{\mathrm{Fit}}(\mathrm{B_s})$, and the number of $\mathrm{B_s} \to \mathrm{J}/\psi\phi$ signal candidates, $N_{\mathrm{B_s}}$, in the $\mathrm{B_s}\pi^{\pm}$ dataset;
- An unbinned maximal likelihood fit is performed on the $m(\mathrm{B_s}\pi^{\pm})$ mass distribution in the $\mathrm{B_s}\pi^{\pm}$ dataset. This fit is performed in two stages:
  - the shape of the background mass PDF is fixed from a background only dataset;
  - a second fit is then performed to obtain the signal contribution, N_{X}, in the $\mathrm{B_s}\pi^{\pm}$ dataset under investigation.

  The results of these fits are used to validate the modelling assumptions used in the fit. Evidence of a signal $X(5568) \to \mathrm{B_s}\pi^{\pm}$ component in the $\mathrm{B_s}\pi^{\pm}$ dataset would be observed by a N_{X} incompatible with zero;
- An asymptotic/modified frequentist CLs [2, 3, 4] is used to extract a 95 % confidence limit on the upper value of N_{X};

- The limits imposed on N_X, along with knowledge of the relative reconstruction efficiencies for $\mathrm{B_s}$ and $X(5568)$ candidates, are used to establish a 95 % confidence limit on the upper value of ρ_X.

The $\mathrm{B_s}$ and $\mathrm{B_s}\pi^\pm$ fit and their results are described in sections 5.3.1 and 5.3.2 and sections 5.4.1 and 5.4.2. Calculation of the CLs limits for N_X and ρ_X are discussed in section 5.4.3.

5.3.1 $\mathrm{B_s}$ Mass Fits

An unbinned maximal likelihood fit is performed using the `RooFit` framework to extract a $\mathrm{B_s}$ rich sample for use in $\mathrm{B_s}\pi^\pm$ mass fits. The negative log likelihood function used in this fit is given by

$$\ln\mathcal{L} = \sum\nolimits_i \ln\left\{f_\mathrm{S}\cdot\mathcal{F}_\mathrm{S} + (1-f_\mathrm{S})\cdot\mathcal{F}_\mathrm{Bck}\right\} \tag{5.3}$$

where f_S is the fitted fraction of signal events that are described by the PDF $\mathcal{F}_\mathrm{S}$, and $\mathcal{F}_\mathrm{Bck}$ describes the combinatorial background component. No specific b-physics backgrounds are modelled.

5.3.1.1 Signal Component

The signal PDF $\mathcal{F}_\mathrm{S}$ consists of the sum of two Gaussians sharing a common mean. The mean, standard deviations, and relative fractions are determined from the fit to data.

5.3.1.2 Combinatorial Background Component

The combinatorial background is modelled by a single positive exponential, with the exponential decay constant determined from the fit to data.

5.3.1.3 The Fit Procedure

Independent fits are performed for the the 7 TeV, 8 TeV, and combined datasets. In addition to these fits, an alternative $\mathrm{B_s}\to \mathrm{J}/\psi\phi$ dataset (and its associated $\mathrm{B_s}\pi^\pm$ dataset) is produced with $p_\mathrm{T}(\mathrm{B_s}) > 15\,\mathrm{GeV}$ for compatibility with the current CMS and LHCb results [187, 188].

The results of these fits are shown in section 5.4.1.

5.3.2 $\mathrm{B_s}\pi^\pm$ Mass Fits

The total PDF fitted in the $\mathrm{B_s}\pi^\pm$ likelihood fit is given by

$$\mathcal{F} = N_\mathrm{X}\cdot\mathcal{F}_\mathrm{S} + (N_\mathrm{Cand} - N_\mathrm{X})\cdot\mathcal{F}_\mathrm{Bck} \tag{5.4}$$

where $\mathcal{F}_\mathrm{S}$ and $\mathcal{F}_\mathrm{Bck}$ are the $\mathrm{B_s}\pi^\pm$ signal and background PDFs respectively, and N_Cand is the number of events within the dataset.

5.3.2.1 Signal Component

The hypothesised signal is modelled as a Breit-Wigner parameterisation [41] appropriate for an S-wave two-body decay near threshold

$$BW\left(m(\mathrm{B_s}\pi^\pm)\right) = \frac{m(\mathrm{B_s}\pi^\pm)\cdot M_\mathrm{X}\cdot\Gamma\left(m(\mathrm{B_s}\pi^\pm)\right)}{\left(M_\mathrm{X}^2 - m(\mathrm{B_s}\pi^\pm)^2\right)^2 + M_\mathrm{X}^2\cdot\Gamma^2\left(m(\mathrm{B_s}\pi^\pm)\right)} \tag{5.5}$$

where the mass dependent width is given by

$$\Gamma\left(m(\mathrm{B_s}\pi^\pm)\right) = \Gamma_\mathrm{X}\cdot\frac{q_1}{q_0} \tag{5.6}$$

and q_1 and q_0 are the magnitudes of the three-momenta of the $\mathrm{B_s}$ meson in the rest frame of the $\mathrm{B_s}\pi^\pm$ system at the invariant mass equal to $m(\mathrm{B_s}\pi^\pm)$ and M_X, respectively. The mass, M_X, and width, Γ_X, are taken from the DØ results [175] where $M_\mathrm{X} = 5567.8\,\mathrm{MeV}$ and $\Gamma_\mathrm{X} = 21.9\,\mathrm{MeV}$.

The signal mass PDF, $\mathcal{F}_\mathrm{S}$, is given by the S-wave Breit-Wigner parameterisation given in eq. (5.5) convoluted by a per-candidate Gaussian whose width is given by the candidate's mass uncertainty.

To examine detector response to such a decay, a 1 000 000 event fully-reconstructed MC sample is generated where the $\mathrm{B_{s,1}}(5830)^0$ particle within `Pythia` is used to simulate a possible $X(5568) \to \mathrm{B_s}\pi^\pm$ decay through manipulation of its properties in the `Pythia` particle and decay tables.

5.3.2.2 Background Component

The background PDF, $\mathcal{F}_\mathrm{Bck}$, is given by the polynomial threshold function [41]

$$\mathcal{F}_\mathrm{Bck} = \left(\frac{m(\mathrm{B_s}\pi^\pm) - m_\mathrm{Thr}}{n}\right)^a \cdot \exp\left(\sum_{i=1}^{4} p_i \cdot \left(\frac{m(\mathrm{B_s}\pi^\pm) - m_\mathrm{Thr}}{n}\right)^i\right) \tag{5.7}$$

where the constants a, n, and p_i are obtained from fits to background-only data samples. The threshold, m_Thr, is given by the sum of the fitted $\mathrm{B_s}$ mass and the world average charged pion mass as given in [18].

5.3.2.3 The Fit Procedure

The background PDF is fitted using an unbinned maximum likelihood fit from a combination of $\mathrm{B_s}\pi^\pm$ events taken from the $\mathrm{B_s} \to \mathrm{J}/\psi\phi$ background sidebands[5],

---

[5] Events with $m(\mathrm{J}/\psi\mathrm{K^+K^-})$ between 5150 MeV to 5210 MeV and 5510 MeV to 5650 MeV.

and MC $\mathrm{B_s} \to \mathrm{J}/\psi\phi$ events used to simulate prompt $\mathrm{B_s}$ production. Relative normalisation of these samples is taken from the expected combinatorial background contribution in the $5346.6\,\mathrm{MeV} < m(\mathrm{J}/\psi\mathrm{K^+K^-}) < 5386.6\,\mathrm{MeV}$ region. The background description is then fixed for use in the fit to the $\mathrm{B_s}\pi^\pm$ dataset.

An unbinned likelihood fit is then used to fit the signal contribution, N_X, to the $\mathrm{B_s}\pi^\pm$ dataset.

5.4 Results

The following results are obtained from the 7 TeV and 8 TeV datasets.

5.4.1 $\mathrm{B_s}$ Mass Fits

Mass fit projections from the assorted $\mathrm{B_s} \to \mathrm{J}/\psi\phi$ datasets are shown in figs. 5.3 and 5.4. For the combined dataset with $p_\mathrm{T}(\mathrm{B_s}) > 10\,\mathrm{GeV}$, the fitted $\mathrm{B_s}$ mass ($m_\mathrm{Fit}(\mathrm{B_s}) = (5366.6 \pm 0.1)\,\mathrm{MeV}$) is consistent with the world average $\mathrm{B_s}$ mass as listed in [18] ($(5366.89 \pm 0.19)\,\mathrm{MeV}$) and the weighted standard deviation of the Gaussians fitted for the signal component of the dataset is consistent with fits to fully-reconstructed MC samples.

For production of the $\mathrm{B_s}$-rich $\mathrm{B_s}\pi^\pm$ datasets, only events with $m(\mathrm{J}/\psi\mathrm{K^+K^-})$ between 5346.6 MeV to 5386.6 MeV are used to form $\mathrm{B_s}\pi^\pm$ candidates. The $\mathrm{B_s}$ signal event counts, for the full $\mathrm{B_s} \to \mathrm{J}/\psi\phi$ datasets, and the mass region used for $\mathrm{B_s}\pi^\pm$ candidate construction is shown in table 5.2.

5.4.2 $\mathrm{B_s}\pi^\pm$ Mass Fits

Mass fit projections for the combined dataset are shown in fig. 5.5. Fit projections for the 7 TeV and 8 TeV $\mathrm{B_s}\pi^\pm$ datasets with $p_\mathrm{T}(\mathrm{B_s}) > 10\,\mathrm{GeV}$ are shown in fig. 5.6. The signal event counts, extracted from the final fits to the $\mathrm{B_s}\pi^\pm$ datasets, and their uncertainty are given in table 5.3. For each fit, the possible signal contribution is consistent with a background only hypothesis.

5.4.3 Upper Limits on ρ_X

The yields of N_X and $N_{\mathrm{B_s}}$ are used to evaluate the relative production rate as

$$\rho_\mathrm{X} = \frac{N_\mathrm{X}}{N_{\mathrm{B_s}}} \cdot \frac{1}{\epsilon_\mathrm{Rel}} \tag{5.8}$$

where

$$\epsilon_\mathrm{Rel} = \frac{\epsilon_\mathrm{X}}{\epsilon_{\mathrm{B_s}}}. \tag{5.9}$$

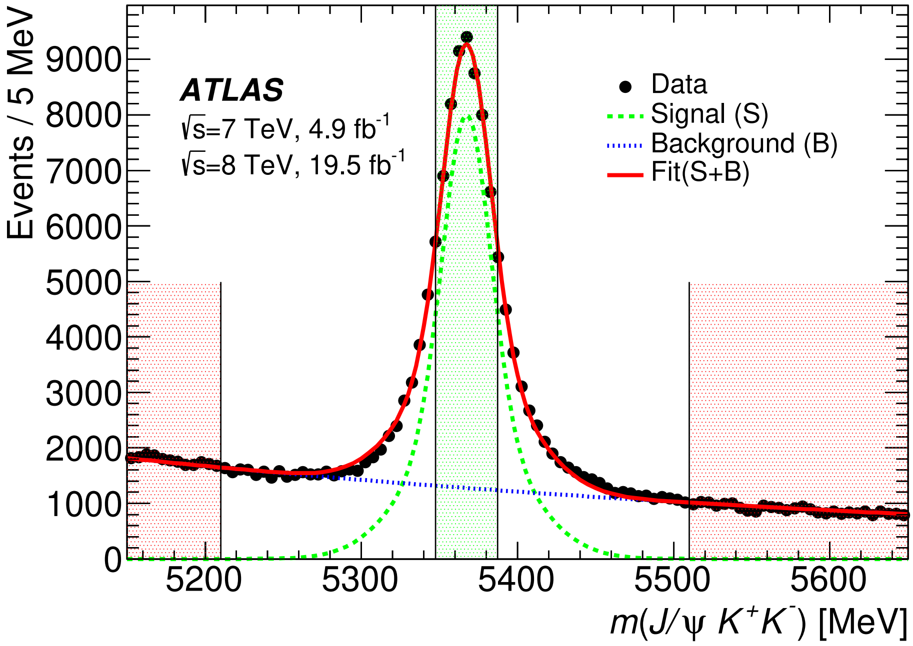

Figure 5.3: Mass fit projection for $\mathrm{B_s}$ candidates with $p_\mathrm{T}(\mathrm{B_s}) > 10\,\mathrm{GeV}$. Shown is the data (black), signal and background PDF projections (green and blue), and the total fit projection (red). The $\mathrm{B_s}$-rich signal region (5346.6 MeV to 5386.6 MeV) is shown in the green band around the $\mathrm{B_s}$ mass peak, while the background $\mathrm{B_s}$ candidates are taken from the red highlighted regions.

Dataset	$p_\mathrm{T}(\mathrm{B_s}) > 10\,\mathrm{GeV}$	$p_\mathrm{T}(\mathrm{B_s}) > 15\,\mathrm{GeV}$
7 TeV	8364 ± 361	6914 ± 235
8 TeV	76 452 ± 417	64 113 ± 363
Combined	84 668 ± 443	70 897 ± 386

(a) $\mathrm{B_s}$ signal candidates in the full dataset

Dataset	$p_\mathrm{T}(\mathrm{B_s}) > 10\,\mathrm{GeV}$	$p_\mathrm{T}(\mathrm{B_s}) > 15\,\mathrm{GeV}$
7 TeV	5109 ± 183	4146 ± 140
8 TeV	47 650 ± 261	39 320 ± 223
Combined	52 751 ± 276	43 460 ± 237

(b) $\mathrm{B_s}$ signal candidates in the signal region

Table 5.2: $\mathrm{B_s}$ signal candidates event counts for the full $\mathrm{B_s} \to \mathrm{J}/\psi\phi$ datasets (top) and for the 5346.6 MeV to 5386.6 MeV signal region.

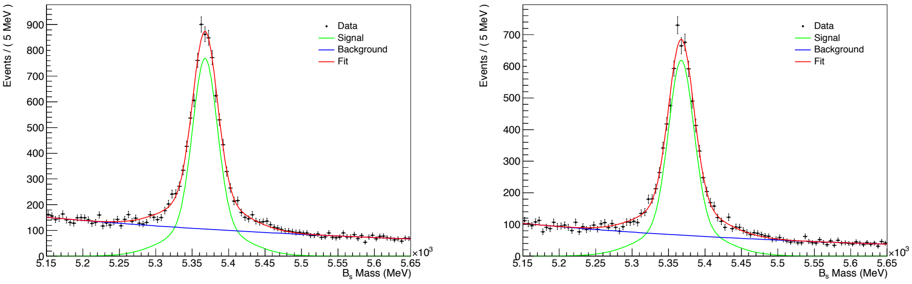

(a) 7 TeV, $p_{\mathrm{T}}(\mathrm{B_s}) > 10\,\mathrm{GeV}$ (b) 7 TeV, $p_{\mathrm{T}}(\mathrm{B_s}) > 15\,\mathrm{GeV}$

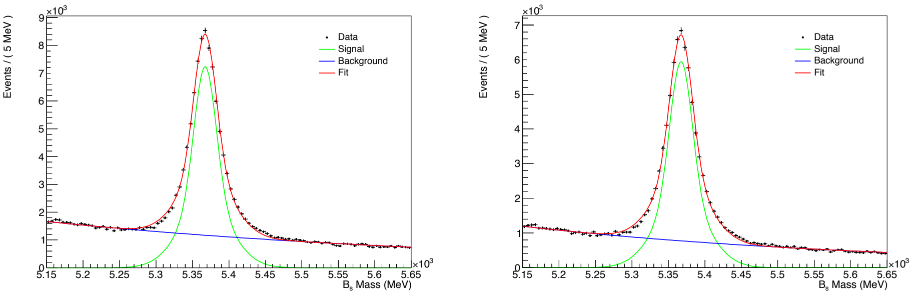

(c) 8 TeV, $p_{\mathrm{T}}(\mathrm{B_s}) > 10\,\mathrm{GeV}$ (d) 8 TeV, $p_{\mathrm{T}}(\mathrm{B_s}) > 15\,\mathrm{GeV}$

Figure 5.4: Mass fit projections for 7 TeV (upper) and 8 TeV (lower) $\mathrm{B_s}$ candidates with $p_{\mathrm{T}}(\mathrm{B_s}) > 10\,\mathrm{GeV}$ (left) and $p_{\mathrm{T}}(\mathrm{B_s}) > 10\,\mathrm{GeV}$ (right). Shown is the data (black), signal and background PDF projections (green and blue), and the total fit projection (red).

	N_{X}	
Dataset	$p_{\mathrm{T}}(\mathrm{B_s}) > 10\,\mathrm{GeV}$	$p_{\mathrm{T}}(\mathrm{B_s}) > 15\,\mathrm{GeV}$
7 TeV	12 ± 43	16 ± 32
8 TeV	-50 ± 136	-37 ± 112
Combined	64 ± 142	-29 ± 146

Table 5.3: X event counts.

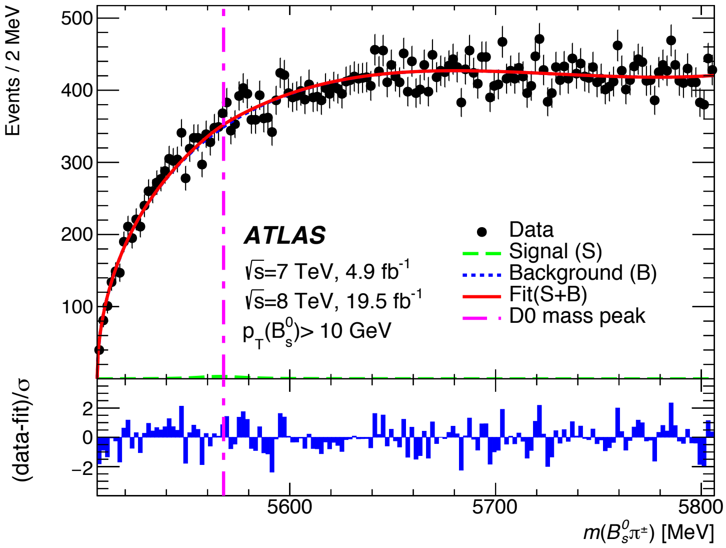

(a) $p_{\mathrm{T}}(\mathrm{B_s}) > 10\,\mathrm{GeV}$

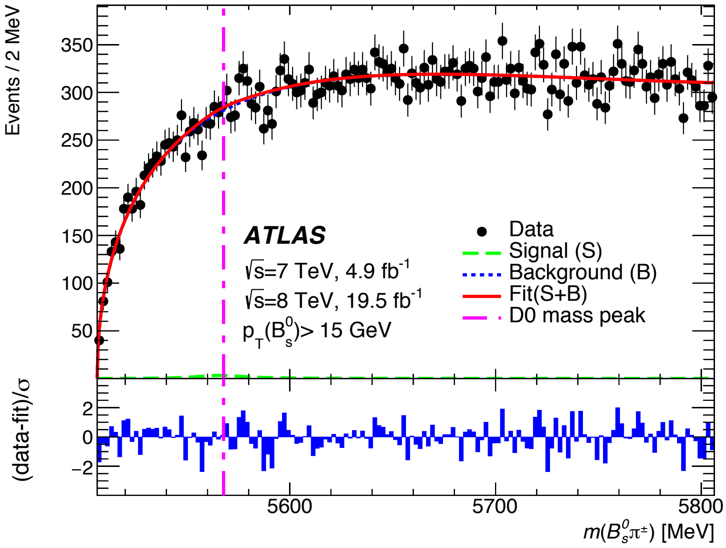

(b) $p_{\mathrm{T}}(\mathrm{B_s}) > 15\,\mathrm{GeV}$

Figure 5.5: $\mathrm{B_s}\pi^{\pm}$ mass fit projections for $p_{\mathrm{T}}(\mathrm{B_s}) > 10\,\mathrm{GeV}$ (upper) and $p_{\mathrm{T}}(\mathrm{B_s}) > 15\,\mathrm{GeV}$ (lower). Shown are the data (black), signal and background PDF projections (green and blue dashes), and the total fit projection (red). The pull distribution (blue) is shown below the fit. The D∅ fitted mass is shown by the pink line. $m(\mathrm{B_s}\pi^{\pm})$ is given by $m(\mathrm{B_s}\pi^{\pm}) = m(\mathrm{J}/\psi\mathrm{K}^{+}\mathrm{K}^{-}\pi^{\pm}) - m(\mathrm{J}/\psi\mathrm{K}^{+}\mathrm{K}^{-}) + m_{\mathrm{Fit}}(\mathrm{B_s})$. Due to the small signal contribution, the background PDF projection is largely obscured by the total fit projection.

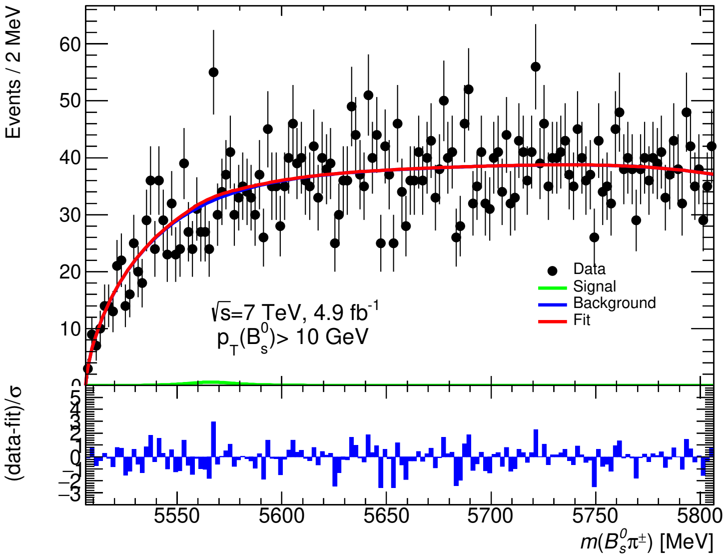

(a) 7 TeV

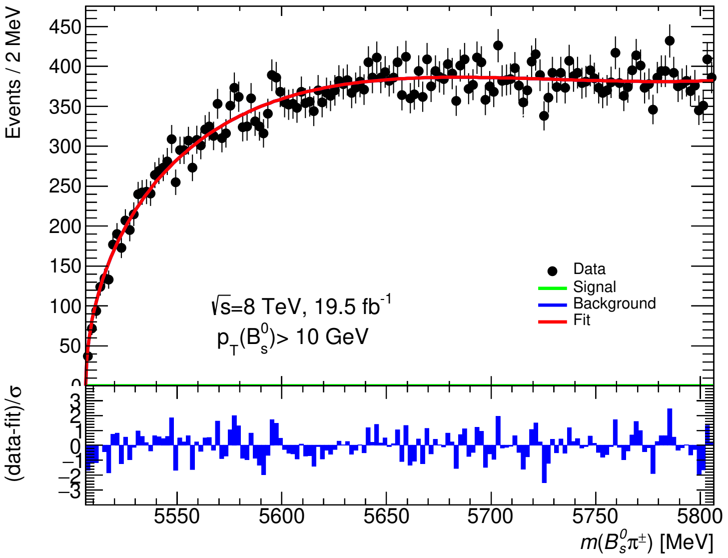

(b) 8 TeV

Figure 5.6: $\mathrm{B_s}\pi^\pm$ mass fit projections for 7 TeV (upper) and 8 TeV (lower) data where $p_\mathrm{T}(\mathrm{B_s}) > 10\,\mathrm{GeV}$. Shown are the data (black), signal and background PDF projections (green and blue dashes), and the total fit projection (red). The pull distribution (blue) is shown below the fit. $m(\mathrm{B_s}\pi^\pm)$ is given by $m(\mathrm{B_s}\pi^\pm) = m(\mathrm{J}/\psi\mathrm{K}^+\mathrm{K}^-\pi^\pm) - m(\mathrm{J}/\psi\mathrm{K}^+\mathrm{K}^-) + m_\mathrm{Fit}(\mathrm{B_s})$. As with fig. 5.5, the background PDF projection is largely obscured by the total fit projection.

Factorisation of ϵ_{X} allows the common $\epsilon_{\mathrm{B_s}}$ terms to be cancelled[6]. For this analysis, the pion reconstruction and selection efficiencies are parameterised as a function of $\mathrm{B_s}$ p_{T}, as this removes the need to tune the MC p_{T} distributions from data.

5.4.3.1 CLs Limits on Signal Event Counts

CLs limits on N_{X} are obtained using the CLs functionality within the `RooStats` package. 95 % CLs confidence limits for N_{X} are given in table 5.4.

Systematic uncertainties that potentially effect the limit placed on N_{X} from the default fit $\mathrm{B_s}\pi^{\pm}$ mass fit are assessed through a number of alternative fit models and procedures:

- Signal Model Variations:
  - The S-wave Breit-Wigner distribution is replaced by a P-wave Breit-Wigner distribution appropriate for a resonance near threshold;
  - The per-candidate Gaussian convolution used to model detector reconstruction inefficiencies is replaced by a per-candidate triple Gaussian convolution. The relative normalisation between the Gaussians, and the width of the second and third Gaussian relative to the first is fixed from fully reconstructed $X(5568) \to \mathrm{B_s}\pi^{\pm}$ MC events.
- Background Model Variations:
  - The order of the polynomial used in the threshold function, that describes the background mass distribution, is increased by one;
  - The threshold function is replaced with a seventh-order Chebyshev polynomial [41].
- Alternative Fit Procedures:
  - The background mass PDF is fitted and fixed from the full $\mathrm{B_s}\pi^{\pm}$ dataset, with the signal region excluded from the background only fit;
  - An additional term is added to the $\mathrm{B_s}\pi^{\pm}$ total PDF (eq. (5.4)) to accommodate a possible difference between the $\mathrm{B_s}\pi^{\pm}$ mass distributions:
    - fake $\mathrm{B_s} + 1$ track and prompt $\mathrm{B_s} + 1$ track combinatorial background;

---

[6] Under the assumption that the p_{T} spectra of $\mathrm{B_s}$ candidates between the two production sources are not significantly dissimilar.

	95 % CLs Limits	
Fit Type	$p_T(\mathrm{B_s}) > 10\,\mathrm{GeV}$	$p_T(\mathrm{B_s}) > 15\,\mathrm{GeV}$
Default Fit	$N_\mathrm{X} < 264$	$N_\mathrm{X} < 213$
Including Systematics	$N_\mathrm{X} < 382$	$N_\mathrm{X} < 356$

Table 5.4: 95 % CLs limits on N_X for the combined dataset.

  - ∗ a contribution from true $\mathrm{B_s} + 1$ track backgrounds where the $\mathrm{B_s}$ candidate is from a true $X(5568) \to \mathrm{B_s}\pi^\pm$ decay. The shape of this self-background is fixed from MC events;

  The fraction of this background, relative to the non self-background shape, is determined in the background only fit.

95 % CLs confidence limits for N_X, including these systematic considerations, are given in table 5.4.

5.4.3.2 CLs Limits on ρ_X

The reconstruction efficiency for the pion is parameterised as

$$\epsilon_\mathrm{Rel} = \epsilon_\mathrm{Det} \cdot \epsilon_0 \tag{5.10}$$

where ϵ_Det accounts for detector reconstruction and analysis selection efficiency, and ϵ_0 corrects for pions under the p_T selection threshold. These efficiency functions[7] are parameterised by $\mathrm{B_s}$ p_T and pseudo-rapidity[8] and determined from $X(5568) \to \mathrm{B_s}\pi^\pm$ MC events using a binned χ^2 fit.

For the calculation of ρ_X, the weighted-average ϵ_Rel is taken from the signal region of the $\mathrm{B_s}\pi^\pm$ dataset, and results in $\epsilon_\mathrm{Rel} = 0.53 \pm 0.09$ for $\mathrm{B_s}\pi^\pm$ candidates with $p_T(\mathrm{B_s}) > 10\,\mathrm{GeV}$, and $\epsilon_\mathrm{Rel} = 0.60 \pm 0.10$ for $p_T(\mathrm{B_s}) > 15\,\mathrm{GeV}$. 95 % CLs confidence limits for ρ_X are given in table 5.5.

Systematic uncertainties potentially effecting the limit placed on ρ_X arise from three sources:

- N_X: Systematic uncertainties on N_X are discussed in section 5.4.3.1.
- $N_{\mathrm{B_s}}$:

---

[7] A single positive exponential and a second-order Chebyshev polynomial whose relative normalisation and shape parameters are determined from a fit to data.

[8] To accommodate the varying detector resolution.

	95 % CLs Limits	
Fit Type	$p_{\mathrm{T}}(\mathrm{B_s}) > 10\,\mathrm{GeV}$	$p_{\mathrm{T}}(\mathrm{B_s}) > 15\,\mathrm{GeV}$
Default Fit	$\rho_{\mathrm{X}} < 0.010$	$\rho_{\mathrm{X}} < 0.012$
Including Systematics	$\rho_{\mathrm{X}} < 0.015$	$\rho_{\mathrm{X}} < 0.016$

Table 5.5: 95 % CLs limits on ρ_{X} for the combined dataset.

  - Signal Model Variations: An alternative signal mass model, with a triple Gaussian, is used to estimate the uncertainty due to possible mis-modelling of the signal PDF.
  - Background Model Variations: Alternative background models, the sum of an exponential and a constant, and an exponential and linear function, are used to estimate the uncertainty due to possible mis-modelling of the background PDF.

- ϵ_{Rel}:
  - Average ϵ_{Rel}: 10 000 alternative fits are performed where the weighted-average ϵ_{Rel} includes an additional per-candidate Poisson smearing. The width of the distribution of ϵ_{Rel} from these variant fits are included as a systematic uncertainty on ϵ_{Rel}.
  - Pseudo-Rapidity Intervals: The pseudo-rapidity dependence of ϵ_{Det} and ϵ_0 by default separates barrel and end-cap $\mathrm{B_s}$ candidates. Alternative binnings (1, 3, 4, and 5) are used to estimate the systematic uncertainty due to the default binning.
  - Inner Detector Material Description: Estimates of the systematic uncertainty due to the pion reconstruction is assessed through the use of the method developed for [189]. The results of this procedure yield a relative uncertainty of 7 % compared to the baseline ϵ_{Rel} calculation.

95 % CLs confidence limits for ρ_{X}, including these systematic considerations are given in table 5.5.

5.4.3.3 Generalised Search for a $\mathrm{B_s}\pi^{\pm}$ Resonance

As no statistically significant signal contribution is found at the mass and decay width proposed by D0, a hypothesis test is performed for a possible signal contribution with a signal mass every 5 MeV between 5550 MeV to 5700 MeV. The scan limits are selected such that 99 % of a S-wave Breit-Wigner resonance

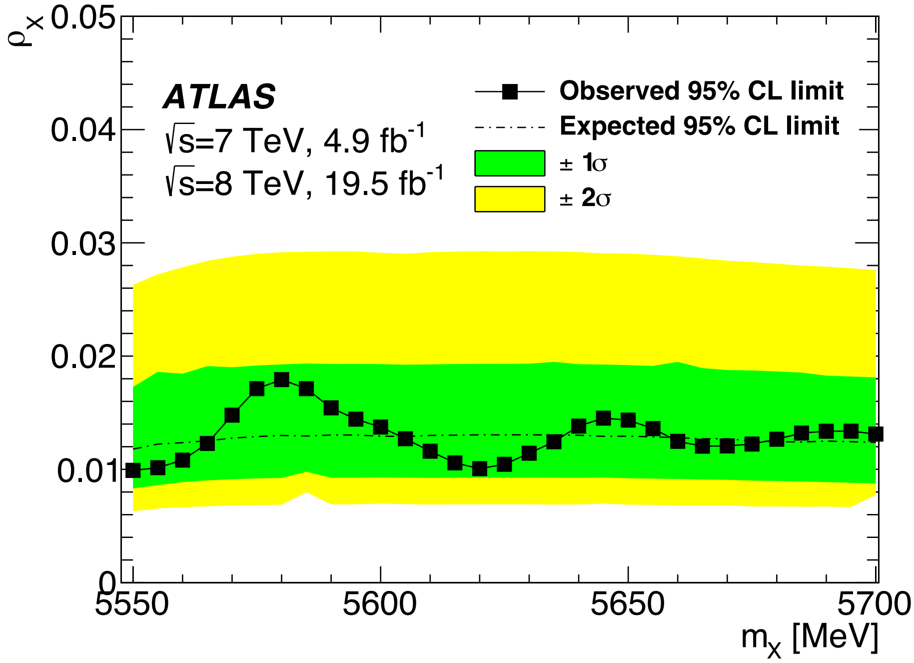

Figure 5.7: ρ_{X} scan as a function of $m(\mathrm{X})$. Shown are the expected and observed 95 % confidence limits on ρ_{X} (black line and black points), and the $\pm 1\sigma$ (green) and $\pm 2\sigma$ (yellow) limits. CLs limits are statistical only.

would be retained in the mass interval from the $\mathrm{B_s}\pi^{\pm}$ threshold to 6000 MeV after a per-candidate Gaussian convolution. Furthermore, six mass dependent ϵ_{Det} and ϵ_0 functions are fitted from MC to accommodate the ϵ_{Rel} dependence upon the mass of the mother particle (for a given signal hypothesis).

Chapter 6

Conclusions

The results of the two analyses described in this thesis are discussed below.

6.1 Measuring $\mathcal{CP}$-Violation in the $B_s \to J/\psi\phi$ Decay

A measurement of the $B_s \to J/\psi\phi$ decay parameters, extracted using $14.3\,\mathrm{fb}^{-1}$ of ATLAS data collected during 2012 at a centre of mass energy of 8 TeV has been performed, and the result of this analysis statistically combined with a previous ATLAS analysis [127] using $4.9\,\mathrm{fb}^{-1}$ of data at a centre of mass energy of 7 TeV to produce the final ATLAS Run1 result:

$$\begin{aligned}\phi_s &= -0.090 \pm 0.078\ (\text{stat.}) \pm 0.041\ (\text{syst.})\ \text{rad}\\ \Delta\Gamma_s &= 0.085 \pm 0.011\ (\text{stat.}) \pm 0.007\ (\text{syst.})\ \text{ps}^{-1}\\ \Gamma_s &= 0.675 \pm 0.003\ (\text{stat.}) \pm 0.003\ (\text{syst.})\ \text{ps}^{-1}.\end{aligned}$$

These results are consistent with recent LHCb [190] and CMS [191] results for this decay channel (see fig. 6.1), and offer no evidence of BSM physics.

The $B_s \to J/\psi\phi$ analysis will remain a cornerstone of ATLAS b-physics, with a Run2 analysis already underway. The expected increase in integrated luminosity, coupled with the improvements to the detector (the *Insertable b-Layer* (IBL)) will allow the collection of a large, high-quality $B_s \to J/\psi\phi$ dataset, while the ongoing development of a $B^\pm \to J/\psi K^\pm$ online mass/lifetime fit will allow the swift correction of functionally deficient triggers. Coupled to these hardware changes, a number of improvements to the $B_s \to J/\psi\phi$ likelihood fit have been proposed for the Run2 analysis:

- The statistical combination of the 7 TeV and 8 TeV results should be replaced by a simultaneous fit of the Run1 and Run2 datasets. Furthermore, the assumption of inter- and intra-analyses systematics being uncorrelated should be assessed through the use of ensemble toy MC;

- An additional $\mathrm{B_s} \rightarrow \mathrm{J}/\psi\phi$ fit should be performed, where a $m(\mathrm{K^+K^-})$ dependence is included in the fit of the parameters related to S-wave $\mathrm{B_s} \rightarrow \mathrm{J}/\psi \mathrm{K^+K^-}$ decays. Such a fit would allow ATLAS to unambiguously determine the sign of $\Delta\Gamma_\mathrm{s}$;
- The current $\mathrm{B_d}$ background description should replace the independent proper decay time and transversity angle PDFs with a single PDF to correctly model the proper decay time dependence of the transversity angle distribution for $\mathrm{B_d}$ decays;
- The Λ_b transversity angle PDF is based on the assumption of a flat transversity angle distribution shaped only by detector acceptance. It is expected that measurements of the transversity angle distribution in the central rapidity region will become available from ATLAS and CMS during Run2.

In the long term future, the muon *New Small Wheels* (NSW) (additional tracking chambers in the far-forward region of the ATLAS MS, installation expected during LS2) will allow additional trigger optimisation, while the addition of an online track trigger (expected for the HL-LHC) would allow simultaneous fitting of the $\mathrm{B_s} \rightarrow \mathrm{J}/\psi\phi$ and $\mathrm{B_s} \rightarrow \phi\phi$ decay channels and provide a second probe (via gluonic-penguin decays) of BSM physics in the $\mathrm{B_s}$ system.

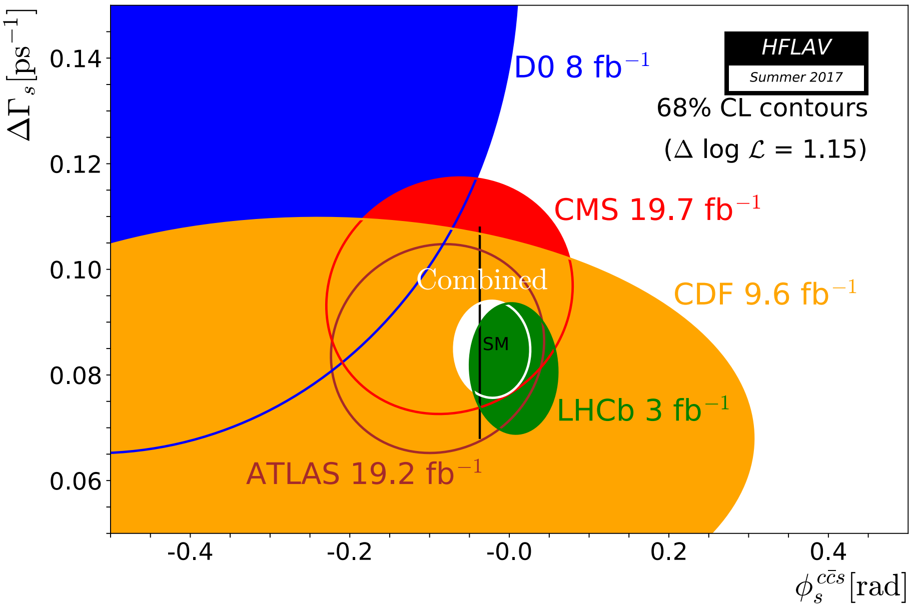

Figure 6.1: 2D profile likelihood scans in the ϕ_s–$\Delta\Gamma_s$ plane for the $\mathrm{B_s} \to \mathrm{J}/\psi\phi$ decay. Shown are the 68 % confidence limits for ATLAS (dark red), CMS (light red), LHCb (green), DØ (blue), and CDF (yellow). Also shown is the world average for these measurements (white) and the SM prediction [172] (black). Figure from [192].

6.2 Searches for Resonant Structures in the $\mathrm{B_s}\pi^{\pm}$ Mass Spectrum

A search for a state decaying to a $\mathrm{B_s}\pi^{\pm}$ pair, consistent with that observed by DØ [175] has been performed, and no evidence of this state is found in the combined 7 TeV (4.9 fb^{-1}) and 8 TeV (19.5 fb^{-1}) ATLAS datasets. This is consistent with recent LHCb [188], CMS [187], and CDF [193] results for searches of the $X(5568) \to \mathrm{B_s}\pi^{\pm}$ decay.

The 95 % CLs confidence limits on the number of $X(5568) \to \mathrm{B_s}\pi^{\pm}$ candidates observed by ATLAS is 382 and 356 for $p_{\mathrm{T}}(\mathrm{B_s}) > 10$ GeV and $p_{\mathrm{T}}(\mathrm{B_s}) > 15$ GeV respectively. For these candidates, the 95 % CLs confidence limits on ρ_{X}, the relative production rate between observed $X(5568)$ and $\mathrm{B_s}$ candidates, are determined to be $\rho_{\mathrm{X}} < 0.015$ and $\rho_{\mathrm{X}} < 0.016$, and are comparable to the CMS results (1.1 % and 1.0 %) in the central rapidity region.

95 % CLs confidence limits for ρ_{X} are calculated for alternative mass hypotheses of the mother particle. No deviation larger than $\pm 1\sigma$ from a background only

hypothesis is observed in these tests, and the CLs confidence limit, as a function of mass, is comparable to the most recent CMS results [187].

Appendix A

$B_s \rightarrow J/\psi\phi$, Additional Information

The `DQ2` datasets used in the $B_s \rightarrow J/\psi\phi$ default fit are shown in table A.1(a), while the GRL used to select events 'Good-for-Physics' are shown in table A.1(b).

`data12_8TeV.periodB.physics_Bphysics.PhysCont.DAOD_JPSIMUMU.grp14_v03_p1425/`
`data12_8TeV.periodC.physics_Bphysics.PhysCont.DAOD_JPSIMUMU.grp14_v04_p1425/`
`data12_8TeV.periodE.physics_Bphysics.PhysCont.DAOD_JPSIMUMU.grp14_v03_p1425/`
`data12_8TeV.periodF.physics_Bphysics.PhysCont.DAOD_JPSIMUMU.grp14_v03_p1425/`
`data12_8TeV.periodG.physics_Bphysics.PhysCont.DAOD_JPSIMUMU.grp14_v03_p1425/`
`data12_8TeV.periodH.physics_Bphysics.PhysCont.DAOD_JPSIMUMU.grp14_v04_p1425/`
`data12_8TeV.periodI.physics_Bphysics.PhysCont.DAOD_JPSIMUMU.grp14_v03_p1425/`
`data12_8TeV.periodJ.physics_Bphysics.PhysCont.DAOD_JPSIMUMU.grp14_v03_p1425/`
`data12_8TeV.periodL.physics_Bphysics.PhysCont.DAOD_JPSIMUMU.grp14_v03_p1425/`

(a) DQ2 Datasets

`data12_8TeV.periodAllYear_DetStatus-v61-pro14-02_DQDefects-00-01-00_PHYS_StandardGRL_All_Good.xml`

(b) GRLs

Table A.1: $\mathrm{B_s} \to \mathrm{J}/\psi\phi$ `DQ2` datasets and GRLs.

Appendix B

Glossary of Terms

A glossary of terms used in this thesis:

AIC	Akaike Information Criterion
AOD	Analysis Object Data
BIC	Bayesian Information Criterion
BSM	Beyond the Standard Model
$\mathcal{C}$	Charge parity
CERN	European Organisation for Nuclear Research
CKM Matrix	The Cabibbo–Kobayashi–Maskawa Matrix
CLs Limit	Limit set using the CLs method
CP-Violation	Violation of the combined C and P symmetries
CSC	Cathode Strip Chambers
CTP	Central Trigger Processor
DAQ	Data Acquisition system
DCS	Detector Control System
DQ2	The ATLAS distributed dataset management software
EB	Event Builder
EF	Event Filter
ELMB	Embedded Local Monitor Board
EMEC	Electromagnetic End-Caps
ESD	Event Summary Data
GCS	Global Control Stations
HL-LHC	High Luminosity - Large Hadron Collider
HLT	High Level Trigger
IBL	The Insertable b-Layer
ID	The ATLAS Inner Detector
LCS	Local Control Stations

LHC	Large Hadron Collider
LINAC2	Linear accelerator 2
LS1	Long Shutdown 1
LS2	Long Shutdown 2
LVL1	Level-1 Trigger
LVL2	Level-2 Trigger
MBTS	Minimum Bias Trigger Scintillators
MC	Monte Carlo
MDT	Monitored Drift Tube
MLE	Maximal-Likelihood Estimate
MS	Muon Spectrometer
NSW	New Small Wheels
$\mathcal{P}$	Space parity
PMNS Matrix	The Pontecorvo-–Maki-–Nakagawa–-Sakata Matrix
PS	Proton Synchrotron
PSB	Proton Synchrotron Booster
PV	Primary Vertex
RDO	Raw Data Object
ROB	Readout Buffers
ROD	Readout Drivers
ROI	Regions of Interest
RPC	Resistive Plate Chambers
Run1	Run 1 of LHC data taking
Run2	Run 2 of LHC data taking
SCS	Sub-Detector Control Stations
SCT	Semiconductor Tracker
SM	Standard Model of Particle Physics
SPS	Super Proton Synchrotron
SSB	Spontaneous Symmetry Breaking
SU(N)	The special unitary group of degree N
SV	Secondary Vertex
SVM	Split-Vertex Method
$\mathcal{T}$	Time parity
TDAQ	Trigger and Data Acquisition system
TGC	Thin Gap Chambers
TOT	Time Over Threshold
TRT	Transition Radiation Tracker
VEV	Vacuum Expectation Value
WLCG	Worldwide LHC Computing Grid

Bibliography

[1] J. P. Ellis. "TikZ-Feynman: Feynman diagrams with TikZ". In: *Comput. Phys. Commun.* 210 (2017), pp. 103–123. DOI: `10.1016/j.cpc.2016.08.019`.

[2] G. Cowan et al. "Asymptotic Formulae for Likelihood-Based Tests of New Physics". In: *Eur. Phys. J.* C71, 1554 (2011). DOI: `10.1140/epjc/s10052-011-1554-0`.

[3] G. Cowan et al. "Erratum: Asymptotic Formulae for Likelihood-Based Tests of New Physics". In: *Eur. Phys. J.* C73, 2501 (2013). DOI: `10.1140/epjc/s10052-013-2501-z`.

[4] A. L. Read. "Presentation of Search Results: The CLs Technique". In: *J. Phys.* G28.10 (2002), pp. 2693–2704. DOI: `10.1088/0954-3899/28/10/313`.

[5] S. L. Glashow. "Partial-Symmetries of Weak Interactions". In: *Nucl. Phys.* 22.4 (1961), pp. 579–588. DOI: `10.1016/0029-5582(61)90469-2`.

[6] A. Salam and J. C. Ward. "Electromagnetic and Weak Interactions". In: *Phys. Lett.* 13.2 (1964), pp. 168–171. DOI: `10.1016/0031-9163(64)90711-5`.

[7] S. Weinberg. "A Model of Leptons". In: *Phys. Rev. Lett.* 19 (1967), pp. 1264–1266. DOI: `10.1103/PhysRevLett.19.1264`.

[8] G. 't Hooft and M. Veltman. "Regularization and Renormalization of Gauge Fields". In: *Nucl. Phys.* 44.1 (1972), pp. 189–213. DOI: `10.1016/0550-3213(72)90279-9`.

[9] C. N. Yang and R. L. Mills. "Conservation of Isotopic Spin and Isotopic Gauge Invariance". In: *Phys. Rev.* 96 (1954), pp. 191–195. DOI: `10.1103/PhysRev.96.191`.

[10] M. Gell-Mann. "Symmetries of Baryons and Mesons". In: *Phys. Rev.* 125 (1962), pp. 1067–1084. DOI: `10.1103/PhysRev.125.1067`.

[11] F. Englert and R. Brout. “Broken Symmetry and the Mass of Gauge Vector Mesons”. In: *Phys. Rev. Lett.* 13 (1964), pp. 321–323. DOI: `10.1103/PhysRevLett.13.321`.

[12] P. W. Higgs. “Broken Symmetries and the Masses of Gauge Bosons”. In: *Phys. Rev. Lett.* 13 (1964), pp. 508–509. DOI: `10.1103/PhysRevLett.13.508`.

[13] R. P. Feynman. “Space-Time Approach to Quantum Electrodynamics”. In: *Phys. Rev.* 76 (1949), pp. 769–789. DOI: `10.1103/PhysRev.76.769`.

[14] M. Drewes. “The Phenomenology Of Right Handed Neutrinos”. In: *Int. J. Mod. Phys.* E22.8, 1330019 (2013). DOI: `10.1142/S0218301313300191`.

[15] I. J. R. Aitchison and A. J. G. Hey. *Gauge Theories in Particle Physics.* Vol. 1: *From Relativistic Quantum Mechanics to QED.* 4th ed. CRC Press, 2013. ISBN: 978-14-6651-299-3.

[16] I. J. R. Aitchison and A. J. G. Hey. *Gauge Theories in Particle Physics.* Vol. 2: *Non-Abelian Gauge Theories: QCD and The Electroweak Theory.* 4th ed. CRC Press, 2013. ISBN: 978-14-6651-307-5.

[17] J. Goldstone. “Field theories with «Superconductor» solutions”. In: *J. Nuovo Cim* 19.1 (1961), pp. 154–164. DOI: `10.1007/BF02812722`.

[18] Particle Data Group. “Review of Particle Physics”. In: *Chin. Phys.* C40.10, 100001 (2016). DOI: `10.1088/1674-1137/40/10/100001`.

[19] M. Peskin and D. Schroeder. *An Introduction To Quantum Field Theory.* Westview Press, 1995. ISBN: 978-02-0150-397-5.

[20] M. Kobayashi and T. Maskawa. “CP-Violation in the Renormalizable Theory of Weak Interaction”. In: *Progr. Theor. Phys.* 49.2 (1973), pp. 652–657. DOI: `10.1143/PTP.49.652`.

[21] E. Noether. “Invariant Variation Problems”. In: *Transp. Theory. Stat. Phys.* 1.3 (1971), pp. 186–207. DOI: `10.1080/00411457108231446`.

[22] J. D. Jackson. *Classical Electrodynamics.* 3rd ed. Wiley, 1998. ISBN: 978-04-7130-932-1.

[23] I. I. Bigi and A. I. Sanda. *CP Violation.* 2nd ed. Cambridge University Press, 2009. ISBN: 978-05-2184-794-0.

[24] M. S. Sozzi. *Discrete Symmetries and CP Violation.* Oxford University Press, 2012. ISBN: 978-01-9965-542-7.

[25] W. Pauli. “Exclusion Principle, Lorentz Group and Reflection of Space-Time and Charge”. In: *Niels Bohr and the Development of Physics.* Ed. by W. Pauli, L. Rosenfeld, and V. Weisskopf. Pergamon Press, pp. 30–51. ISBN: 978-11-1460-742-2.

[26] R. Jost. “Eine Bemerkung zum CTP-Theorem”. In: *Helv. Phys. Acta.* 30 (1957), pp. 409–416. URL: `http://www.e-periodica.ch/digbib/view?pid=hpa-001:1957:30`.

[27] O. W. Greenberg. “*CPT* Violation Implies Violation of Lorentz Invariance”. In: *Phys. Rev. Lett.* 89, 231602 (2002). DOI: `10.1103/PhysRevLett.89.231602`.

[28] T. D. Lee and C. N. Yang. “Question of Parity Conservation in Weak Interactions”. In: *Phys. Rev.* 104 (1957), pp. 254–258. DOI: `10.1103/PhysRev.104.254`.

[29] T. D. Lee and C. N. Yang. “Question of Parity Conservation in Weak Interactions”. In: *Phys. Rev.* 106 (1957), pp. 1371–1371. DOI: `10.1103/PhysRev.106.1371`.

[30] R. T. Cox, C. G. McIlwraith, and B. Kurrelmeyer. “Apparent Evidence of Polarization in a Beam of β-Rays”. In: *Proc. Natl. Acad. Sci. U.S.A.* 17.7 (1928), pp. 544–549. URL: `http://www.pnas.org/content/14/7/544.citation`.

[31] C. T. Chase. “The Scattering of Fast Electrons by Metals. II. Polarization by Double Scattering at Right Angles”. In: *Phys. Rev.* 36 (1930), pp. 1060–1065. DOI: `10.1103/PhysRev.36.1060`.

[32] C. S. Wu et al. “Experimental Test of Parity Conservation in Beta Decay”. In: *Phys. Rev.* 105 (1957), pp. 1413–1415. DOI: `10.1103/PhysRev.105.1413`.

[33] R. L. Garwin, L. M. Lederman, and M. Weinrich. “Observations of the Failure of Conservation of Parity and Charge Conjugation in Meson Decays: the Magnetic Moment of the Free Muon”. In: *Phys. Rev.* 105 (1957), pp. 1415–1417. DOI: `10.1103/PhysRev.105.1415`.

[34] J. H. Christenson et al. “Evidence for the 2π Decay of the K_2^0 Meson”. In: *Phys. Rev. Lett.* 13 (1964), pp. 138–140. DOI: `10.1103/PhysRevLett.13.138`.

[35] V. L. Fitch et al. “Evidence for Constructive Interference Between Coherently Regenerated and CP-Nonconserving Amplitudes”. In: *Phys. Rev. Lett.* 15 (1965), pp. 73–76. DOI: `10.1103/PhysRevLett.15.73`.

[36] CERN-Dortmund-Edinburgh-Mainz-Orsay-Pisa-Siegen Collaboration. “First Evidence for Direct CP Violation”. In: *Phys. Lett.* 206.1 (1988), pp. 169–176. DOI: `10.1016/0370-2693(88)91282-8`.

[37] J. J. Aubert et al. “Experimental Observation of a Heavy Particle J”. In: *Phys. Rev. Lett.* 33 (1974), pp. 1404–1406. DOI: `10.1103/PhysRevLett.33.1404`.

[38] J. -E. Augustin et al. "Discovery of a Narrow Resonance in e^+e^- Annihilation". In: *Phys. Rev. Lett.* 33 (1974), pp. 1406–1408. DOI: `10.1103/PhysRevLett.33.1406`.

[39] S. W. Herb et al. "Observation of a Dimuon Resonance at 9.5 GeV in 400-GeV Proton-Nucleus Collisions". In: *Phys. Rev. Lett.* 39 (1977), pp. 252–255. DOI: `10.1103/PhysRevLett.39.252`.

[40] Z. Maki, M. Nakagawa, and S. Sakata. "Remarks on the Unified Model of Elementary Particles". In: *Progr. Theor. Phys.* 28.5 (1962), pp. 870–880. DOI: `10.1143/PTP.28.870`.

[41] G. B. Arfken, H. J. Weber, and F. E. Harris. *Mathematical Methods for Physicists*. 7th ed. Academic Press, 2012. ISBN: 978-01-2384-654-9.

[42] C. Jarlskoga and R. Storab. "Unitarity Polygons and CP Violation Areas and Phases in the Standard Electroweak Model". In: *Phys. Lett.* B208.2 (1988), pp. 268–274. DOI: `10.1016/0370-2693(88)90428-5`.

[43] L. Wolfenstein. "Parametrization of the Kobayashi-Maskawa Matrix". In: *Phys. Rev. Lett.* 51 (1983), pp. 1945–1947. DOI: `10.1103/PhysRevLett.51.1945`.

[44] P. Koppenburg. "CP violation and CKM studies". In: *The European Physical Society Conference on High Energy Physics*. Proceedings of Science, 2015. URL: `https://pos.sissa.it/234/`.

[45] E. Schrödinger. "An Undulatory Theory of the Mechanics of Atoms and Molecules". In: *Phys. Rev.* 28 (1926), pp. 1049–1070. DOI: `10.1103/PhysRev.28.1049`.

[46] V. Weisskopf and E. Wigner. "Berechnung der natürlichen Linienbreite auf Grund der Diracschen Lichttheorie". In: *Z. Phys.* 63 (1930), pp. 54–73. DOI: `10.1007/BF01336768`.

[47] V. Weisskopf and E. Wigner. "Über die natürliche Linienbreite in der Strahlung des harmonischen Oszillators". In: *Z. Phys.* 65 (1930), pp. 18–29. DOI: `10.1007/BF01397406`.

[48] P. A. M. Dirac. *The Principles Of Quantum Mechanics*. 4th ed. Oxford University Press, 1998. ISBN: 978-01-9852-011-5.

[49] BABAR Collaboration. "Measurements of Branching Fractions and $\mathcal{CP}$-Violating Asymmetries in $B^0 \to \pi^+\pi^-, K^+\pi^-, K^+K^-$ Decays". In: *Phys. Rev. Lett.* 89, 281802 (2002). DOI: `10.1103/PhysRevLett.89.281802`.

[50] O. Brüning et al., eds. *LHC Design Report*. Vol. 1: *The LHC Main Ring*. CERN, 2004. ISBN: 92-9083-224-0. DOI: `10.5170/CERN-2004-003-V-1`.

[51] O. Brüning et al., eds. *LHC Design Report.* Vol. 2: *The LHC Infrastructure and General Services.* CERN, 2004. ISBN: 92-9083-236-3. DOI: `10.5170/CERN-2004-003-V-2`.

[52] M. Benedikt et al., eds. *LHC Design Report.* Vol. 3: *The LHC Injector Chain.* CERN, 2004. ISBN: 92-9083-239-8. DOI: `10.5170/CERN-2004-003-V-3`.

[53] *ECFA-CERN Workshop on Large Hadron Collider in the LEP tunnel.* CERN, 1984. URL: `http://cds.cern.ch/record/154938`.

[54] ATLAS Collaboration. "The ATLAS Experiment at the CERN Large Hadron Collider". In: *J. Instrum.* 3, S08003 (2008). DOI: `10.1088/1748-0221/3/08/S08003`.

[55] CMS Collaboration. "The CMS experiment at the CERN LHC". In: *J. Instrum.* 3, S08004 (2008). DOI: `10.1088/1748-0221/3/08/S08004`.

[56] ALICE Collaboration. "The ALICE experiment at the CERN LHC". In: *J. Instrum.* 3, S08002 (2008). DOI: `10.1088/1748-0221/3/08/S08002`.

[57] LHCb Collaboration. "The LHCb Detector at the LHC". In: *J. Instrum.* 3, S08005 (2008). DOI: `10.1088/1748-0221/3/08/S08005`.

[58] LHCf Collaboration. "The LHCf detector at the CERN Large Hadron Collider". In: *J. Instrum.* 3, S08006 (2008). DOI: `10.1088/1748-0221/3/08/S08006`.

[59] TOTEM Collaboration. "The TOTEM Experiment at the CERN Large Hadron Collider". In: *J. Instrum.* 3, S08007 (2008). DOI: `10.1088/1748-0221/3/08/S08007`.

[60] MoEDAL collaboration. "Search for Magnetic Monopoles with the MoEDAL Prototype Trapping Detector in 8 TeV Proton-Proton Collisions at the LHC". In: *J. High Energy Phys.* 2016.8, 67 (2016). DOI: `10.1007/JHEP08(2016)067`.

[61] C. De Melis. *The CERN accelerator complex.* URL: `https://cds.cern.ch/record/2197559`.

[62] *CAS – CERN Accelerator School. Intermediate Accelerator Physics.* CERN, 2003. ISBN: 92-9083-267-3. DOI: `10.5170/CERN-2006-002`.

[63] *CAS – CERN Accelerator School. Advanced Accelerator Physics.* CERN, 2014. ISBN: 978-92-9083-411-3. DOI: `10.5170/CERN-2014-009`.

[64] W. Herr and B. Muratori. "Concept of Luminosity". In: *CAS – CERN Accelerator School. Intermediate Accelerator Physics.* CERN, 2003, pp. 361–377. ISBN: 92-9083-267-3. DOI: `10.5170/CERN-2006-002`.

[65] T. Golling et al. “The ATLAS Data Quality Defect Database System”. In: *Eur. Phys. J.* C72, 1960 (2012). DOI: `10.1140/epjc/s10052-012-1960-y`.

[66] ATLAS Collaboration. *Luminosity Public Results*. URL: `https://twiki.cern.ch/twiki/bin/view/AtlasPublic/LuminosityPublicResults`.

[67] ATLAS Collaboration. *ATLAS: Letter of Intent for a General-Purpose pp Experiment at the Large Hadron Collider at CERN*. Letter of Intent CERN-LHCC-92-004. CERN, 1992. URL: `https://cds.cern.ch/record/291061`.

[68] ATLAS Collaboration. *ATLAS Detector and Physics Performance: Technical Design Report. Volume I*. ATLAS Technical Design Report ATLAS-TDR-14. CERN, 1999. URL: `https://cds.cern.ch/record/391176`.

[69] ATLAS Collaboration. *ATLAS Detector and Physics Performance: Technical Design Report. Volume II*. ATLAS Technical Design Report ATLAS-TDR-15. CERN, 1999. URL: `https://cds.cern.ch/record/391177`.

[70] ATLAS Collaboration. *Expected Performance of the ATLAS Experiment*. Vol. 1: *Performance*. CERN, 2009. ISBN: 978-92-9083-321-5. URL: `https://cds.cern.ch/record/1125884`.

[71] ATLAS Collaboration. *Expected Performance of the ATLAS Experiment*. Vol. 2: *Standard Model, Top Quark, B-Physics*. CERN, 2009. ISBN: 978-92-9083-321-5. URL: `https://cds.cern.ch/record/1125884`.

[72] ATLAS Collaboration. *Expected Performance of the ATLAS Experiment*. Vol. 3: *Higgs Boson, Supersymmetry, Exotic Processes*. CERN, 2009. ISBN: 978-92-9083-321-5. URL: `https://cds.cern.ch/record/1125884`.

[73] ATLAS Collaboration. *ATLAS Muon Spectrometer: Technical Design Report*. ATLAS Technical Design Report ATLAS-TDR-10. CERN, 1997. URL: `https://cds.cern.ch/record/331068`.

[74] F. Akesson et al. *ATLAS Tracking Event Data Model. Version for AtlasOffline release 12.0.0*. ATLAS Public Note ATL-SOFT-PUB-2006-004. CERN, 2006. URL: `https://cds.cern.ch/record/973401`.

[75] T. Cornelissen et al. *Updates of the ATLAS Tracking Event Data Model (Release 13)*. ATLAS Public Note ATL-SOFT-PUB-2007-003. CERN, 2007. URL: `https://cds.cern.ch/record/1038095`.

[76] ATLAS Collaboration. *ATLAS Magnet System: Technical Design Report. Magnet Project TDR: Volume 1*. ATLAS Technical Design Report ATLAS-TDR-6. CERN, 1997. URL: `https://cds.cern.ch/record/338080`.

[77] ATLAS Collaboration. *ATLAS Central Solenoid: Technical Design Report. Magnet Project TDR: Volume 4*. ATLAS Technical Design Report ATLAS-TDR-9. CERN, 1997. URL: `https://cds.cern.ch/record/331067`.

[78] ATLAS Collaboration. *ATLAS Barrel Toroid: Technical Design Report. Magnet Project TDR: Volume 2*. ATLAS Technical Design Report ATLAS-TDR-7. CERN, 1997. URL: `https://cds.cern.ch/record/331065`.

[79] ATLAS Collaboration. *ATLAS End-Cap Toroid: Technical Design Report. Magnet Project TDR: Volume 3*. ATLAS Technical Design Report ATLAS-TDR-8. CERN, 1997. URL: `https://cds.cern.ch/record/331066`.

[80] J. J. Goodson. "Search for Supersymmetry in States with Large Missing Transverse Momentum and Three Leptons including a Z-Boson". PhD Thesis. Stony Brook University, 2012. URL: `https://cds.cern.ch/record/1449722`.

[81] ATLAS Collaboration. *ATLAS Inner Detector: Technical Design Report. Volume 1*. ATLAS Technical Design Report ATLAS-TDR-4. CERN, 1997. URL: `https://cds.cern.ch/record/331063`.

[82] ATLAS Collaboration. *ATLAS Inner Detector: Technical Design Report. Volume 2*. ATLAS Technical Design Report ATLAS-TDR-5. CERN, 1997. URL: `https://cds.cern.ch/record/331064`.

[83] ATLAS Collaboration. *ATLAS Pixel Detector: Technical Design Report*. ATLAS Technical Design Report ATLAS-TDR-11. CERN, 1998. URL: `https://cds.cern.ch/record/381263`.

[84] ATLAS Collaboration. *ATLAS Calorimeter Performance: Technical Design Report*. ATLAS Technical Design Report ATLAS-TDR-1. CERN, 1996. URL: `https://cds.cern.ch/record/331059`.

[85] ATLAS Collaboration. *ATLAS Liquid Argon Calorimeter: Technical Design Report*. ATLAS Technical Design Report ATLAS-TDR-2. CERN, 1996. URL: `https://cds.cern.ch/record/331061`.

[86] ATLAS Collaboration. *ATLAS Tile Calorimeter: Technical Design Report*. ATLAS Technical Design Report ATLAS-TDR-3. CERN, 1996. URL: `https://cds.cern.ch/record/331062`.

[87] G. F. Knoll. *Radiation Detection and Measurement*. 4th ed. John Wiley & Sons, 2010. ISBN: 978-04-7013-148-0.

[88] ATLAS Collaboration. *ATLAS Level-1 Trigger: Technical Design Report.* ATLAS Technical Design Report ATLAS-TDR-12. CERN, 1998. URL: `https://cds.cern.ch/record/381429`.

[89] ATLAS Collaboration. *ATLAS High-Level Trigger, Data Acquisition and Controls: Technical Design Report.* ATLAS Technical Design Report ATLAS-TDR-16. CERN, 2003. URL: `https://cds.cern.ch/record/616089`.

[90] CERN. *The first LHC protons run ends with new milestone.* URL: `https://press.cern/press-releases/2012/12/first-lhc-protons-run-ends-new-milestone`.

[91] ATLAS Collaboration. *ATLAS Computing: Technical Design Report.* ATLAS Technical Design Report ATLAS-TDR-17. CERN, 2005. URL: `https://cds.cern.ch/record/837738`.

[92] ATLAS Collaboration. "The Detector Control System of the ATLAS Experiment". In: *J. Instrum.* 3, P05006 (2008). DOI: `10.1088/1748-0221/3/05/P05006`.

[93] ETM. *ETM Professional Control.* URL: `http://www.etm.at`.

[94] CERN. *Rucio.* URL: `https://rucio.cern.ch/`.

[95] CERN. *The PanDA Production and Distributed Analysis System.* URL: `https://twiki.cern.ch/twiki/bin/view/PanDA/PanDA`.

[96] ROOT Collaboration. "ROOT – A C++ Framework for Petabyte Data Storage, Statistical Analysis and Visualization". In: *Comput. Phys. Commun.* 180.12 (2009), pp. 2499–2512. DOI: `10.1016/j.cpc.2009.08.005`.

[97] CERN. *Welcome to the Persistency Web.* URL: `https://twiki.cern.ch/twiki/bin/view/Persistency`.

[98] M. Mambelli et al. "Job Optimization in ATLAS TAG-Based Distributed Analysis". In: *J. Phys. Conf. Ser.* 219.7, 072042 (2010). DOI: `10.1088/1742-6596/219/7/072042`.

[99] P. J. Laycock et al. *Derived Physics Data Production in ATLAS. Experience with Run 1 and Looking Ahead.* ATLAS Public Note ATL-SOFT-PROC-2013-021. CERN, 2013. URL: `https://cds.cern.ch/record/1609646`.

[100] CERN. *The Gaudi Project.* URL: `https://gaudi.web.cern.ch/gaudi/`.

[101] G. Barrand et al. "GAUDI – A Software Architecture and Framework for Building HEP Data Processing Applications". In: *Comput. Phys. Commun.* 140.1 (2001), pp. 45–55. DOI: `10.1016/S0010-4655(01)00254-5`.

[102] CERN. *ROOT Data Analysis Framework*. URL: `https://root.cern.ch/`.

[103] F. James and M. Roos. "Minuit - A System for Function Minimization and Analysis of the Parameter Errors and Correlations". In: *Comput. Phys. Commun.* 10.6 (1975), pp. 343–367. DOI: `10.1016/0010-4655(75)90039-9`.

[104] CERN. *RooFit*. URL: `https://root.cern.ch/roofit`.

[105] CERN. *Welcome to the RooStats Wiki*. URL: `https://twiki.cern.ch/twiki/bin/view/RooStats/WebHome`.

[106] ATLAS Collaboration. "The ATLAS Simulation Infrastructure". In: *Eur. Phys. J.* C70, 823 (2010). DOI: `10.1140/epjc/s10052-010-1429-9`.

[107] A. D. Martin et al. "Parton Distributions for the LHC". In: *Eur. Phys. J.* C63, 189 (2009). DOI: `10.1140/epjc/s10052-009-1072-5`.

[108] O. Behnke et al., eds. *Data Analysis in High Energy Physics*. Wiley-VCH, 2013. ISBN: 978-35-2741-058-3.

[109] I. Narsky and F. C. Porter. *Statistical Analysis Techniques in Particle Physics*. Wiley-VCH, 2013. ISBN: 978-35-2741-086-6.

[110] T. Sjöstrand et al. "High-Energy-Physics Event Generation with Pythia 6.1". In: *Comput. Phys. Commun.* 135.2 (2001), pp. 238–259. DOI: `10.1016/S0010-4655(00)00236-8`.

[111] M. Bähr et al. "Herwig++ Physics and Manual". In: *Eur. Phys. J.* C58, 639 (2008). DOI: `10.1140/epjc/s10052-008-0798-9`.

[112] M. Gyulassy and X-N. Wang. "HIJING 1.0: A Monte Carlo Program for Parton and Particle Production in High Energy Hadronic and Nuclear Collisions". In: *Comput. Phys. Commun.* 83.2 (1994), pp. 307–331. DOI: `10.1016/0010-4655(94)90057-4`.

[113] E. Barberio, B. van Eijk, and Z. Was. "Photos – A Universal Monte Carlo for QED Radiative Corrections in Decays". In: *Comput. Phys. Commun.* 66.1 (1991), pp. 115–128. DOI: `10.1016/0010-4655(91)90012-A`.

[114] P. Golonka et al. "The Tauola-Photos-F Environment for the TAUOLA and PHOTOS packages, Release II". In: *Comput. Phys. Commun.* 174.10 (2006), pp. 818–835. DOI: `10.1016/j.cpc.2005.12.018`.

[115] M. Smizanska. *PythiaB. An Interface to Pythia6 Dedicated to Simulation of Beauty Events*. ATLAS Public Note ATL-COM-PHYS-2003-038. CERN, 2003. URL: `https://cds.cern.ch/record/%3C%3C%5CToDo%3E%3E`.

[116] D. J. Lange. "The EvtGen Particle Decay Simulation Package". In: *Nucl. Instr. Meth. Phys. Res.* A462.1–2 (2001), pp. 152–155. DOI: `10.1016/S0168-9002(01)00089-4`.

[117] J. R. Catmore. "$\mathrm{B}_s^0 \to \mathrm{J}/\psi\phi$ with LHC-ATLAS: Simulations and Sensitivity Studies". PhD Thesis. Lancaster University, 2007. URL: `http://cds.cern.ch/record/1504715`.

[118] Geant4 Collaboration. "Geant4 – A Simulation Toolkit". In: *Nucl. Instr. Meth. Phys. Res.* A506.3 (2003), pp. 250–303. DOI: `10.1016/S0168-9002(03)01368-8`.

[119] T. Cornelissen et al. "The New ATLAS Track Reconstruction (NEWT)". In: *J. Phys. Conf. Ser.* 119.3, 032014 (2008). DOI: `10.1088/1742-6596/119/3/032014`.

[120] R. Frühwirth. "Application of Kalman Filtering to Track and Vertex Fitting". In: *Nucl. Instr. Meth. Phys. Res.* 262.2 (1987), pp. 444–450. DOI: `10.1016/0168-9002(87)90887-4`.

[121] P. Billoir. "Track Fitting with Multiple Scattering: A New Method". In: *Nucl. Instr. Meth. Phys. Res.* 22.2 (1984), pp. 352–366. DOI: `10.1016/0167-5087(84)90274-6`.

[122] ATLAS Collaboration. "Track and vertex reconstruction in the ATLAS experiment". In: *J. Instrum.* 8, C02035 (2013). DOI: `10.1088/1748-0221/8/02/C02035`.

[123] ATLAS Collaboration. "Primary Vertex Reconstruction at the ATLAS Experiment". In: *J. Phys. Conf. Ser.* 898.4, 042056 (2017). DOI: `10.1088/1742-6596/898/4/042056`.

[124] ATLAS Collaboration. "Reconstruction of Primary Vertices at the ATLAS Experiment in Run 1 Proton–Proton Collisions at the LHC". In: *Eur. Phys. J.* C77, 332 (2017). DOI: `10.1140/epjc/s10052-017-4887-5`.

[125] ATLAS Collaboration. *Characterization of Interaction-Point Beam Parameters Using the pp Event-Vertex Distribution Reconstructed in the ATLAS Detector at the LHC*. ATLAS Public Note ATLAS-CONF-2010-027. CERN, 2010. URL: `https://cds.cern.ch/record/1277659`.

[126] S. Hassani et al. “A Muon Identification and Combined Reconstruction Procedure for the ATLAS Detector at the LHC Using the (MUONBOY, STACO, MuTag) Reconstruction Packages”. In: *Nucl. Instr. Meth. Phys. Res.* A572.1 (2007), pp. 77–79. DOI: `10.1016/j.nima.2006.10.340`.

[127] ATLAS Collaboration. “Flavor Tagged Time-Dependent Angular Analysis of the $B_s^0 \to J/\psi\phi$ decay and extraction of $\Delta\Gamma_s$ and the weak phase ϕ_s in ATLAS”. In: *Phys. Rev.* D90, 052007 (2014). DOI: `10.1103/PhysRevD.90.052007`.

[128] ATLAS Collaboration. “Measurement of the CP-Violating Phase ϕ_s and the B_s^0 Meson Decay Width Difference with $\mathrm{B}_\mathrm{s}^0 \to \mathrm{J}/\psi\phi$ Decays in ATLAS”. In: *J. High Energy Phys.* 2016.8, 147 (2016). DOI: `10.1007/JHEP08(2016)147`.

[129] A. E. Barton. “Looking for new physics in the $\mathrm{B}_\mathrm{s}^0 \to \mathrm{J}/\psi\phi$ decay”. PhD Thesis. Lancaster University, 2013. URL: `https://cds.cern.ch/record/1956688`.

[130] S-U. Chung. *Spin Formalism*. URL: `https://suchung.web.cern.ch/suchung/spinfm1.pdf`.

[131] S. Stone and L. Zhang. “S-waves and the Measurement of CP Violating Phases in B_s Decays”. In: *Phys. Rev.* D79, 074024 (2009). DOI: `10.1103/PhysRevD.79.074024`.

[132] Y. Xie et al. “Determination of $2\beta_s$ in $\mathrm{B}_\mathrm{s}^0 \to \mathrm{J}/\psi\mathrm{K}^+\mathrm{K}^-$ Decays in the Presence of a $\mathrm{K}^+\mathrm{K}^-$ S-Wave Contribution”. In: *J. High Energy Phys.* 2009.9, 074 (2009). DOI: `10.1088/1126-6708/2009/09/074`.

[133] BABAR Collaboration. “Search for the $Z(4430)^-$ at BABAR”. In: *Phys. Rev.* D79, 112001 (2009). DOI: `10.1103/PhysRevD.79.112001`.

[134] ATLAS Collaboration. *Trigger Operation Public Results*. URL: `https://twiki.cern.ch/twiki/bin/view/AtlasPublic/TriggerOperationPublicResults`.

[135] ATLAS Collaboration. “Performance of the ATLAS Trigger System in 2010”. In: *Eur. Phys. J.* C72, 1849 (2012). DOI: `10.1140/epjc/s10052-011-1849-1`.

[136] ATLAS Collaboration. “Performance of the ATLAS Muon Trigger in pp Collisions at $\sqrt{s} = 8\,\mathrm{TeV}$”. In: *Eur. Phys. J.* C75, 120 (2015). DOI: `10.1140/epjc/s10052-015-3325-9`.

[137] ATLAS Collaboration. *Performance of the ATLAS muon trigger in 2011*. ATLAS Public Note ATLAS Collaboration. CERN, 2012. URL: `https://cds.cern.ch/record/1462601`.

[138] ATLAS Collaboration. “The Muon High Level Trigger of the ATLAS Experiment”. In: *J. Phys. Conf. Ser.* 219.3, 032025 (2010). DOI: 10.1088/1742-6596/219/3/032025.

[139] E. Piccaro. “Measurement of the ATLAS di-muon trigger efficiency in proton-proton collisions at 7 TeV”. In: *XXXI International Conference on Physics in Collision*. SLAC National Accelerator Laboratory, 2011. URL: https://arxiv.org/abs/1111.4329.

[140] ATLAS Collaboration. *Trigger Public Results*. URL: https://twiki.cern.ch/twiki/bin/view/AtlasPublic/TriggerPublicResults.

[141] ATLAS Collaboration. *Muon Trigger Public Results*. URL: https:https://twiki.cern.ch/twiki/bin/view/AtlasPublic/MuonTriggerPublicResults.

[142] ATLAS Collaboration. *B Physics Trigger Public Results*. URL: https://twiki.cern.ch/twiki/bin/view/AtlasPublic/BPhysicsTriggerPublicResults.

[143] ATLAS Collaboration. “Time-Dependent Angular Analysis of the Decay $\mathrm{B}_\mathrm{s}^0 \to \mathrm{J}/\psi\phi$ and Extraction of $\Delta\Gamma_s$ and the CP-violating weak phase ϕ_s by ATLAS”. In: *J. High Energy Phys.* 2012.12, 72 (2012). DOI: 10.1007/JHEP12(2012)072.

[144] W. J. Dearnaley. “A Trigger Study of CP-Violation and Lifetimes in $\mathrm{B}_\mathrm{s}^0 \to \mathrm{J}/\psi\phi$ Decays in ATLAS”. PhD Thesis. «», 2014. URL: http://eprints.lancs.ac.uk/78629/1/2014dearnaleyphd.pdf.

[145] ATLAS Collaboration. *Measurement of the CP-Violating Phase ϕ_s and the B_s^0 Meson Decay Width Difference with $B_s^0 \to J/\psi\phi$ Decays in ATLAS*. ATLAS Public Note ATLAS-COM-PHYS-2014-598. CERN, 2014. URL: https://cds.cern.ch/record/1708913.

[146] Particle Data Group. “Review of Particle Physics”. In: *Chin. Phys.* C38.9, 090001 (2014). DOI: 10.1088/1674-1137/38/9/090001.

[147] ATLAS Collaboration. *ATLAS B-physics studies at increased LHC luminosity, potential for CP-violation measurement in the $B_s^0 \to J/\psi\phi$ decay*. ATLAS Public Note ATL-PHYS-PUB-2013-010. CERN, 2013. URL: https://cds.cern.ch/record/1604429.

[148] ATLAS Collaboration. “Measurement of the Differential Cross-Sections of Inclusive, Prompt and Non-Prompt J/ψ Production in Proton-Proton Collisions at $\sqrt{7} = 7\,\mathrm{TeV}$”. In: *Nucl. Phys.* B850.3 (2011), pp. 387–444. DOI: 10.1016/j.nuclphysb.2011.05.015.

[149] R. D. Field and R. P Feynman. “A Parametrization of the Properties of Quark Jets”. In: *Nucl. Phys.* B136.1 (1978), pp. 1–76. DOI: 10.1016/0550-3213(78)90015-9.

[150] ATLAS Collaboration. *Jet Charge Studies with the ATLAS Detector Using $\sqrt{s} = 8\,\text{TeV}$ Proton-Proton Collision Data*. ATLAS Public Note ATLAS-CONF-2013-086. CERN, 2013. URL: `https://cds.cern.ch/record/1572980`.

[151] R. Nicolaidou et al. "Muon Identification Procedure for the ATLAS Detector at the LHC Using Muonboy Reconstruction Package and Tests of its Performance using Cosmic Rays and Single Beam Data". In: *J. Phys. Conf. Ser.* 219.3, 032052 (2010). DOI: `10.1088/1742-6596/219/3/032052`.

[152] ATLAS Collaboration. "Electron Performance measurements with the ATLAS Detector using the 2010 LHC Proton-Proton Collision Data". In: *Eur. Phys. J.* C72, 1909 (2012). DOI: `10.1140/epjc/s10052-012-1909-1`.

[153] M. Cacciari, G. P. Salam, and G. Soyez. "The Anti-k_t Jet Clustering Algorithm". In: *J. High Energy Phys.* 2008.4, 063 (2008). DOI: `10.1088/1126-6708/2008/04/063`.

[154] ATLAS Collaboration. "Performance of b-Jet Identification in the ATLAS Experiment". In: *J. Instrum.* 11, P04008 (2016). DOI: `10.1088/1748-0221/11/04/P04008`.

[155] LHCb Collaboration. "Opposite-side flavour tagging of B mesons at the LHCb experiment". In: *Eur. Phys. J.* C72, 2022 (2012). DOI: `10.1140/epjc/s10052-012-2022-1`.

[156] O. Behnke and L. Moneta. "Parameter Estimation". In: *Data Analysis in High Energy Physics*. Ed. by O. Behnke et al. Wiley-VCH, 2013. ISBN: 978-35-2741-058-3.

[157] F. James. *Statistical Methods In Experimental Physics*. World Scientific Publishing Company, 2006. ISBN: 978-98-1270-527-3.

[158] S. S. Wilks. "The Large-Sample Distribution of the Likelihood Ratio for Testing Composite Hypotheses". In: *Ann. Math. Statist.* 9.1 (1938), pp. 60–62. DOI: `10.1214/aoms/1177732360`.

[159] G. Punzi. "Comments on Likelihood Fits with Variable Resolution". In: *PHYSTAT2003*. SLAC National Accelerator Laboratory, 2003. URL: `https://www.slac.stanford.edu/econf/C030908/index.html`.

[160] A. Gut. *Probability: A Graduate Course*. 2nd ed. Springer, 2013. ISBN: 978-14-6144-707-8.

[161] ATLAS Collaboration. *ATLAS Tunes of PYTHIA 6 and Pythia 8 for MC11*. ATLAS Public Note ATL-PHYS-PUB-2011-009. CERN, 2011. URL: `https://cds.cern.ch/record/1363300`.

[162] ATLAS Collaboration. *Summary of ATLAS Pythia 8 Tunes.* ATLAS Public Note ATL-PHYS-PUB-2012-003. CERN, 2012. URL: `https://cds.cern.ch/record/1474107`.

[163] LHCb Collaboration. "Measurement of b Hadron Production Fractions in 7 TeV pp Collisions". In: *Phys. Rev.* D85, 032008 (2012). DOI: `10.1103/PhysRevD.85.032008`.

[164] LHCb Collaboration. *Updated average f_s/f_d b-hadron production fraction ratio for 7 TeV pp collisions.* LHCb Public Note LHCb-CONF-2013-011. CERN, 2013. URL: `https://cds.cern.ch/record/1559262`.

[165] LHCb Collaboration. "Study of the Kinematic Dependences of Λ_b^0 Production in pp Collisions and a Measurement of the $\Lambda_b^0 \to \Lambda_c^+\pi^-$ Branching Fraction". In: *J. High Energy Phys.* 2014.8, 143 (2014). DOI: `10.1007/JHEP08(2014)143`.

[166] LHCb Collaboration. "Study of the Production of Λ_b^0 and $\overline{B}^0$ Hadrons in pp Collisions and First Measurement of the $\Lambda_b^0 \to J/\psi pK^-$ Branching Fraction". In: *Chin. Phys.* C40.1, 011001 (2016). DOI: `10.1088/1674-1137/40/1/011001`.

[167] LHCb Collaboration. "Measurement of the Polarization Amplitudes in $B^0 \to J/\psi K^*(892)^0$ Decays". In: *Phys. Rev.* D88, 052002 (2013). DOI: `10.1103/PhysRevD.88.052002`.

[168] LHCb Collaboration. "Observation of $J/\psi p$ Resonances Consistent with Pentaquark States in $\Lambda_b^0 \to J/\psi K^- p$ Decays". In: *Phys. Rev. Lett.* 115, 072001 (2015). DOI: `10.1103/PhysRevLett.115.072001`.

[169] J. Friedman. "DATA ANALYSIS TECHNIQUES FOR HIGH ENERGY PARTICLE PHYSICS". In: *PROCEEDINGS OF THE 1974 CERN SCHOOL OF COMPUTING.* CERN, 1974, pp. 271–366. DOI: `10.5170/CERN-1974-023`.

[170] G. Schwarz. "Estimating the Dimension of a Model". In: *Ann. Statist.* 6.2 (1978), pp. 461–464. DOI: `10.1214/aos/1176344136`.

[171] H. Akaike. "A New Look at the Statistical Model Identification". In: *IEEE Trans. Autom. Control.* 19.6 (1974), pp. 716–723. DOI: `10.1109/TAC.1974.1100705`.

[172] CKMfitter Group. "Predictions of Selected Flavor Observables Within the Standard Model". In: *Phys. Rev.* D84, 033005 (2011). DOI: `10.1103/PhysRevD.84.033005`.

[173] ATLAS Collaboration. *Alignment of the ATLAS Inner Detector and its Performance in 2012.* ATLAS Public Note ATLAS-CONF-2014-047. CERN, 2014. URL: `https://cds.cern.ch/record/1741021`.

[174] R. Nisius. “On the Combination of Correlated Estimates of a Physics Observable”. In: *Eur. Phys. J.* C74, 74 (2014). DOI: 10.1140/epjc/s10052-014-3004-2.

[175] D0 Collaboration. “Evidence for a $B_s^0\pi^\pm$ State”. In: *Phys. Rev. Lett.* 117, 022003 (2016). DOI: 10.1103/PhysRevLett.117.022003.

[176] W. Chen et al. “Decoding the $X(5568)$ as a Fully Open-Flavor $\mathrm{su\bar{b}\bar{d}}$ Tetraquark State”. In: *Phys. Rev. Lett.* 117, 022003 (2016). DOI: 10.1103/PhysRevLett.117.022002.

[177] Y-R. Liu, X. Liu, and S-L. Zhu. “$X(5568)$ and its Partner States”. In: *Phys. Rev.* D93, 074023 (2016). DOI: 10.1103/PhysRevD.93.074023.

[178] W. Wang and R. Zhu. “Can $X(5568)$ be a Tetraquark State?” In: *Chin. Phys.* C40.9, 093101 (2016). DOI: 10.1088/1674-1137/40/9/093101.

[179] Z-G. Wang. “Analysis of the Strong Decay $X(5568) \to B_s^0\pi^\pm$ with QCD Sum Rules”. In: *Eur. Phys. J.* C76, 279 (2016). DOI: 10.1140/epjc/s10052-016-4133-6.

[180] F. L. Stancu. “$X(5568)$ as a $\mathrm{su\bar{d}\bar{b}}$ Tetraquark in a Simple Quark Model”. In: *J. Phys.* G43.10, 105001 (2016). DOI: 10.1088/0954-3899/43/10/105001.

[181] LHCb Collaboration. “Search for a Structure in the $B_s^0\pi^\pm$ Invariant Mass Spectrum with the ATLAS Experiment”. In: *Phys. Rev. Lett.* 120, 202007 (2018). DOI: 10.1103/PhysRevLett.120.202007.

[182] U. Kulshreshtha, D. S. Kulshreshtha, and J. P. Vary. “Hamiltonian, Path Integral and BRST Formulations of Large N Scalar QCD_2 on the Light-Front and Spontaneous Symmetry Breaking”. In: *Eur. Phys. J.* C75, 174 (2015). DOI: 10.1140/epjc/s10052-015-3377-x.

[183] Belle Collaboration. “Observation of a Narrow Charmoniumlike State in Exclusive $B^\pm \to K^\pm\pi^+\pi^- J/\psi$ Decays”. In: *Phys. Rev. Lett.* 91, 262001 (2003). DOI: 10.1103/PhysRevLett.91.262001.

[184] Belle Collaboration. “Observation of a Resonancelike Structure in the $\pi^\pm J/\psi^{'}$ Mass Distribution in Exclusive $B \to K\pi^\pm J/\psi^{'}$ Decays”. In: *Phys. Rev. Lett.* 100, 142001 (2008). DOI: 10.1103/PhysRevLett.100.142001.

[185] F. -K. F. -K. Guo, C. Hanhart, and U. -G. Meißner. “Interactions Between Heavy Mesons and Goldstone Bosons from Chiral Dynamics”. In: *Eur. Phys. J.* A40, 171 (2009). DOI: 10.1140/epja/i2009-10762-1.

[186] ATLAS Collaboration. *Time Dependent Angular Analysis of the $B_s^0 \to J/\psi\phi$ Decay and Extraction of $\Delta\Gamma$ and the Weak Phase of B_s Mesons in ATLAS.* ATLAS Public Note ATL-COM-PHYS-2013-293. CERN, 2013. URL: `https://cds.cern.ch/record/1523661`.

[187] CMS Collaboration. *Search for the $X(5568)$ state decaying into $B_s^0\pi^\pm$ in proton-proton collisions at $s\surd= 8$ TeV.* CMS Public Note CMS-BPH-16-002-003. CERN, 2016. URL: `https://cds.cern.ch/record/2298234`.

[188] LHCb Collaboration. “Search for Structure in the $\mathrm{B_s^0}\pi^\pm$ Invariant Mass Spectrum”. In: *Phys. Rev. Lett.* 117, 152003 (2016). DOI: `10.1103/PhysRevLett.117.152003`.

[189] ATLAS Collaboration. “Study of the $\mathrm{B_c^+} \to \mathrm{J}/\psi \mathrm{D_s^+}$ and $\mathrm{B_c^+} \to \mathrm{J}/\psi \mathrm{D_s^{*+}}$ Decays with the ATLAS Detector”. In: *Eur. Phys. J.* C76, 4 (2016). DOI: `10.1140/epjc/s10052-015-3743-8`.

[190] LHCb Collaboration. “Precision Measurement of CP Violation in $\mathrm{B_s^0} \to \mathrm{J}/\psi \mathrm{K^+K^-}$ Decays”. In: *Phys. Rev. Lett.* 114, 041801 (2015). DOI: `10.1103/PhysRevLett.114.041801`.

[191] CMS Collaboration. “Measurement of the CP-Violating Weak Phase ϕ_s and the Decay Width Difference $\Delta\Gamma_s$ Using the $\mathrm{B_s^0} \to \mathrm{J}/\psi\phi(1020)$ Decay Channel in pp Collisions at $\sqrt{s} = 8\,\mathrm{TeV}$”. In: *Phys. Lett.* B757.3, 46 (2016). DOI: `10.1016/j.physletb.2016.03.046`.

[192] CERN. *Heavy Flavor Averaging Group.* URL: `https://hflav.web.cern.ch/`.

[193] CDF Collaboration. *A Search for the Exotic Meson $X(5568)$ with the Collider Detector at Fermilab.* CDF Public Note FERMILAB-FN-1048-E. Fermilab, 2017. URL: `https://www-cdf.fnal.gov/physics/new/bottom/180503.blessed-Bspi/`.